

Walter Schottky Institut
Zentralinstitut der physikalischen Grundlagen der Halbleiterelektronik
Technische Universität München

New Substrates for Epitaxy of Group III Nitride Semiconductors: Challenges and Potential

Claudio Ronald Miskys

Vollständiger Abdruck der von der Fakultät für Physik der Technischen Universität München
zur Erlangung des akademischen Grades eines

Doktors der Naturwissenschaften

(Dr. rer. nat.)

genehmigten Dissertation.

Vorsitzender: Univ.-Prof. Dr. H. Friedrich

Prüfer der Dissertation: 1. Univ.-Prof. Dr. M. Stutzmann
2. Univ.-Prof. Dr. Dr.h.c. A. Laubereau

Die Dissertation wurde am 30. Juni 2004 bei der Technischen Universität München eingereicht und durch die Fakultät für Physik am 12. Oktober 2004 angenommen.

*„Es gibt die Zeit zu kommen,
es gibt die Zeit zu gehen...
und man sollte die nicht verpassen.“*

für meine Eltern

*“There is time to come,
there is time to go...
and one should not miss them.“*

Zusammenfassung

Die erstaunliche Herausforderung der Gruppe-III Nitride sowohl in der grundlegenden Physik aber auch in den technologischen Anwendungen scheint unbegrenzt zu sein. Kein anderes Material hat das Potential, die Welt, die wir kennen, sehen und hören in naher Zukunft so zu verändern, wie GaN und seine verwandten Legierungen. Der Paradigmenwechsel hat bereits begonnen, bei dem elektrisch erzeugtes Licht langsam von elektronisch erzeugtem abgelöst wird, ähnlich der Ersetzung der Kerzen, Öl- und Gaslampen durch elektrische Glühlampen vor gut 100 Jahren. Aber das ist längst nicht alles, es steckt noch viel mehr dahinter. Das Ziel dieser Dissertation ist es, einen kleinen Teil dieser Möglichkeiten und der sich ergebenden Probleme zu erforschen.

Bei der GaN-basierten Dünnschichttechnologie haben die allgemein benutzten Substratmaterialien deutlich andere materielle Eigenschaften als die elektronische Bauteilschicht selbst. Die Entwicklung der GaN-basierten Bauelemente brachte eine Änderung im herkömmlichen Denken bezüglich der für eine erfolgreiche Herstellung der Bauelemente notwendigen Materialanforderungen mit sich. Im Gegensatz zu den meisten im Handel erhältlichen Halbleitermaterialien, wurde die Kommerzialisierung von GaN-basierten Bauelementen ausschließlich über die Verwendung von fremden Substraten, Saphir und SiC, erzielt. Überraschenderweise haben selbst hohe Versetzungsdichten, die bis zu vier Größenordnungen über dem für eine leistungsfähige Lumineszenz maximal tolerierbaren Schätzwert liegen, die Anwendung von GaN als effizienten lichtemittierenden Halbleiter nicht verhindert, dessen Lichtspektrum vom sichtbaren zum ultravioletten Bereich reicht. Für die Produktion von Bauelementen in industriellem Maßstab, muss das Substrat der Wahl eine Reihe von Kriterien, wie eine minimalen Größe (2"), atomar glatte Oberflächen und die Verfügbarkeit in großen Quantitäten zu einem annehmbaren Preis erfüllen. Saphir war und ist

noch die übliche Wahl für GaN-basierte Leuchtdioden (LED) wegen seiner recht niedrigen Kosten und seiner guten Verfügbarkeit. Eigentlich sind seine Eigenschaften unpassend, wenn die entsprechenden typischen Anforderungen, die ein Substrat für erfolgreiche Epitaxie erfüllen sollte, berücksichtigt werden. Die Gitterfehlpassung mit GaN ist sehr groß, ebenso die Differenz der entsprechenden Wärmeausdehnungskoeffizienten. Die hohen Versetzungsdichten sind für die Leistung von Bauelementen mit kritischeren Anforderungen als LEDs, wie z.B. Hochleistungslaserdioden, schädlich. Außerdem stellen die Eigenschaften des Saphirs doch Begrenzungen für die endgültige Qualität der epitaktischen Schicht dar, trotz seiner vielseitigen Verwendbarkeit in der GaN-basierten Verfahrenstechnik. Heteroepitaxie war die einzige Alternative für GaN-Wachstum, da Halbleiterscheiben aus GaN-Volumenkristallen nicht käuflich erhältlich waren und noch immer nicht sind.

Die Eigenschaften und die Qualität der GaN-Schicht sind hauptsächlich vom Substrat abhängig, auf dem sie abgeschieden wird. Das Substrat bestimmt die Kristallrichtung, die Polarität, die Oberflächenmorphologie, die Verspannung und die Störstellendichte der GaN-Schicht, und ist somit direkt für das Erzielen einer optimalen Leistung des Bauelementes verantwortlich. Viele unterschiedliche Materialien einschließlich Metalloxide, Metallnitride und andere Halbleiter wurden im Hinblick auf die GaN Epitaxie untersucht. Um das große Anwendungspotential der Gruppe-III-Nitride vollständig nutzen zu können, ist es wünschenswert, epitaktisches Wachstum auf gitterangepassten Substraten einzusetzen. Die Möglichkeit, überlegene strukturelle Qualität durch homoepitaktisches Wachstum von GaN auf GaN-Volumenkristallen oder Volumenschichten, so genannten Quasi- oder Pseudo-Substraten, zu erzielen ist bereits demonstriert worden. Es gelang eine Reduzierung der Versetzungsdichten um sechs Größenordnungen, das Erreichen einer höheren Ladungsträgermobilität sowie von schmaleren Photolumineszenz-Linienbreiten im Vergleich zum üblichen heteroepitaktischen Wachstum. Durch Homoepitaxie kann zweidimensionales Wachstum von GaN ohne zusätzliche Depositionsschritte wie Oberflächennitridation,

Niedertemperatur-Nukleationsschichten oder dicken Pufferschichten erzielt werden. Kantenemittierende Laser können durch Spalten anstatt durch zeitaufwendige reaktive Ionen-Ätz-Prozesse, die auch noch zusätzlich Defekte auf der Kristalloberfläche produzieren, hergestellt werden. Zusätzlich kann das GaN-Substrat n- oder p- dotiert werden, was eine bedeutende Vereinfachung in der Verarbeitung der Bauelemente und deren Integration in elektronische Schaltkreise ermöglicht.

Da der Weg zur besten strukturellen Qualität nach wie vor über homoepitaktisches Wachstum führt, wurde konzentriert an Methoden für die Produktion von GaN- und AlN-Volumenkristallen geforscht. Viel Arbeit wurde aber auch in die Herstellung von dicken, großflächigen und freitragenden GaN- und AlN- Schichten investiert, die in der Gruppe III Nitrid-basierten Epitaxie verwendet werden sollen. Die strukturellen Eigenschaften von GaN und die Epitaxie z.B. auf Saphir, SiC, Silizium, GaAs oder LiGaO₂, werden dargestellt und betrachtet. Außerdem werden die Herstellung und die praktische Bedeutung der Volumen- und der Pseudo-Substrate diskutiert. Zusätzlich wird noch Diamant als mögliches Substratmaterial für Gruppe III-Nitride Epitaxie einbezogen. Er stellt einen neuen Ansatz für die Entwicklung einer neuen Generation von Bauelementen für Lichtemission und Hochleistungsanwendungen dar.

Besondere Aufmerksamkeit wurde der Herstellung der freistehenden GaN Pseudo-Substrate gewidmet. Die bemerkenswerten optischen und strukturellen Eigenschaften, die aus der GaN-Homoepitaxie auf solchen Substraten resultieren, werden demonstriert. Ein Hauptziel der vorliegenden Arbeit war die Optimierung des Laser Ablösungs-Prozesses für die Delaminierung der GaN-Schichten mit Dicken von einigen Mikrometern bis zu 120 µm. Der Effekt der Laser-Ablation auf GaN und Saphir wird gezeigt und analysiert, sowie auch das kritische Problem einer erfolgreichen Trennung der GaN-Schichten. Außerdem wurde die Flexibilität des Laser-Ablöseverfahrens in der Verarbeitung dünner InGaN/GaN-Heterostrukturen für die Produktion freistehender *flip-chip* kontaktierter blaue/violetter LEDs

demonstriert. Ein Modell für thermischen Transport während der Behandlung mit dem Hochenergie-Laser wurde entwickelt, um den Effekt des plötzlichen Temperaturanstieges während eines Laser-Impulses und die möglichen Konsequenzen Nitrid-basierte Bauelemente zu simulieren.

Dicke GaN-Volumenschichten können durch Hydrid-Gasphasenepitaxie (HVPE) produziert werden. Hochqualitative, 2“ große und 300 µm dicke freitragende GaN-Substrate, hergestellt durch den an HVPE-GaN angewendeten Laser-Ablöse Prozess, sind nach vorsichtiger Vorbehandlung der Schichtoberfläche als Substrate für die Nitrid-Epitaxie verwendbar. Dies wurde durch homoepitaktisches Wachstum von 2 µm dicken GaN-Schichten mittels MOCVD bestätigt. Die guten elektrischen und optischen Eigenschaften der homoepitaktischen Schichten machen freitragendes HVPE-GaN zu einem attraktiven Substrat für die Herstellung der GaN-basierten Bauelemente. Motiviert durch diese Erfolge der Laser-Induzierten-Ablöse Technik, implementieren einige Firmen momentan diese Technologie für die Massenproduktion freitragender GaN-Substrate und *flip-chip* kontaktierter GaN-basierter Bauelemente.

Abschließend wird die Realisierbarkeit von UV-lichtemittierenden Bauelementen durch Nitrid-Heteroepitaxie auf einkristallinen Diamantsubstraten demonstriert. Nach der Herstellung von stark leuchtenden InGaN-basierten LEDs mit Emissionwellenlängen vom nahen Ultraviolett (UV) bis grün, hat es ein wachsendes Interesse an Emittoren mit Wellenlängen im tiefen UV-Bereich (200 bis 360 nm) gegeben. Die intensive Aufmerksamkeit für die tiefen UV-Emitter liegt an einer beträchtlichen Anzahl von möglichen Anwendungen. Zum Beispiel können UV-LEDs mit Dreiband-Phosphor (rot, grün und blau leuchtend) beschichtet werden, um weißes Licht zu produzieren. Solche LEDs könnten auch benutzt werden, um biologische Moleküle anzuregen, die chemische Bindungen mit starken optischen Resonanzen innerhalb der spektralen UV-Region enthalten (240 bis 350 nm). Ebenso würden Speichervorrichtungen mit hoher Dichte, Lithographieinstrumente

und chemische Prozesse in medizinischen Anwendungen und Recycling aus der kurzen Wellenlänge der UV-Strahlung profitieren.

Epitaktisches Wurtzit (0001) AlN:Si (n-Typ) ist mittels PIMBE erfolgreich auf (100) Diamantsubstraten mit natürlicher Bor-Dotierung (p-Typ) gewachsen worden. Die überraschend gute strukturelle Qualität der AlN-Schicht ist durch Hochauflösungsröntgenbeugung bestätigt worden. Die hergestellten p-n Heteroübergangsdioden zeigen klare Diodenkennlinien mit einem Gleichrichtungsverhältnis („*rectification ratio*“) zwischen 10^3 und 10^4 bei kleinen Spannungen. Unter Vorwärtvorspannung wird eine Emission im Blauen und im UV erreicht. Außerdem erlaubt die spektrale Photostromanalyse die Aussage, dass die UV-Emission mit einer Defektstelle an der Grenzfläche und nicht in der AlN-Schicht oder im Diamantsubstrat zusammenhängt. Die gemessene „*built in*“ Spannung ist in Übereinstimmung mit dem Vorhandensein einer Rekombinationstelle an der Diodengrenzfläche. Die erreichten Ergebnisse bestätigen offenbar das Entwicklungspotenzial von heteroepitaktischem Wachstum der III-Nitride auf Diamant. Dadurch werden interessante Perspektiven für zukünftige optoelektronische Bauelemente, die im tiefen UV arbeiten, eröffnet.

Table of Contents

1 The Substrate Issue for Group III Nitride Epitaxy	1
1.1 Material Properties of GaN	5
1.2 Sapphire	6
1.3 SiC	12
1.4 Si	18
1.5 GaAs	23
1.6 LiGaO ₂	27
1.7 AlN	32
1.8 GaN Substrates	37
1.9 Diamond	42
2 Laser-Induced Lifting Method for GaN on Sapphire	54
2.1 Sapphire Detachment from GaN Films	54
2.2 Laser-Induced Thermal Decomposition of GaN	56
2.3 Experimental Setup for Laser-Induced GaN Delamination	64
2.4 Laser-Induced Lifting of Thick HVPE-GaN Wafers	66
2.5 Laser-Induced Lifting of HVPE-GaN Membranes	68
2.6 Delamination of Wafer Bonded GaN Thin Films and Heterostructures	74
2.7 Cracking Mechanics of GaN Films on Sapphire	78
2.8 Sapphire-Wafer Recycling after GaN Delamination	88
2.9 Laser Lifting for the Production of Blue/Violet InGaN/GaN LEDs	90
2.9.1 Highly Efficient GaN-based LEDs: current state-of-the-art	91
2.9.2 Flip-Chip Technique for LED Production	96
2.9.3 Flip-Chip Mounting of InGaN-LEDs for Laser-Induced Lifting	99
2.9.4 Laser-Induced Lifting for Freestanding Violet Nitride-LEDs	100
2.9.5 Laser/Target Interaction	107

3	Homoepitaxy on Freestanding GaN Substrates	115
3.1	Preparation of Freestanding GaN Films for Homoepitaxy	116
3.2	Homoepitaxy on Freestanding HVPE-GaN Substrates	122
3.3	Structural Characterization of Homoepitaxial GaN	127
3.4	Optical and Electrical Characterization of Homoepitaxial GaN	129
4	AlN Heteroepitaxy on Diamond for Ultraviolet Light Emission	139
4.1	Nitrides on Diamond: the Doping Issue	139
4.2	AlN Heteroepitaxy on Diamond	144
4.2.1	Texture Analysis	148
4.2.2	Epitaxial Relation: in-plane offset	150
4.2.3	Relaxation and Film Quality	155
4.2.4	Surface Morphology	158
4.3	AlN/Diamond Heterojunction Diode	162
4.4	Concluding Remarks and Outlook	172
5	Summary	176
	References	180
	List of Publications	196
	List of Abbreviations	199
	Acknowledgements	201

1 The Substrate Issue for Group III Nitride Epitaxy

Some of the most challenging aspects of GaN-based thin-film technology, as compared to other device material systems such as Si or GaAs, come from the fact that the commonly used substrate materials have very different material properties than the device layer itself. The development of GaN-based devices has brought a change in the conventional thinking about the material requirements for successful device fabrication. In contrast to the majority of commercially available semiconductors, commercialization of GaN-based devices was achieved exclusively by using heteroepitaxial substrates. Surprisingly, dislocation densities 4 orders of magnitude higher than the minimum thought to be required for efficient luminescence did not make GaN fail as a promising light emitter, from the visible to the ultraviolet spectral range. In the standard vapour phase epitaxy methods (VPE, MOCVD) for GaN growth the high concentration of ammonia and hydrogen at high temperatures (1000°C) reduces the choice of possible substrates. The need of a low-temperature buffer layer in the first step of device fabrication is essential to allow the use of substrates such as Si, GaAs and GaP (Tab. 1.1). Even for molecular beam epitaxy (MBE) with growth temperatures about 250°C lower than for VPE and MOCVD, the stability of the substrate surface during growth is a critical issue because of the influence of nitrogen radicals at 800°C. For device production on an industrial scale, the substrate of choice has to fulfill a number of criteria, such as a minimum size (2"), atomically flat surfaces and availability in large quantities at an acceptable price. Sapphire was and still is the most common choice for GaN-based light-emitting diodes (LEDs) because of its reasonably low cost and wide availability, although its properties are seemingly unsuitable according to the usual assumptions made in choosing a substrate for epitaxy. It has large lattice constant and thermal expansion coefficient mismatches with GaN.

Nevertheless, in agreement with the conventional knowledge, high dislocation densities are detrimental to the performance of devices with more critical requirements than LEDs, such as laser diodes operating at high power densities [1]. Furthermore, the properties of sapphire do set limits on the final quality of the epitaxial film despite its versatility in the GaN-based processing technology. Heteroepitaxy was the only alternative for GaN growth, since bulk wafers were and still are not commercially available. The properties and quality of the GaN film is primarily dependent on the substrate on which it is deposited. The lattice constant mismatch has been the primary criteria for determining the suitability of a material as a substrate for GaN, but in practice other material's issues including crystal structure, composition, reactivity, chemical, surface termination, thermal, and electrical properties have strong influence on the final epitaxial layer. The substrate determines the crystal orientation, polarity, surface morphology, strain, and the defect concentration of the GaN film and is directly responsible for achieving optimal device performance. Many different materials have been investigated for GaN epitaxy including metal oxides, metal nitrides, and other semiconductors. A list of possible candidates and their crystal structure and lattice constants is given in Tab. 1.1.

The influence of the substrate on the crystal polarity and polarization characteristics of the group III nitrides is particularly important. Thus, the chemical reactivity and the conditions required for good quality epitaxy depend on the polarity of the III-nitride crystal. The substrate determines the crystal polarity and the magnitude and sign (tensile or compressive) of the strain incorporated into the epitaxial film, and consequently the magnitude of the polarization effect. Heteroepitaxy brings many problems to the GaN growth. The misfit and threading dislocation densities of GaN films deposited on the commonly used substrates sapphire and SiC are typically between 10^8 and 10^{10} cm^{-2} . For comparison, in GaAs and silicon homoepitaxy the dislocation densities are as low as 10^2 to 10^4 cm^{-2} , or almost zero, respectively [2].

Material	Structure	Lattice constants (Å)			Thermal expansion coefficient (10 ⁻⁶ K ⁻¹)	References
		<i>a</i>	<i>b</i>	<i>c</i>		
Semiconductor substrates						
w-GaN	wurtzite	3.1885		5.185	5.45 (<i>a</i>)	[3]
zb-GaN	zinblende	4.511				[4]
r-GaN	rocksalt	4.22				[5]
w-AlN	wurtzite	3.1106		4.9795	4.2 (<i>a</i>)	[6]
zb-AlN	zinblende	4.38				[7][8]
r-AlN	rocksalt	4.04				[9]
ZnO	wurtzite	3.2496		5.2065	2.9	[10][11]
β-SiC	3C-zinblende	4.3596			3.9	[12][13]
SiC	4H-wurtzite	3.073		10.053		[12]
SiC	6H-wurtzite	3.0806		15.1173	4.46 (<i>a</i>)	[12][13]
C - diamond	diamond	3.567			0.80	[14] [15]
GaAs	zinblende	5.6533			6.0	[16]
GaP	zinblende	5.4309				[17][18]
Si	diamond	5.4310			2.59	[19]
Oxides and sulphide substrates						
Al ₂ O ₃ - sapphire	rhomboidal	4.758		12.982	7.50 (<i>a</i>)	[20][21]
MgAl ₂ O ₄ - spinel		8.083			7.45	[22][23][24]
MgO	rocksalt	4.21			10.5	[7][25]
LiGaO ₂	orthorhombic	5.4063	6.3786	5.0129	9.0 (<i>a</i>)	[26]
Γ-LiAlO ₂		5.169		6.267	15 (<i>a</i>)	[27][28][29]
NdGaO ₃	orthorhombic	5.428	5.498	7.71	11.9 (<i>a</i>)	[30][31][32]
ScAlMgO ₄	wurtzite	3.236		25.15		[33][34]
Ca ₈ La ₂ (PO ₄) ₆ O ₂	apatite	9.446		6.922		[35]
MoS ₂						[36][37]
LaAlO ₃	rhomboidal	5.364		13.11		[38]
(Mn,Zn)Fe ₂ O ₄	spinel	8.5				[39]
Ca ₈ La ₂ (PO ₄) ₆ O ₂	apatite	9.446		6.922		[35]
Metals and metal nitride substrates						
Hf	HCP	3.18		5.19		[40][41]
Zr	HCP	3.18		5.19		[41]
ZrN	rocksalt	4.5776				[42]
Sc	HCP	3.309		5.4		[43]
ScN	rocksalt	4.502				[43][44]
NbN	rocksalt	4.389				[45]
TiN	rocksalt	4.241				[46][47]

Tab. 1.1: Substrates for GaN epitaxy.

In addition, inversion domains boundaries and stacking faults caused by the heteroepitaxy [48][49], create non-radiative recombination centers in the band gap, thereby reducing minority carrier lifetimes. Threading dislocations form an undesirable path for easy impurity diffusion, causing an inhomogeneous impurity distribution throughout the GaN film and a degradation of pn junction abruptness [50] and optical properties. The amount and the non-uniformity of the various defects created by the heteroepitaxy at present definitively prevent GaN-based devices to achieve their optimum performance. Many efforts were made in GaN heteroepitaxy, mainly based on sapphire, to improve the crystal quality of the grown films. Successful approaches include an appropriate surface preparation of the substrate such as nitridation, deposition of a low-temperature (LT) AlN or GaN buffer layer, multiple intermediate LT buffer layers [51], epitaxial lateral overgrowth (ELOG) [52], *pendeo* (from Latin: be suspended)-epitaxy [53], and other techniques [54-56]. GaN layers with dislocation densities as low as 10^7 cm^{-2} have been produced by such techniques. Despite this success, even lower defect densities are necessary for more sophisticated devices operating at more extreme conditions of temperature, voltages, and current densities. Thus, substrates capable of producing better quality GaN epitaxial layers are needed for realizing the full potential of GaN-based devices. As the key for the best material quality is still homoepitaxial growth, this has concentrated research on methods of producing GaN and AlN bulk crystals. But also much work was focused in the production of large and thick GaN and AlN freestanding films to be used as pseudo-substrates in the group III nitride-based epitaxy.

In the following sections some considerations of the material properties of GaN and epitaxy *e.g.* on sapphire, SiC, Si, GaAs, or LiGaO₂ will be presented. Furthermore, the discussion will involve the production and the practical relevance of bulk and pseudo-substrates. In the last section, diamond is considered as a possible substrate material for group III nitrides epitaxy.

1.1 Material Properties of GaN

GaN has become an attractive semiconductor for many optoelectronic applications due to its interesting physical properties (Tab. 1.2). The direct band gap of GaN together with its good thermal and chemical stability (if compared to Si and GaAs) make this semiconductor suitable for short wavelength emitters (LEDs and diode lasers) and detectors, but also for high power and high temperature electronic devices. The group III nitrides (AlN, InN and GaN) have the ability to form alloys in the energy band gap range from 0.8 eV (InN) to 6.2 eV (AlN), enabling the creation of heterojunctions.

Properties	Values	References
Melting point (K) (@ 60 kbar)	>2573	[57]
Density (g/cm ³)	6.1	[57]
Lattice constants <i>a</i> and <i>c</i> (Å) (@ 300 K)	3.188 and 5.185	[3]
Thermal expansion $\Delta a/a$ and $\Delta c/c$ (%) (@ 300 to 1400 K)	0.575 and 0.503	[3]
Thermal conductivity (W/cm K) (@ 300 K)	2.1	[58]
Heat capacity (J/mol K) (@ 300 K)	35.3	[59]
Young's modulus of elasticity (GPa)	210	[60]
Yield strength (MPa) (@ 1000 K)	100	[61]
Hardness (GPa) – nanoindentation (@ 300 K)	15.5	[62]
Energy band gap (eV) (@ 300 K)	3.44	[63]
Maximum electron mobility (cm ² /Vs)		
300 K	1245	[64]
77 K	7500	[64]
Maximum hole mobility (cm ² /Vs) (@ 300 K)	13	[65]
Controlled carrier density range (cm ⁻³) (@ 300 K)		
n – type	10 ¹⁶ to 4 × 10 ²⁰	[66]
p – type	10 ¹⁶ to 6 × 10 ¹⁸	[66]

Tab. 1.2: Material and electrical properties of wurtzite GaN.

The homodynamically stable structure of gallium nitride is the wurtzite lattice consisting of alternating close-packed planes of Ga and N atoms stacked in an ABABAB sequence in the (0001) direction (Fig. 1.1). The wurtzite GaN cell forms a tetrahedron with a non-centro symmetric atomic arrangement. In wurtzite nitrides, the high electronegativity difference between Ga and N is responsible for one of its most interesting characteristics: a strong piezoelectricity and spontaneous polarization [67-71].

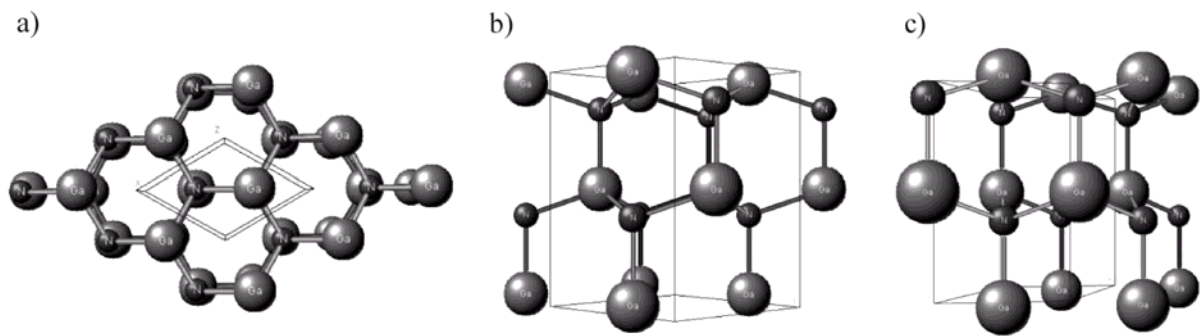


Fig. 1.1: Atomic structure views of wurtzite GaN along the crystallographic directions a) (0001), b) $(11\bar{2}0)$, and c) $(10\bar{1}0)$.

The crystal faces perpendicular to the c -axis in the group III nitrides have either a group III element (Al, Ga, In) polarity, designated as (0001) or (0001)A or a N-polarity, designated as $(000\bar{1})$ or $(000\bar{1})B$ [72].

1.2 Sapphire

The aluminum oxide (Al_2O_3) single crystal was originally used in 1969 by Maruska and Tietjen in their pioneering work on GaN epitaxy by hydride vapour phase epitaxy (HVPE) [73], and it remains the most commonly employed substrate for GaN epitaxy. In the case of GaN growth on (0001) c -plane sapphire substrates, an effective 13.9% lattice constant mismatch $\{f = (a_{\text{sapph}} - a_{\text{GaN}}) / a_{\text{GaN}}\}$ induces dislocations soon after the start of growth to

compensate the strain [74]. Much of the progress in GaN-based technology has been achieved using tricks [51-56] to reduce the dislocation density of about 10^{10} cm^{-2} in the GaN epitaxial films [2]. However, even if sapphire were perfectly lattice matched to GaN during growth, the difference in thermal expansion coefficients between the two materials, $7.50 \times 10^6 \text{ K}^{-1}$ for sapphire and $5.45 \times 10^6 \text{ K}^{-1}$ for GaN [75], would still induce strong biaxial compressive stress in the GaN after cooling down from growth temperatures around 1000°C . This stress is one of the reasons why a critical thickness for GaN layers exists, beyond which cracking is induced [76].

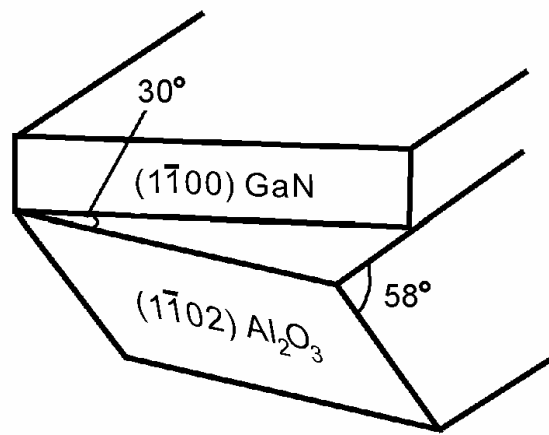


Fig. 1.2: Cleavage plane of wurtzite GaN (0001) on sapphire (0001) substrate.

Sapphire's thermal conductivity at room temperature of 0.3 W/cm K [21] is about 7 times lower than of GaN, 2.1 W/cm K [77]. Therefore, sapphire is a bad heat dissipater compared to some other substrates, which is a big disadvantage for high power devices. Sapphire is electrically insulating with a resistivity higher than $10^{11} \Omega \text{ cm}$ [21], therefore only planar device structures with contacts on the front side are possible. In addition, the cleavage planes of sapphire do not have the same direction than those of epitaxial wurtzite GaN (Fig. 1.2), making laser facet formation by cleavage very difficult. A summary of the main material properties of sapphire is presented in Tab. 1.3.

Properties	Values
Melting point (K)	2003
Density (g/cm^3)	3.98
Lattice constants a and c (\AA) (@ 300 K)	4.758 and 12.982
Thermal expansion $\Delta a/a$ and $\Delta c/c$ (%) (@ 293 to 1300 K)	0.83 and 0.892
Thermal conductivity (W/cm K) (@ 296 K)	0.3
Heat capacity (J/mol K) (@ 300 K)	77.9
Modulus of elasticity (GPa)	452-460 in (0001) direction
Yield strength (MPa) (@ 300 K)	190
Hardness (GPa) – nanoindentation (@ 300 K)	23.9
Energy band gap (eV) (@ 300 K)	8.1 - 8.6
Resistivity ($\Omega \text{ cm}$) (@ 300 K)	$>10^{11}$

Tab. 1.3: Material and electrical properties of sapphire [20][21][78].

Although sapphire has a rhombohedral structure, it can be described by a hexagonal cell that is larger than the basic rhombohedral unit cell. The crystal structure of the hexagonal unit cell of sapphire and a perspective view along the (0001) direction is shown in Fig. 1.3.

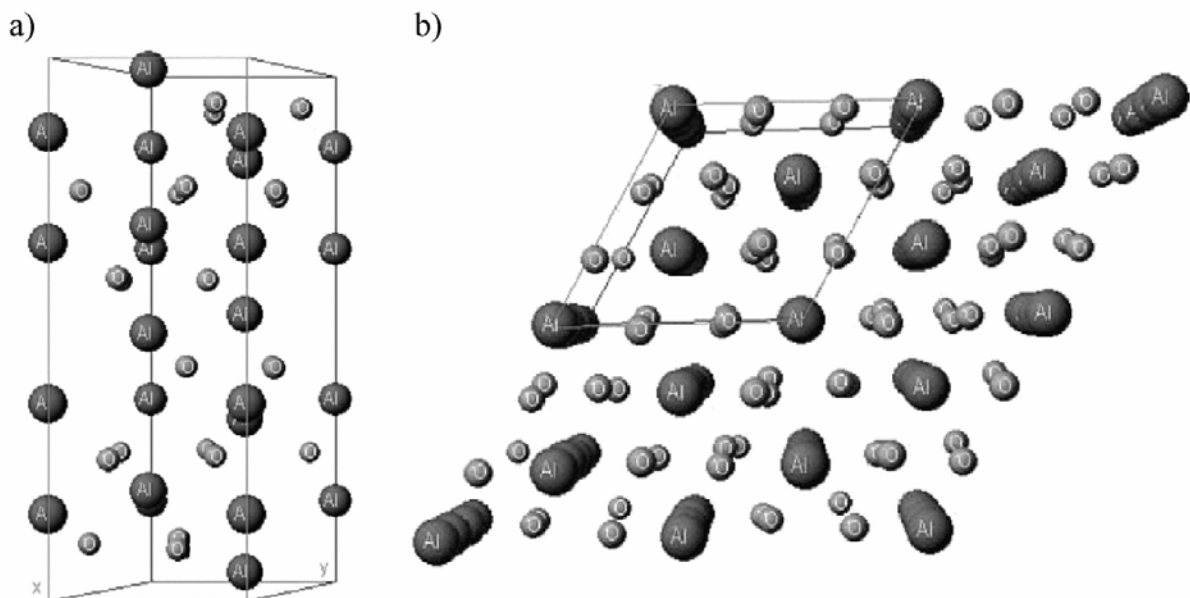


Fig. 1.3: Crystal structure of hexagonal sapphire: a) the unit cell; b) perspective view along the (0001) direction [77].

The hexagonal unit cell of sapphire has a volume of 254.7 \AA^3 [77] and is formed by 12 Al^{3+} ions and 18 O^{2-} ions. The unit cell consists of six closed packed (0001) planes of O^{2-} ions intercalated within 12 planes of Al^{3+} ions. The crystal facets of sapphire are shown in Fig. 1.4.

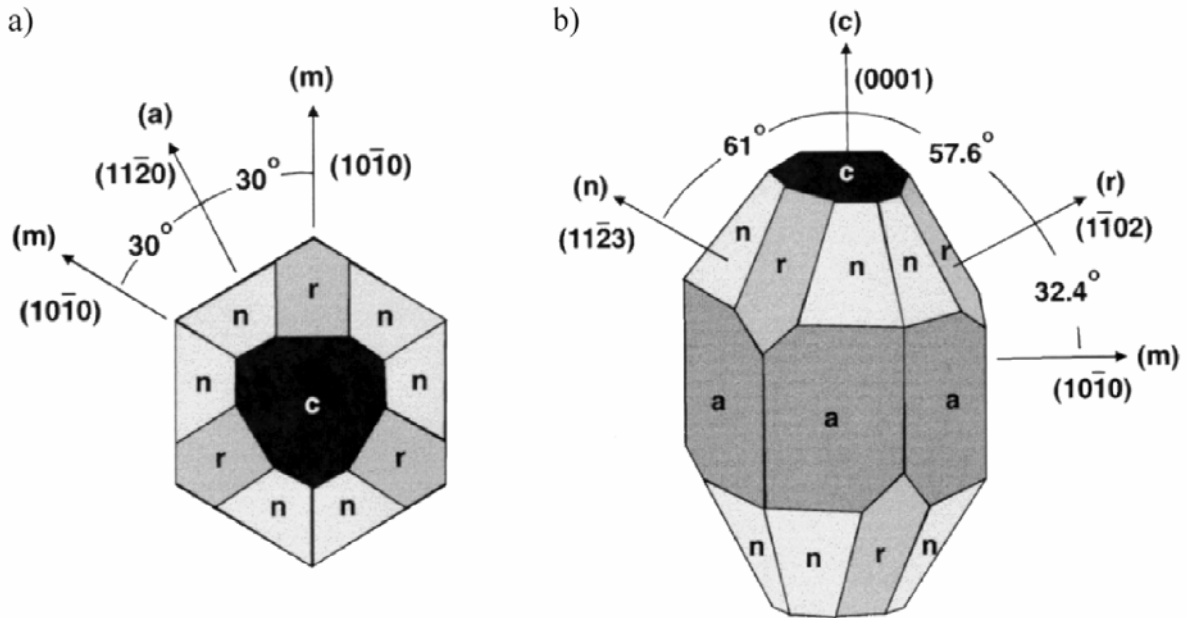


Fig. 1.4: Facets of hexagonal sapphire: a) view along the c -axis; b) perpendicular to the c -axis [79].

As the surfaces employed for GaN epitaxy, the c -plane (0001) and m -plane ($10\bar{1}0$) directions, are non-polar, the crystal polarity of the GaN film is directly dependent on the growth conditions and procedure adopted. To date, the five orientations of sapphire (0001), ($000\bar{1}$), ($10\bar{1}0$), ($2\bar{1}\bar{1}0$), and ($1\bar{1}\bar{1}0$) have been used as substrates. c -plane sapphire is the most commonly used in GaN heteroepitaxy. The orientation of the GaN film on c -plane sapphire has been experimentally determined as shown in Fig. 1.5 [80]. The GaN c -plane is parallel to the c -plane in the sapphire with an in-plane rotation of 30° .

The m -plane of sapphire is the best orientation for to GaN growth considering lattice misfit and crystal symmetry. Nevertheless, the big disadvantage of m -plane substrates comes from the non-alignment of the c -axis of the resulting GaN film and the substrate, allowing the formation of undesirable crystalline twins.

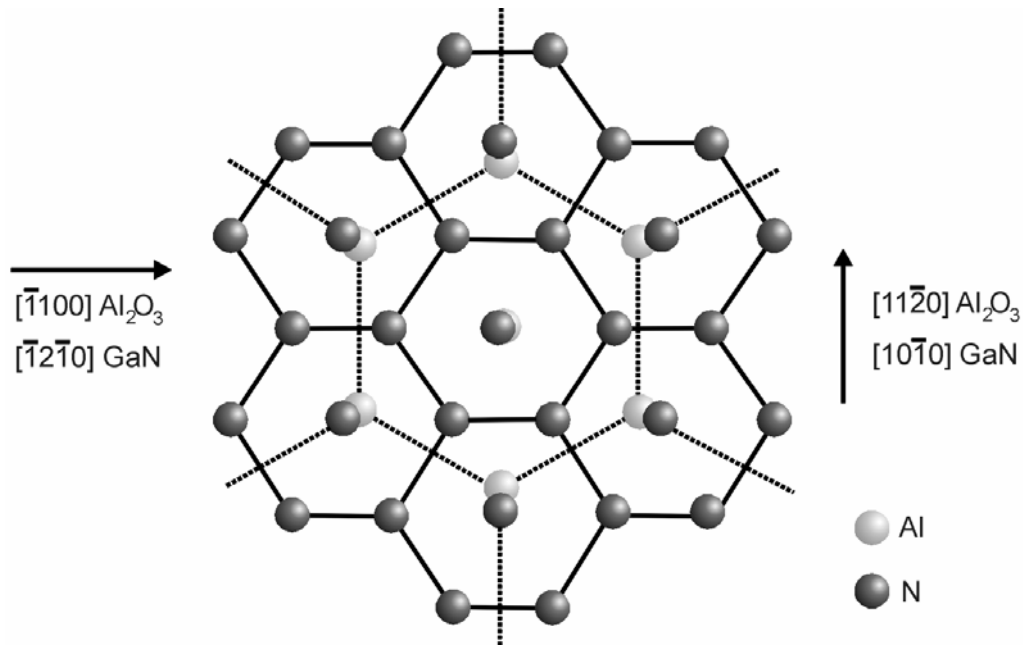


Fig. 1.5: In-plane view of c -plane (0001) GaN on c -plane (0001) sapphire.

The attempts to use different sapphire orientations in GaN growth were also conducted to overcome the big difficulty of cleaving GaN on sapphire substrate. GaN epitaxy on c -plane sapphire generates c -plane oriented films with a 30° in-plane rotation (Fig. 1.2 and Fig. 1.5) to avoid an even higher lattice mismatch. This is the main reason that prevents smooth cleavage planes on the edge of the GaN layer. GaN films grown on a -plane sapphire were also investigated [81] and can be easily cleaved along the r -plane (Fig. 1.4). The first promising result of the fabrication of edge emitting lasers on a -plane sapphire was obtained by Nakamura et. al [82], who reported a pulsed MQW laser with cleaved facet mirrors. It is also interesting to note that, although the lattice mismatch for GaN films grown on a -plane sapphire is much less (2%) than on c -plane (13.9%), no significant crystal quality improvement has been reported. GaN or AlN epitaxy on r -plane sapphire will produce films aligned with the a -axis ($11\bar{2}0$) and not to the usual c -axis direction perpendicular to the substrate surface. This untypical orientation for GaN epitaxy is preferred for AlN and ZnO-based surface acoustic wave (SAW) devices, as it increases the electromechanical coupling coefficient [83][84].

In a comparison of GaN growth by MBE on *c*-, *a*-, *r*-, and *m*-plane sapphire substrates [85] smooth and flat films were obtained on *c*-plane, and somewhat rougher ones on *a*-plane sapphire. The growth on *r*- and *m*-plane substrates resulted in rougher GaN layers with mixed orientations (0002) and (11 $\bar{1}$ 0), as measured by XRD diffraction. Considering rocking curves and photoluminescence data, the best crystalline quality was obtained on the *c*-plane sapphire. Some authors [82][86] observed significant improvements in the quality of GaN films grown on sapphire substrates with orientations other than the usual *c*-plane, by growing smooth, single crystal GaN on *m*-plane sapphire misoriented by 15° to 20°. In this way twinning and rough surfaces could be avoided, but the dislocation density was still 50% higher compared to GaN growth on *c*-plane sapphire.

Due to the large lattice mismatch between GaN and sapphire, the epitaxial GaN film grows almost completely relaxed right from the beginning. The high defect density is concentrated at the interface by forming a coincidence lattice which relieves a large portion (11.8%) of the mismatch in the form of a dislocation network [74]. For example, a 1 μm thick MBE-GaN film has a density of non-confined dislocations of $\sim 10^{10} \text{ cm}^{-2}$ after this relaxation process and the residual strain at its surface is about -0.2% [74]. For a growth temperature of 800°C a lattice mismatch of -13.75% can be calculated taking in account the thermal expansion coefficients of GaN and sapphire perpendicular to the *c*-axis. The residual strain determined at the GaN/Al₂O₃ interface after cooling down is -0.12%, which is comparable to the strain of -0.2% measured at the GaN surface of the 1 μm thick film. From this result it can be derived that GaN films grow almost completely relaxed at the growth temperature and the residual strain is due to a thermal effect. In this highly mismatched heteroepitaxial growth, the first monolayers of GaN form a mosaic of columnar islands before the surface is completely covered. Confined dislocations are generated in these islands with a typical grain size of the order of a tenth to a few micrometers. The confined dislocations lead to the relaxation of a

large part of the lattice misfit. After this initial growth process the final GaN film will contain the dislocation density of about 10^{10} cm^{-2} as mentioned above.

1.3 SiC

Silicon carbide in the hexagonal 4H and 6H polytype has many advantages over sapphire as a substrate for GaN epitaxy. It has a smaller lattice mismatch of 3.1% for (0001) oriented films and a 12 times higher thermal conductivity (3.7 W/cm K) [87]. In addition, electrically conductive SiC substrates can be produced for backside contacting, which is an advantage for some device applications. SiC has a polar crystal structure like GaN with a carbon and silicon polarity, enabling in principle an easier control of the nitride film polarity. The Si-polarity is indeed the most commonly used one for GaN epitaxy. Furthermore, for the production of laser cavity mirrors, the substrate has its cleavage plane perpendicular to the surface because cleavage becomes more reproducible with a perpendicular cleavage than with an inclined one. Among all the hetero-substrate candidates, only SiC fulfils this requirement (Fig. 1.6).

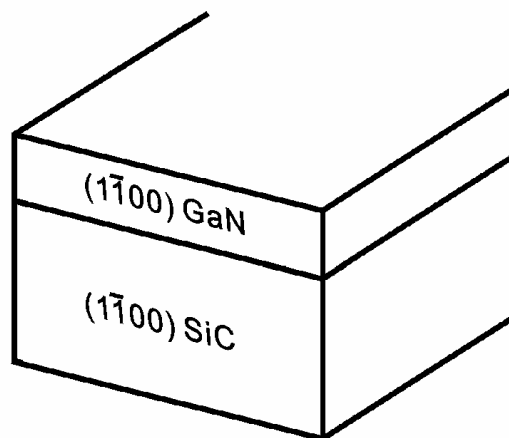


Fig. 1.6: Cleavage plane of wurtzite GaN (0001) on 6H-SiC (0001) substrate.

Difficulties in the use of SiC for GaN growth arise from the poor wetting behavior between these two materials [88]. The use of an AlN or AlGa_N nucleation layer is a possible

solution to overcome this problem, but with the consequence of increasing the electric resistance between device and substrate. Despite of the smaller lattice mismatch, the dislocation density of GaN films grown on SiC is also of the order of 10^{10} cm^{-2} , similar to GaN epitaxy on sapphire. The propagation of crystalline defects from the SiC substrate into the GaN film is mainly responsible for this relative high dislocation density [89]. Compared to GaN, the thermal expansion coefficient of SiC is smaller, resulting in films under biaxial tension after cooling down from growth temperature. The production cost of high quality SiC substrates is high and the market is dominated by one big producer. SiC is a very hard material to handle and polish, complicating the preparation of smooth surfaces for epitaxial needs. The typical surface rms roughness of 1 nm is one order of magnitude higher than that of sapphire (0.1 nm). In spite of these problems, GaN heteroepitaxy on SiC has been successfully optimized and SiC substrates are currently being used as the base for a large fraction of the world production of green, blue, and ultraviolet LEDs. Because of its high thermal conduction coefficient, SiC is the preferred substrate for high power and high frequency devices [90][91].

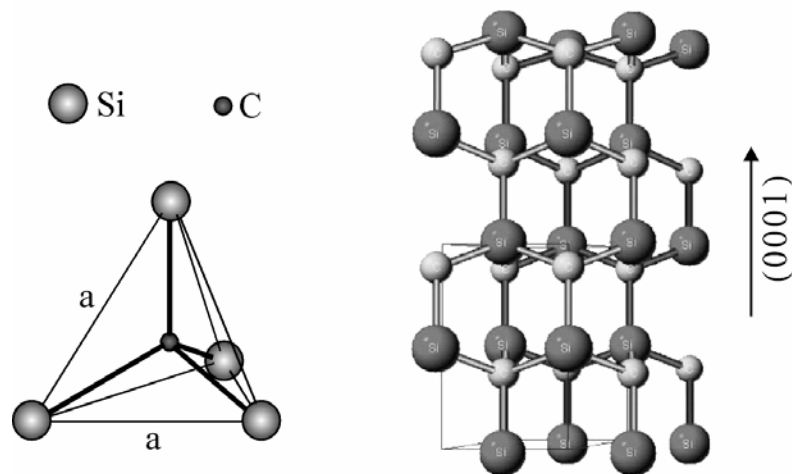


Fig. 1.7: Basic tetrahedral structure of SiC. The distance a of a Si-Si bond and of a C-Si bond are 3.08 \AA and 1.89 \AA , respectively. A three-dimensional view of 2H-SiC is shown on the right.

SiC can crystallize in more than 250 polytypes (one-dimensional variations of the stacking sequence of the closed packed biatomic planes – Fig. 1.8) [92]. The 6H polytype can be

purchased since a long time, but also the 4H-SiC wafers are now commercially available, despite their high prices. The basic structural unit of all polytypes is a covalently bonded tetrahedron with carbon atoms at the corners and a silicon atom in its center or vice-versa (Fig. 1.7).

The crystalline structure results from the periodic repetition (stacking parallel to the c -axis) of this basic-cell and the various polytypes are formed by different stacking arrangements between double layers of C and Si atoms (Fig. 1.8). The distance between neighboring Si and C atoms is approximately 1.89 Å for all polytypes, the c value depends on the stacking mode and the ratios c/a are 1.641, 3.271 and 4.908 for the 2H-, 4H- and 6H-SiC, respectively [93].

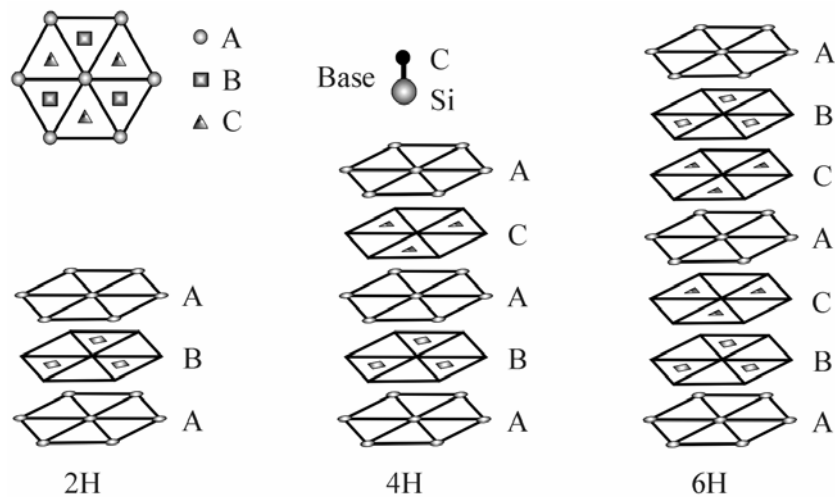


Fig. 1.8: The stacking sequence of 2H-, 4H- and 6H-SiC polytypes.

Bulk SiC is produced by sublimation in a variation of the Lely process developed by Tairov and Tsvetkov in 1978 [94]. A SiC seed crystal is used to control the polytype and the crystal orientation. One big difficulty to produce high quality SiC wafers was caused by the high screw dislocation densities present also in form of micropipes or nanopipes parallel to the c -axis (hollow core screw dislocations) [95]. This particular type of defect was successfully controlled to less than 1 cm^{-2} [96], but much effort is still being done to reduce the high density of residual dislocations of the order of 10^3 to 10^4 cm^{-2} . These defects are

detrimental for SiC-based devices [97][89] and probably also for GaN devices on SiC substrates, but no systematic investigation in this field has been published yet.

Properties	Polytype	Values	References	
Melting point (K)		3086	[98]	
Density (g/cm ³) (@300 K)	6H	3.211	[99]	
Lattice constants a and c (Å) (@ 300 K)	4H	3.0753 and 10.053	[12]	
	6H	3.0806 and 15.117	[12]	
Thermal expansion $\Delta a/a$ and $\Delta c/c$ (%) (@ 300 to 1400 K)	6H	0.4781 and 0.4976	[3]	
Thermal conductivity (W/cm K) (@ 300 K)	4H	3.7	[100]	
	6H	3.6	[100]	
Heat capacity (J/g K) (@ 300 K)	6H	0.71	[101]	
Modulus of elasticity (GPa)		440	[102]	
Energy band gap (eV) (@ 5 K)	4H	3.26	[103]	
	6H	3.02	[103]	
Electron mobility (cm ² /Vs) (@ 300 K)	4H	1000	[103]	
	6H	400	[103]	
Hole mobility (cm ² /Vs) (@ 300 K)	4H	115	[103]	
	6H	101	[103]	
Resistivity (Ω cm) (@ 300 K)				
	Undoped	4H,6H	10 ² to 10 ³	[104]
	semi-insulating	4H,6H	10 ⁵	[104]

Tab. 1.4: Material and electrical properties of SiC.

Table 4 shows some general properties of the most common polytypes 4H- and 6H-SiC used as substrates for GaN epitaxy. 4H- and 6H-SiC wafers are commercially available in low resistivity, semi-insulating, n- and p-type form. Semi-insulating wafers have recently been of interest in group III nitride heteroepitaxy on SiC for AlGaIn-based microwave power devices.

As mentioned, surface preparation is one of the critical problems of SiC substrates. The poor surface finish for epitaxial growth, due to SiC's extreme hardness and high chemical stability produces scratches and subsurface damage [105][106]. Furthermore, the surfaces of as received substrates may terminate at any step position A, B or C (Fig. 1.8). Several

methods have been applied to remove the damage from the SiC surface, including oxidation of the SiC and subsequent etching in hydrofluoric acid [107], etching in HCl + H₂ atmosphere [108][109], high temperature (1500°C) etching in hydrogen [110][111], and reactive ion etching [112][113]. Etching in H₂ is successful to remove all low scale scratches and produces a uniform terrace structure with steps of 1.5 nm height [114].

The nucleation behavior of GaN and AlN on hexagonal SiC is complex. Ga-N does not grow on 6H-SiC at temperatures lower than ~720°C [115]. Above this threshold, three dimensional islands start to form randomly over the SiC surface. On the other hand, AlN nucleation on 6H-SiC starts at lower temperatures (650°C), but also with poor crystallinity and rough surface morphology. The islands have a diameter comparable to their height, suggesting high nucleation rates, but slow growth kinetics, different from to the 3D-columnar growth seen at the initial stages of GaN-AlN epitaxy on sapphire. At temperatures higher than 1100°C AlN forms from the beginning a complete epitaxial film covering the 6H-SiC surface (two-dimensional growth mode). Contrary to the direct growth of GaN on SiC, AlN wets the SiC surface and helps to reduce the lattice constant mismatch to the substrate (3.4%).

In the case of GaN epitaxy on sapphire, AlN low temperature nucleation layers are the key for good quality films [116]. This is not the case for GaN epitaxy on SiC: the AlN crystallites formed on SiC at low temperatures will coalesce to bigger grains during an annealing temperature ramp, but the quality of a subsequent GaN layer is sensibly better with a high temperature AlN nucleation layer [117][118]. Due to its smaller lattice misfit and lower resistivity, AlGaN has been also considered as an alternative to pure AlN nucleation layers [119].

The direct nucleation of GaN at high and low temperatures with posterior annealing ramps has been investigated for the growth on SiC substrates by MBE [120][121] and MOCVD [88][122]. To achieve GaN wetting in MBE growth, a low nucleation temperature is required, which is detrimental for the structural perfection of the individual GaN nuclei [123]. It was

found that any thermal or native oxide has to be completely removed from the SiC surface, otherwise voids are formed in the deposited GaN film [124]. Nitridation in NH_3 flow at 1050°C can be also of benefit for the surface quality, due to a combination of chemisorption and etching [124].

GaN films grown on SiC are typically strained due to the smaller thermal expansion coefficient of SiC with an average biaxial stress up to 1 GPa. This is confirmed by optical characterization of MOCVD and MBE-GaN samples grown on SiC [125], where a tensile stress was quantified in contrast to compressive stressed wurtzite GaN films grown on sapphire. The strain value and sign can vary depending on the initial growth process. In principle, the tensile strain can be avoided by growing GaN on thin coherently strained AlN nucleation layers, minimizing the formation of microcracks in the films. The misorientation of the SiC substrate causes a significant change of the wetting behavior for GaN and AlN epitaxy. The steps on the SiC reduce the distance atoms have to diffuse before being incorporated in the crystal, which enhances two-dimensional growth of GaN [126]. A miscut angle of 4° can relieve the stress at the GaN/SiC interface [127], but induces the formation of many stacking faults at the step edges on the SiC substrate [128]. In contrast, a rougher AlN surface was obtained by MBE growth of AlN on off-angle 6H-SiC (0001) in comparison with growth on on-axis SiC [129]. This is the result of a larger density of AlN islands that can coalesce on the on-axis substrate leading to a two-dimensional growth mode rather than on the misoriented surface.

A last aspect to be considered is the strong influence of the polarity of SiC substrates on the morphology and crystal quality of the epitaxial GaN films. From electronic structure calculations for the (0001) interface, the stronger bonds are expected at the Si/N and C/Ga interfaces [130]. Consequently, Si-face SiC substrates should produce Ga-face epitaxial GaN in (0001) orientation. Different techniques were used to investigate this assumption [131-133], however some experimental results from the literature are in conflict. Stirman

et al. [133] compared high resolution electron microscope images with simulated atomic arrangements for a GaN/SiC heterostructure.

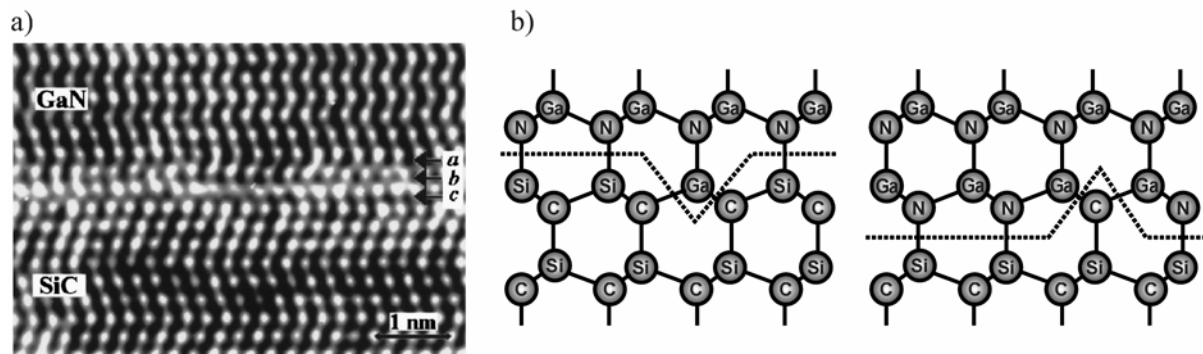


Fig. 1.9: (a) High-resolution electron micrograph of a region of the SiC/GaN interface (atomic columns appear with black contrast). (b) Possible atomic arrangements for GaN/SiC interface with (0001) oriented substrate and epilayer [133].

They concluded that the interface should consist mainly of N atoms bonded to Si atoms, but also with some Ga-C bonds (Fig. 1.9) to prevent a built-in of charge caused by the different electronegativities of the atoms: the interface can be either negatively (N-Si bonding) or positively (Ga-Si bonding) charged. The extra charges can induce an instability of the interface, which usually leads to formation of poor quality films [134]. The growth of Ga-face GaN on Si-face SiC and of N-face GaN on C-face SiC is considered as the “standard framework” [72] and most of the published data is consistent with this conclusion.

1.4 Si

Silicon, the most widely used semiconductor worldwide is a very attractive substrate for GaN heteroepitaxy since it is available in very high quality, from small to very large size and at very low price in comparison with other commercial semiconductors. Also other physical properties of Si are favorable, *e.g.* its high crystal perfection with almost perfect surfaces and

a good thermal stability at GaN growth temperatures. A GaN-on-silicon technology could help to accelerate the acceptance of GaN for microelectronic and optoelectronic applications.

The main physical, chemical, mechanical, and optical properties of Si are listed in Tab. 1.5. The advantages of Si as a substrate and the possibility of monolithic integration of GaN devices with Si electronic devices [135] motivated many research groups to try to overcome the difficulties of GaN heteroepitaxy on Si substrates in particular the very large lattice and thermal expansion coefficient mismatch. A further problem of silicon is its tendency to form an amorphous silicon nitride film when exposed to reactive nitrogen sources. Silicon (111) has a cleavage direction that coincides with that of wurtzite GaN (0001) as shown in Fig. 1.10, which enables the production of cavity mirrors for lasers using cleavage.

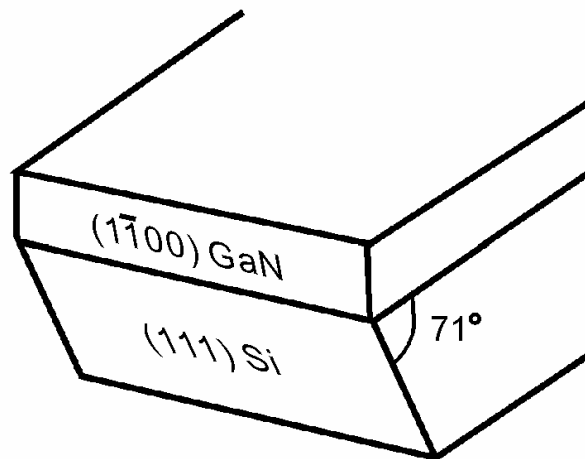


Fig. 1.10: Cleavage plane of wurtzite GaN (0001) on a Si (111) substrate.

The quality of GaN on Si has not reached the same standard as for sapphire or SiC. Nevertheless, GaN-based devices like LEDs and HEMTs were demonstrated on Si substrates by using different concepts like insertion of low-temperature AlN interlayers, introducing multiple AlGaIn/GaN interlayers, and growing on pre-patterned substrates (epitaxial lateral overgrowth or *pendeo*-epitaxy) to reduce the defect density of the overgrown layers [136-139].

Properties	Values	References
Melting point (K)	1787	[140]
Density (g/cm ³)	2.329	[141]
Lattice constants a (Å) (@ 300 K)	5.431	[141]
Thermal expansion coeff. $\Delta a/a$ (%) (@ 300 to 1300 K)	0.3995	[142]
Thermal conductivity (W/cm K) (@ 300 K)	1.56	[143]
Heat capacity (J/g K) (@ 300 K)	0.70	[144]
Modulus of elasticity (GPa)	165.6	[145]
Energy band gap (eV) (@ 300 K)	1.124	[146]
Electron mobility (cm ² /Vs) (@ 300 K)	1448	[147]
Hole mobility (cm ² /Vs) (@ 300 K)	495	[148]
Resistivity (k Ω cm) (undoped, @ 300 K)	50	[144]

Tab. 1.5: Material and electrical properties of Si.

The structure of silicon (diamond lattice) belongs to the cubic-crystal family with two interpenetrating face-centered cubic (*fcc*) sublattices, shifted with respect to each other by one quarter of the body diagonal ($a\sqrt{3}/4$, where $a = 0.543$ nm). Fig. 1.11 shows perspective views of a Si unit cell in different directions:

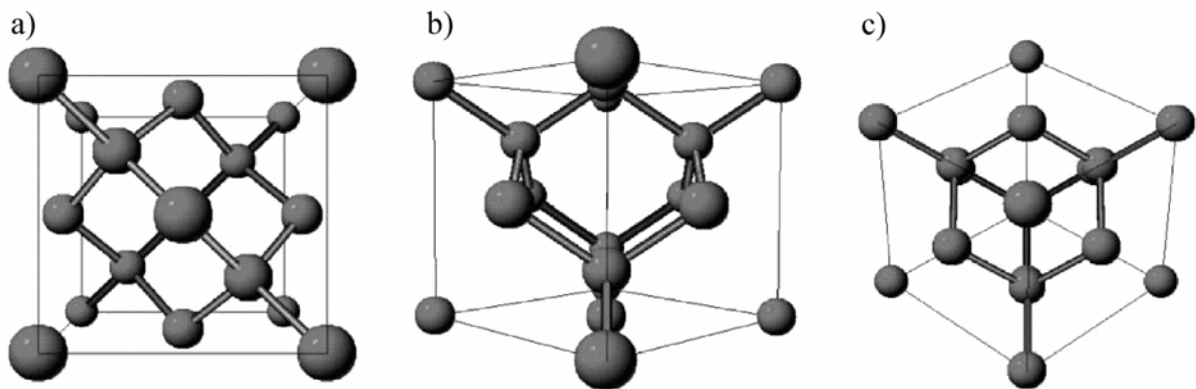


Fig. 1.11: Atomic structure views of a Si unit cell in the crystallographic directions a) (001), b) (011), and c) (111).

The large lattice constant mismatch between Si and GaN makes the growth of pure zincblende GaN or good quality wurtzite GaN on Si (001) extremely difficult [149][150].

Moreover, the interface GaN/Si may be formed by an amorphous Si_xN_y layer (Fig. 1.12 b) causing phase mixture in the subsequent GaN film with a substantial diffusion of Si into the GaN film, or growth of polycrystalline material [151]. The epitaxy of GaN on Si (111) substrates is preferred as the improved quality of the resulting layers allowed the production of GaN-based devices such as LEDs [152], field effect transistors [153], and ultraviolet detectors [154]. The possible atomic arrangement at the interface GaN to Si (111) is shown in Fig. 1.12 a). Different types of nucleation layers including AlN, low temperature GaN, GaAs, and ZnO were tested to overcome the problems caused by the large lattice misfit and the strength of Si-N bonding. The formation of Si_xN_y at the GaN/Si (111) interface can be suppressed by the growth of an AlN nucleation layer in MBE [155] or MOCVD [156] epitaxy. AlN grows on Si in a two-dimensional mode with an abrupt interface as shown in the HRTEM image of Fig. 1.12 c), despite of the 23.4% lattice constant mismatch between AlN and Si. GaN films deposited on Si (111) substrates with an AlN nucleation layer by MOCVD have Ga-face polarity, whereas GaN films grown directly on Si (111) presented N-face polarity [157][72].

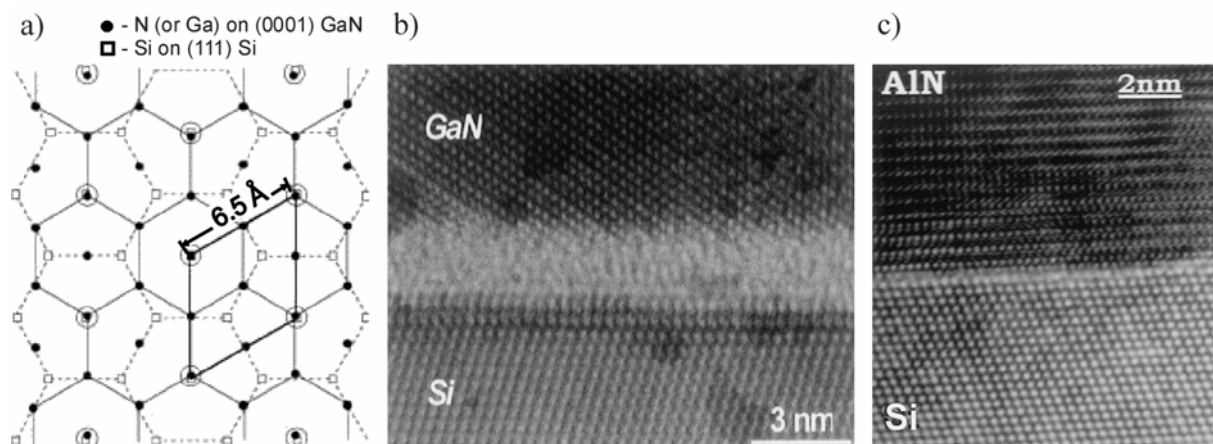


Fig. 1.12: a) atomic arrangement at the interface between a GaN grain and a Si (111) substrate. b) HRTEM micrograph showing the development of a thin (20-30 Å) amorphous Si_xN_y layer at the GaN/Si (111) interface. c) HRTEM micrograph of a sharp and clean AlN/Si (111) interface [155].

Nevertheless, the difference in thermal expansion coefficient between GaN (5.6×10^{-6} K) and Si (2.6×10^{-6} K) results in crack formation in the GaN film after cooling down from the growth temperature in MBE and MOCVD epitaxy. Based on the difference in thermal expansion coefficients for GaN and Si, the strain due to cooling from growth to ambient temperature was estimated to be tensile with value +0.06% [158] (the residual strain of GaN grown on sapphire is -0.12% at room temperature). However, residual stress due to lattice mismatch cannot be excluded. Also in this respect, the nucleation layer plays an important role: for instance, a high temperature AlN nucleation layer deposited on Si by MOCVD may produce good quality GaN, but it is not sufficient to relieve the stress and avoid cracking of the deposited GaN film [159]. The crack density could be significantly reduced or even eliminated by many variations of nucleation layers before GaN growth such as low temperature AlN in MOCVD epitaxy, or alternated high temperature layers of AlN and AlGaN [160], AlN/GaN superlattices [161], and step-graded $\text{Al}_x\text{Ga}_{1-x}\text{N}$ in MBE epitaxy [162]. The GaN film stress can be reduced to values below the yield strength of 400 MPa for GaN under tensile stress, thus completely avoiding the formation of cracks in the films after cooling down from growth temperature. Beyond their effect on the mechanical characteristics of the GaN films, nucleation layers were also applied to improve the structural and optical properties of GaN epilayers on Si. Some effort has been made recently in the optimization of a thin SiC layer [163][164], grown by carbonization of Si, as a buffer layer for subsequent GaN epitaxy. This was thought to be an alternative to reduce the relatively high defect density generated at the interface which propagates through the epitaxial GaN film, when using an AlN nucleation layer directly on Si. Although the application of special techniques like *pendeo*-epitaxy are promising for achieving almost defect free GaN also on Si substrates [138], the defect density including threading dislocations and inversion domain boundaries is still high (of the order of 10^9 cm^{-2} [163]), and therefore further optimization is necessary to reach the quality of GaN films grown on sapphire substrates. Nitronex Corporation claims to

have solved the thermal expansion and lattice misfit problems for depositing GaN on large-area silicon wafers [165]. The composition of the buffer layer scheme is proprietary, but the layer components were chosen after examining and comparing their thermal expansions versus GaN and silicon as a function of temperature. Precise temperature, composition and film thickness control must be obtained to eliminate radial stress gradients. The room temperature mobility of GaN-based HEMT structures grown using this technique is supposed to exceed $1600 \text{ cm}^2/\text{Vs}$ [166].

1.5 GaAs

There are several advantages that make GaAs an interesting substrate for GaN epitaxy, principally due its isoelectronic structure, the potential to convert a GaAs surface to GaN by nitridation, and the presence of parallel cleavage planes between film and substrate. From the technological point of view, GaAs is a well established compound semiconductor in large scale industrial production. High quality substrates (typical defect density $< 10^4 \text{ cm}^{-2}$) with different crystallographic orientations and specifications can be purchased at reasonable prices compared to the very expensive SiC wafers. On the negative side, GaAs has a large lattice constant and thermal expansion coefficient mismatch to GaN, a poor thermal conductivity, and an unsatisfactorily low thermal stability. The relatively low chemical stability of GaAs can also be a positive characteristic, since it allows GaN films to be separated more easily from GaAs than sapphire. As GaAs is mechanically softer than GaN, it will preferentially crack or suffer plastic deformation rather than the epitaxial GaN film. GaAs (111) is a potential substrate for the achievement of freestanding thick wurtzite GaN films to be used as pseudo-substrates for subsequent epitaxy and device fabrication.

Properties	Values	References
Melting point (K)	1515	[167]
Density (g/cm ³)	5.32	[168]
Lattice constants a (Å) (@ 300 K)	5.653	[16]
Thermal expansion $\Delta a/a$ (%) (@ 300 to 1200 K)	0.5876	[3]
Thermal conductivity (W/cm K) (@ 300 K)	0.45	[169]
Heat capacity (J/g K) (@ 300 K)	0.327	[170]
Modulus of elasticity (GPa)	85.5	[171]
Energy band gap (eV) (@ 300 K)	1.423-1.430	[171]
Electron mobility (cm ² /Vs) (@ 300 K)	8500	[171]
Hole mobility (cm ² /Vs) (@ 300 K)	400	[171]
Resistivity (k Ω cm) (undoped, @ 300 K)	10	[171]

Tab. 1.6: Material and electrical properties of GaAs.

The most relevant material and electrical properties of GaAs are listed in Tab. 1.6. GaAs is less stable than sapphire and SiC, starting to decompose thermally at temperatures above 700°C in vacuum. The crystal structure of GaAs is shown in Fig. 1.13. It is similar to the zincblende structure of GaN. The stacking sequence for the (111) close-packed planes in this structure is ABCABC.

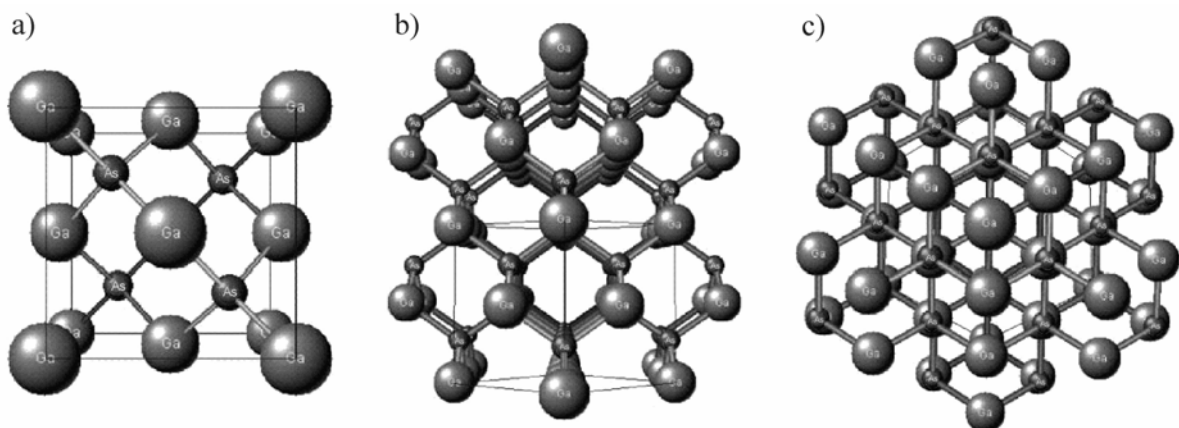


Fig. 1.13: Atomic structure views of a GaAs unit cell in the crystallographic directions a) (100), b) (110), and c) (111).

Since zincblende GaN was first grown on GaAs substrates in 1992, many additional studies have been done [172]. The production of zincblende GaN requires substrates with four-fold symmetry, that is (001) substrates. Zincblende GaN has been prepared on several substrates including Si, 3C-SiC, GaP, and MgO, but the most commonly employed substrate for this is GaAs (001). Zincblende GaN possesses superior electronic properties for device applications, such as a higher mobility, and isotropic properties due to its cubic symmetry and high optical gain. Nevertheless, both zincblende and wurtzite structures of GaN films may coexist because of the small difference between their energies of formation [173]. A surface roughening or faceting due to GaAs decomposition has to be avoided during growth to prevent the inclusion of hexagonal polytype in the GaN film. Consequently, in practice, the difficulty in producing low defect content polytype pure material hindered the large scale application of cubic GaN in contrast to wurtzite GaN. The lower growth temperature needed for GaN epitaxy in MBE systems is an advantage compared to MOCVD and HVPE, but a low temperature GaN buffer layer can protect the GaAs surface from decomposition at higher temperatures and under aggressive NH_3 atmosphere, making the MOCVD and HVPE techniques also practicable for the use of GaAs substrates in GaN heteroepitaxy.

Both GaAs (111)A and GaAs (111)B crystal orientations can result in single wurtzite phase GaN in MBE growth [174]. Namerikawa *et al.* [175] grew GaN simultaneously on GaAs (111) A and B surfaces by HVPE at different growth parameters and conditions. It was found that by covering the whole GaAs (111) substrate with GaN at 850°C , GaN growth on GaAs substrate at 1000°C without deterioration of the GaAs substrate was achieved. Furthermore, GaN grown at high temperatures always had Ga-face polarity, independent of the polarity of the GaAs substrate and/or the GaN buffer layer. Motoki *et al.* [176] produced a freestanding GaN (0001) substrate of over 2" size and thickness of $495\ \mu\text{m}$ ($\pm 10\ \mu\text{m}$) by HVPE on GaAs (111)A, employing two new methods for the reduction of dislocations. First a variant of ELOG was applied for dislocation reduction by forming a SiO_2 mask directly on

the GaAs substrate. Then, a thick GaN layer was grown with numerous large hexagonal inverse-pyramidal pits as shown in Fig. 1.14, constructed mainly by $\{11\bar{2}2\}$ facets maintained on the GaN surface (insert in Fig. 1.14 d). The dislocations are “collected” to the center of the hexagonal pit during GaN growth, reducing the defect concentration except at its center.

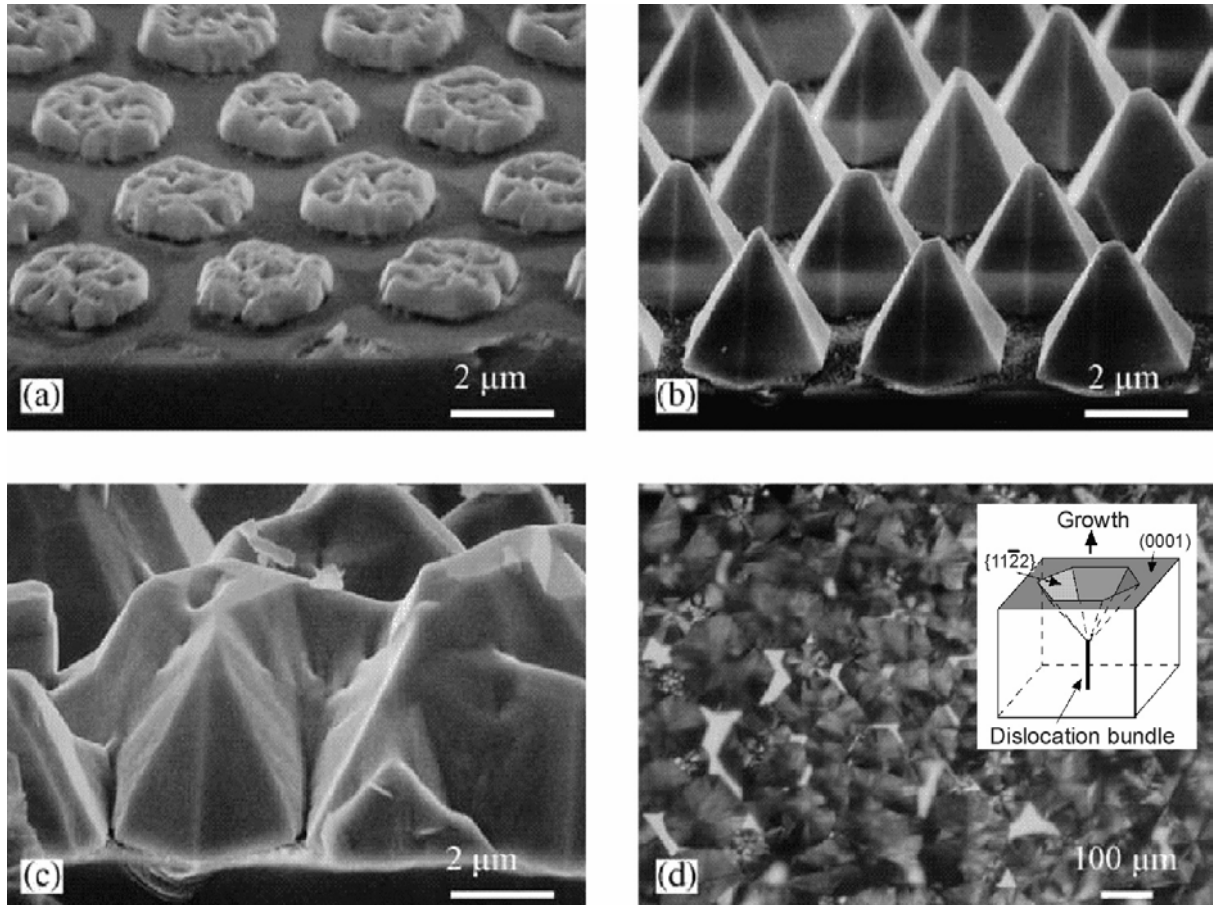


Fig. 1.14: Surface morphology of GaN on a GaAs substrate with SiO_2 mask at various growth stages. SEM image after (a) 0.5 min, (b) 4 min and (c) 10 min of GaN growth. Optical micrograph (d) at the end of the GaN growth. The insert shows a diagram of growth with hexagonal pits constructed from $(11\bar{2}2)$ facets concentrating dislocations at the bottom of the pit [176].

After removing the GaAs substrate the freestanding GaN film was lapped and polished. The distribution of dislocations was not homogeneous over the GaN layer. Etch pit density (EPD) measurements revealed that etch pits exist in groups with relatively high EPD ($2 \times 10^8 \text{ cm}^{-2}$) surrounded by an area with EPD as low as $5 \times 10^5 \text{ cm}^{-2}$. The crystalline

structure and quality of the obtained GaN substrate were examined by XRD rocking curves, showing a full-width at half maximum (FWHM) of 106 arcsec in the (002) crystallographic direction. Hall-measurements showed a typical n-type carrier concentration of $5 \times 10^{18} \text{ cm}^{-3}$ and a typical carrier mobility of $170 \text{ cm}^2/\text{V s}$. The resistivity of the GaN substrate was typically $8.5 \times 10^{-3} \Omega \text{ cm}$. The obtained GaN substrate is transparent with a slight grayish color [176].

Despite of the successful fabrication of this large freestanding GaN-based on GaAs substrates, the inhomogeneous defect distribution and the need of mechanical polishing causing structural damage to the surface are disadvantageous. No publication could be found in the literature on homoepitaxy or group-III nitride based growth on these freestanding GaN pseudo-substrates so far. Finally, it will depend on the results of such overgrowth experiments to evaluate the application of the freestanding GaN films originally grown on GaAs.

1.6 LiGaO₂

To overcome the large lattice misfit between GaN and sapphire, lithium gallate (LiGaO₂) substrates have been used for GaN growth in an exploratory study. Indeed, lithium gallate is the most closely lattice matched substrate candidate for GaN heteroepitaxy (Fig. 1.15). It is also a polar crystal which enables a better control of the polarity of the subsequent GaN film. The low chemical stability of LiGaO₂ is beneficial for the fabrication of thick freestanding GaN pseudo-substrates or enables a transfer of the GaN layer to another substrate with better heat dissipation. The undesirable properties of LiGaO₂ include its low thermal stability at the high MOCVD growth temperatures ($>1000^\circ\text{C}$) that may cause a phase change of the crystal [177], high thermal expansion coefficients, and the low electrical conductivity. Despite of the relatively low cost of LiGaO₂ compared to SiC, commercially available wafers do not have

the same optimal surface characteristics like sapphire or SiC. The LiGaO₂ substrates typically exhibit a rough surface with equidistant grooves about 10 nm deep, probably due to mechanical polishing. The resulting highly defective interface between GaN and LiGaO₂ is then responsible for a three-dimensional growth mode of the GaN film. The use of LiGaO₂ as a sacrificial substrate for the fabrication of thick freestanding GaN films makes it an alternative to be considered for the development of GaN-based devices.

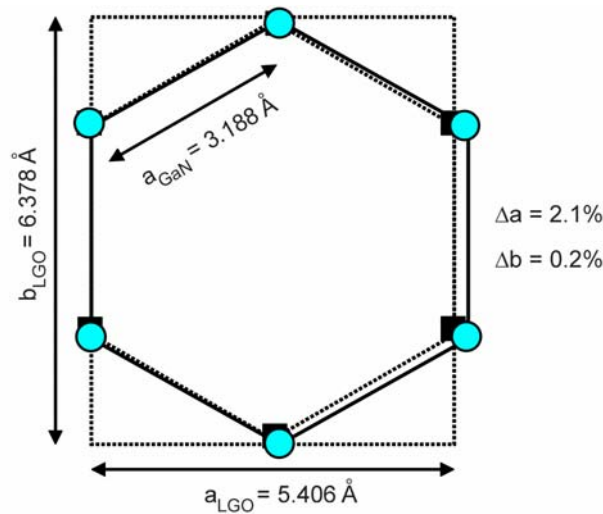


Fig. 1.15: Relative orientation of gallium nitride to lithium gallate.

At ambient pressure LiGaO₂ crystallizes in the orthorhombic crystal structure (right image in Fig. 1.16). The lattice parameters $a = 5.4063 \text{ \AA}$, $b = 6.3786 \text{ \AA}$, and $c = 5.0129 \text{ \AA}$ were determined by X-ray powder diffraction measurements at room temperature [177]. LiGaO₂ has no natural cleavage planes. The left image in Fig. 1.16 shows the projection onto the a-b plane of LiGaO₂ displaying the underlying pseudo-hexagonal symmetry suitable for the growth of hexagonal GaN ($a = 3.188 \text{ \AA}$). The crystal structure deviates slightly from the hexagonal symmetry to accommodate the two different Ga and Li atoms. The pseudo-hexagonal average basal plane lattice constant equals 3.152 \AA for LiGaO₂, which results in a lattice mismatch with respect to GaN of about 0.2%, much less than that of Al₂O₃ with a lattice constant mismatch of about 14% or 6H-SiC with a lattice mismatch of about 3%.

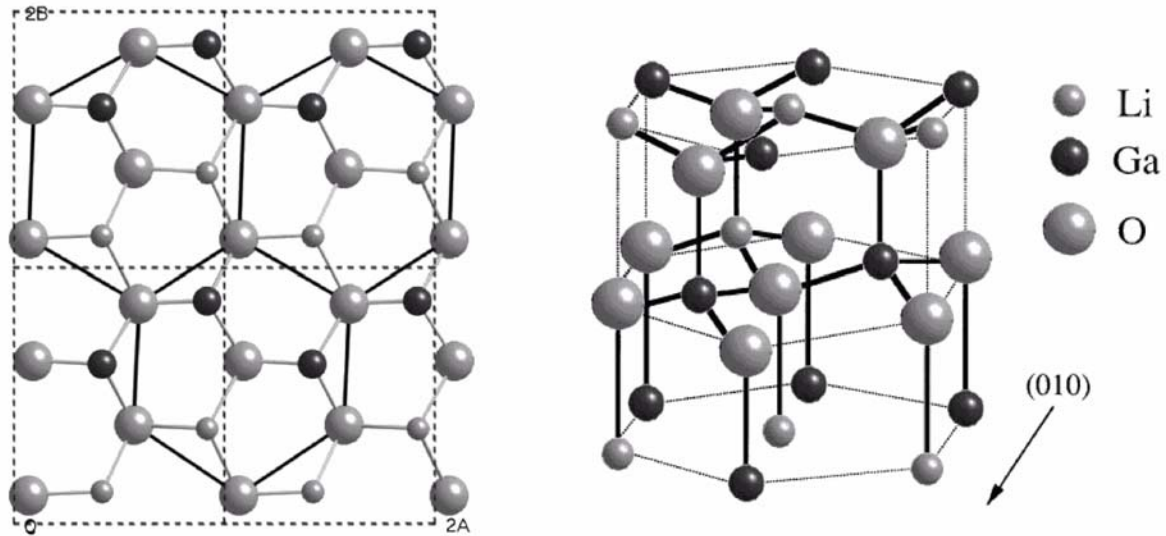


Fig. 1.16: Projection of LiGaO_2 lattice structure on the a - b plane displaying the underlying hexagonal symmetry (left), and three-dimensional view of the orthorhombic crystal structure of lithium gallate.

One further advantage of LiGaO_2 compared to sapphire is its polarity along the c -axis or (001) direction. The surface contains an anion (oxygen) or cation (gallium and lithium) polar termination. Lithium gallate reacts differently to acids and bases depending on the crystal polarity. The oxygen terminated surface (A-face) can be easily etched in aqueous solution of nitric acid ($\text{HNO}_3 : \text{H}_2\text{O} = 1 : 1$), whereas the gallium or lithium terminated surface (B-face) is difficult to etch [178]. In contrast, the B-face (metal) is chemically less stable than the A-face (oxygen) in a basic solution. An entire LiGaO_2 substrate can be etched away in less than 5 min in a base without attacking the GaN film grown on top [179]. The material properties of LiGaO_2 have not been well studied until now. Some of them are shown in Tab. 1.7. Although the thermal conductivity of this particular material has also not been studied, it is part of a class of tetrahedrally bonded materials with low atomic number elements, which generally are known to have high phonon-mediated thermal conductivity [180]. The asymmetry in the crystal structure along the (100) and (010) directions, parallel to a and c lattice constants, respectively, results in different thermal expansion coefficients in each of these directions. There is still some discrepancy in the literature about the thermal expansion coefficient values

of LiGaO₂. The strong anisotropy may lead to compressive or tensile strain in the GaN epilayer grown on LiGaO₂, but until present there has been no experimental study published.

Properties	Values
Melting point (K)	1600
Density (g/cm ³)	4.187
Lattice constants (Å) (@ 300 K)	5.4063 (<i>a</i>)
	6.3786 (<i>b</i>)
	5.0129 (<i>c</i>)
Thermal expansion coefficient (10 ⁻⁶ K ⁻¹)	6 (<i>a</i>)
	9 (<i>b</i>)
	7 (<i>c</i>)
Hardness (Mohs' scale)	7.5
Modulus of elasticity (GPa)	150
Energy band gap (eV) (@ 300 K)	5.6

Tab. 1.7: Material properties of LiGaO₂ [181][182].

Despite of the small lattice misfit between GaN and LiGaO₂, a dislocation density of about $6 \times 10^8 \text{ cm}^{-2}$ was found by TEM for GaN films grown by MBE, due to the highly disordered GaN/LiGaO₂ interface [183]. The preparation of clean and well-ordered substrate surfaces is a considerable challenge for compound materials such as LiGaO₂ due to the differing chemical activities of the atomic species. Contaminants on the substrate surface can interfere with the initial nucleation, inducing roughening and surface states which degrade the device performance.

The structural quality of the GaN film is much better compared to direct deposition on other substrates like sapphire and SiC. No nucleation layer is necessary for GaN epitaxy on LiGaO₂. AlGaIn/GaN heterostructures showing surfaces generated by linear step flow growth have been successfully obtained on LiGaO₂ substrates with the MBE technique [184]. Nevertheless, lithium and gallium atoms can degrade the interface and crystal quality at temperatures above 840°C using MBE conditions. The small atomic size of Li allows it to

diffuse easily in the solid state and leads to an incorporation in the GaN film. In addition, diffusion and reaction at the GaN/LiGaO₂ interface produce an amorphous or nanocrystalline transitional layer such as Li₅GaO₂ [184]. MOCVD grown epitaxial two-dimensional smooth GaN films can also be produced on lithium gallate, although, the films deposited at 1000°C peeled-off as soon as they had contact to water vapour from the ambient atmosphere [185]. Nitrogen has rather to be used as a carrier gas instead of hydrogen to avoid the pre-decomposition of the LiGaO₂ metalorganic. The incorporation of Li into the GaN film can be avoided by nitridation of the substrate surface prior to growth. An intermediate thin layer with the same orientation as the substrate will be formed [186]. MBE epitaxy was only possible on the metal face (B-face) at 700°C. No deposition could be achieved on the oxygen face (A-face) [187].

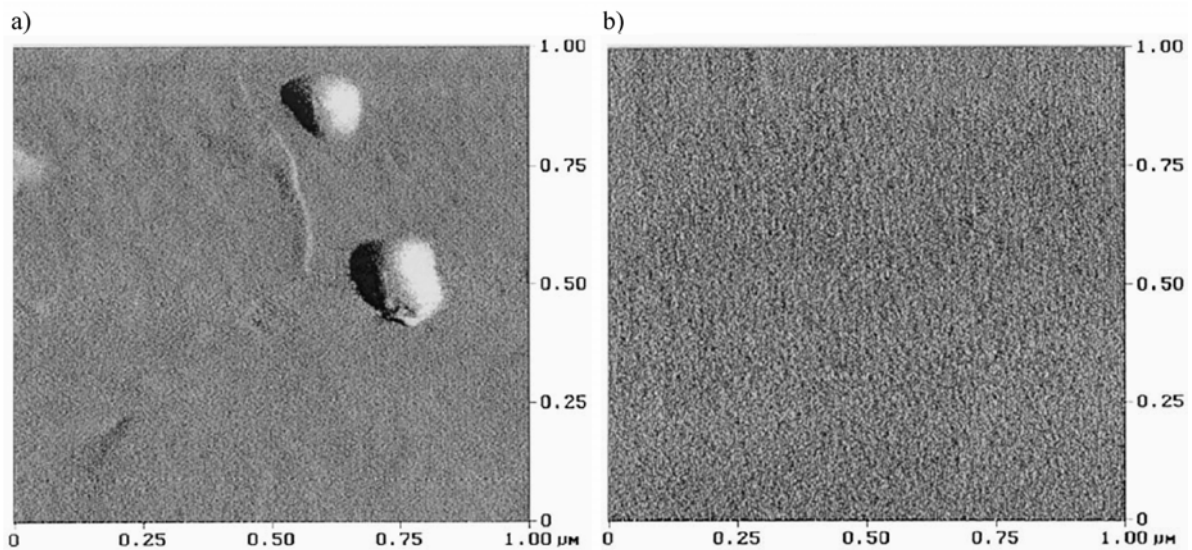


Fig. 1.17: AFM images of: a) HVPE-GaN film, rms roughness = 0.20 nm; b) HVPE-GaN with MOCVD-GaN cap layer, roughness = 0.03 nm [186].

Although large and thin GaN films grown on LiGaO₂ substrates tended to crack due to the residual strain [183], single GaN pseudo-substrates with thickness up to 300 μm were grown by HVPE on LiGaO₂ without cracks and residual strain [186]. The average X-ray peak width ranged from 100 to 300 arcsec. The smooth surface morphology of the samples with and

without a MOCVD cap layer is shown in Fig. 1.17. The surface morphology examined by atomic force microscopy (AFM) presented a rms roughness of 0.3 nm for the thick HVPE-GaN film and a roughness of only 0.03 nm after an overgrowth with a thin 200 nm MOCVD-GaN cap layer. Recent improvements on the LiGaO₂ crystal growth and substrate preparation have reduced the problems with surface roughness and inversion domains. It was determined that LiGaO₂ substrate nitridation and cooling processes are critical for film-substrate self-separation [188]. Therefore, the high etch rate of LiGaO₂ by HCl is not needed for substrate removal. Control of the surface chemistry and cooling schedule allow the GaN film to spontaneously separate from the underlying substrate. As a sacrificial layer, LiGaO₂, but also similar compounds including NdGaO₃ [189] provide an alternative for obtaining freestanding GaN films suitable for homoepitaxy.

1.7 AlN

The particular thermal and dielectric properties of polycrystalline aluminum nitride (AlN) already have established this material as an insulating heat sink substrate to improve the reliability and performance of high power microelectronic and optoelectronic devices [190]. For group III nitride epitaxy, single crystalline AlN can serve as an ideal substrate considering the similarity of the crystal structure, lattice constants, and thermal expansion coefficients. Abrupt compositional junctions that are almost strain free can be produced. It can be wet etched in KOH similar to GaN [191], and it is also electrically insulating, which is convenient for microwave devices. Furthermore, stacking mismatch boundaries (SMB) can be avoided because of the absence of steps on the substrate surface. The SMBs are the result of individual island growth and coalescence and must be considered as inevitable during growth of GaN on non-isomorphic substrates such as sapphire and SiC [192]. Indeed, AlN is even better

compared to GaN as a substrate due to its higher thermal conductivity (nearly twice), and the smaller lattice misfit for AlGaN epitaxy with high Al content. To push the optical emission/detection wavelength to the deep UV region ($\lambda < 280$ nm) high-quality $\text{Al}_x\text{Ga}_{1-x}\text{N}$ alloys with Al-mole fractions in excess of $x = 0.5$ are needed. In addition, high-optical-quality AlN layers are an excellent choice for the cladding region in heterostructure devices, thus the AlN material system is of great interest due to its largest direct gap (6.2 eV) among all group III nitrides. Many efforts are undertaken to make single-crystal AlN substrates commercially available. They are considered to be extremely valuable also for high temperature electronics, for space electronics where radiation hardness is imperative, and for UV solid-state emitters and detectors needed for missile defence, optical communications, and data storage.

Hexagonal AlN has the same structure as wurtzite GaN (Fig. 1.1). The material purity strongly determines the properties of aluminum nitride. Oxygen is the main contaminant in AlN due to the high affinity of Al to O and the large exothermic formation energy of Al_2O_3 (-1.58×10^6 J/mol). A large presence of oxygen is responsible for point defects, stacking faults, and secondary phases at the grain boundaries which reduce the thermal conductivity in the AlN crystal [193]. Tab. 1.8 summarizes the most important properties of wurtzite AlN.

Properties	Values	References
Melting point (K) (@ 100 atm)	3070	[194]
Density (g/cm^3)	3.255	[195]
Lattice constants a and c (\AA) (bulk crystal @ 300 K)	3.1106 and 4.9795	[6]
Thermal expansion $\Delta a/a$ and $\Delta c/c$ (%) (@ 300 to 1400 K)	0.6415 and 0.5349	[3]
Thermal conductivity (W/cm K) (bulk crystal @ 300 K)	3.20	[194]
Heat capacity (J/mol K) (@ 300 K)	30.64	[196]
Young's modulus of elasticity (GPa) (bulk crystal @ 300K)	308	[194]
Energy band gap (eV) (bulk crystal @ 300K)	6.2	[194]
Resistivity ($\Omega \text{ cm}$) (undoped)	10^7 to 10^{13}	[197]

Tab. 1.8: Material and electrical properties of AlN.

Bulk growth of single crystalline AlN has been attempted in several laboratories via sublimation, vaporization, and solution routes [198]. While the growth of AlN single crystals has been investigated during the past four decades, no AlN single crystals of high quality have been produced in considerable volume to date. The equilibrium nitrogen vapour pressure over AlN at its melting temperature is 6 orders of magnitude lower than that over GaN, but it is still impossible to grow bulk AlN crystals at atmospheric or subatmospheric pressure. Melt growth of AlN is not practical due to its extremely high melting point, estimated to exceed 3070 K.

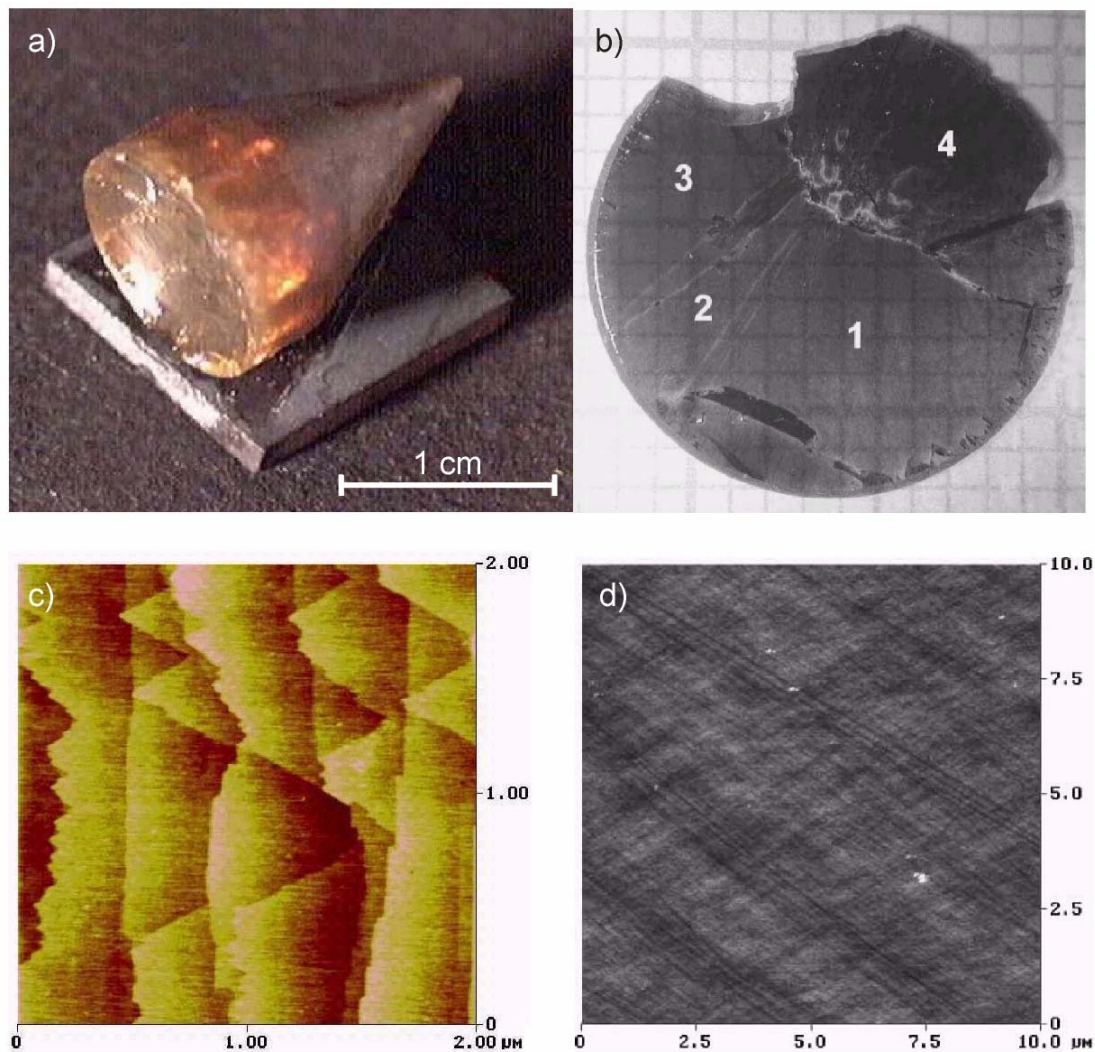


Fig. 1.18: a) AlN bulk crystal; b) Slice of a 14 mm diameter AlN bulk after CMP showing three main single crystal grains (1, 2 and 3) and a polycrystalline region (4); c) AFM image of the step flow growth mechanism on the (0001) direction, before CMP of the AlN wafer; d) AFM image of a substrate surface after CMP processing with a typical rms roughness of 1.4 nm [200][202].

Most studies of AlN bulk crystal growth have employed the sublimation method. A bulk AlN crystal of 470 mm³ was produced by self-seeding in the sharp tip of a sealed tungsten crucible by Slack and McNelly [199]. The source material was prepared by the direct reaction of aluminum and nitrogen at 1850°C. The crystal was grown at a temperature of 2250°C in nitrogen atmosphere. The group of Schowalter and Slack *et al.* continues to improve on this technique and have reported producing crystals up to 1" diameter and with dislocation density in the range of 10³ to 10⁴ cm⁻² [200][201]. The AlN wafers were chemical-mechanically polished (CMP) and a surface roughness of about 1.4 nm was achieved (Fig. 1.18 d). Fig. 1.18 a) shows an example of an AlN bulk of 10 mm of diameter produced by Schowalter's group at Crystal IS Inc. facilities using a sublimation-recondensation technique [202]. The atomic arrangement of the facets on the growing front of the crystal, shown in Fig. 1.18 c), corresponds to the characteristic structure of *c*-face fronts of hexagonal wurtzite-type crystals.

6H-SiC substrates offer an alternative method for seeding even larger AlN crystals by sublimation due to the easy nucleation and crystal orientation control. Balkas *et al.* [203] grew seeded single crystalline platelets of AlN less than 1 mm thick on a 10 × 10 mm² 6H-SiC substrate in a resistively heated graphite furnace. Growth rates up to 0.5 mm/h were achieved at 2150 to 2250°C and a nitrogen pressure of 500 torr. However, the AlN platelets contained individual hexagonal crystals of up to 2 × 2 mm², and the SiC coated graphite crucible induced Si, C and O incorporation into the AlN film. The AlN film cracked and contained a high screw dislocation density due to the stress caused by the thermal expansion coefficients mismatch between SiC and AlN. Other growth parameters were tried by Sarney *et al.* [204] also on 6H-SiC, but the ensuing problems could not be solved. Summarizing, AlN deposited on SiC generally has high dislocation densities and multiple small-sized grains showing the need of more research work to improve the growth technique.

Using a vaporization method, Schlessler and Sitar [205] have reported AlN crystals of up to 50 mm² with a growth rate of 0.2 mm/h along the *c*-axis. An increase of the growth temperature resulted in a better crystal quality and the formation of platelets instead of needles. Recently, freestanding AlN films of up to 3 × 3 cm² were also fabricated by the HVPE technique on Si substrates at TDI Inc. [206], nevertheless, the crystal quality was worse compared to AlN samples obtained with the sublimation technique.

Until the present date only the group of Schowalter has presented results on group III nitride epitaxy on AlN substrates [201][207]. High quality Al_xGa_{1-x}N layers were deposited by MOCVD on AlN substrates cut from 15 mm diameter large boules. Ion channelling measurements along the (11 $\bar{2}$ 0) direction gave a channelling minimum yield of 1.5% for an AlN film and 2.2% for an Al_{0.5}Ga_{0.5}N film, indicating a very good quality of the epitaxial layers grown on the (11 $\bar{2}$ 0) (A-face) of the AlN substrate [201], but also an increased surface roughness compared to the substrate. In their latest results they have demonstrated smooth surface morphologies for both homoepitaxial and heteroepitaxial growth on on-axis (< 2° offcut) substrates (Fig. 1.19).

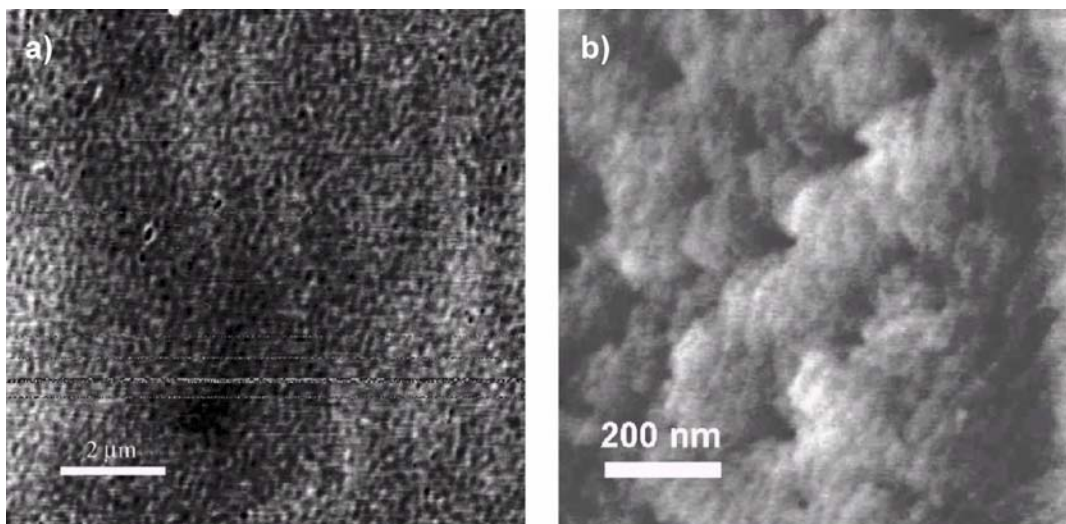


Fig. 1.19: a) AFM imaging of a homoepitaxial layer grown on AlN on-axis substrates showing the flatness of the epilayer and the characteristic nanomorphology. The vertical contrast range is 2 nm. b) AFM image showing the typical morphology of the 2DEG structure surface grown on a *c*-axis grain. The vertical contrast range is 3 nm [207].

They grew two-dimensional electron gas (2DEG) structures consisting of an 100 nm AlN buffer layer, a GaN layer of 500 nm, and an $\text{Al}_{0.2}\text{Ga}_{0.8}\text{N}$ barrier layer of 30 nm. The device epilayer structure was grown by low-pressure metal organic chemical vapour deposition (MOCVD) on insulating single crystal bulk AlN substrates. On one of these oriented substrates, a 2DEG with a mobility of $1000 \text{ cm}^2/\text{V s}$ and a sheet density of $8.5 \times 10^{12} \text{ cm}^{-2}$ at room temperature was demonstrated for the first time [207].

The competition for producing commercial AlN substrates for the group III nitride epitaxy is ongoing. The results obtained principally by the sublimation method for AlN bulk growth are promising. GaN bulk crystals can not be grown with this method due to the extremely high dissociation pressure of nitrogen in GaN. Nevertheless, considering the high reactivity of aluminum at the high sublimation temperatures (about 2000°C) of AlN, there are still many problems that need to be solved for AlN bulk growth, such as a high purity AlN source and an inert crucible for the growth. Moreover there is still the critical task to obtain controlled and reproducible conditions for the production of 100% single crystal boules.

1.8 GaN Substrates

GaN is obviously the best substrate choice for GaN epitaxy, considering also the good thermal and electrical characteristics for GaN-based device fabrication. Epitaxy on the native substrate material eliminates all problem related to heteroepitaxy and provides a better control of crystal polarity, dopant concentration, and strained layer thickness. The growth on epitaxially grown GaN substrates does not require nitridation or nucleation layers as on sapphire and SiC. Several techniques have been employed for the fabrication of GaN bulk crystals including growth by vapour phase transport (sublimation method) [208-210], growth from supercritical fluids [211], and growth from sodium fluxes [212].

Despite of all those efforts, only high pressure growth from solution and HVPE has produced relatively large area crystals or films for research purposes, well suited for subsequent GaN homoepitaxy. The group of Porowski, Grzegory, and coworkers at the High Pressure Research Center - UNIPRESS in Warsaw, Poland, have produced the samples for the most extensive investigation of bulk GaN up to now. The thermodynamic properties of nitrides eliminate any standard method of melt growth like the Czochralski or Bridgman techniques used for Si, GaAs, InP, and other group III-V compounds. The GaN bulk material was grown by a method called high nitrogen pressure solution (HNPS) from a Ga melt saturated with 1% N at temperatures of 1700°C under a nitrogen pressure of 20 k atm [213][214]. Crystal growth was carried out in gas pressure chambers with an internal diameter of 30 or 40 mm, and a furnace with internal diameter of 10 or 14 mm. The crystals were grown in boron nitride (BN) crucibles containing Ga, with a temperature gradient and at N₂ pressures for which the nitride was stable over the whole temperature range along the crucible. The crystallization experiments were performed without an intentional seeding, and the crystals nucleated spontaneously on the crucible walls at the cooler zone of the solution. The typical duration of the growth process was 120–150 h. This growth method results in GaN single crystals in the form of hexagonal platelets of about 10 mm in size, as shown in Fig. 1.20.

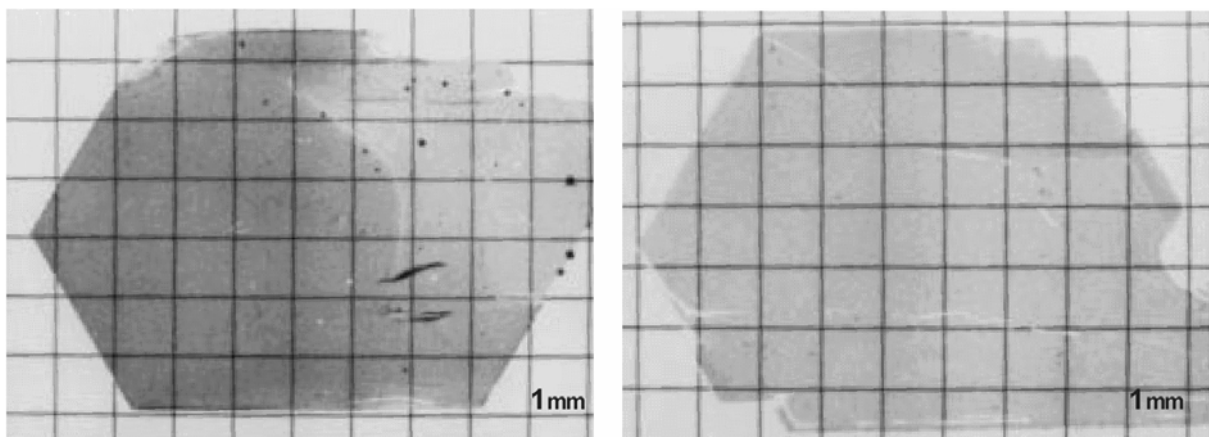


Fig. 1.20: GaN crystal platelets grown from the solution in liquid Ga at high N₂ pressure [214].

These bulk crystals have very good structural properties, in particular narrow X-ray rocking curves in all crystallographic directions, low dislocation densities, and negligible strain. Nevertheless, a high concentration of residual impurities and point defects is detrimental to the optical and electrical characteristics of these GaN crystals. Some properties of the bulk GaN obtained by HNPS are summarized in Tab. 1.9.

Properties	Undoped GaN	Mg doped GaN
Rocking curve in (002) direction (arcsec)	30-40	20-30
Carrier concentration (cm ⁻³)	3×10^{19} to 6×10^{19}	10^4 to 10^6
Mobility (cm ² /Vs)	30-90	
Oxygen concentration (cm ⁻³)	10^{19} to 10^{20}	
Ga vacancy concentration (cm ⁻³)	2×10^{17}	$\leq 6 \times 10^{16}$
Resistivity (Ω cm)	10^{-3} to 10^{-2}	10^4 to 10^6
Dislocation density (cm ⁻²)	10 to 10^5	

Tab. 1.9: Properties of bulk GaN produced by HNPS [213][215][216].

Non-intentionally doped GaN grown by HNPS typically shows a high electron background concentration ($> 10^{19}$ cm⁻³) resulting from the high oxygen concentration in the crystals. This causes a slight dilatation in the *c*-lattice constant in comparison to low electron concentration material and consequently, homoepitaxial films with much lower electron carrier concentration grown on these substrates will be slightly strained [217]. Semi-insulating bulk GaN can be produced by adding magnesium during the growth. Mg compensates the donor activity of the oxygen atoms, but also reduces the gallium vacancy (V_{Ga}) concentration and increases the structural quality in comparison to undoped bulk crystals [213].

The GaN platelets show an atomically smooth (0001) Ga-face polarity, while the opposite N-face is relatively rough, with pyramids of several tens of nanometers in height. Furthermore, the N-face of the HNPS-bulk GaN presents a much higher defect density than the Ga-face, but due to their chemical reactivity it is relatively easy to produce atomically flat N-face polarity surfaces by chemo-mechanical polishing. Despite the inferior optical and

electrical properties of the substrates, the MOCVD and MBE homoepitaxial GaN layers grown on these platelets exhibited considerably better structural, optical, and electrical properties than any other GaN layers so far [218][219].

Some devices like blue [220] and UV-LEDs [221] have been fabricated on HPNS-GaN, with improved characteristics compared to the standard heteroepitaxial ones. Nevertheless, the biggest disadvantage of the HPNS growth technique is the enormous difficulty to scale it up to larger size crystals. This will probably restrict the application of this method to only scientific investigations and device demonstrations.

For industrial scale GaN substrate production, a different approach offers more promising results. Thick and large size epitaxial GaN films can be grown by HVPE and then separated from the original substrate (sapphire, GaAs, or SiC) by polishing or etching [176][222][223]. Other approaches include self-detachment from LiGaO₂ substrates [188] or from GaN/AlN seeds structured on sapphire [224], but also laser-induced delamination of sapphire [225]. Once removed from the substrate, the GaN film is freestanding and both Ga- and N-face surfaces are accessible and can be prepared for further epitaxial growth. The equipment required for HVPE is relatively simple and growth rates as high as 100 μm/h can be easily reached. GaN wafers of up to 2" diameter and 300 μm thickness on sapphire substrates have been produced by HVPE almost routinely [226][227].

Although the structural quality of heteroepitaxial HVPE-GaN is not as good as compared to real bulk material obtained by HNPS, the fast growth rates of HVPE allow the improvement of the crystal quality by increasing the thickness of the GaN film. On the other hand, the electrical and optical properties are better than for HNPS bulk-GaN, since the residual carrier concentrations are much lower and the electron mobility higher. The best results obtained with HVPE-GaN are summarized in Tab. 1.10.

Properties	Value	Reference
Rocking curve width in (002) direction (arcsec)	69	[228]
Minimum carrier concentration (cm^{-3})	8×10^{15}	[228]
Maximum mobility (cm^2/Vs) (@ 300 K)	903	[229]
Dislocation density (cm^{-2})	5×10^5	[228]
Maximum resistivity ($\Omega \text{ cm}$), Zn doped	1×10^{12}	[230]
RMS surface roughness (nm), Ga-face	0.4	[231]
RMS surface roughness (nm), N-face	1	[228]

Tab. 1.10: Properties of high quality HVPE-GaN freestanding substrates.

The low residual impurity concentrations are beneficial for a better control of the electrical characteristics of the semiconductor material. A high level doping is detrimental to the crystal quality. The material's resistivity can be varied to reach semi-insulating GaN films by adding Zn to compensate the natural n-type background impurities. The doping with Si results in highly conductive substrates for specific device applications.

The properties of homoepitaxial GaN films deposited by MOCVD or MBE on these pseudo-substrates are even better than the substrate itself, as will be demonstrated in the chapter "Homoepitaxy on Freestanding GaN Substrates". Despite of the promising results, there are still some critical problems for the growth of large size and thick HVPE-GaN films, mainly due to the thermal expansion mismatch between the GaN film and the substrate. A strongly bowed and, in most of the cases, also cracked GaN film results after cooling down from the growth temperature. The utilization of ELOG MOCVD-GaN templates and/or the introduction of growth-stops for stress relaxation during the HVPE epitaxy have helped to increase the reproducibility of large size and thick GaN films. A yet unexplored possible solution for this problem could be also given by an *in-situ* laser-induced delamination of the GaN film at the growth temperature to avoid bowing and consequent cracks at room temperature. Moreover, the polishing process mainly of Ga-face material has to be improved to achieve epi-ready planar and atomically flat surfaces. These challenges will have to be

overcome for the production of HVPE-GaN pseudo-substrates for group-III nitride epitaxy on an industrial scale.

1.9 Diamond

For centuries, diamonds have captured the hearts and minds of millions, also scientists. For most, the word diamond immediately relates to a brilliant gem, wealth, status and/or prosperity. For scientists, diamond is known as one of the strongest and most chemically inert material that has singular attractive physical, thermal, and optical properties. The word diamond is derived from the Greek word *adamos*, meaning the unconquerable. However, diamonds have been known in India even before it was given this Greek name. The first gems of diamond were found in India as alluvial deposits about 2800 years ago. These first diamond stones were not particularly regarded for their brilliance. It was found to be extremely hard and impossible to break with known tools of that time. In a 6th century text on gems called “Ratnapariksa”, the hardness of diamond has been realized and quoted as *“The gems and the metals that exist on earth are all scratched by the diamond: the diamond is not (scratched) by them. A noble substance scratches that which is noble and that which is not; the diamond scratches even the ruby. The diamond scratches all and is not scratched by any.”* It was also found to withstand attack of most chemicals, enhancing the curiosity, and popular faith attributed to these mysterious stones to a manifestation of God with magical powers.

Diamond crystals are formed deep in the earth’s mantle, and are transported to the surface by magma. As the magma ascends, many crystals do not have time to revert to their stable form graphite. Even so, diamonds are quite rare in their source rock, normally less than 100 parts per billion. Most known diamond deposits are associated with old, continental shield areas, *e.g.*, in Africa, South America, Siberia, and Canada. Recent investigations

have shown evidence for nanometer-sized diamond grains (nanodiamonds) in meteorites of pre-solar origin. The diamond grains are composed of almost pure carbon with less than 1% by mass of impurities with atomic masses greater than six. These diamond particles and their impurities and structure can provide valuable information about and validation of the many theories for the origin of interstellar matter. Some of these interstellar diamonds are even older than our planet. Diamond particles have also been found to form deep under the earth's crust by continental collisions and plate tectonics, for example in Kazaksthan [14][232-235].

Properties	Values
Melting point (K)	3542
Density (g/cm ³)	3.52
Lattice constant a (Å) (@ 300 K)	3.567
Thermal expansion coefficient (10 ⁻⁶ K ⁻¹) (@ 293 K)	0.80
Thermal conductivity (W/cm K) (@ 296 K)	20
Heat capacity (J/mol K) (@ 300 K)	6.1
Modulus of elasticity (GPa)	700 to 1200
Yield strength (GPa) (@ 927 K)	15
Hardness (GPa) (nanoindentation, @ 300 K)	80 to 180
Radiation resistance	very high
Energy band gap (eV) (@ 300 K)	5.47
Refractive index	2.41
Electron mobility (cm ² /Vs)	1800
Hole mobility (cm ² /Vs)	2100
Breakdown field (10 ⁵ V/cm)	100
Resistivity (Ω cm) (@ 300 K)	10 ¹²

Tab. 1.11: Material and electrical properties of diamond bulk crystals [14][232][233].

Apart from being the hardest known naturally occurring material, diamond also exhibits several other superior properties. Diamond has a very high wear resistance and a low coefficient of friction. Diamond is also inert to most chemical environments and hence

diamond coatings can be used for corrosive and/or corrosion-erosion applications as well. It has the highest known bulk modulus (~1200 GPa) and the highest thermal conductivity at room temperature. It is optically transparent over large spectral range, from the deep UV to the far IR region. Diamond has a very high room temperature electrical resistivity of about $10^{12} \Omega \text{ cm}$, but can be made a semiconductor by substitutional doping with boron or phosphorus. It has a very low thermal expansion coefficient at room temperature. Diamond also has a small or even negative electron affinity, and is a biocompatible material. The main material and electrical properties of diamond are summarized in Tab. 1.11. By virtue of these extraordinary properties, diamond has a potential for a wide range of applications: for wear and corrosion resistance, field emission and high power electronic devices, heat sinks, optical windows, etc [236]. However the high costs of natural diamonds severely restricts their application potential.

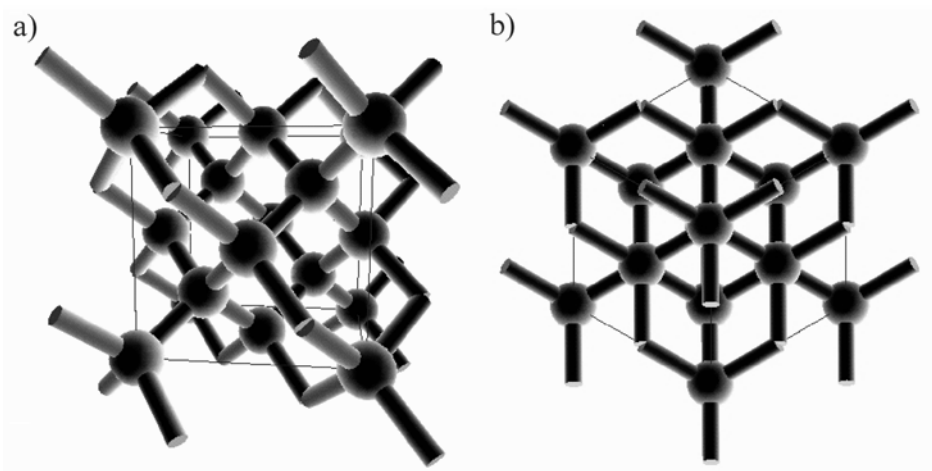


Fig. 1.21: Atomic structure of diamond in the crystallographic directions a) 001 and b) 111. At each atom are shown the 4 sp^3 bondings characteristic for the diamond structure.

Diamond is carbon in its most concentrated form. Except for trace impurities like boron and nitrogen, diamond is composed solely of carbon, the chemical element that is fundamental to all life. But diamond is distinctly different from its close cousin, the common mineral graphite. The strength and symmetry of its bonding structure in the crystal are the key to the unique properties of diamond. Four of the electrons in a carbon atom are valence

electrons available to form bonds with other atoms. Within diamond, one s-orbital and three p-orbitals undergo sp^3 hybridization. The four sp^3 -orbitals form a tetrahedral. The bond strength of covalent bonds is proportional to $1/d^2$ (d = distance between atoms). In carbon, the small d is responsible for strong bonds. This makes diamond stronger, stiffer, and harder than any other known material. The *fcc* crystal structure of diamond is shown in Fig. 1.21. In graphite, each carbon atom bonds only 3 of its 4 valence electrons with neighboring carbons. One s-orbital and two p-orbitals undergo sp^2 hybridization. The geometry of the hybridized orbitals is trigonal planar. The resulting structure of these bonds is a flat sheet of connected carbon atoms. Though individually strong, these layers are only weakly connected to one another, and the ease with which they can be separated is what makes graphite a “sliding” material.

Natural diamond always contains impurities. These impurities can strongly influence the transmission in the ultraviolet and infrared range of the spectrum. In type I diamond there is an absorption edge at ~ 300 nm and broad absorption bands between 7 and 10 μm . The predominant impurity in type I diamonds is nitrogen. Type Ia diamond contain nitrogen in fairly substantial amounts (up to 0.1 %), which forms small aggregates. Type Ib diamonds, which have a characteristic yellow colour, have lower concentrations of substitutional nitrogen which can be detected by electron spin resonance of the single electron in the stretched C-N bond. Type II diamonds can simply be said to be those diamonds which are not type I. They are rather rare: only approximately 0.5% of mined diamonds are type II. There are two classifications within type II. Type IIa diamonds are the purest diamonds available; the high purity results in an ultraviolet transmission down to approximately 230 nm and the absence of infrared absorption in the 7-10 μm bands. Type IIb diamonds have boron as a trace impurities, which cause unusual phosphorescence in these diamonds when excited by ultraviolet light. Type IIb diamonds are semiconductors [237]. The classification presented above is also used for synthetic diamonds.

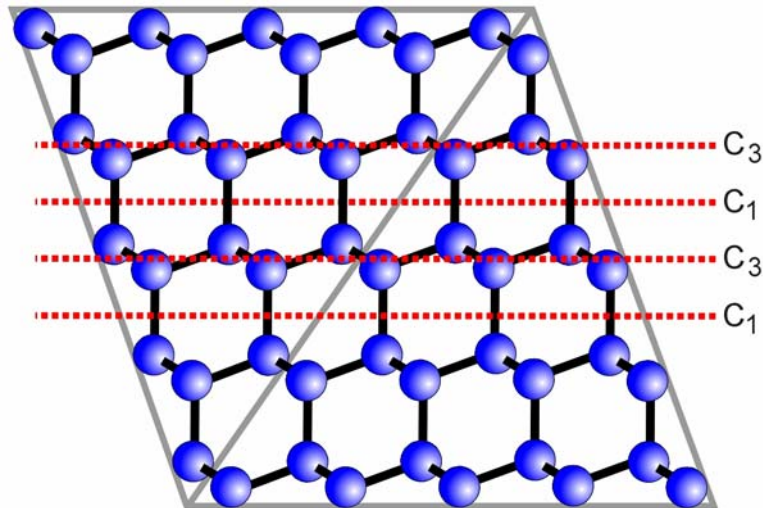


Fig. 1.22: Projection of the diamond lattice onto the (110) plane (octahedral face), with the [111] direction pointing in the vertical direction. The lines C_1 and C_3 indicate the cleavage planes for 1 dangling bond (db) and 3db cleavage (shuffle and glide-planes, respectively).

Due to its particular crystal structure, diamond has certain planes suited for cleavage with considerably fewer bonds along the plane of its octahedral face than in other directions (Fig. 1.22). Conventionally, the basic assumption for the determination of the (111) cleavage plane is that only the one bond oriented normal to the surface is cut, *i.e.* the cleavage-plane C_1 in Fig. 1.22 is the so-called shuffle-plane with 1 dangling bond (db). The other possibility is that the diamond crystal cleaves between the double layers (the cleavage plane being the glide-plane), leading to a (111) surface with 3db (C_3 in Fig. 1.22). The 1db and 3db surfaces necessarily alternate during growth.

Diamond was discovered to be carbon in 1796, but it took more than 150 years until a method of diamond synthesis was invented (Fig. 1.23). The attempts were all fruitless, although the idea to perform such experiments at high pressure and temperature was correct. The invention of tungsten carbide in the 1930s provided a material that could achieve the pressure containment necessary for growing diamond. Experiments in the 1940s by Percy Bridgman were unsuccessful, but finally in the early 1950s two teams succeeded. The first was led by Baltazar von Platen, at the Allmanna Svenska Elektriska Aktiebolaget (ASEA)

Laboratory in Stockholm, Sweden, but this initial success in 1953 was not publicized or published. Thus, on February 15, 1955, the General Electric (GE) team of Francis Bundy, Tracy Hall, Herbert Strong, and Robert Wentorf claimed credit for the first reproducible transformation of graphite to diamond. They succeeded to produce small crystallites of diamond a few millimeters in diameter by high pressure-high temperature (HPHT) Synthesis. Now some 80 tons of synthetic diamonds are produced annually, with GE being the largest producer, followed by De Beers, and many other manufacturers also contributing to this annual output. Substrates suitable for semiconductor application are also available in the multitude of diamond products, but at very high cost for some square millimeters of high quality material.

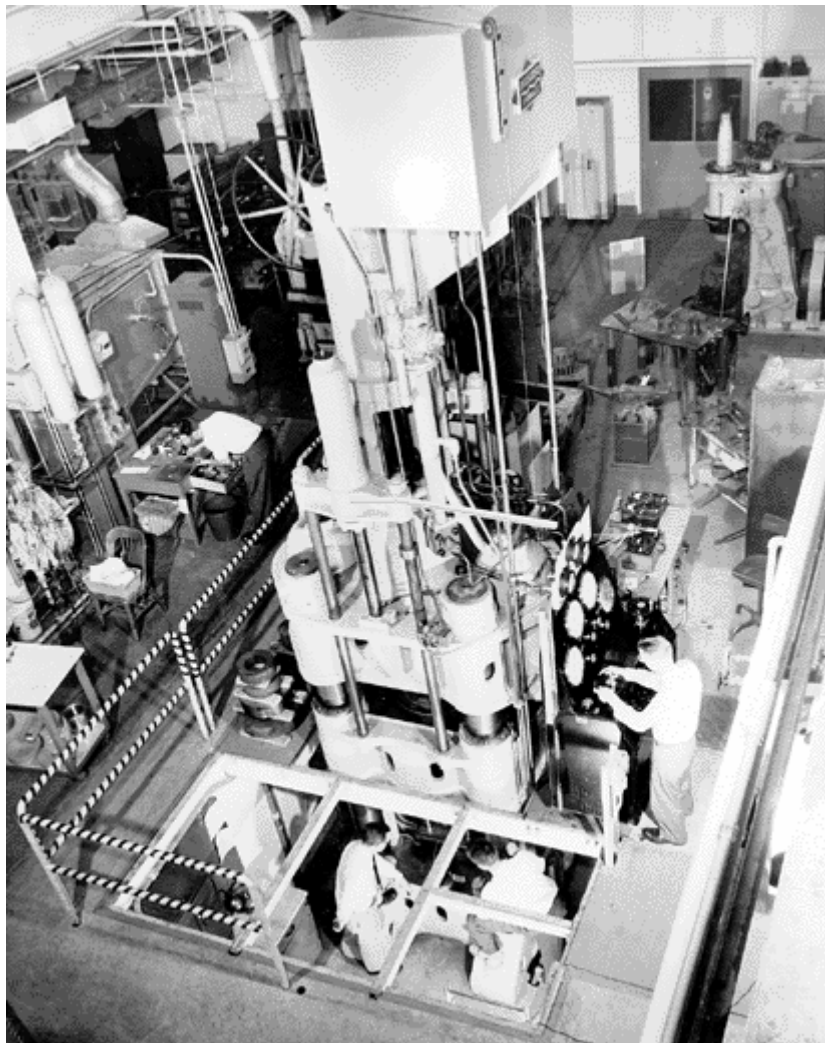


Fig. 1.23: View of General Electric's 1,000-ton press for diamond synthesis, capable of achieving pressures of 100,000 bar, in 1955 [233].

It can be seen from the carbon phase diagram (Fig. 1.24) that the diamond structure is stable only at very high temperatures and pressures. For conversion of graphite into diamond, a pressure of about 15-20 GPa and temperatures of about 3000 K would be normally required. However, by catalytic methods involving liquid metal solvents, HPHT synthesis of diamond has been achieved at pressures of about 7-10 GPa and at temperatures of less than 2000 K.

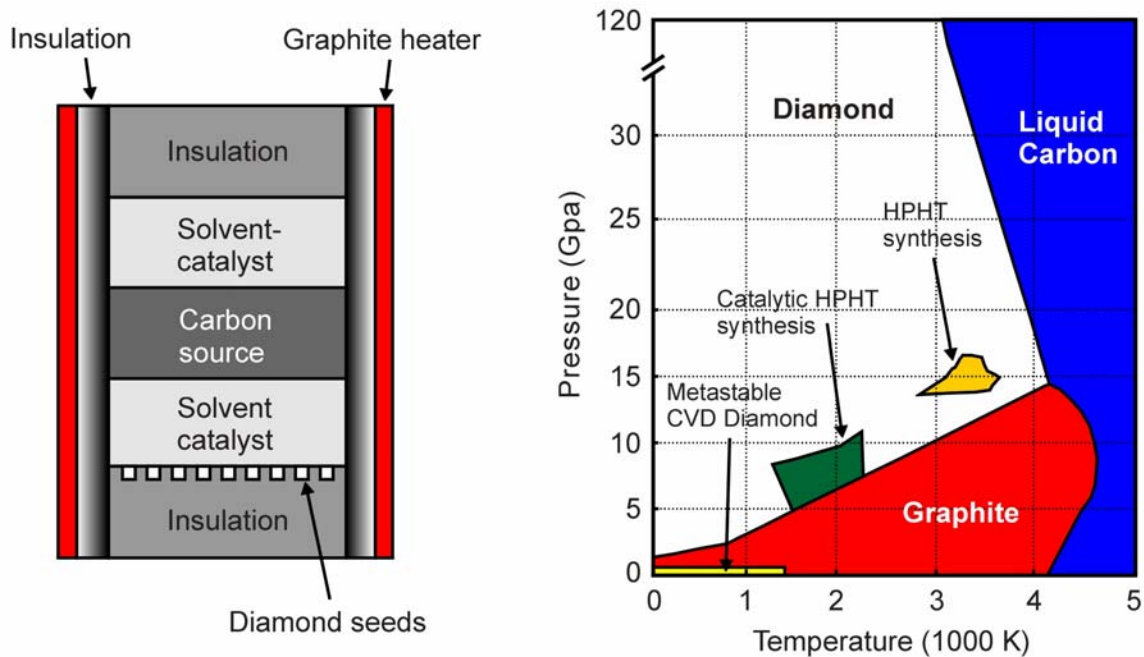


Fig. 1.24: On the left: schematic view of a capsule for diamond catalytic high pressure-high temperature (HPHT) seeded synthesis. Molten iron or cobalt is usually used as solvent catalyst. The right image represents the carbon phase diagram [233].

The schematic diagram in Fig. 1.24 shows the geometry of the growth capsule for the synthesis of large diamonds. Small diamonds are placed at the bottom of the active part of the capsule as seeds for the growth of large diamonds. Graphite dissolves into molten metal, usually iron or cobalt, and precipitates as diamond on the seeds at the colder bottom. It takes a few days to grow diamonds a few mm across. Smaller diamonds grow much faster, taking a few tens of minutes. The high pressures and temperatures are needed for conversion of graphite into diamond because of the high activation barrier involved. Although at room temperature the free energy of graphite is lower than that of diamond by only about

2.9 kJ/mol, the high activation energy (~ 728 kJ/mol) is mainly because there are no other metastable structures to aid the transformation of the graphitic to the diamond structure, which requires to break a significant number of the covalent bonds in graphite and to rebond them into sp^3 hybridisation. Due to the high binding energy of the carbon bonds, the associated activation energy is also high. For the same reason, once diamond is formed, though metastable from thermodynamic considerations, it is kinetically stabilised by the same high activation barrier.

In contrast to the HPHT technique, diamond films can be synthesized at atmospheric pressures and temperatures below 1000°C by chemical vapour deposition [238]. This is because, unlike for the HPHT route, there is no conversion of graphite to diamond in such a CVD process. CVD involves direct deposition of a carbon film from an activated carbon radical source and optimizing the parameters to stabilize the growing carbon film with a diamond structure. Ever since the discovery of CVD techniques to synthesise diamond in mid 1950's, there has been a spurt of activities in Russia, Japan and USA. In 1962, Eversole improved the CVD method to obtain good quality diamond with low graphitic phase. Angus *et al.*, further made significant contributions to the CVD diamond technology and also elaborated the role of hydrogen in preferential *in-situ* etching of graphite during the deposition process [14][232]. However it was only in 1981 that the first success of depositing diamond on non-diamond substrates was reported by Spitsyn *et al.* [233]. Ever since, there has been a remarkable progress in the deposition of diamond on several substrates and also in improving the deposition techniques to obtain better quality diamond films with higher deposition rates [239][240].

Chemical vapour deposition requires gas phase activation to facilitate deposition of diamond on a solid substrate. Gas phase activation can be achieved by several different routes like a) thermal (hot filament CVD), b) plasma (DC, RF, microwave, etc) or c) combustion

CVD using an oxyacetylene flame. A typical schematic of a hot filament CVD reactor (HFCVD) is shown in Fig. 1.25.

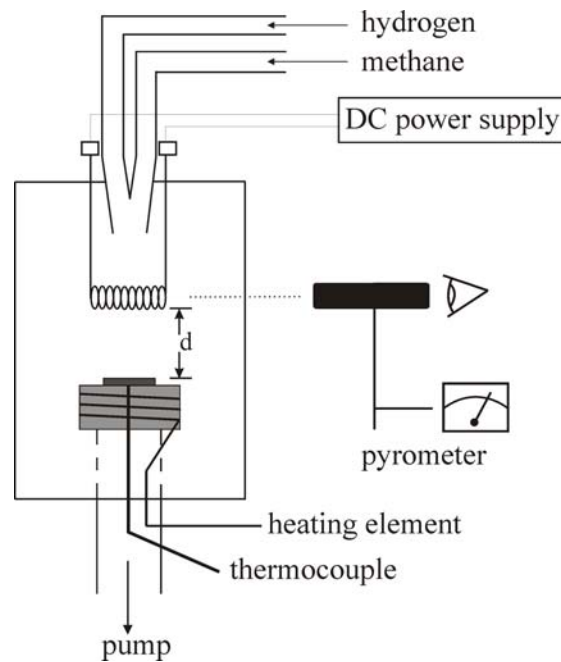


Fig. 1.25: Schematic view of a hot filament CVD reactor for diamond epitaxy.

The resulting diamond films are normally poly-, micro- or nano-crystalline, depending on the deposition conditions. But also single crystalline material can be obtained by homoepitaxy on bulk diamond substrates. The most important deposition parameters influencing the diamond film quality (sp^3 to sp^2 bonding ratio), microstructure and defect density are the filament temperature, substrate temperature, distance between filament and substrate surface, gas phase composition, gas pressure and flow rate. Apart from grain boundaries, the other most common defects in CVD diamond films are vacancies, impurities like nitrogen and hydrogen, micro twins and multiply twinned particles (MTP). The film deposition rate is normally in the range of $0.1 - 10 \mu/\text{hour}$ in HF CVD to about $100-500 \mu/\text{hour}$ in the flame combustion technique. The diamond films generally exhibit predominant $\{111\}$ facets, since this is the slowest growing plane. However, by suitable modification of the deposition parameters, square $\{100\}$ facets or rectangular $\{110\}$ facets can be achieved, usually resulting in smoother films. Factors such as increasing the methane concentration in the gas phase,

higher substrate temperatures, higher chamber pressures, and doping with nitrogen have found to promote {100} facets compared to {111} facets.

With the discovery of processes for depositing synthetic diamond films by means of chemical vapour deposition (CVD), it has become possible to commercially utilise many of the advantageous and unique properties of diamond for engineering applications like tribology, corrosion resistant coatings, electroanalytical and electrosynthesis electrodes, bio-compatible coatings, optical windows, heat sinks, gas and particle sensors, field emission devices, MEMS, etc. Diamond has a very high thermal conductivity, roughly four times superior to that of copper, and it is an electrical insulator. It is therefore developed specifically for applications in laser diodes and VLSI coatings.

Single crystal material is available, but not with large areas, since it is produced through the homoepitaxial growth of a high purity layer on an affordable, but small, substrate (typically $2 \times 2 \times 0.5 \text{ mm}^3$ to $4 \times 4 \times 0.5 \text{ mm}^3$). The only doping technology mastered by most laboratories is p-type doping with boron, which has an activation energy of 370 meV. Much effort is being made to obtain n-type doped material using phosphorus or sulphur [241][242]. Recently, it has been reported that deuterating boron doped diamond converts the material from p-type to n-type with conductivities as high as $2 \Omega^{-1}\text{cm}^{-1}$ at room temperature [243]. Teukam and co-workers grew 500 nm thick homoepitaxial layers of boron doped diamond on synthetic diamond substrates in a microwave plasma chemical vapour deposition system and exposed the samples to a microwave deuterium plasma at 550°C for eight hours. Subsequent annealing under a vacuum at temperatures of 520, 600, and 650°C for various durations led to changes in the electrical properties of the samples, including a return to p-type conductivity. The reproducibility of these results, including the effect of unintentional contamination of samples due to boron, is a latent problem and is still causing controversial discussion in the diamond community.

Apart from the difficulty to achieve n-type doping and despite the relatively high cost, and reduced availability of single crystalline diamond substrates, diamond/AlN heterostructures recently are attracting more and more interest due to their unique properties. The goal of heteroepitaxial growth is to make use of the characteristic advantages of both the substrate material and the thin epitaxial layer. Both materials exhibit wide electronic band gaps, high thermal conductivity and stability, as well as high chemical and physical inertness suitable for high temperature/high power devices. The fact that diamond shows the highest sound velocity among all solids but is not piezoelectric itself, motivates the combination with a thin film of a piezoelectric material such as AlN. Indeed, such AlN/diamond surface acoustic wave (SAW) devices with promising properties have already been reported [244][245]. Such devices are of interest for signal processing in the high frequency range, *e.g.* for wireless communication.

Polycrystalline or textured AlN/diamond heterostructures for SAW devices are commonly prepared by reactive magnetron sputtering [246] or chemical beam epitaxy (CBE) [247]. In contrast, almost nothing is known about epitaxial growth of AlN on diamond. Spitsyn *et al.* have investigated CVD-grown AlN films on (111)-, (110)-, and (100)-oriented diamond faces by reflection high-energy electron diffraction (RHEED) [248]. Whereas AlN was found to grow textured on (110) and (100) substrates, evidence for epitaxial growth on diamond (111) was provided. Later, the same authors reported the epitaxial orientation relationship $(00.1)[11.0] \text{ AlN} \parallel (111)[110] \text{ C}_\alpha$ [249].

Another promising example for the use of the complementary material properties of AlN and diamond is the recent realization of the first light emitting p-n diamond/AlN heterojunction diode [250]. Here, the difficulty of p-type doping in AlN or AlGaN compounds with a high Al content as well as the difficulty of n-type doping in diamond [243][251] have been overcome by combining both materials. Thus, the construction of other optoelectronic and electronic applications such as laser diodes or bipolar devices based on AlN/diamond seems feasible as well.

In Chapter 4 we will be present the first detailed study of the structural, morphological, and electrical properties of AlN thin films heteroepitaxially grown on diamond (100) and (111) substrates by molecular beam epitaxy. High resolution X-ray diffraction (HRXRD) analysis was used to prove epitaxial growth and particularly to determine the epitaxial orientation relationship of the AlN/diamond heterostructures.

2 Laser-Induced Liftoff Method for GaN on Sapphire

In this chapter, the laser-induced processing of GaN on sapphire is described. Based on laser-induced thermal decomposition, the detachment of GaN films from the sapphire substrate as well as a method for fast GaN etching is discussed. Continuing the work initiated by M. Kelly [225] in 1999, special attention focus was paid to the production of freestanding GaN pseudo-substrates. The remarkable optical and structural properties resulting from GaN homoepitaxy on such substrates will be discussed in the next chapter. The main goal of the work presented here has been the optimization of the laser liftoff process for the delamination of GaN films with thicknesses ranging from a few micrometers up to 120 μm . The effect of laser ablation on the surface structure of irradiated GaN and sapphire is discussed. The critical issue of a crack formation for a successful separation of the GaN films is analyzed. Furthermore, the flexibility of laser-induced liftoff was also demonstrated for the processing of thin InGaN/GaN heterostructures for the production of freestanding flip-chip bonded blue/violet LEDs.

2.1 Sapphire Detachment from GaN Films

The capability to produce superior material quality with a density of dislocation reduced by six orders of magnitude and narrower photoluminescence linewidths [252][253] by GaN homoepitaxy on bulk or bulk-like material compared to the usual heteroepitaxial growth on sapphire or SiC has been demonstrated by several groups. Two-dimensional growth can be achieved without the need for additional steps like surface nitridation, and nucleation or buffer layers. Laser cavities can be obtained by simple facet cleaving [254][255]. In addition,

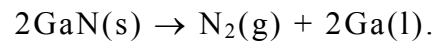
the GaN substrate can be electrically conductive, providing significant simplification in device processing and circuit integration.

An alternative to homoepitaxial substrates is the growth of bulk-like thick GaN films by hydride vapour phase epitaxy (HVPE). In the last years, much effort has led to the improvement of the quality of these films and also to overcoming the critical problem of obtaining large-area crack-free wafers of up to 2" diameter and 300 μm thickness [227][226]. However, the surface roughness of HVPE-GaN in the range of several micrometers is detrimental and surface polishing is required to prepare epi-ready GaN substrates. Polishing procedures are hampered by the brittleness of sapphire and the bowing of the GaN/ Al_2O_3 structures, which is caused by the differences in thermal expansion coefficients between GaN and sapphire, leading to the accumulation of thermal stress during the cool down from the high growth temperature ($\approx 1050^\circ\text{C}$). In order to solve such problems or to facilitate thermal and electrical backside contacts, however, it is desirable to remove the Al_2O_3 substrate. Nakamura *et al.* obtained improvements in the lifetime of laser diodes and cleaved facets after polishing the sapphire away [254][222]. In 2002, an epitaxial procedure was developed to cause GaN film self-detachment from the sapphire substrate during cool down from growth temperature due to the thermal stress and the lattice misfit between GaN and sapphire [224]. A GaN/ AlN structure was primarily grown by MOCVD on *a*-plane sapphire substrate and then structured into stripes by photolithography and reactive ion etching (RIE). The etching depth was extended into the sapphire substrate through the exposed GaN/ AlN layers. After removing the mask, GaN stripes remained on the sapphire surface as seed for the subsequent HVPE-GaN growth. With this relatively complex method of spontaneous delamination Tomita *et al.* have claimed to produce freestanding GaN wafers 100 to 500 μm thick and size of 23 mm \times 23 mm. Nevertheless, no information was given about the reproducibility of this process due to non-intentional cracking or the possibility to achieve complete spontaneous detachment of 2" GaN wafers.

Besides the mechanical methods for the removal of sapphire substrates mentioned above, a relative inexpensive and rapid laser-induced liftoff process was developed for GaN delamination [225]. This simple liftoff technique with large process latitude will be described in this chapter. After planarization and polishing, the GaN wafers can be used for homoepitaxy of GaN by MOCVD or MBE. In addition to high quality GaN which can be achieved by homoepitaxy on such bulk-like substrates [231], a variety of GaN applications require a range of options for patterning and etching. Since GaN strongly resists wet etchants, more complex, poisonous and expensive processes have been necessary, primarily those using Cl-based reactive ion etching (RIE) [256]. Before discussing the laser delamination of GaN on sapphire wafers we elaborate on the etching of GaN films which is achieved by laser-induced thermal decomposition.

2.2 Laser-Induced Thermal Decomposition of GaN

Under normal ambient conditions, the thermal stability of GaN is limited by the decomposition of the crystal into nitrogen gas and liquid gallium:



The flux of nitrogen atoms, $\Phi(\text{N})$, leaving the crystal surface in vacuum increases exponentially with temperature T and can be described by

$$\Phi(\text{N}) = 1.2 \times 10^{31} \exp\left(\frac{-3.9\text{eV}}{kT}\right) \frac{1}{\text{cm}^2\text{s}}, \quad \text{Eq. (2.1)}$$

(Fig. 2.1) [257]. The corresponding decomposition rate of GaN reaches one monolayer per second at a temperature of 930°C. This result confirms the fact that the decomposition temperature of GaN is far below the melting point and indicates that GaN can be etched

through thermal decomposition by methods which provide a local heating of the sample to temperatures above 830°C.

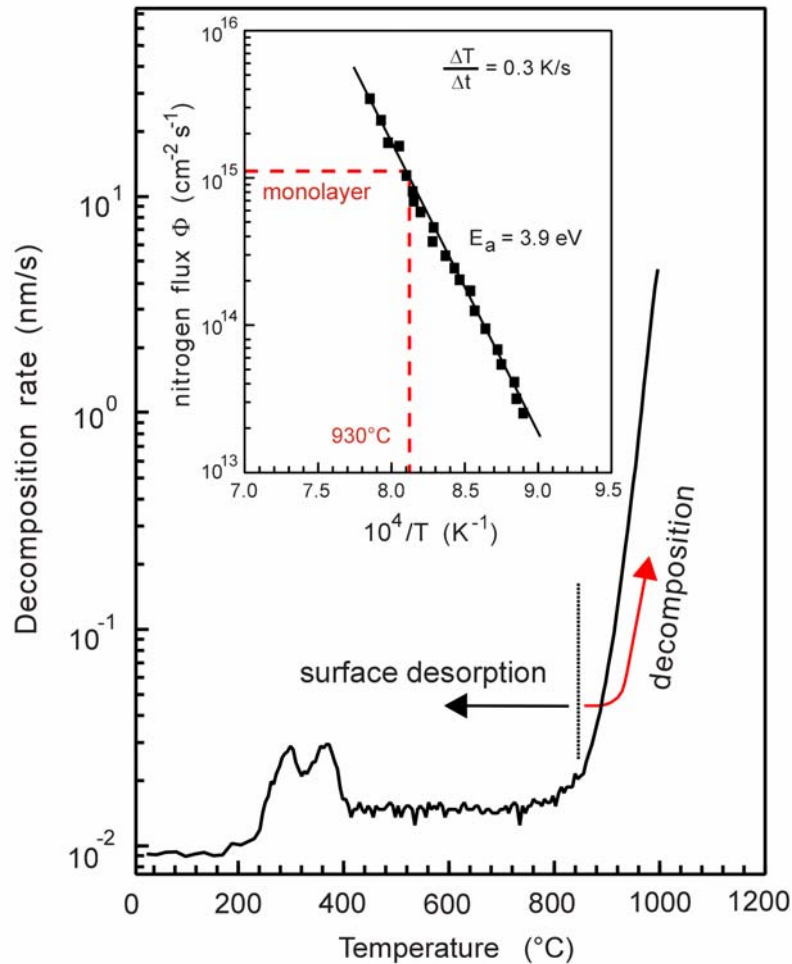


Fig. 2.1: Thermal induced decomposition of GaN and the corresponding flux of nitrogen from the GaN surface using a heat rate of 0.3 K/s [257].

One possibility to decompose GaN is to use intense irradiation with photon energies above the band gap of GaN (3.42 eV), e.g. the 355 nm (3.49 eV) third harmonic of a Nd:YAG pulse laser (Fig. 2.2) [258][259]. The properties of neodymium-doped yttrium aluminum garnet (Nd:YAG) are the most widely studied and best understood of all solid-state laser media [260]. The active medium is triply ionized neodymium, which is optically pumped by flash lamps whose output matches principle absorption bands in the red and near infrared, thus generating pulses at 1064 nm. The pulse width is smaller than 10 ns, the peak of optical

power is tens of megawatts, and very stable with intensity variation from pulse to pulse of less than 3%. The high peak power of the pulses permits frequency multiplication to 532 nm (2nd harmonic) and 355 nm (3rd harmonic) in non-linear potassium di-deuterium phosphate (KD*P) crystals.

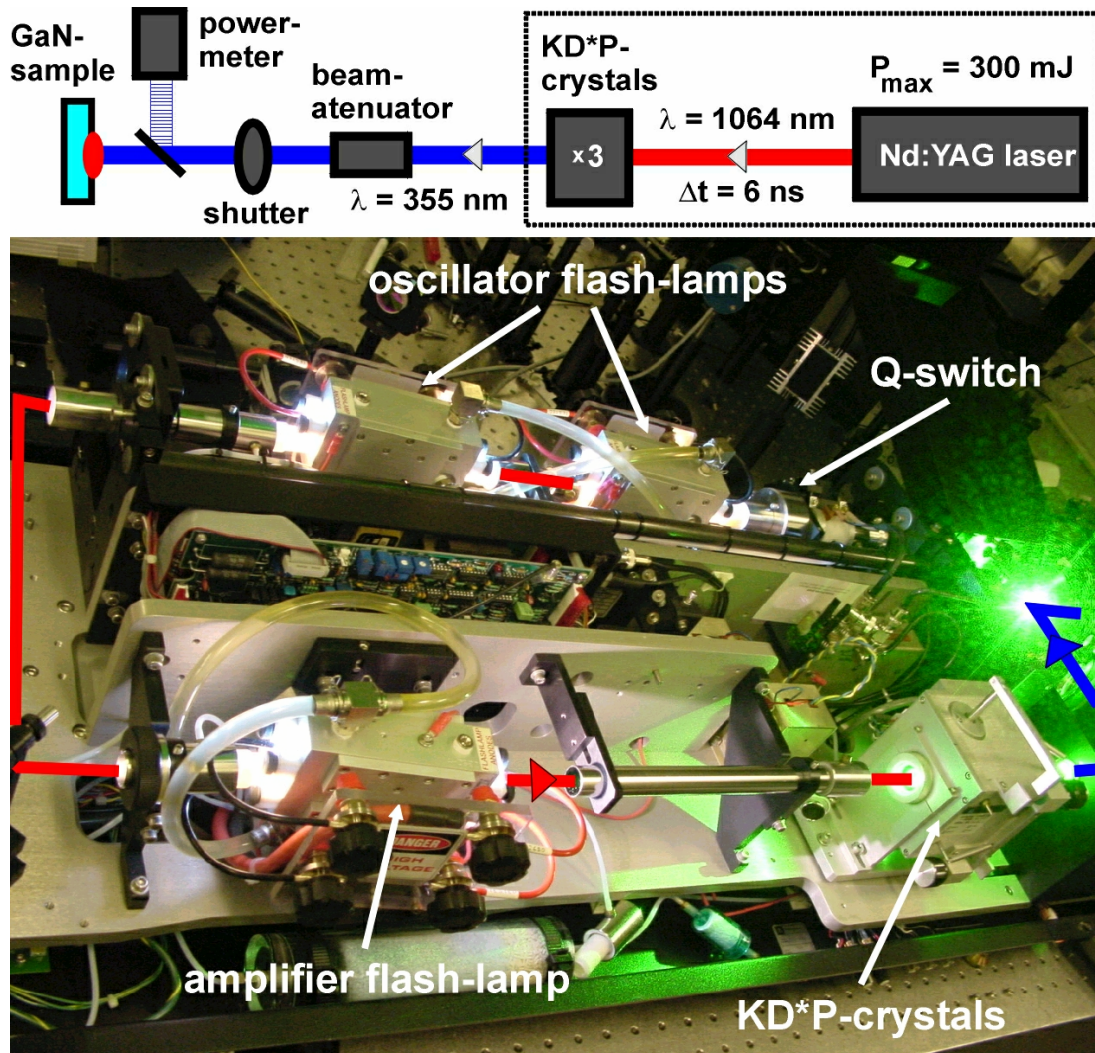


Fig. 2.2: Schematic view of the experimental setup for the laser-induced thermal decomposition of GaN with the 3rd harmonic of a Nd:YAG laser. The picture shows the inside of the Spectra-Physics Quanta-Ray model GRC-200 laser used for GaN processing.

The penetration depth of the 355 nm laser line in undoped GaN is shown in Fig. 2.3 for incident intensities from 220 to 26 J/cm². The high energy densities can be generated by focusing the Nd:YAG laser beam to a spot down to 1 mm in diameter with a sapphire lens. All laser processing was performed in air using a Spectra-Physics Quanta-Ray model

GRC-200 Nd:YAG laser (Fig. 2.2) that provides a maximum pulse energy of 300 mJ integrated over the beam diameter of about 7 mm. The pulse length and repetition rate is 6 ns and 10 Hz, respectively.

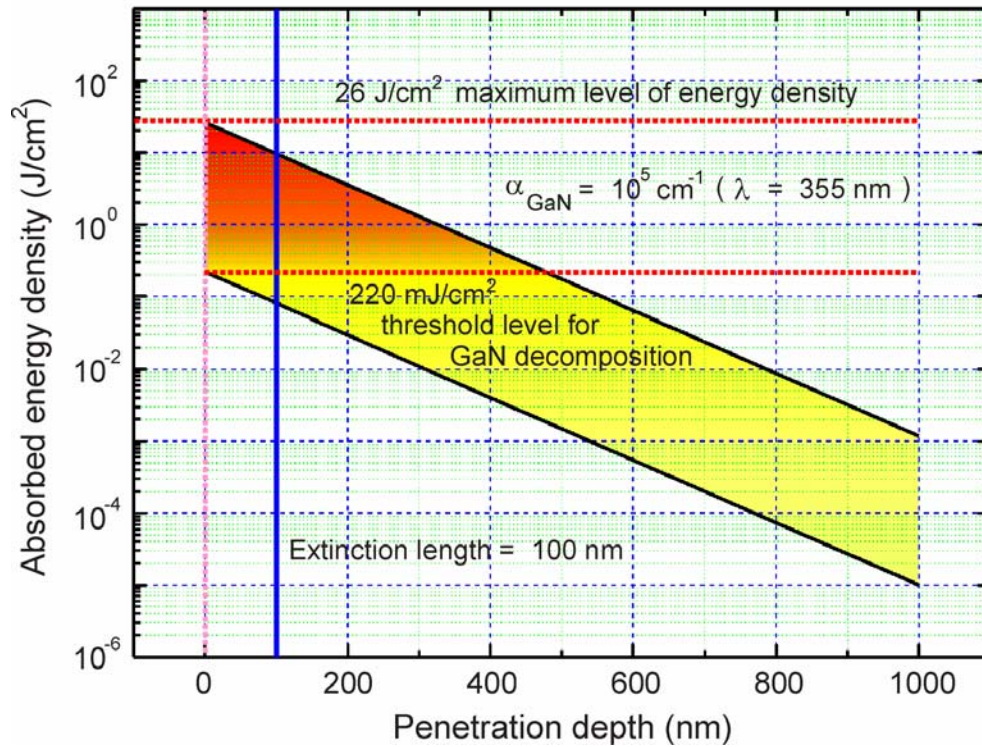


Fig. 2.3: Penetration depth in undoped GaN at 355 nm for the energy density range that can be generated by the 3rd harmonic of the Nd:YAG laser used in this thesis. The extinction length of 100 nm defines the depth reached by the absorbed light in the GaN material when the energy density is $1/e$ of the incident light power.

The real beam profile shown in Fig. 2.4 presents the energy distribution across the beam diameter which is determined by the mirror assembly chosen for this system. The profile is formed by a sequence of concentric rings with regions of lower power density in between. Indeed it is rather difficult to obtain a flat energy profile with a Nd:YAG laser. In contrast, Excimer laser systems can generate a flat beam energy profile and can also be used for GaN processing [261], but due to their typical pulse period of tens of nanoseconds higher power densities are needed to cause thermal decomposition of GaN. The decomposition rate increases strongly with the pulse intensity at constant pulse duration [262]. The shorter 6 ns

pulse of the Nd:YAG laser is absorbed faster in less volume, thus causing less thermal stress in the GaN layer. This is principally of advantage in the processing of thin film devices of a few micrometers thickness. This issue is discussed in more detail in the section “Freestanding GaN-based LEDs”.

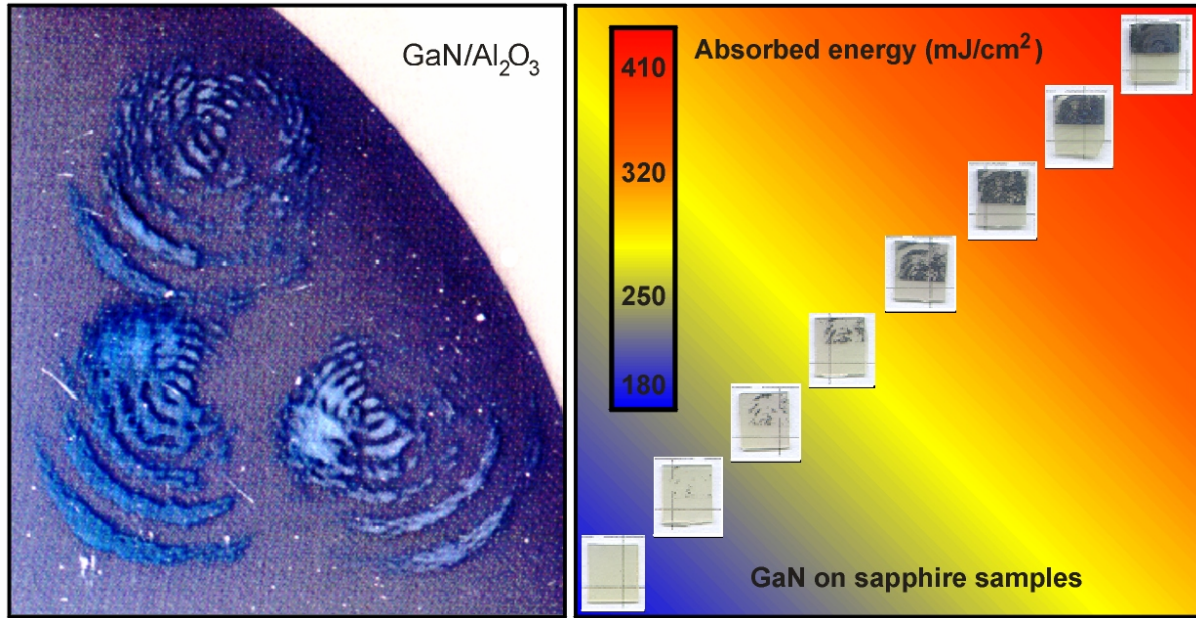


Fig. 2.4: Nd:YAG laser shots on GaN/sapphire templates. The left image shows the shots with a diameter of ~ 7 mm at an absorbed energy density of 320 mJ/cm^2 . The right image features the monotonic increase of the GaN decomposition with the laser intensity, recognizable by the residual Ga (grey area of the irradiated sample).

In order to determine the maximum etch or decomposition depth of GaN achieved by a single laser pulse we have irradiated epitaxial films with a thickness of $1 \mu\text{m}$ which were partly covered by a reflective coating. The pulse energy at the sample surface was adjusted with a polarizing beam attenuator. The formation of Ga-droplets was visible for laser output pulse intensities above 310 mJ/cm^2 . It should be mentioned that the intensity which is absorbed by the GaN film and causes the decomposition is about 30% below the laser output intensity because of losses due to reflections in the optical elements and at the air/GaN interface. The laser pulse intensity during the experiments and the attenuation induced by optical setup to be shown in Fig. 2.8 was measured with a power meter, which detects the

flow of energy through an array of thermoelectric cells. The values given in Fig. 2.5 are the intensities really absorbed by the GaN films at room temperature.

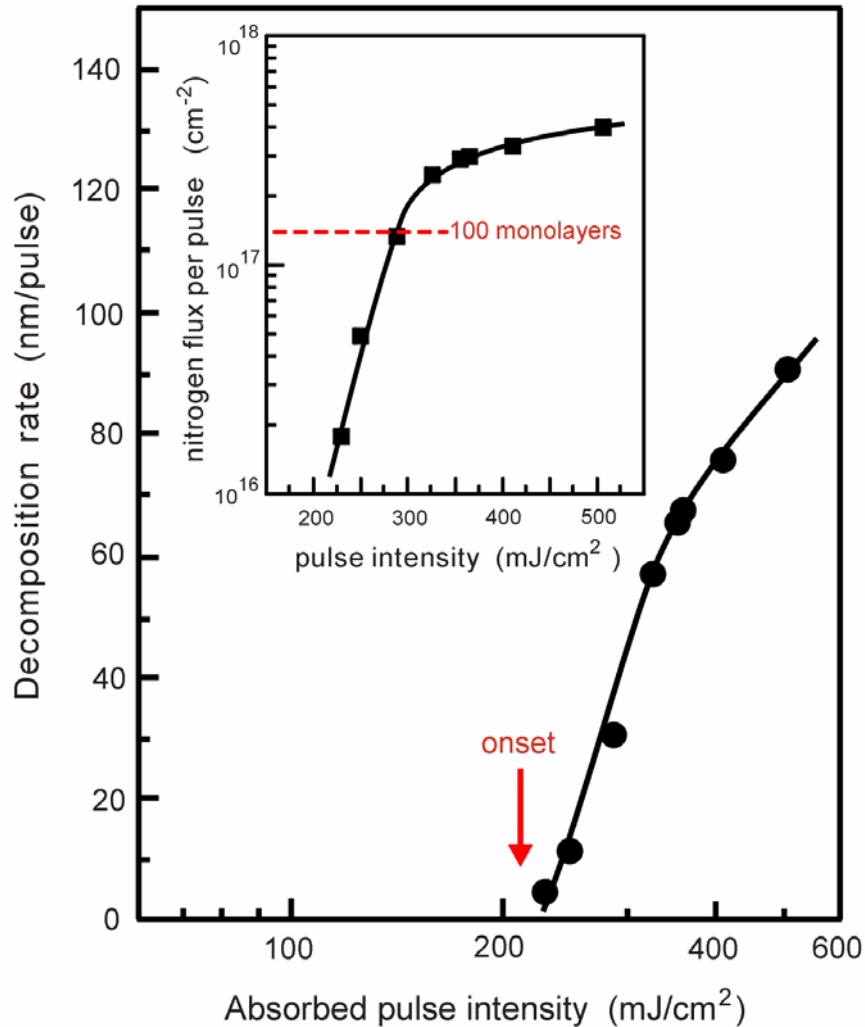


Fig. 2.5: Decomposition rate and nitrogen flux from the GaN surface versus the absorbed light intensity of single 6 ns laser pulses with a photon energy of 3.54 eV. At intensities of 290 mJ/cm² a decomposition rate of 100 monolayers/pulse is measured.

After wet chemical etching of the liquid Ga, the decomposition depths were measured by surface profiling (Fig. 2.5). The observed decomposition rate increases logarithmically with increasing pulse energy above a threshold of about 220 mJ/cm², reaching a rate of 100 monolayers per pulse at 290 mJ/cm². For intensities above 320 mJ/cm² the slope

decreases, probably because of a change in the optical properties of GaN during the decomposition of the surface layers.

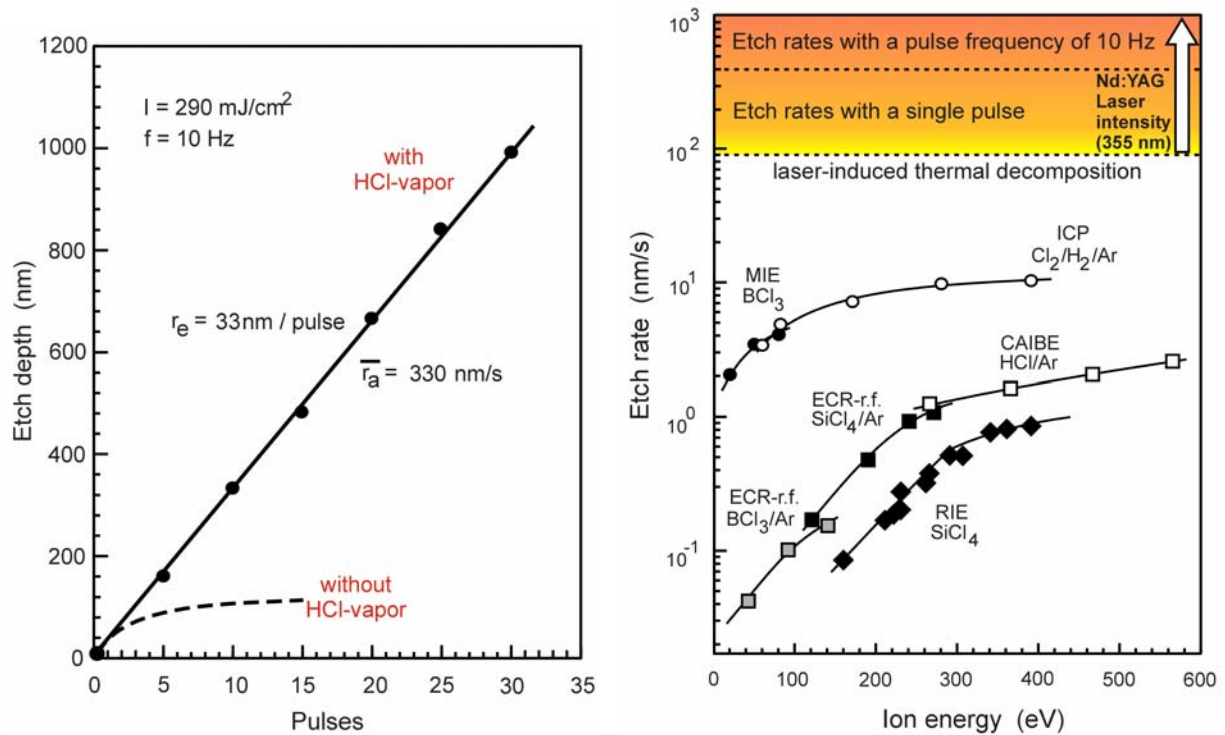


Fig. 2.6: The left graph shows the etch-depth dependence on the number of laser pulses without and under HCl-vapour. The graphic on the right presents the laser-induced etch rates on GaN among several commonly used reactive ion-etching methods [263].

The liquid Ga can be removed continuously between the laser pulses *e.g.* under HCl vapour flow. The limiting effect of the remaining Ga on the etch rate without using HCl-vapour can be clearly observed in the left graph in Fig. 2.6. Indeed, with a repetition rate of 10 Hz and higher energy densities an etch rate close to $1 \mu\text{m/s}$ can be achieved well in excess of other etching methods. The right graph of Fig. 2.6 shows a comparison of laser-induced etch rates with different types of reactive ion etching (RIE) methods, including electron cyclotron resonance plasma etching (ECR), chemical assisted ion beam etching (CAIBE), high-density magnetron reactive ion etching (RIE-MIE), and inductively coupled plasma etching (ICP) [263]. Despite of the advantages of having fast etching rates, light diffraction at mask edges and borders is detrimental for the application of laser ablation in the processing

and isolation of small size devices (mesa-structures). A high resolution laser structuring of GaN down to a dimension of 100 nm can be achieved with holographic patterning without the use of masks on the surface and therefore avoiding the effect of light scattering and diffraction at edges and borders.

The capability to produce GaN surface morphologies suitable for antireflection coatings, highly absorbing layers or distributed feedback lasers, striped, rectangular or sine wave patterns with periods between 100 and 500 nm is of high technological interest. Kelly *et al.* [258] used the 3rd harmonic of a Nd:YAG laser to fabricate periodic structures on GaN, as shown in Fig. 2.7. In order to produce such small period patterns the laser beam was split into two beams and superimposed at the GaN surface to achieve a holographic grating (Fig. 2.7 a). Angles between the interfering beams from $\Omega = 45^\circ$ to 90° were used to generate the relevant grating periods.

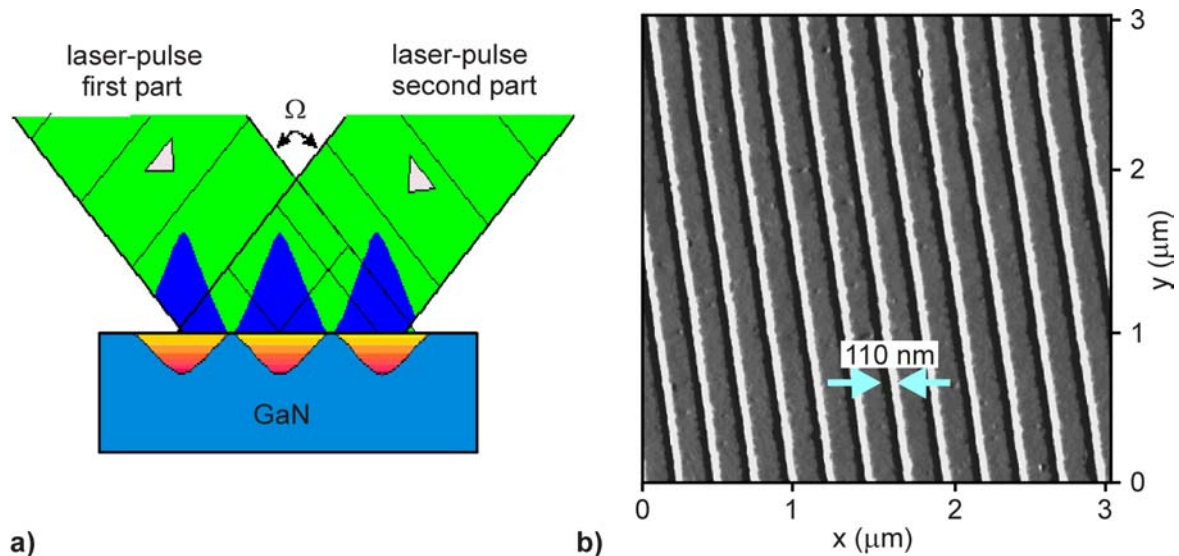


Fig. 2.7: a) a grating is produced by splitting the laser beam and bringing the two parts together on the sample surface to make a striped interference pattern. The GaN is decomposed in areas of constructive interference with intensities above 220 mJ/cm^2 . b) AFM image of a 250 nm period structure in GaN fabricated by laser-induced holographic patterning [258].

Fig. 2.7 b) shows an atomic force microscope picture of a surface pattern obtained with a single laser pulse (with a peak intensity of 485 mJ/cm^2), using an incidence angle of 45° of the

split laser beams. Trenches with a width of about 110 nm and a typical depth of 20 nm were obtained. In order to etch deeper structures, the sample can be exposed to HCl vapour during a multiple pulses processing to remove the residual liquid Ga.

2.3 Experimental Setup for Laser-Induced GaN Delamination

As already mentioned, the Nd:YAG laser pulses can be used to thermally decompose a thin layer of GaN at the film-sapphire interface causing the detachment of the sapphire and enabling the fabrication of freestanding GaN substrates starting from sufficiently thick HVPE-films [225][259]. The delamination of GaN areas larger than the attainable beam size was achieved by sequentially scanning the pulses across the transparent backside of the sapphire. To produce large area, freestanding, up to 2" GaN pseudo-substrates, the liftoff process was automatized. The experimental setup for the laser-induced liftoff is shown in Fig. 2.8.

The scanning of large areas with the Nd:YAG laser beam was made possible by a motorized table movable in 2 perpendicular directions. The high-precision step motors are controlled with user-friendly software specifically developed to allow spiral, and linear back-and-forth scans with different step sizes (1 to 20 mm). A complete illumination of the scanned area is achieved by choosing step sizes between pulses smaller than the beam diameter compensating also the beam profile inhomogeneities (Fig. 2.4). The Win-Lab program includes an automatic control of the beam-shutter for a safe use of the harmful class-IV Nd:YAG laser. All the optical elements in the beam path were adjusted to avoid back-reflections that would destroy the laser-cavity mirrors and Nd:YAG rods.

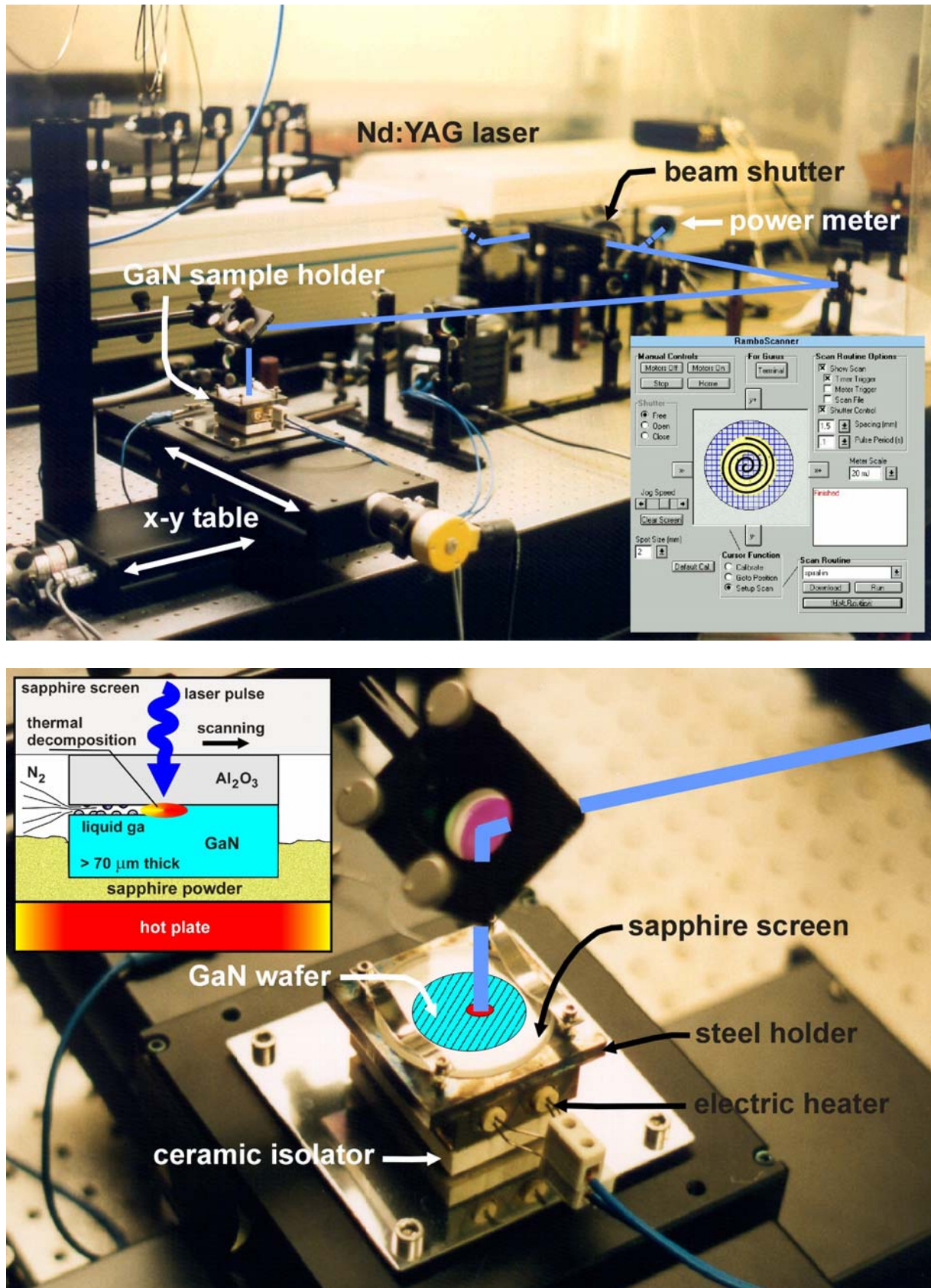


Fig. 2.8: Experimental setup of the laser process for sapphire substrate removal from thick HVPE-grown GaN films. An overview of the Nd:YAG laser with the optical elements is shown in the upper figure. The small image at right is a copy of the working window of the controlling software. A detailed view of the sample mounting is presented in the bottom figure with a schematic diagram for laser delamination of GaN thick films.

2.4 Laser-Induced Liftoff of Thick HVPE-GaN Wafers

A successful separation of HVPE-GaN films from sapphire depends on several factors including film thickness and thickness homogeneity across the wafer, growth procedure, and resulting stress and stress gradient caused by the large thermal expansion coefficient mismatch. We have processed HVPE-GaN wafers grown with different growth procedures including thick GaN multilayer samples performed with *in-situ* growth stops (ATMI Inc.-USA) and HVPE-GaN grown on MOCVD-GaN templates structured with the ELOG technique (NEC-Japan). Due to the commercial relevance of GaN pseudo-substrates and the technological difficulty of growing thick crack free GaN films, it was not possible to obtain much information about growth details. Nevertheless, the results of delamination could be ordered and interpreted according to structural and morphological characteristics of the GaN samples.

For substrates with maximum thickness ranging from 70 to 300 μm (comparable to the sapphire thickness of 330 μm), the thermal expansion coefficient differences result in substantial bowing of the wafer. The sapphire substrate contraction is stronger than the GaN layer. Despite of the bowing, most of the wafers exhibited very little or even no near-surface cracking across the whole wafer area. To protect the GaN layer during laser processing, the film side of the GaN/ Al_2O_3 structure was temporarily bonded to a metal support with liquid Ga using a metal solder. Incident pulse intensities of about 400 mJ/cm^2 were required for the interface decomposition at room temperature. Additional 15% loss of pulse intensity was considered due to reflection at the standard polished sapphire backside. However, the bowing of the samples with thicker GaN films ($> 100 \mu\text{m}$) conflicted with this procedure because the strain inhomogeneity at the boundary of the released and thus relaxed spots caused extensive fracturing. To reduce the bowing-induced fracturing, we investigated heating of the sample during the laser liftoff. The strain in the sample and, consequently, the bowing was visibly

reduced and hardly noticeable through simple specular observation of the GaN surface at temperatures around 600°C. This is consistent with temperature-dependent X-ray diffraction measurements performed by Leszczynski [264], in which he showed the convergence of the lattice constant values of bulk GaN and a 2 µm-thick GaN film on sapphire at about 800 K, and indicated the possibility of inelastic relaxation above this temperature. Ideally, the performance of *in-situ* laser liftoff close to the growth temperature would be the best solution to avoid all bowing/cracking problems caused by the thermal expansion coefficient mismatch between GaN and the sapphire substrate.

Extended areas could be sequentially released without sample damage by performing the laser treatment at temperatures above 600°C, but below 830°C (decomposition temperature of GaN). The threshold energy density for laser-induced GaN decomposition at 650°C is reduced to 250 mJ/cm², resulting in less thermal impact to the GaN layer. The wafer is positioned in a steel holder filled with a thin layer of sapphire powder (see schematic insert in the bottom image of Fig. 2.8). A transparent sapphire window on top prevents involuntary wafer movement during scanning and laser shooting. The role of the small grain sapphire powder is to embed the GaN during the controlled heating up time of 60 min to allow a free increasing of the bowing radius with temperature. The powder is also important after the delamination during the cooling down time of also 60 min to support the freestanding GaN film.

Prior to mounting the wafer for laser liftoff it is important to check if there is no residual GaN on the backside of the sapphire substrate. The undesired GaN is formed during the HVPE growth and will prevent laser absorption at the GaN/Al₂O₃ interface. Due to bowing of the wafers, a polishing procedure was developed using a diamond pad (grain size = 125 µm) to provide a meticulous and careful lapping of these GaN regions under water flow. To avoid cracking during lapping the wafers were first fixed to an aluminum plate with a transparent thermoplastic adhesive (melting point of 120°C) soluble in acetone.

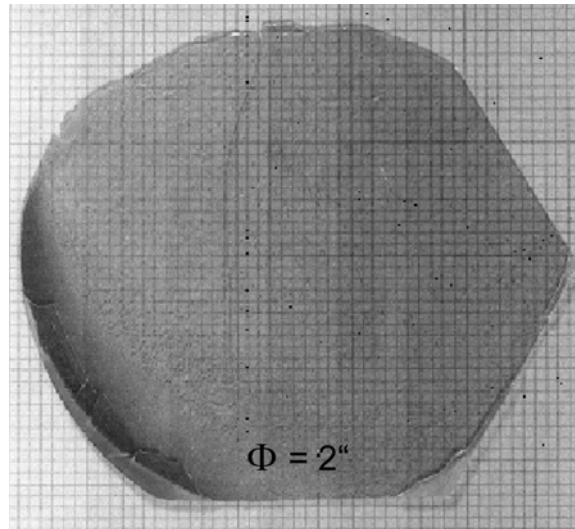


Fig. 2.9: Image of a 275 μm thick freestanding GaN film, after removal from the 2" sapphire substrate [225]. The missing wafer border pieces broke off right after the HVPE growth.

The HVPE-GaN film was finally mounted in the sample holder shown in Fig. 2.8. The laser scanning itself takes only 3 min with a step size of 2 mm. A spiral scan shape towards the center of the wafer was found to be best suited for delaminating circular samples in comparison to the linear row by row scan, due to the more symmetrical stress distribution between the free and still connected parts of the wafer. A consecutive second scan of 3 min can be performed to insure full area laser illumination, but it is not strictly necessary. In this way, freestanding GaN films were separated from 2" sapphire wafers, as shown in Fig. 2.9 for a film of 275 μm thickness.

2.5 Laser-Induced Liftoff of HVPE-GaN Membranes

In this section we discuss next the delamination of HVPE-films in the thickness range from a few micrometers up to about 60 μm . These films are mechanically too fragile to be separated in the same way as described in the preceding section for thick GaN films. It is necessary to attach a supporting layer to the top GaN layer to avoid large area fracturing after

laser liftoff. The choice of a proper material which allows thin self-supporting GaN films is of crucial importance. It should have a very low elastic modulus, comparable to GaN, and be easily removable. On the other side, it should be flexible enough to accommodate changes in the bowing radius during liftoff. Finally, a material stable at high temperatures up to 650°C would be desirable. To the best of our knowledge no such material is commercially available. We succeeded by using different types of commercial adhesives and glues, like a two-component epoxy resin, or a silicone thermoresistant elastomer. Sticking GaN samples to a “blue tape” used in semiconductor production for fixing samples during sawing is also a possible approach.

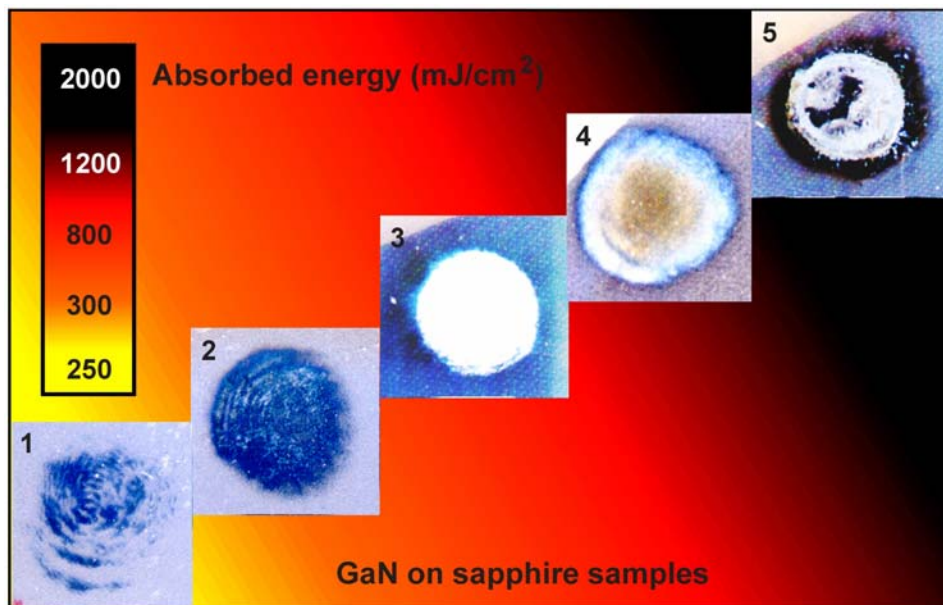


Fig. 2.10: Sequence of single Nd:YAG laser pulses on 1 μm thick GaN samples for focused beam calibration (shot diameter of 3 mm). The consequence of increasing the energy density can be observed by the colour change due to Ga drop formation (1, 2, 3) and sapphire substrate deterioration (4, 5).

All delamination processes were performed at room temperature due to the relatively low temperature resistance of the applied adhesives. The integrity of films processed at room temperature will drastically depend on the bowing radius and thickness homogeneity. The stress gradient between the freed part of the film and the GaN still on sapphire is considerably increased at temperatures below 600°C, which is detrimental for a crack-free liftoff. The

normal 7 mm laser beam diameter was focused to a diameter of 3 mm with sapphire lens to improve the beam profile by narrowing the spacing between the circular rings of maximum energy density (Fig. 2.4). Much higher power densities can obviously be reached with the focused beam and therefore a new calibration of the laser output power density is required. The sequence of shots in Fig. 2.10 shows the effect of the focused laser beam on a thin GaN film grown on sapphire. The single pulse Nr. 2 with an absorbed energy density of 300 mJ/cm^2 has a homogeneous energy distribution which is best suited for GaN liftoff. With increased laser power, the shots Nr. 3 to 5 show excessive GaN decomposition with strong Ga-drop formation up to the level of sapphire damage, visible in the dark regions in shot Nr. 5 with an absorbed energy density of about 2 J/cm^2 .

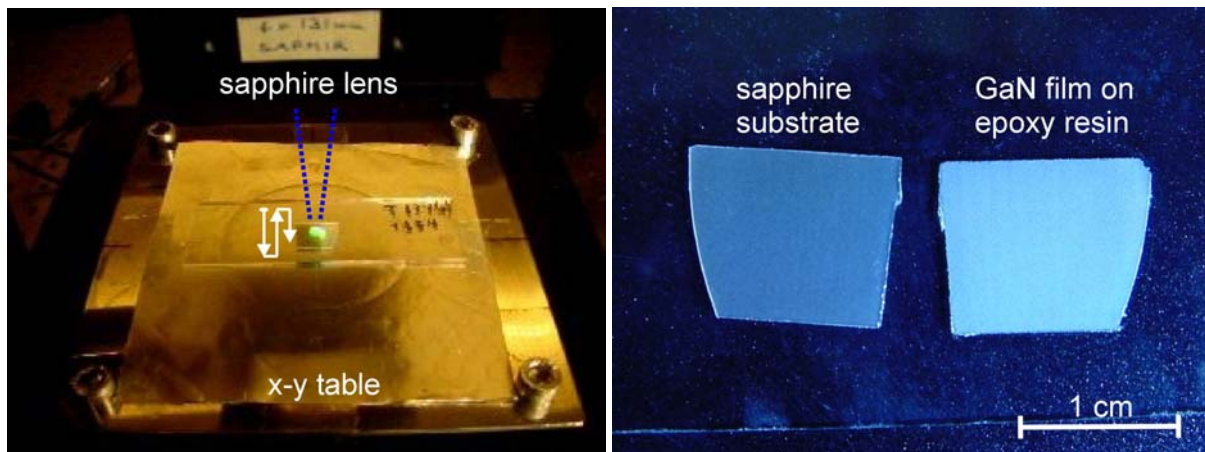


Fig. 2.11: Snapshot during laser delamination of a HVPE-GaN sample with an area of about 1 cm^2 and a thickness of $30 \mu\text{m}$ fixed with epoxy resin to a glass holder. On the right: delaminated sapphire substrate next to the completely crack-free GaN sample.

Completely crack-free GaN films were delaminated by fixing them to two-component epoxy resin prior to laser scanning. Proper delamination is confirmed by optical microscopy with backside illumination. A glass carrier was used to support the GaN sample, which was pressed onto a thin less than 0.5 mm layer of the transparent resin. It is important to avoid the inclusion of air bubbles during the mixing of the glue to provide a homogeneous covering of the GaN film. The laser liftoff was performed 5 min after curing the glue at room temperature.

The left image in Fig. 2.11 shows a snapshot of the linear back-and-forth scanning with the focused beam. The sapphire substrate is completely free at the end of the process (right image in Fig. 2.11). The strong adhesion characteristics of the two-component epoxy resin used is advantageous for a perfectly crack-free GaN liftoff, but on the other hand it hampers its separation from the GaN film after sapphire removal due to the high chemical stability of such glues. Nevertheless, this epoxy can be solved with dichloromethane (methylenechloride) or in boiling water after several minutes.

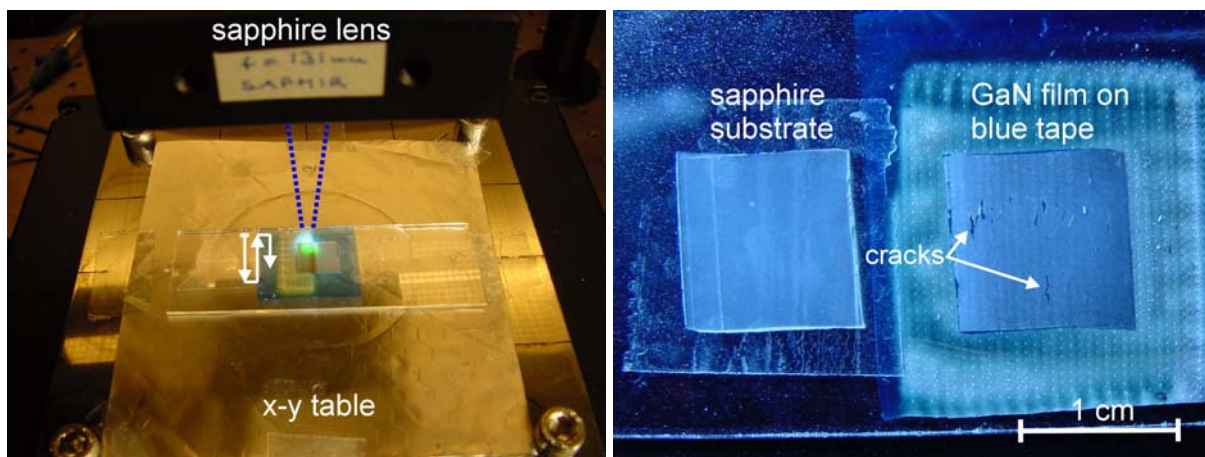


Fig. 2.12: Snapshot during laser delamination of a HVPE-GaN sample with an area of about 1 cm^2 and thickness of $30 \text{ }\mu\text{m}$ stuck to a piece of blue tape. On the right: delaminated sapphire substrate close to the GaN membrane. Some cracks were formed due to the shrinkage of the tape after laser shots.

Less adhesion is provided by a so-called “blue tape” and the preparation for liftoff is quite simple. The free side of a HVPE-GaN sample with a thickness of about $30 \text{ }\mu\text{m}$ is placed on a piece of blue tape fixed to a glass holder as shown in Fig. 2.12. The delaminated film remains stuck to the tape, but can be easily detached after laser liftoff. The laser shots with an absorbed energy density of 300 mJ/cm^2 affect also the blue tape at the border of the sample, shrinking it and changing its color. This shrinkage bended the fragile GaN film and consequently some cracks were generated as can be observed in the right image of Fig. 2.12. The fracturing can be avoided by covering the edge of the sample with a reflecting material.

The application of blue tape as a transitory holder for thin freestanding GaN membranes represents a cheap and uncomplicated alternative for sapphire delamination by laser induced liftoff.

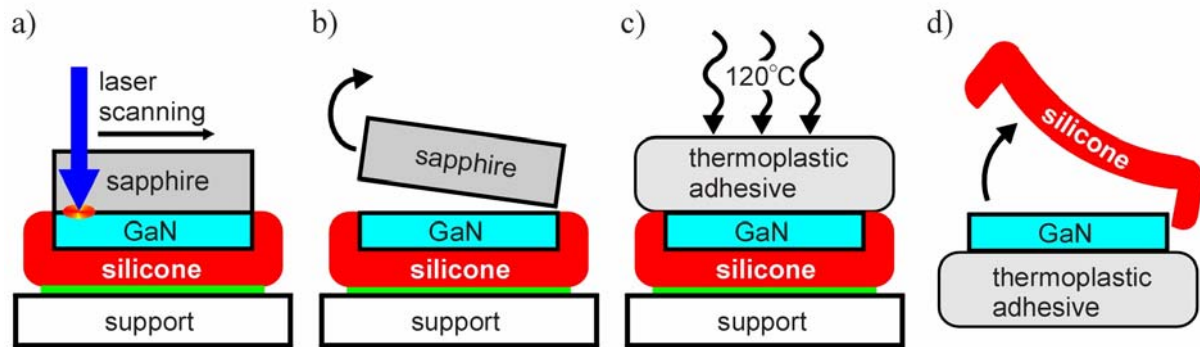


Fig. 2.13: Sequence of steps to produce large size GaN membranes. a) laser liftoff of the GaN film covered with silicone elastomer and mounted onto a support; b) sapphire removal after laser scanning; c) deposition of a ~ 3 mm thick layer of thermoplastic adhesive at 120°C ; d) peel-off of the silicone elastomer. The GaN film can be easily isolated by solving the adhesive in an acetone bath.

A procedure to produce freestanding full size 2'' GaN membranes using silicone elastomer during laser liftoff and a thermoplastic adhesive to support the film after sapphire removal was developed. A schematic step by step view is shown in Fig. 2.13. The free side of the HVPE-GaN film on sapphire was covered with the thermoresistant (up to 300°C) silicone elastomer forming a ~ 3 mm thick stiffening layer. The complete elastomer curing occurs in approximately 12 hours with air humidity through elimination of acetic acid. The film was then fixed to a metallic plate with double faced adhesive tape to avoid moving of the flexible silicone rubber. After laser scanning at room temperature the sapphire substrate can be removed. Consecutively, the freed side of the fragile GaN film is protected with a ~ 3 mm thick transparent thermoplastic adhesive allowing a safe peel-off of the silicone elastomer (Fig. 2.13 d). A $60\ \mu\text{m}$ thick GaN membrane with a diameter of 2'' is shown in Fig. 2.14. The membrane is still protected by the thermoplastic adhesive, which can be easily dissolved in acetone without too much mechanical stress. The flexibility of the silicone rubber allows the accommodation of the GaN film bowing. After fixing the membrane with the much more

viscous thermoplastic adhesive, the residual bowing of the thin film and some cleavage lines can be observed through specular light reflection in the left images of Fig. 2.14.

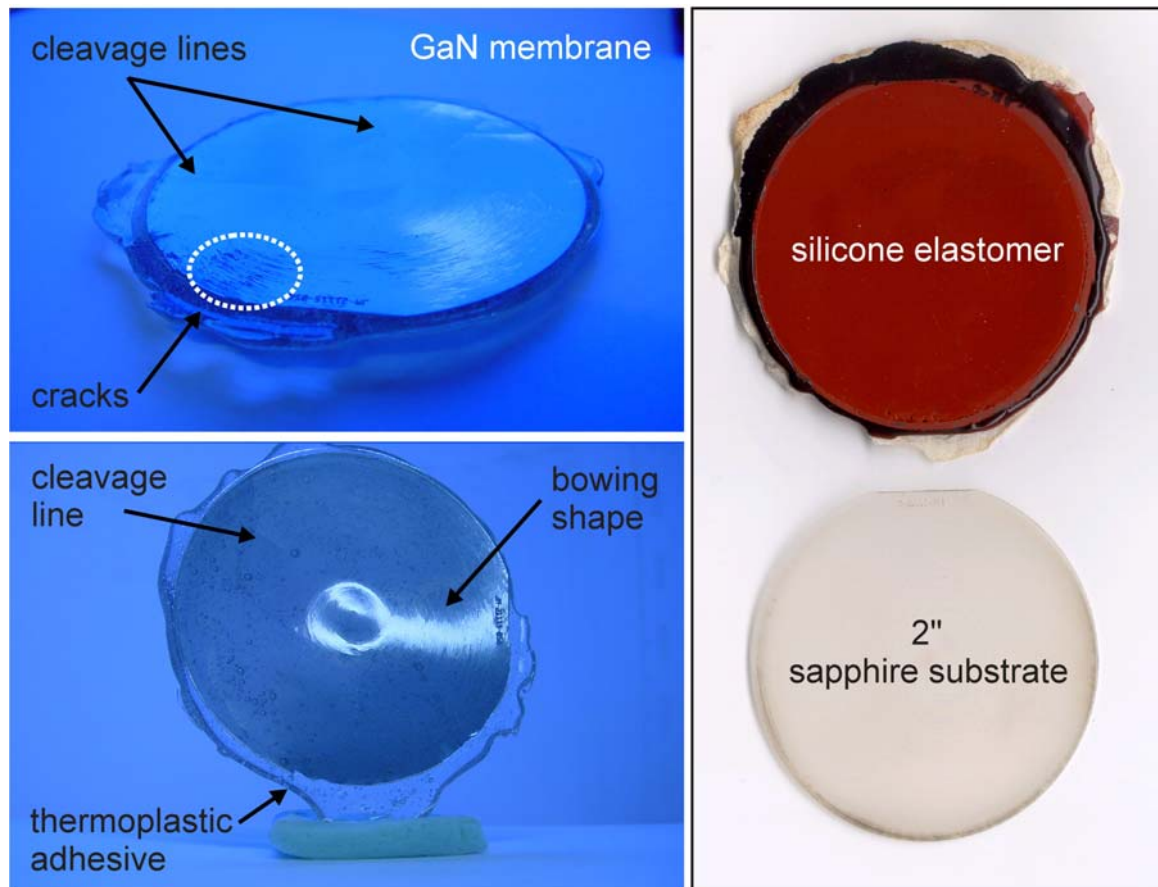


Fig. 2.14: The left images show the HVPE-GaN membrane with a diameter of 2" and thickness of 60 μm attached to thermoplastic adhesive. Among the indicated features one can see the curved specular light reflection due to the bowing of the film. The silicon elastomer can be completely peeled-off as shown on the right image close to the sapphire substrate after laser liftoff.

Despite of some cracks distributed over the GaN membrane, the described procedure is fully reproducible and applicable to the delamination of large HVPE-GaN films with an average thickness of some tens of micrometers. A different approach to produce completely crack-free thin and large size GaN-based heterostructure wafers for device production is based on the wafer bonding technique discussed in the following section.

2.6 Delamination of Wafer Bonded GaN Thin Films and Heterostructures

The monolithic integration of two dissimilar materials onto one platform with wafer-bonding and laser liftoff is a convenient alternative to heteroepitaxial growth when this is not possible or too problematic. In the case of group III nitrides, the integration is motivated by combining the optoelectronic functionality of GaN-based heterostructures to receptor substrates with much better thermal and electrical properties than the original sapphire. For devices processed on sapphire, all electrical contacts must be made from the top side. This complicates contact and packaging schemes, resulting in higher operation voltages and a spreading-resistance handicap [261]. The poor thermal conductivity of sapphire is detrimental for high-current device performance of LEDs, LDs and high-power transistors and hence the transfer to other substrates with better thermal properties is of enormous benefit. The cheap and readily available Si is one of the most attractive candidates, but GaAs, Ge, Mo, and copper are also advantageous receptor wafers. The bonding layers have to fulfil some requirements: the bonding alloy has to be adherent to both the epitaxial film and the receptor substrate providing full surface contact despite of sub-micron surface asperities; the bonding temperature should be low ($< 200^{\circ}\text{C}$) to avoid thermal stress to the film, but without leaving behind any alloy phases with a melting point below the bonding temperature; and it should have low electrical resistance for a circuit connection of the devices. Wong *et al.* have used a Pd-In metal bonding to connect GaN to Si [265], whereas Funato and co-workers integrate GaN to Si with an AuGe-mediated wafer bonding technique [266]. Jasinski *et al.* succeeded in producing GaN/GaAs structures by direct wafer fusion [267]. The 2 μm thick GaN films grown on sapphire were fused to GaAs substrates in nitrogen ambient under uniaxial pressure of 2 MPa at bonding temperatures of 550 and 750 $^{\circ}\text{C}$.

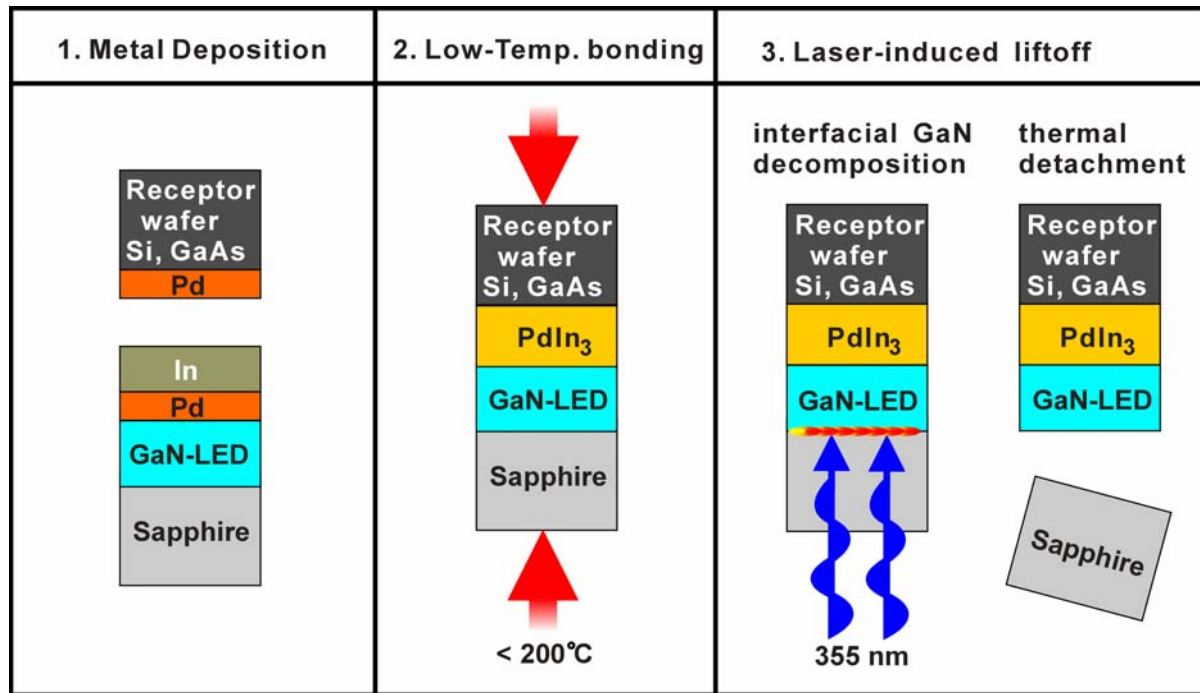


Fig. 2.15: Process flow for bonding and transfer of a nitride based LED from sapphire onto a receptor wafer.

Individual devices on a GaN-based wafer can be scribed or isolated via mesa-etching prior to wafer bonding, thus enabling the production of separated devices after the laser liftoff. The technological process-flow diagram for the production of highly efficient nitride based LEDs using a metal bonding and laser delamination procedure is illustrated in Fig. 2.15. In this way the individualized devices on a wafer can be transferred to a receptor substrate like Si, GaAs or Cu. To increase the efficiency of light emission of LEDs and LDs, an anti-reflection coating can be also deposited on the free side after sapphire delamination.

By using thin GaN films grown on sapphire the effect of the laser shots on the edges and borders of pre-scribed heterostructures was simulated. A $6\ \mu\text{m}$ thick GaN film was softly scribed with a diamond pen to quasi-squares of approx. $500 \times 500\ \mu\text{m}^2$ (Fig. 2.16 a) and its top side (Ga-face) was covered with epoxy glue. In Fig. 2.16 b,c), the N-face of the GaN film is showed after sapphire removal. The thin film interference lines prove the absence of cracks in the squares, and also no broken edges are observed in Fig. 2.16 c).

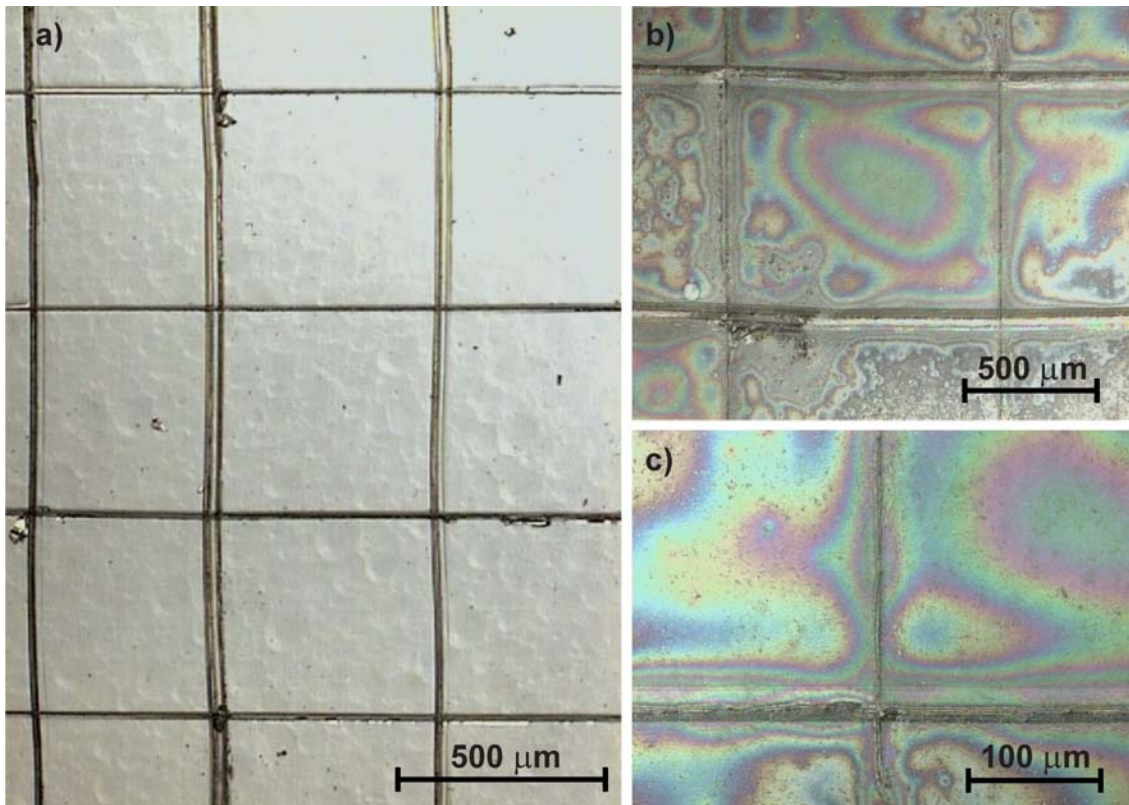


Fig. 2.16: Effect of laser liftoff on edges and borders on a thin GaN film: a) GaN on sapphire manually scribed with a diamond pen (Ga-face up); b) freestanding GaN film fixed on epoxy, N-face up; c) magnified view of the edges of the free squares.

In collaboration with OSRAM Opto Semiconductors, we have optimized the laser-induced liftoff technique for the delamination of wafer bonded GaN films and GaN-based heterostructures. Films with thicknesses of some micrometers were bonded with different metallic alloys containing In, Pd, Sn and other metals with a low melting point. The delamination was performed using similar parameters as in section 2.5 with a focused beam and absorbed energy density in the range of 300 mJ/cm^2 . After a series of experiments it was clear that the correct choice of the bonding alloy and bonding conditions were the limiting factor for obtaining completely crack-free films without defective regions where the film peels-off. The GaN-based heterostructures are typically thinner than $5 \mu\text{m}$, resulting in practically no bowing of the wafers and permitting a laser liftoff at room temperature. Nevertheless, the energy density of the laser shots should be kept as close as possible to

threshold value necessary for GaN decomposition. Any additional energy will mechanically stress the film, favouring film spalling and peel-off after sapphire removal.

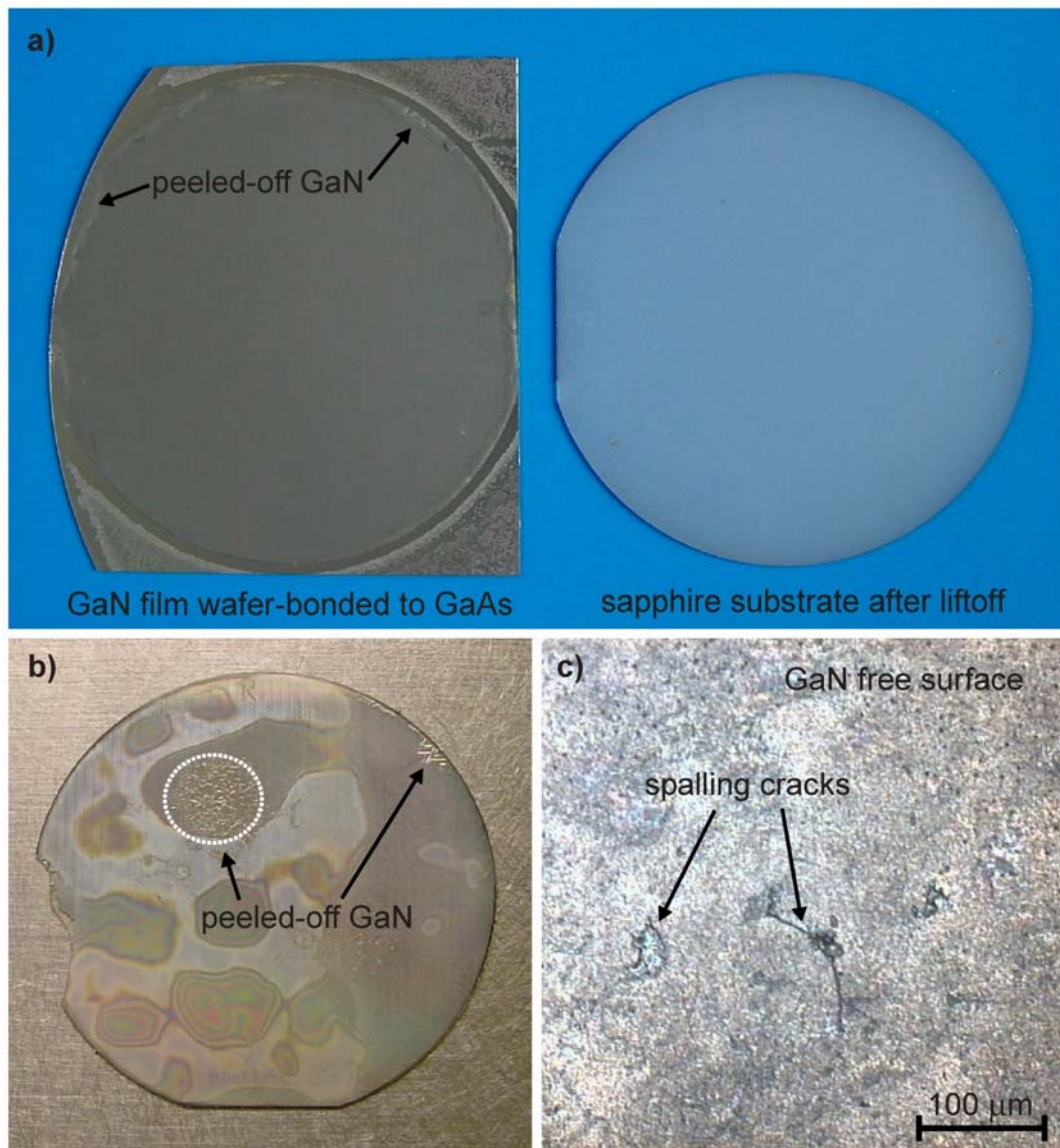


Fig. 2.17: a) Delaminated 3 μm thick 2" GaN film (not structured) wafer-bonded on GaAs on the left and GaN-free sapphire substrate on the right. b) Effect of inhomogeneous wafer-bonding on a GaAs receptor wafer on the GaN thin film after laser liftoff. c) Magnified view of the GaN surface after sapphire delamination in a region with wafer-bonding problems.

Fig. 2.17 a) shows a successfully delaminated GaN film wafer-bonded to GaAs, where some peeling-off occurred only at the very border of the wafer. Fig. 2.17 b) represents the worst case considering the wafer bonding homogeneity over the 2" GaN wafer surface. The speckles on the wafer mark the regions with bonding material segregation, probably due to

different phase formation. This result in local spalling or complete peeling-off of the GaN film in this areas (Fig. 2.17 b,c). This is obviously detrimental to the production of devices, but practically only the external ~5 mm up to the wafer borders are really critical in the production of GaN-heterostructures due to peeling-off after laser delamination. The isolation of the devices prior to wafer-bonding prevents the propagation of cracks and spalling formation, guaranteeing the integrity of the heterostructures during laser delamination. A yield as high as 90% and above can be reproducibly achieved for 2" wafers. In the last section of the chapter it will be shown for freestanding flip-chip bonded blue/violet GaN-LEDs that no degradation of the device performance occurs from laser-induced liftoff. The following section considers the mechanisms of crack formation on GaN films due to strained growth on sapphire and laser liftoff.

2.7 Cracking Mechanics of GaN Films on Sapphire

Crack formation mechanisms are of interest for laser-induced delamination as crack free GaN films are desired. Nevertheless, an extended and comprehensive analysis is not in the scope of this work. We show some relevant aspects of the cracking mechanism in order to qualitatively understand the cracking problem of GaN film delamination with the laser liftoff method.

Cracking in GaN/Al₂O₃ structures is a consequence of the high lattice and thermal expansion coefficient mismatch [268]. Typically, a GaN layer exhibits compressive strain, whereas the substrate exhibits tensile strain near the interface due to cooling down after the growth, leading to a convex bowing of the GaN film side, as shown in Fig. 2.18. The bending allows partial relaxation of internal stress, but a residual stress persists in the structure as shown in Fig. 2.18 b) [269][270]. Considering that the thickness of the film, t_f , is much

smaller than that of the substrate, t_s , in the absence of cracks a homogeneous compressive stress σ_f exists across the film. The stress distribution in the substrate σ_s can be assumed to be linear, with a maximum tensile $\sigma_{s \max}$ at the interface, half of $\sigma_{s \max}$ at the backside, and neutral at $2/3 t_s$ ($\sigma_s = 0$, stress-neutral plane) [269] (Fig. 2.18 b). The equilibrium of internal stress can be written as:

$$\sigma_f t_f + \int_0^{t_s} \sigma_s dz = 0 \quad \text{Eq. (2.2)}$$

The increase of $\sigma_{s \max}$ is directly proportional to the thickness of the substrate t_s . In brittle materials like sapphire, cracking can occur when tensile stress $\sigma_{s \max}$ exceeds the critical value of 30 MPa [269]. Consequently, a film above a critical thickness will give rise to cracking as shown in Fig. 2.18 c).

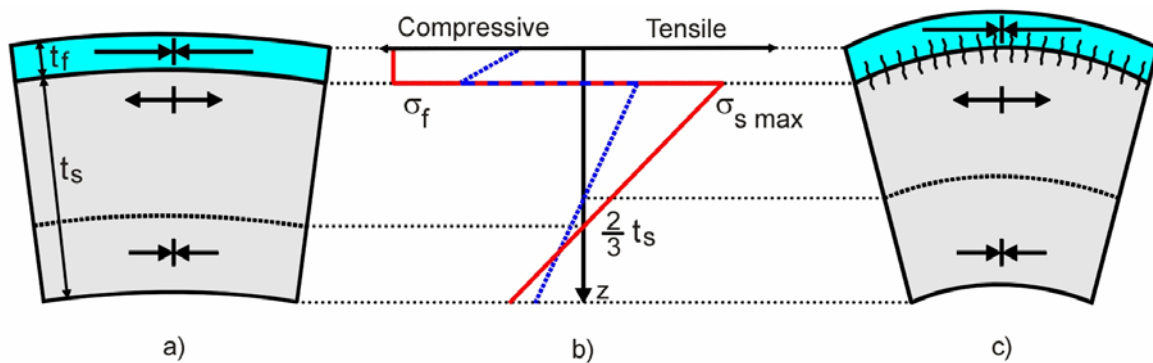


Fig. 2.18: Schematic view of bowing in the GaN/Al₂O₃ film/substrate system a) before and c) after cracking. b) The red line and the blue (dashed) line represent the stress distribution across the structure before and after cracking, respectively.

The epitaxial layer is under compressive stress and therefore cracking perpendicular to the interface is hardly expected to occur. A crack at the interface is not expected to propagate into the film under compressive stress. However, experimentally cracking was observed to occur in the epilayer and the substrate, as is shown in Fig. 2.19 a,b). Since the GaN film is epitaxially grown on sapphire, both form a continuous volume before cracking. A gap is inevitably produced at the interface as soon as a crack is generated in the sapphire by stress

release. Consequently, a gap is also formed in the epitaxial film, *i.e.*, the crack generated in the sapphire continues through the GaN film (Fig. 2.19 a,b). The substrate region under tensile stress is relaxed upon cracking and the residual difference in the elastic energy is converted to surface energy at the cracks. The stronger bowing of the film/substrate structure schematically shown in Fig. 2.18 c) is a consequence of the cracking at the interface. The redistribution of stress after cracking is schematically represented by the blue (dashed) line in Fig. 2.18 b). Eq. (2.2) must be rewritten to still satisfy equilibrium of stress by replacing $\sigma_f t_f$ with $\int_0^{t_f} \sigma_f dz$. By generation of cracks, the elastic energy decreases and surface energy is added to the system at the cracks.

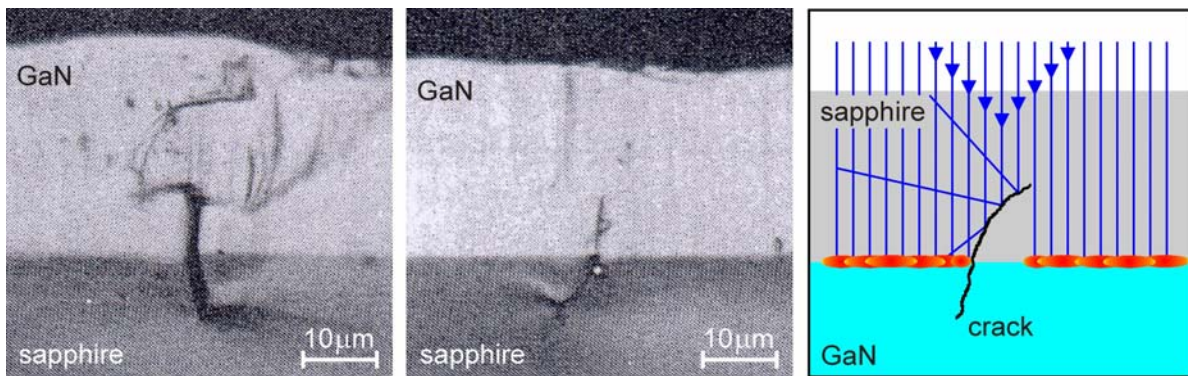


Fig. 2.19: a, b) Cross-sectional shape of cracks at the interface of GaN grown on sapphire [269].
c) Schematic representation of the laser reflection at the borders of cracks in the sapphire substrate.

The described cracking morphology can be attributed to a combination of simultaneous parting of Al_2O_3 and cleavage of GaN [269]. One can distinguish between two types of cracking with regard to GaN grown on sapphire. During the epitaxial growth, the large lattice mismatch causes compressive stress in the film and tensile stress in the substrate. As growth goes on, microcracks may be generated in the substrate, due to the brittleness of sapphire [270][269]. These microcracks will occur when the epitaxial layer is of good crystalline quality, due to a stronger bonding strength at the film/substrate interface. A different cracking process takes place during cooling down from growth to room temperature: the thermal

expansion coefficient mismatch between GaN and sapphire will lead to the formation of cracks, so-called macrocracks, simultaneously generated in the substrate and in the epitaxial film, as soon as $\sigma_{s \max}$ exceeds the critical value. From the theory of fracture mechanism, the structural stress which causes crack extension is smaller the larger the size of a pre-existing crack [269]. Thus, the pre-existing microcracks, caused during the epitaxial growth, will decrease the critical stress for generation of macrocracks during cooling down. Depending on the thicknesses of the substrate and the epitaxial film, this may lead to a complete rupture of the GaN/Al₂O₃ wafer.

The substrate cracking can also cause residual sapphire to remain on the backside of freestanding GaN films, due to reflection of an incident laser light at the crack borders, as illustrated in Fig. 2.19 c). The cracked surface acts as a mirror which prevents the pulses to be absorbed at the GaN/sapphire interface. This undesired effect depends on the extension of the cracks in the sapphire and can hinder the normally easy detachment of the GaN film. Sapphire spikes and lines can be observed on the backside of freed GaN films (Fig. 2.21). A fast lapping with a diamond pad with grain size of 40 μm is sufficient to remove the residual sapphire. Depending on the GaN thickness, the integrity of the film has to be preserved during lapping by fixing it to a base with acetone soluble adhesive.

The decomposition of GaN following the laser shot is accompanied by the local generation of a vapour pressure due to the finite size of the laser beam. If the pressure is confined in the shot area it may cause a variety of deformations and create local stresses which can introduce defects and cracks. Films initially under a residual compressive stress may bulge away from the substrate and the free part of the film is put under biaxial tensile stress that can cause cracking (Fig. 2.20). Alternatively, if the film is fully constrained, radial cracking along the periphery of the illuminated region may occur and, under large driving forces, may even cause spalling of the film.

For an absorbed laser power of 320 mJ/cm^2 approximately 50 nm of GaN are decomposed, corresponding to a nitrogen flux of about 10^{17} cm^{-2} per pulse (see Fig. 2.5). Simple calculation using the ideal gas law can be used to estimate the pressure of the released N_2 bubble. Considering the laser shot size = 0.7 cm and the corresponding shot area = 0.4 cm^2 , the decomposed volume of GaN is given by:

$$V = 50 \text{ nm} \times 0.4 \text{ cm}^2 = 2 \times 10^{-12} \text{ m}^3$$

Neglecting the volume occupied by the residual metallic Ga, the molar fraction of N in the decomposed volume can be calculated as:

$$n = 10^{17} \text{ cm}^{-2} \times 0.4 \text{ cm}^2 / 6 \times 10^{23} \approx 7 \times 10^{-8} \text{ Mol of N atoms}$$

At the decomposition temperature of GaN (830°C) we can finally obtain the pressure of the N_2 bubble:

$$p = n R T / V \approx 3 \times 10^8 \text{ J / m}^3 \approx 300 \text{ MPa} \approx 3 \text{ kbar}$$

The calculated pressure of 300 MPa is comparable with the high temperature yield strength of GaN of about 200 MPa at 900°C [61]. Below the yield strength value, the material is elastic and above this threshold a plastic deformation will occur. In the dynamic real case the N_2 is released explosively during the short laser pulse of 6 ns , generating a compressional shock wave, which will propagate in the film and substrate. Tavernier and Clarke have given a detailed description of this phenomenon and the relevant parameters [271]. The compressional pressure wave will be reflected at the free film surface and at the substrate backside, turning into a tensile wave which can contribute to film fracturing radial to the laser shot area if it returns to the interface during the laser pulse or while the N_2 gas bubble is still hot [271]. If the N_2 is confined after the GaN decomposition, the internal pressure causes the film to deflect away from the substrate through bulging, as schematically shown in Fig. 2.20. The film is strained until mechanical equilibrium is attained. A fissure may occur depending

mainly on the size of the beam generated flaw and the thickness of the film. This can be avoided by starting the delamination at an edge and moving the laser in across the film so that the gas generated by the laser pulse can escape along the already debonded portions of the film to the edge, thereby lowering the maximum pressure attained. In our samples, bulging alone is less probable to cause cracking due to the adopted laser scan procedure, always progressing from the borders to the center of the films in steps many times smaller than the beam diameter.

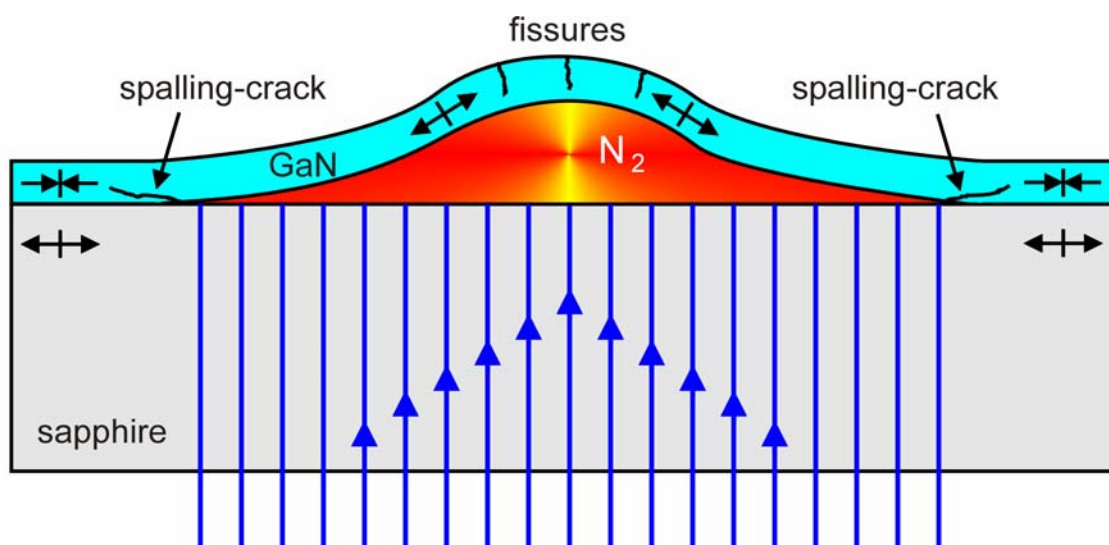


Fig. 2.20: Schematic diagram of bulging of a GaN thin film after laser pulse irradiation and consequent GaN decomposition at the interface to sapphire. The crack lines at the borders and on top of the film indicate how the film is going to preferentially crack if the deformation occurs above the elastic limit.

Buckling is another mechanical instability that can occur if a compressed film is no longer attached to its substrate over a region with critical size [271]. As epitaxial GaN grown on sapphire is under in-plane compressive stress, the film is susceptible to stretch away from the substrate once the interface has been debonded. Based on the observation of the crack shapes we consider that a combination of buckling and the consequences of the explosive generation of hot N_2 gas during the laser pulse are responsible for fissures at the perimeter of the laser shots in freestanding GaN films thinner than $120\ \mu\text{m}$. The typical cracking shape and other

features resulting from the delamination are shown in Fig. 2.21. The GaN wafer with an average thickness of $60\ \mu\text{m}$ was lifted at 650°C with a laser energy density of $300\ \text{mJ}/\text{cm}^2$ following the procedure described in section 2.4.

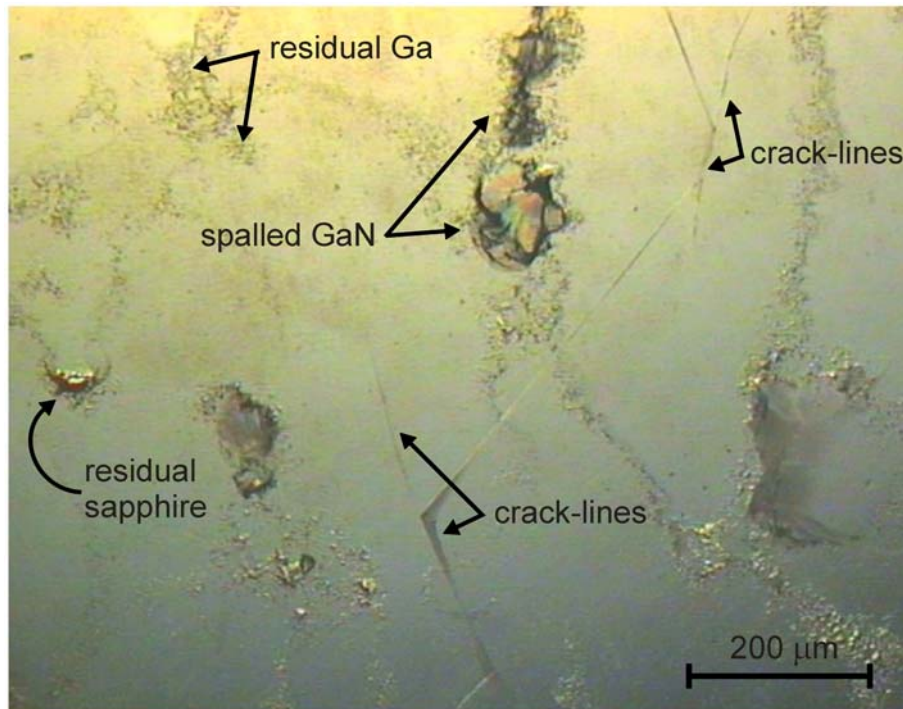


Fig. 2.21: Micrograph of a $60\ \mu\text{m}$ thick GaN film showing the delaminated side. The indicated straight and curved crack-lines mark the places where the film started to spall. Thin GaN pieces also cracked away after liftoff and residual sapphire can be seen on the left.

A stiffening material with a very low elastic modulus comparable to the elastic modulus of GaN was found to reduce crack formation or completely prevent cracking during the delamination of thin GaN films from sapphire. Furthermore, the best results with respect to cracking were obtained by reducing the beam diameter for a more homogeneous energy density profile as shown in Fig. 2.10. Indeed, the ideal situation to avoid most of the cracking mechanisms would be single-shot delamination of the whole GaN film. This is not practicable for large area liftoff with present commercial lasers due to the limited energy density available and the increased difficulty to achieve a homogeneous beam energy profile. A different strategy for the delamination of thin films relevant for device manufacturing is the individualization of the devices by scribing or mesa-etching prior to liftoff. In this case the

area to be lifted is commensurate with the laser spot diameter or even much smaller as was shown, *e.g.*, in Fig. 2.16. The segmented areas preferentially crack at the pre-scribed lines enabling their complete and instantaneous delamination. Using this liftoff strategy it is also indispensable to support the structures from the top with a stiffening material or by wafer bonding to allow further processing.

Some of the wafers exhibited a bowing in the opposite direction than expected after removing the sapphire substrate. Bowing of the free film occurs to compensate residual biaxial strain perpendicular to the crystal surface [272]. This opposite bowing is strongly dependent on the thickness and the lateral strain homogeneity from the middle to the borders of the GaN wafer. The films are usually thinner at the border causing the accentuated warping. Typical HVPE-GaN film shapes with the respective bowing behavior after delamination are schematically shown in Fig. 2.22.

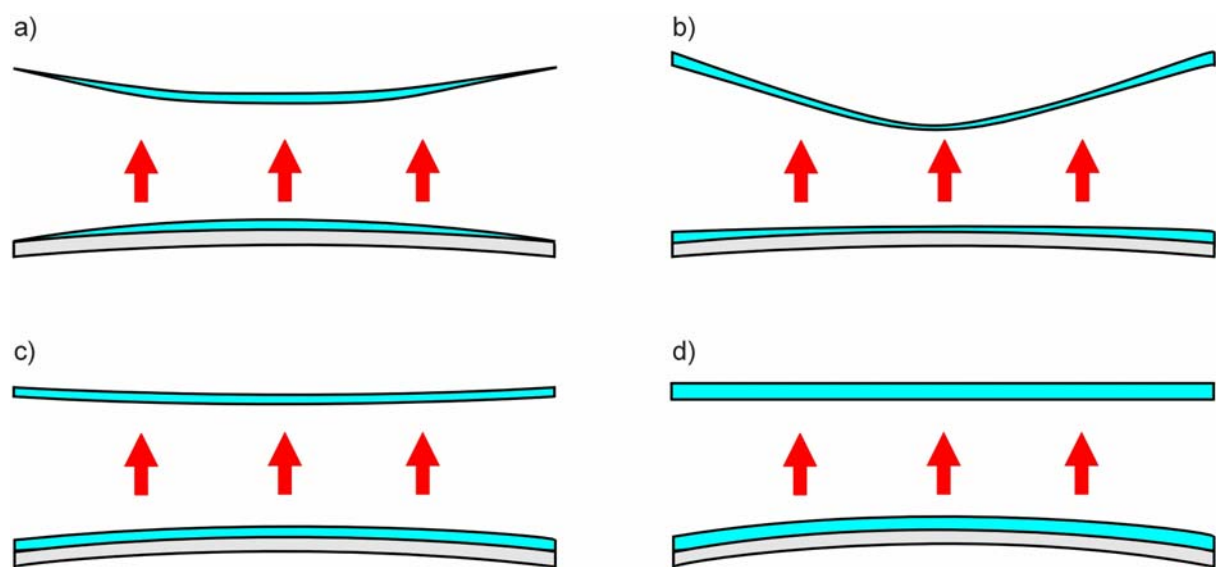


Fig. 2.22: Typical bowing shape before and after laser liftoff of HVPE-GaN wafers grown on 330 μm thick sapphire substrate. a) thin film $<120 \mu\text{m}$, thicker in the center area of the wafer; b) thin film $<120 \mu\text{m}$, thicker at the borders; c) 100 μm thick film with small thickness variation; d) thick film (200 μm to 300 μm) with homogeneous thickness over the wafer. The bowing radius of GaN/Al₂O₃ wafers increases in the sequence: d) \rightarrow c) \rightarrow a) \rightarrow b). After delamination the bowing radius of the freestanding GaN films decreases as: b) \rightarrow a) \rightarrow c) \rightarrow d). Note the inversion of the GaN curvature after laser processing.

Fig. 2.22 b) represents the worst situation for laser liftoff. Both cases shown in Fig. 2.22 a,b) are the most critical for producing crack-free GaN films. Sometimes the wafers already start to crack during the temperature increase to 650°C preceding delamination. Those relatively thin films can be delaminated only in pieces, with the final size depending on the damage prior to liftoff. The best results were obtained for films with small thickness variation (cases *c* and *d* in Fig. 2.22), whereas the residual bowing depends also on the initial GaN growth procedure. HVPE wafers with 100 μm thickness grown on ELOG structured GaN were almost flat after delamination. Wafers represented in Fig. 2.22 d) with thickness ranging from 200 to 300 μm are practically flat after liftoff and without cracks. Flat surfaces are desired for lithography, and GaN-wafer handling and homoepitaxial growth is facilitated. The preparation of epi-ready free-stranding GaN samples and homoepitaxy by MOCVD is subject of the next chapter.

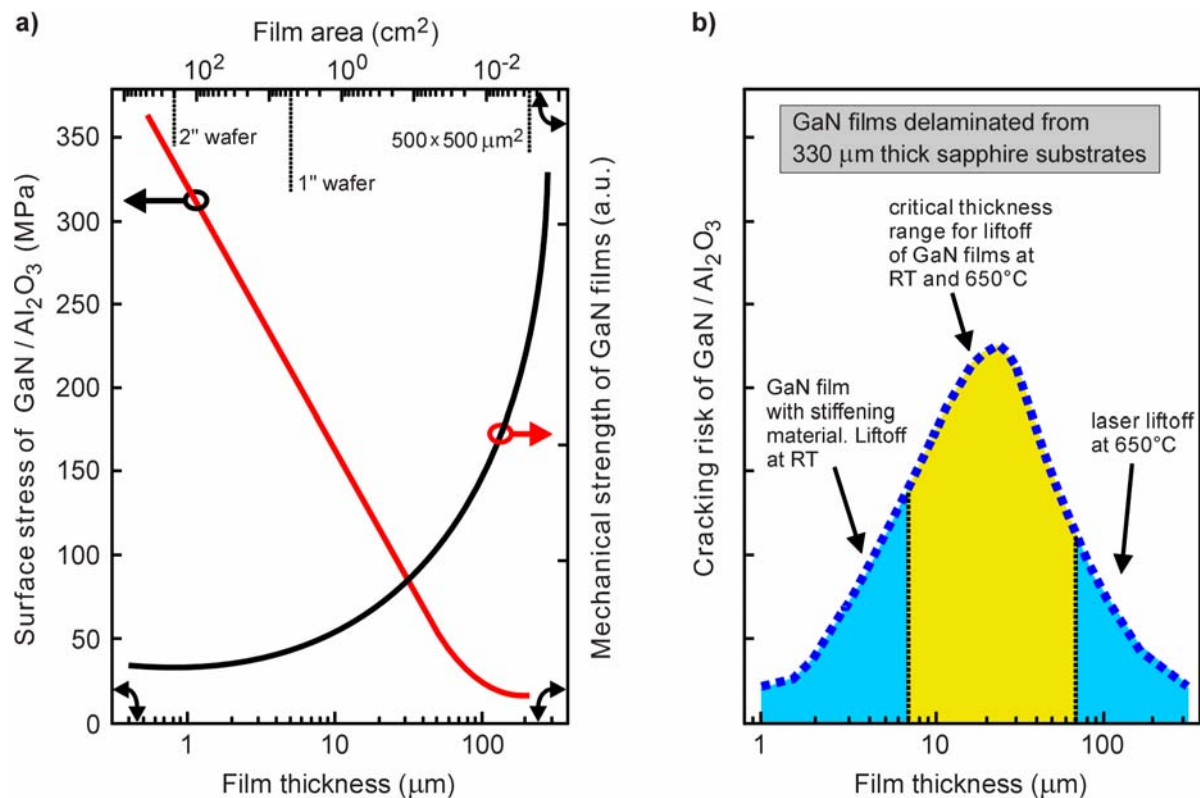


Fig. 2.23: a) Surface stress of GaN/Al₂O₃ and semi-quantitative mechanical strength of GaN as a function of the film thickness and area. b) Schematic cracking risk profile for GaN/Al₂O₃ films as a function of the film thickness. For this study, the GaN films were delaminated from 300 μm thick sapphire substrates at different conditions.

As commented by HVPE growers, sometimes thick GaN films can survive the growth process without any apparent cracks, but after hours or even days the samples are found completely fissured in to many pieces. In the liftoff process, some samples split-up during heating to 650°C. Others cracked after cooling down to room temperature. In this work, approximately 150 samples in many different sizes, thicknesses, shapes, wafer-bonded, single GaN films and GaN-based devices were delaminated. In Fig. 2.23 b) is shown a schematic summary of the results obtained with laser-induced liftoff considering the relationship of surface stress and strength to thickness and size of the GaN films (Fig. 2.23 a). The right axis in Fig. 2.23 a) is related to the mechanical strength or fracture resistance of GaN freestanding films. It increases linearly with the film thickness, but is inversely proportional to the sample area. Unlike metals and polymers, the fracture strength of ceramic materials tends to vary greatly between samples. Listed fracture strength values are often an average of the strength of several samples, depending on many factors like crystal grain size and growth coherence, residual stress in the layers, and pre-existing micro and macrocracks. To the best of our knowledge, no quantitative results of fracture strength as a function of film thickness and film size have been published for GaN films so far.

A distinction has to be drawn between stress at the surface and in the bulk of a material. That is, the stresses are not equal in the two zones. For structural applications, surface stresses, in general, are not the part of critical design parameters. For applications, like thin film or semiconductor devices, the surface is not too far removed from the bulk to induce effect on material properties. In Fig. 2.23 a), the surface stress of GaN/sapphire due to the high thermal and lattice mismatch was calculated from the normal component of the surface strain e_{zz} as a function of GaN epilayer thickness estimated by Reynolds *et al.* from reflectance measurements [273]. The surface stress/strain decreases gradually until about 150 μm and becomes constant for thicker films. This is in agreement with measurements and analysis of the thermal strain relaxation process in GaN/Al₂O₃ heterostructures derived from

Detchprohm *et al.* [270]. The cracking risk profile in Fig. 2.23 b) is to qualitatively show the effect of stress reduction associated with increased physical strength of thin GaN films fixed to an appropriate stiffening layer. The area below $7\ \mu\text{m}$ delineates where the limit of plastic deformation is not reached and consequent crack generation is avoided, due to the stiffening layer. For GaN films thicker than $\sim 70\ \mu\text{m}$ it is strongly recommended to perform the laser delamination at high temperatures of about 650°C to reduce wafer bowing which can lead to strong crack formation in the freed GaN film.

2.8 Sapphire-Wafer Recycling after GaN Delamination

A very attractive side-effect of GaN laser liftoff would be the recycling of the expensive sapphire substrates for regrowth. To evaluate this possibility the surface morphology of the delaminated sapphire wafers was analyzed by scanning electron microscopy (SEM) and atomic force microscopy (AFM) to see the influence of thermal GaN decomposition and detachment caused by the laser treatment.

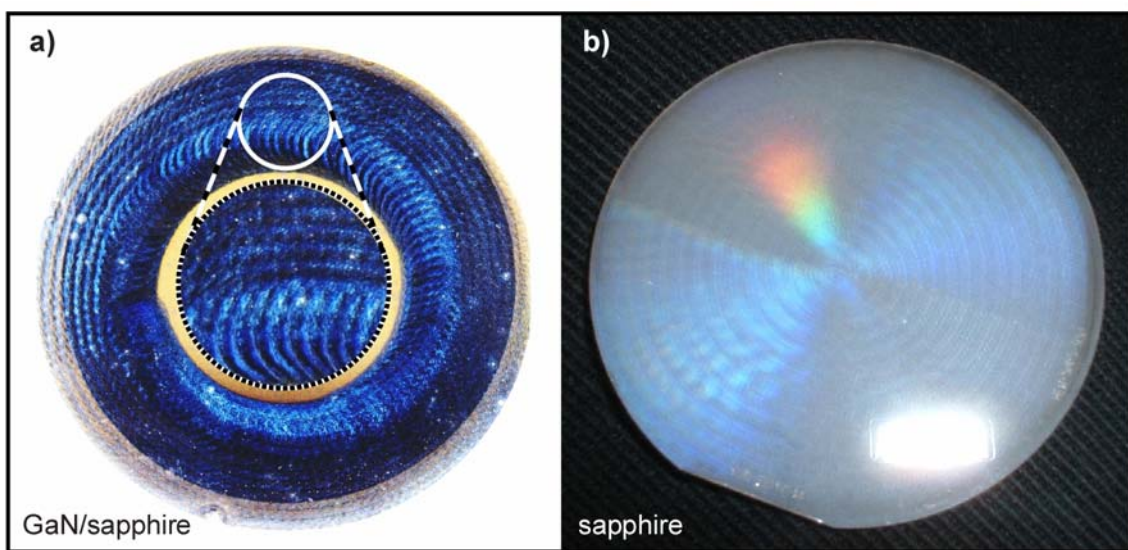


Fig. 2.24: a) Profile generated on a GaN film with Nd:YAG laser scanning in a spiral shape. b) Sapphire wafer surface after GaN delamination. The specular light diffraction pattern is formed due to the sequential overlap of the laser shots at the GaN/ Al_2O_3 interface.

It is possible to observe macroscopically the traces of laser scanning caused by the sequential overlap of laser pulses on top of a GaN film and similarly on a sapphire wafer after GaN liftoff as shown in Fig. 2.24. The SEM images in Fig. 2.25 show the sapphire surface morphology after laser liftoff processing of a HVPE-GaN film with an energy fluence of 300 mJ/cm^2 . No change in the surface morphology can be observed between an unused sapphire substrate a) and main parts of the wafer represented by Fig. 2.25 b), whereas the features seen in c) correspond to the area where laser-shot overlap is responsible for the light diffraction pattern shown in Fig. 2.24. In these regions the rms surface roughness is increased from 0.3 nm for untreated sapphire to 2.6 nm , as measured by AFM.

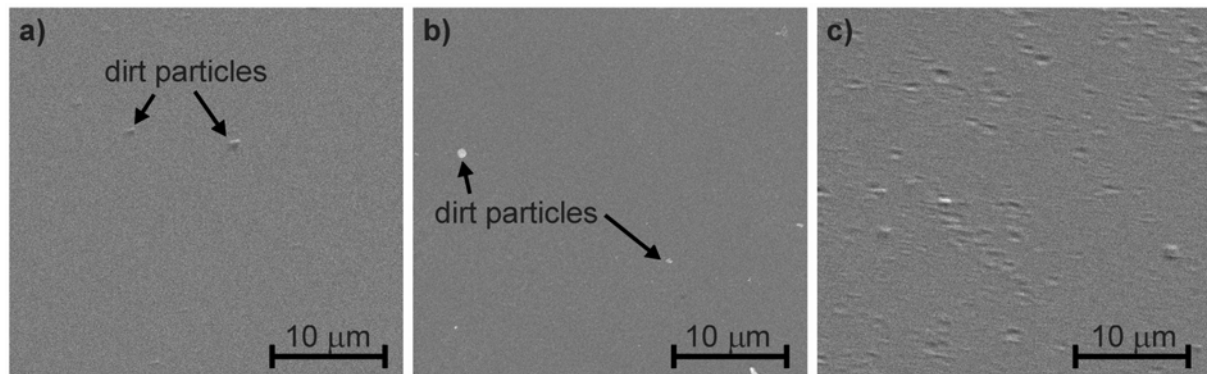


Fig. 2.25: SEM images: a) epi-ready sapphire surface; b) wafer region with unaffected sapphire surface after GaN laser liftoff, and c) sapphire surface with ablation damage.

The effect on the sapphire surface becomes more critical if the laser power fluence is augmented. With a laser fluence of 500 mJ/cm^2 , relatively deep holes are generated on sapphire during GaN delamination (Fig. 2.26). The AFM-profile in Fig. 2.26 b) shows a typical hole with a diameter of almost $1 \mu\text{m}$ and 100 nm depth. The rms surface roughness reaches a value of 15 nm or higher, depending on the hole distribution over the wafer. The temperature increase generated at the GaN/ Al_2O_3 for GaN decomposition (830°C) is much lower than the melting point of sapphire (1730°C), but according to our observations excessively high laser-power fluence will provoke simultaneous sapphire ablation during GaN decomposition (see box nr. 5 in Fig. 2.10).

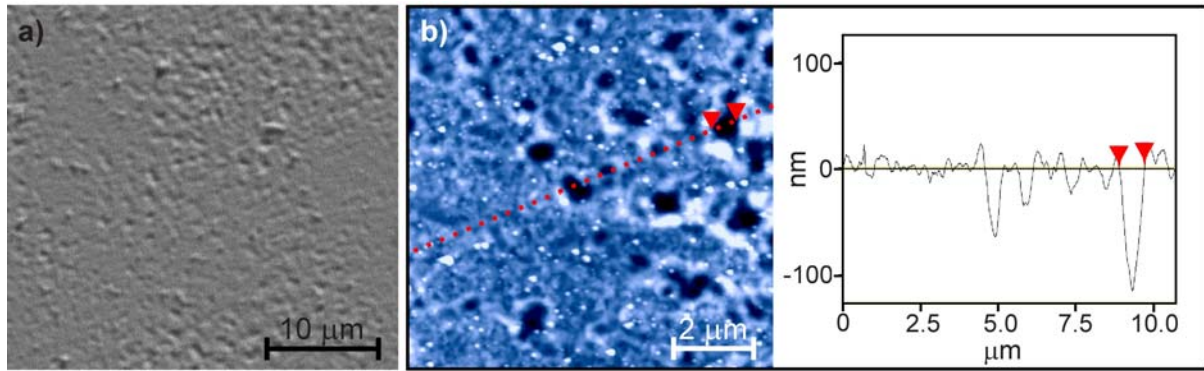


Fig. 2.26: Influence of high laser power fluence on sapphire surface morphology after GaN delamination: a) SEM image showing strong corrugation, and b) AFM image and cut profile along the surface normal.

Certainly, the presence of micro and macrocracks in the sapphire substrate due to thermal and lattice mismatch as discussed in section 2.7 will strongly influence the morphological deterioration of this brittle crystal during GaN liftoff. Nevertheless, if the laser induced process is performed with a energy fluence close to the threshold limit to cause GaN decomposition, the effect on the surface morphology can be considerably reduced as shown in Fig. 2.25 b). The recycling of the sapphire substrates could be an enormous economical and technological advantage in large scale production of large sized GaN pseudo-substrates. With an *in-situ* laser delamination of thick GaN films right after growth at high temperatures, all cracking problems caused could be avoided, and it should be possible to develop a system following a cyclic procedure to remove the freestanding GaN wafer, whereas the sapphire substrate could remain in the system for further regrowth.

2.9 Laser Liftoff for the Production of Blue/Violet InGaN/GaN LEDs

As the final topic of this chapter, the production of freestanding flip-chip bonded blue/violet InGaN/GaN LEDs by laser-induced liftoff is reported. The 4 μm thick and

250 × 250 μm large single-side contacted devices were originally grown on sapphire and integrated by flip-chip bonding to a carrier base. After sapphire delamination, the thin LED membranes remain crack-free and are mechanically connected to the contact pads. The light is then emitted from the top sides of the chip, improving the extraction efficiency. No deterioration of the device characteristics occurred after the exposure to the short 6 ns laser pulse with an absorbed energy density of 300 mJ/cm² and a more intense blue light could be detected from the free active area. The laser to target interaction was analyzed by numerical simulation based on a thermodynamic model, showing that the short laser pulse does not thermally overstress the device heterostructure and the bonding material.

2.9.1 Highly Efficient GaN-based LEDs: current state-of-the-art

Highly efficient LEDs are in widespread use as indicator lamps as well as in display and illumination systems. The advent of (AlGaIn)N-based LEDs made accessible the green to ultraviolet (UV) spectral range through these compact and robust solid-state light sources. The availability of short-wavelength LEDs also prepared the way to luminescence color conversion, where the short wavelength emission from the LED is converted into light at longer wavelengths. The luminescence converting medium can be either an organic dye or an inorganic phosphor. Luminescence conversion LEDs (LucoLEDs) allow the emission of a multitude of mixed colors including "white". New applications continue to be found for high-brightness LEDs, including the automotive sector with brake lights and dashboard and interior lighting, in addition to their use in outdoor displays and traffic lights. Device and package improvements are still bringing advantages for signalling and indicator applications and allow compact emitters to be employed in other markets such as cellphone backlights. Nevertheless, the big market for LEDs is in general illumination in areas such as spot lighting. However,

considering the actual development this market will become really important only 5 to 10 years from now. The requirements placed on devices used in indicator or signalling applications and in illumination are very different. Several manufacturers are looking at larger area chips to allow higher drive currents and outputs for illumination, while others try to optimize the efficiency of their standard-sized chips. This is mainly determined by which markets are being targeted and the different companies are employing different approaches for enhanced nitride-based LEDs.

Cree's early generations of GaN on SiC devices consisted of relatively low-brightness chips. However, over the last three years and in particular in the last 12 months, the company has increased the brightness of its standard 5 mm LEDs by a factor of three. Cree's latest commercial product, the X-Bright, is a series of new blue and UV-InGaN on SiC LEDs [274]. In these new devices, losses due to total internal reflection are effectively reduced by geometric shaping, as well as flip-chip mounting to increase light extraction in the forward direction. They have a radiant flux of 16 mW at 20 mA, obtained at a forward voltage of 3.7 V. The company's earlier generation 505 nm green device, which is not flip-chip mounted, provides 8 mW under the same conditions and is used in traffic signals and signs. While Cree has demonstrated 21 mW UV-LEDs at an efficiency of 32%, its X-Bright 395 and 405 nm UV chips have an external quantum efficiency (*i.e.* the efficiency of photon extraction from an unpackaged LED die) of 25% in production. Larger diodes can provide more light, but are less efficient. Improved packages and high-power chips can be designed for high-output illumination applications, where large light output is more important than small size and efficiency.

Uniroyal is also augmenting the output power of its blue and near-UV LEDs and it is targeting white-light emitter applications [274]. Operating at 460 nm, Uniroyal's blue LED chips have a radiant flux of 3.4 mW (using a forward voltage of 3.61 V and 20 mA drive current), measured by simply mounting the die on a header without any additional heat

sinking. The output of the device doubles when packaged; it is currently rated at 7.5 mW, and around 15 lm/W. The external quantum efficiency is 13.6%. The company is also developing shorter wavelength devices down to around 385 nm. Uniroyal's 405 nm device offers 2.4 mW in chip form and up to 5.3 mW of radiant power when packaged (measured at 20 mA). The wavelength is more stable than the blue LED, and the device offers around 8.6% external quantum efficiency in the package. However, such devices grown with InGaN QWs and GaN barriers, suffer from a drop in efficiency and power at shorter wavelengths. In collaboration with its lighting subsidiary Norlux, they are developing high-flux LEDs with a packaging that eliminates UV degradation of encapsulants. The Norlux package uses a hexagonal shape for efficient placement in a scalable package, allowing many LEDs to be packaged and driven at a high total current. Using this approach, the company demonstrated a prototype 415 nm violet lamp (Fig. 2.27) that offers over 300 mW of optical output for just under 6 W of input power (measured at a current of around 350 mA and a forward voltage of 16.5 V).

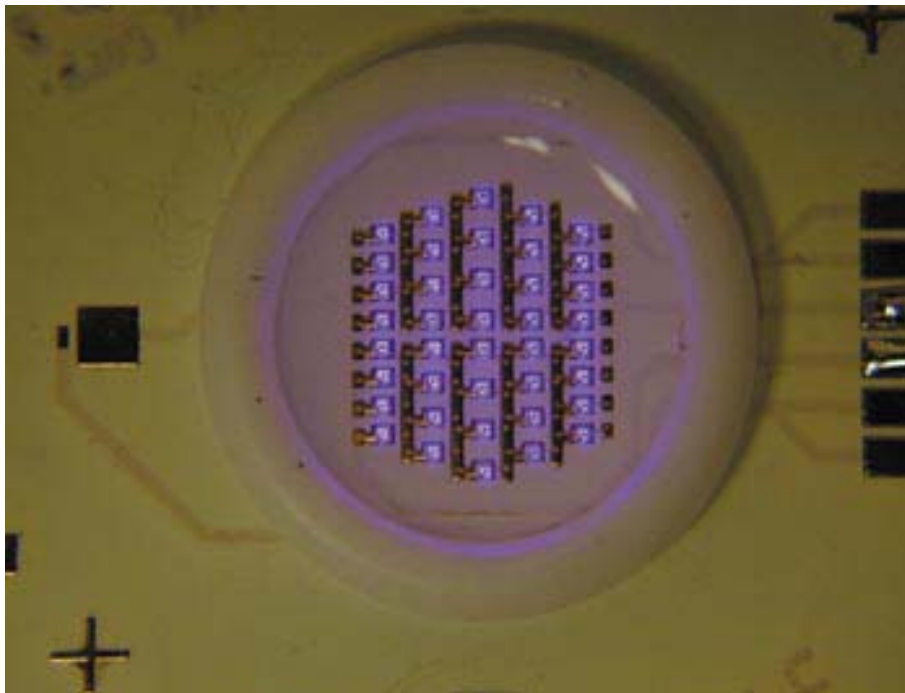


Fig. 2.27: High flux violet-LEDs from Uniroyal and Norlux

An aluminium substrate is used as the heat sink, resulting in a temperature rise of only 10°C per Watt of input power, compared to around 350°C per Watt for a standard 5 mm LED. A preliminary data sheet for Norlux's 470 nm blue HEX package containing 40 LEDs shows a luminous efficiency of 4 lm/W, and a total output power of 0.13 W (*i.e.* 3.25 mW per device). Green 525 nm InGaN packages operate at 9.5 lm/W, while an RGB white package provides around 10 lm/W. The company is also looking at other ways to increase the power of its blue LEDs and has just begun sampling a large-area version of its 450 nm blue LED that offers 60 mW of output, and contains a monolithic array of nine LED devices.



Fig. 2.28: High-current LEDs from LumiLeds mounted in a plastic lens filled with silica gel.

During 2001, LumiLeds launched its Luxeon range of large-area high-current devices, setting new standards for LED output power [274]. The AlInGaP (red and amber) and InGaN (blue, green and white) devices target high-power lighting applications and are the result of a 17 times improvement in flux over the last three years. Featuring die areas up to $1.0 \times 1.0 \text{ mm}^2$, the devices are flip-chip mounted on aluminium or copper heat sinks, which allows them to be driven at currents as high as 1.4 A. The LEDs are mounted in a plastic lens

filled with silica gel, making a robust, reliable package (Fig. 2.28). This package enables a range of fixtures and white lighting sources, but will be too expensive for general lighting applications, despite being twice as efficient as incandescent bulbs. LumiLeds' 450 nm blue InGaN/AlGaIn chip offers a wall-plug efficiency of 24% and a luminous efficiency of 330 lm/W. The wall-plug efficiency, a measure of the amount of energy required to produce the specified light output level, drops significantly when the LED is placed in a YAG-phosphor-coated package to make a white Luxeon device. This is largely due to energy loss from conversion of a blue photon to a yellow photon. The white Luxeon single chip LED has a luminous efficiency of 30 lm/W and produces 150 lm at a drive current of 1.4 A. In comparison, a standard incandescent bulb produces 110 lm with an efficiency of 7 lm/W.

The use of phosphors to produce white LEDs also produces reliability concerns, for example, the degradation of the epoxy can reduce the light output below usable levels, sometimes in less than 5000 hours. This is much shorter than the 100,000 hours typically advertised for standard-colored LEDs in clear glass packages. The white Luxeon devices were tested independently and showed no drop in output over 5000 hours.

AXT is another company that has introduced larger area blue and green LEDs. It has recently launched high-flux AlInGaIn-on-sapphire LEDs covering the 450 to 525 nm range [274]. The large area of $1.25 \times 1.25 \text{ mm}^2$ allows the device to be driven harder, and enables AXT to address applications in traffic signals, automotive interior lighting, dental curing and eventually general illumination. Operating at 350 mA, the device includes current spreading layers to improve the uniformity of light emission, an optimized geometry for current injection, and back reflection to enhance light extraction. In performance terms, the company's larger area 525 nm device provides a radiant flux of 27 mW and a luminous efficiency of 17.5 lm/W, which compares to 2 mW from its newest standard-sized green die. Designed for use in traffic signals, a high-power cyan LED offers 30 mW of radiant power and 12.5 lm/W luminous efficiency. In addition, AXT has a 450 nm blue chip that features a

flux of 35 mW (compared with 4 mW from its conventional blue device) and a luminous efficiency of 6 lm/W. While the output of AXT's new LEDs is considerably higher than its standard chips, the wall-plug efficiency of around 2% is quite low. Preliminary data sheets indicate that these results were obtained on chips mounted on heat sinks that provide 32°C/W, and do not have index matching of the epoxy encapsulant to ensure optimal output. In general, for a high flux LED application AXT is aiming to produce LED devices that can deliver 300 mW, with the chip driving currents up to 1 A in future. This will produce considerable thermal challenges at both the chip and the package level.

2.9.2 Flip-Chip Technique for LED Production

For the realization of high-brightness LEDs with efficient current injection and heat sinking the flip-chip technique used for chip mounting is a promising approach and becomes increasingly important.

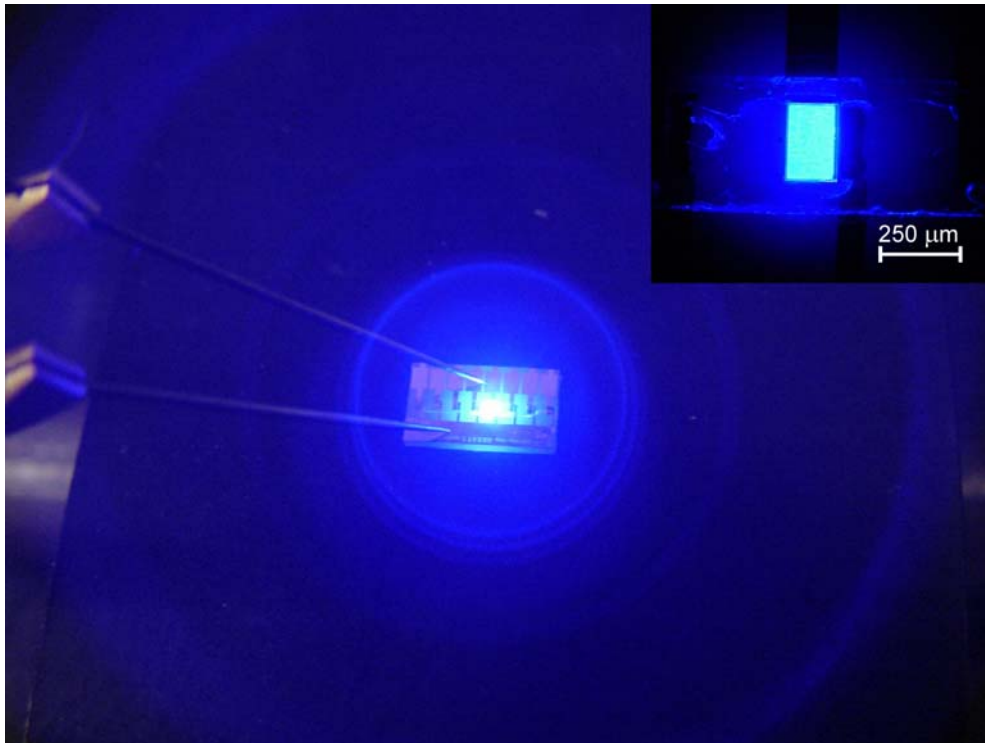


Fig. 2.29: Freestanding violet GaN-based LED flip-chip bonded to a partially gold coated Si-submount. The insert shows the active area of the die with a dimension of $250 \times 150 \mu\text{m}^2$.

Fig. 2.29 shows a violet InGaN/GaN LED provided by the Fraunhofer Institut in Freiburg (IAF) and used in this work. The LEDs are mounted on a linear array of chips, and flip-chip bonded to a partially gold-coated ceramic submount. The sapphire substrate was removed from the epitaxial layer by laser liftoff, leaving behind a freestanding membrane suspended on top of the submount by the bond pads.

There is a wide variety of technological reasons for applying the flip-chip technology. The typical needs include the growth on a thermally conductive substrate. The thermal conductivity of some materials used as substrates or heat sinks is listed below:

- Diamond : 20 W/cm K
- SiC : 3.6 W/cm K
- AlN : 3.2 W/cm K
- Si : 1.6 W/cm K
- GaN: 2.1 W/cm K
- sapphire: 0.3 W/cm K

Advantages of flip-chip mounting are the possibility of higher packaging density, higher frequency operation of the devices due to shorter circuit tracks, productivity at high number of I-O's (input-output), minimum of interconnections ("direct die attach"), and low height of the whole assembly as no bonding wires are necessary. The electronics industry has at its disposal a wide variety of processes for making electrical connections. Essentially, we must differentiate between connections that are meant to be subsequently disengaged (*e.g.* sockets for ICs, connectors) and constant conductive connections. From the later ones, the mounting of bare dies directly onto a substrate (flip-chip) holds the greatest significance for the rapidly growing electronics markets.

Basically, in the flip-chip technology the die is mounted onto a substrate (printed circuit board) with the active switching side face down. The electrical connection is made simultaneously for all contacts in a single step. One of the contact partners must have “bumps”, *i.e.* raised areas composed of electrically conductive material. For virtually all processes, the die must be provided with bumps. Different galvanic and mechanical processes with or without melting of the metallic bumps are currently available for this purpose, but one of the most widely used processes is traditional soldering technology, as modified for direct chip mounting. In this case, metallic alloy solders for the bumping and connection process are used. A schematic view is given in Fig. 2.30.

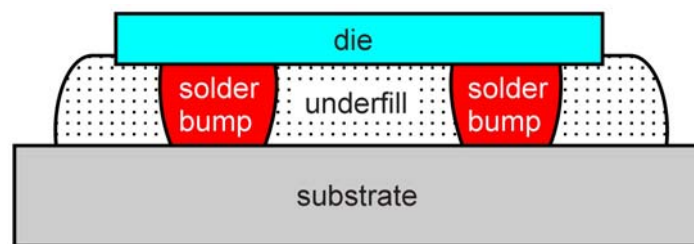


Fig. 2.30: Flip-chip bonding with solder bumps.

The efforts arising for the underfill should not be underestimated. Typical materials are filled epoxy materials with different properties; especially with a curing temperature lower than the solder temperature used. Its disadvantages are due to the relatively high bonding temperatures, limiting the selection to extremely high-grade substrate materials, not exactly a favourable precondition for mobile electronics products. However, a large number of small and large companies and institutes are investigating flip-chip processes for a wide variety of applications, *e.g.* thin flex-boards for smart cards, keyboards, LC-Displays, memory modules, optoelectronic devices, automotive electronics, or MEMS devices like hearing aids and pacemakers and also for nitride based devices [274].

2.9.3 Flip-Chip Mounting of InGaN-LEDs for Laser-Induced Liftoff

The InGaN/GaN LED chips used in this work were provided by the Fraunhofer Institut in Freiburg (IAF), Germany, and were flip-chip bonded to metallized Si-submounts by ball bonding with a wire bonding machine. First, Au-balls are positioned on the interconnecting metallization of a Si-submount consisting of a Ti/Au/Ti plating base covered by an electroplated Au-layer (Fig. 2.31). Consecutively, the LED chips are mounted upside-down by thermal compression welding of the bump/LED contact interface at a temperature of $\sim 200^{\circ}\text{C}$. In Fig. 2.32, a series of isolated LEDs is shown, in this case a sapphire stripe with the devices was sawed away and the individualized LEDs were finally flip-chip bonded to the Si-submount. Furthermore, entire device stripes can be connected to the base substrate in a similar way.

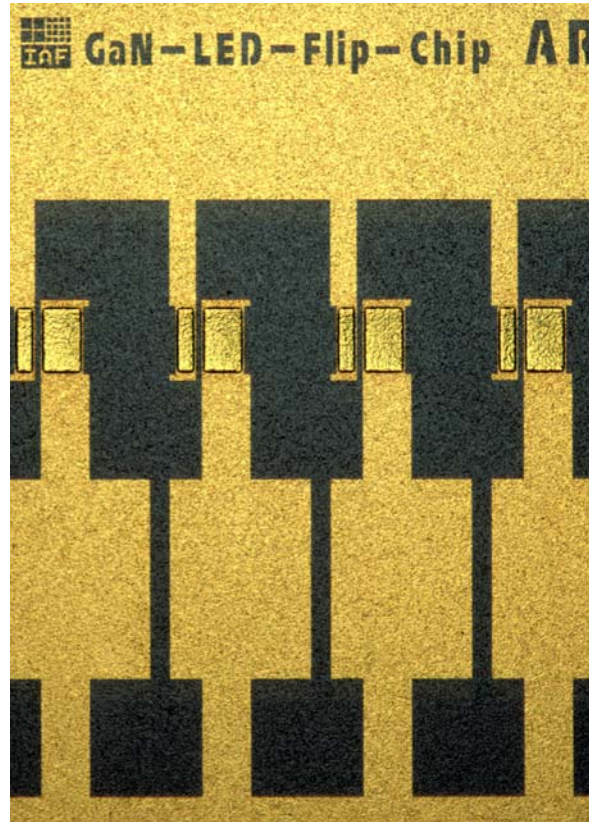


Fig. 2.31: Top view of a Si-submount with interconnecting metallization (golden area). The devices are going to be mounted on top of the rectangular-shaped bumps.

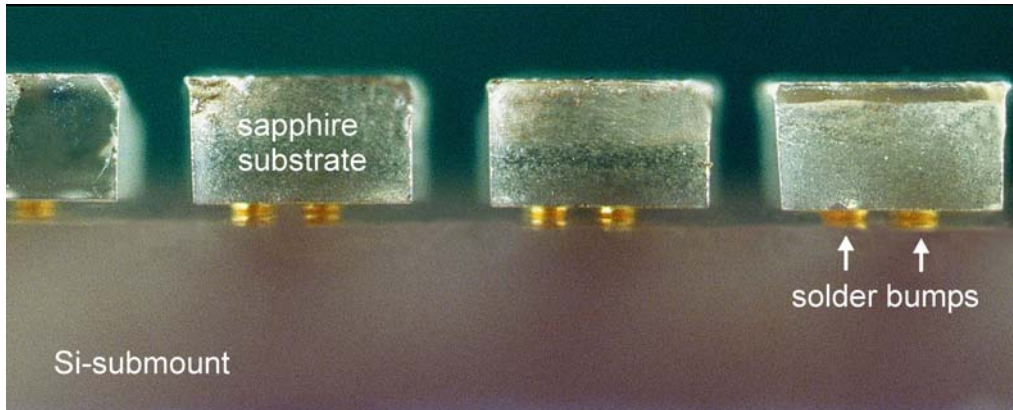


Fig. 2.32: Side view of individualized InGaN/GaN LEDs flip-chip bonded to a Si-submount.

2.9.4 Laser-Induced Liftoff for Freestanding Violet Nitride-LEDs

The laser-induced delamination method was applied directly to flip-chip contacted devices grown on sapphire. As the size of the devices is much smaller than the laser-shot area, a single pulse is sufficient to remove the sapphire substrate, which is beneficial to guarantee the structural integrity and the performance properties of the device. To optimize the light output efficiency, the top side of the LEDs could be covered with an anti-reflective coating (ARC) after the liftoff procedure.

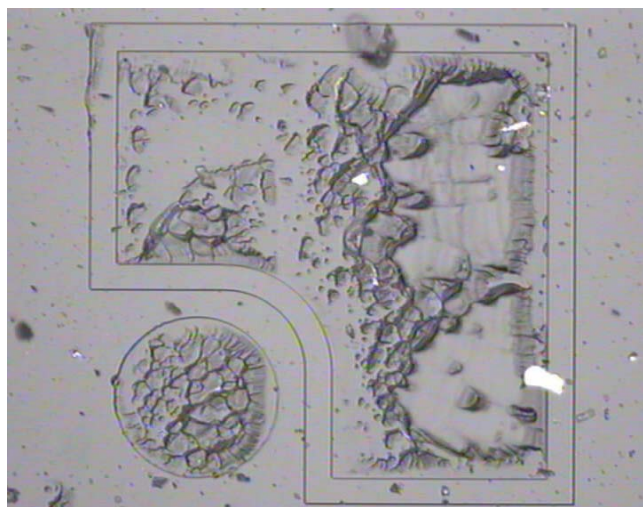


Fig. 2.33: Sapphire substrate after laser liftoff of an InGaN/GaN LED with a laser fluence of $\sim 600 \text{ mJ/cm}^2$. Sapphire pieces were dragged out with the GaN film.

Like in the delamination of GaN wafers, an important aspect for an accurate laser processing of the fragile GaN membranes is to achieve the best parameters to minimize the structural and thermal stress during the short laser/target interaction. A good illustration of the deleterious effect of excessive laser-power used in the delamination of GaN-based heterostructures can be seen in Fig. 2.33.

The use of an epoxy support material is indispensable to absorb the mechanical impact caused by the high power laser pulse on the thin film supported only by the contact bumps. Fig. 2.34 shows the consequence of a single laser pulse for the delamination of a flip-chip mounted LED ($250 \times 250 \mu\text{m}^2$) without any underfill material between the GaN device and the Si-submount. Note that the applied power fluence of 300 mJ/cm^2 is the calibrated threshold value for a “soft” GaN decomposition. Only the GaN film part supported by the contact bumps remained intact.

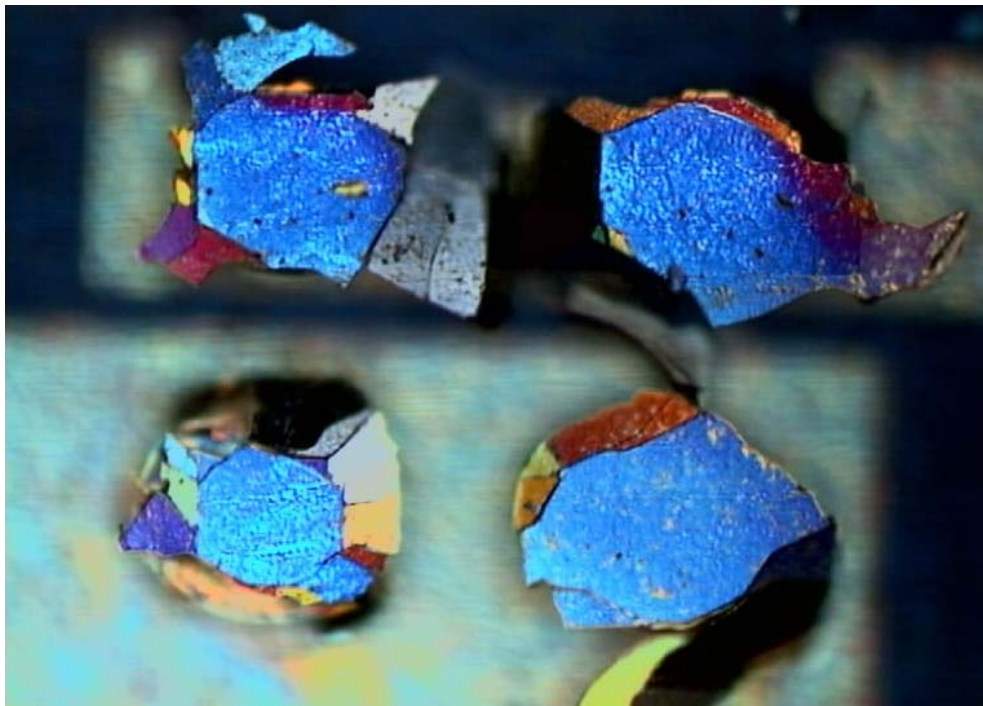


Fig. 2.34: Destroyed flip-chip mounted InGaN/GaN LED on its contact pads after single laser pulse irradiation with a power fluence of 300 mJ/cm^2 . No underfill material was used to protect the device with a dimension of $250 \times 250 \mu\text{m}^2$.

Obviously, the thin GaN films can not stand the thermoelastic stress during laser delamination unless a submount or stiffener layer is fixed to the GaN surface to support the film. As discussed in the former sections, depending on the GaN thickness and sample size, different types of stiffening or underfill material can be successfully used for this purpose. For the specific case of the 4 μm thin flip-chip mounted LEDs a good underfill material was a transparent thermoplastic adhesive. This adhesive has a very low viscosity at its melting point of 120°C, which enables an easy and perfect filling (no enclosed air bubbles) of the region between the device and the Si-submount. Furthermore, the residual adhesive remaining after the sapphire liftoff can be quickly and completely removed with acetone.

The photographs in Fig. 2.35 give an overview of the necessary steps for the preparation and the liftoff procedure of GaN-based LEDs. In Fig. 2.35 a), the flip-chip mounted LEDs are still on the sapphire substrate. After the underfilling with hot adhesive and consecutive laser liftoff, the sapphire is ejected and the residual adhesive surrounding the devices can be observed in Fig. 2.35 b). An acetone bath takes the protective underfilling away, leaving suspended LED membranes connected only to the bond pads, shown by Fig. 2.35 c, d and e). An interesting feature seen in Fig. 2.35 c) are the interference fringes formed due to the thin air gap between half of the contact pad and the 3.8 μm thick InGaN-LED above it. Interrupted interference fringes would indicate that the membrane is fissured or cracked. Moreover, the shape of these interference patterns with parallel lines or knots can show if the thin nitride film is bowed or twisted, giving an indirect idea of the structural stress remaining in the film after its delamination from the sapphire substrate. Most of the patterns observed are surprisingly very similar to that of Fig. 2.35 c).

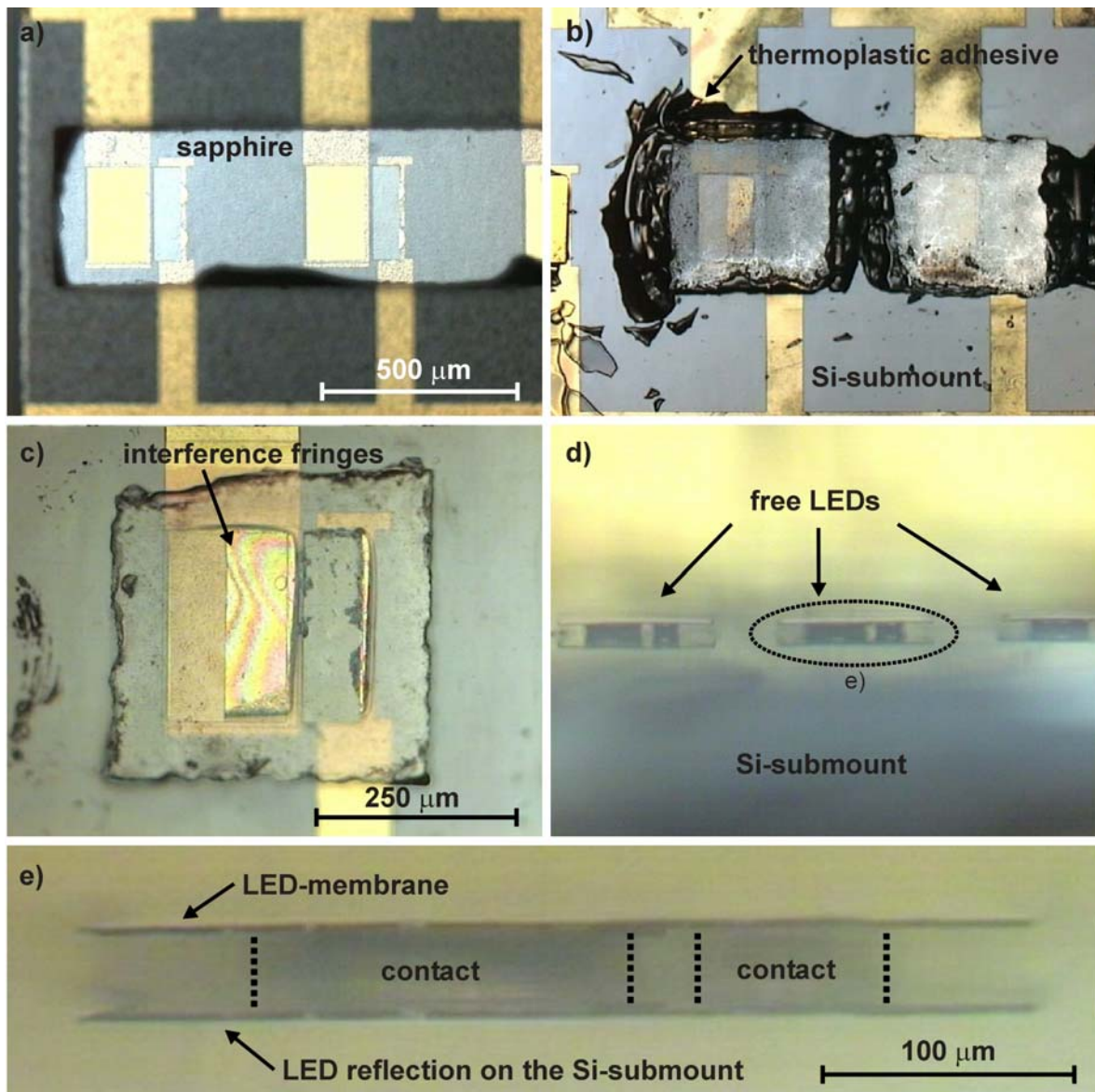


Fig. 2.35: Preparation steps of free InGaN-LEDs: a) flip-chip mounted LEDs on the sapphire bar; b) free-LEDs after laser induced liftoff with the protective underfill; c) close view of a LED after removal of the residual wax with acetone; d) side view of the LED series on the contact pads; e) magnified side view of one of the 3.8 μm thin InGaN-LEDs. The distance of the LED to the Si-submount is 30 μm .

The (AlGaIn)N LEDs were grown by low pressure metal-organic chemical vapour deposition between 750°C and 1100°C on conventional (unpatterned) 2" sapphire substrates [275]. The layer sequence consists of an 25 nm GaN nucleation layer followed by a 2000 nm undoped GaN buffer, a 1500 nm thick GaN:Si n-contact layer, an $\text{In}_x\text{Ga}_{1-x}\text{N}$ single quantum well (SQW) layer with a typical thickness of 2 nm, a 60 nm $\text{Al}_{0.1}\text{Ga}_{0.9}\text{N}:\text{Mg}$ electron barrier, and finally a 200 nm GaN:Mg p-contact layer. The Si and Mg doping levels are typically

$5 \times 10^{18} \text{ cm}^{-3}$ and $6 \times 10^{19} \text{ cm}^{-3}$, respectively. The mesa was defined by CAIBE etching. A Ni(6 nm)Au(300 nm) metallization was used as a p-type contact while the n-type contact was formed by a Ti(15 nm)Al(220 nm)Ni(40 nm)/Au(100 nm) metallization. The typical structure of the (AlGaIn)N LEDs and the corresponding band gap profile are shown in Fig. 2.36.

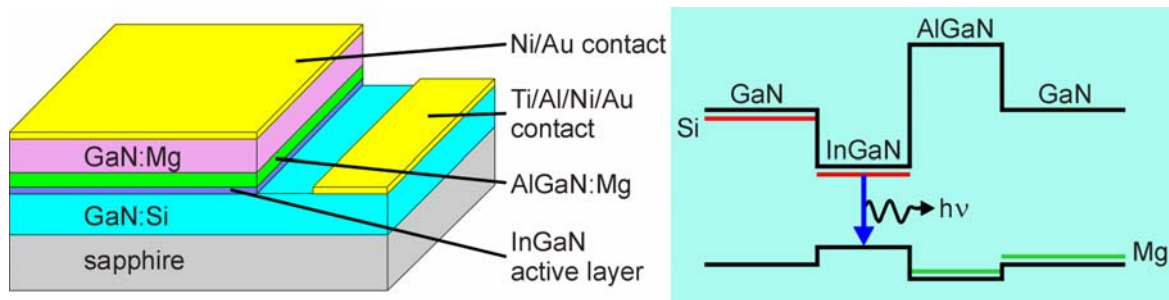


Fig. 2.36: Schematic view of a GaN/(InGa)N/(AlGa)N mesa-structure LED and its typical band gap profile [275].

Depending on the In content of the active layer, the emission wavelength can be tuned between 380 and 450 nm. Up to 3 mW optical power at 20 mA has been achieved in this wavelength range as shown in Fig. 2.37.

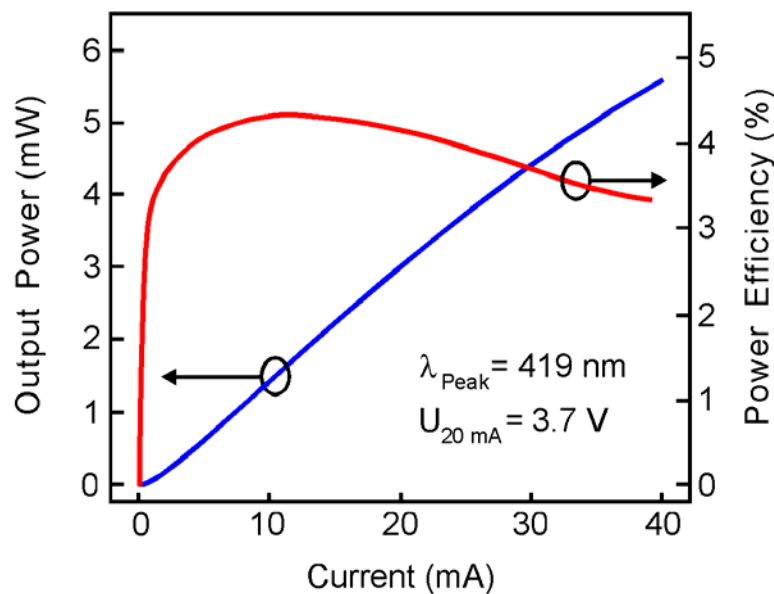


Fig. 2.37: Output-power versus current and power-efficiency versus current characteristics of an encapsulated 5 mm radial size GaInN single QW LED emitting at 419 nm [275].

Wafer stripes of $0.5 \times 25 \text{ mm}^2$ containing a linear series of LEDs (Fig. 2.35 a) and individually sawed LED devices like the ones shown in Fig. 2.32 with a device area of $250 \times 250 \mu\text{m}^2$ and a thickness of $3.8 \mu\text{m}$ were prepared with the underfill adhesive for the laser induced liftoff. The residual Ga on the exposed backside was etched away by HCl vapour in 10 sec. After removing the protective adhesive with acetone, the free LEDs are ready.

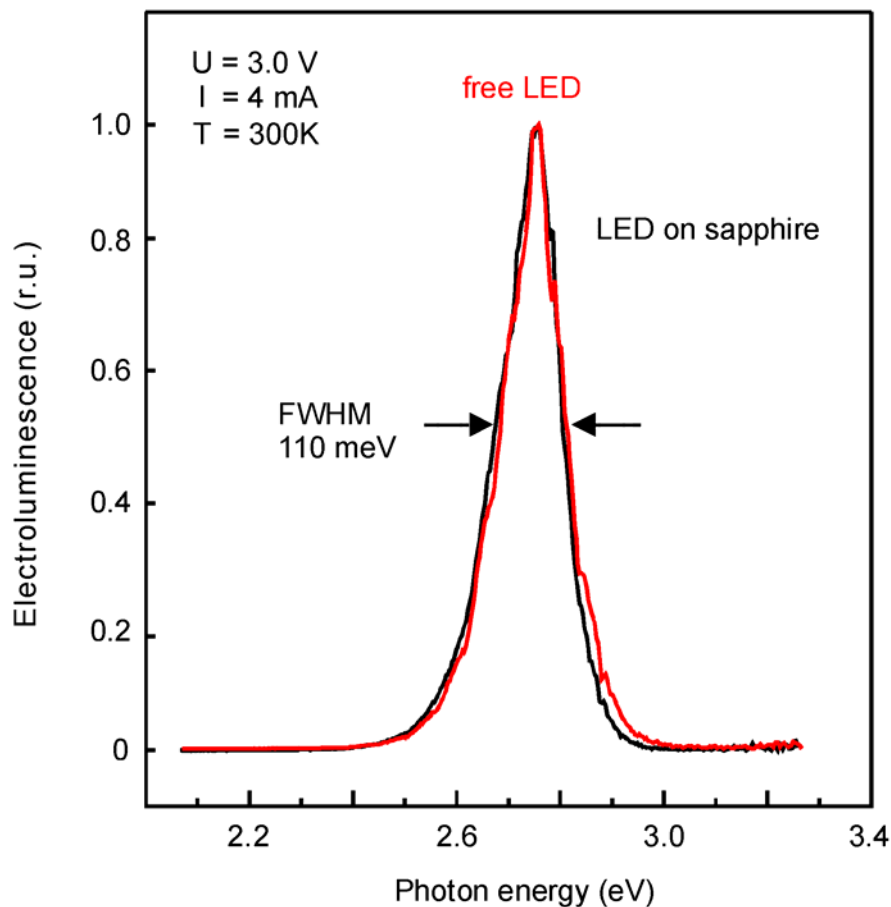


Fig. 2.38: Electroluminescence spectra of an InGaN/GaN-LED before and after the laser liftoff.

Electroluminescence and Current-Voltage measurements were performed to compare the characteristics of the LEDs before and after sapphire removal. The electroluminescence light was dispersed using a double grating spectrometer with focal length of 500 mm and detected by a photomultiplier. The LED was biased with 4 mA in forward direction and no discernible

alteration in light emission was observed after the liftoff process in comparison to the original device still on sapphire, as demonstrated by the two spectra in Fig. 2.38. No measurable wavelength shift or significant linewidth change occurred. According to this result the laser-induced liftoff procedure with the chosen parameters does not cause degradation of the LED devices. LEDs with different active area shapes were delaminated and can be seen in operation in Fig. 2.39.

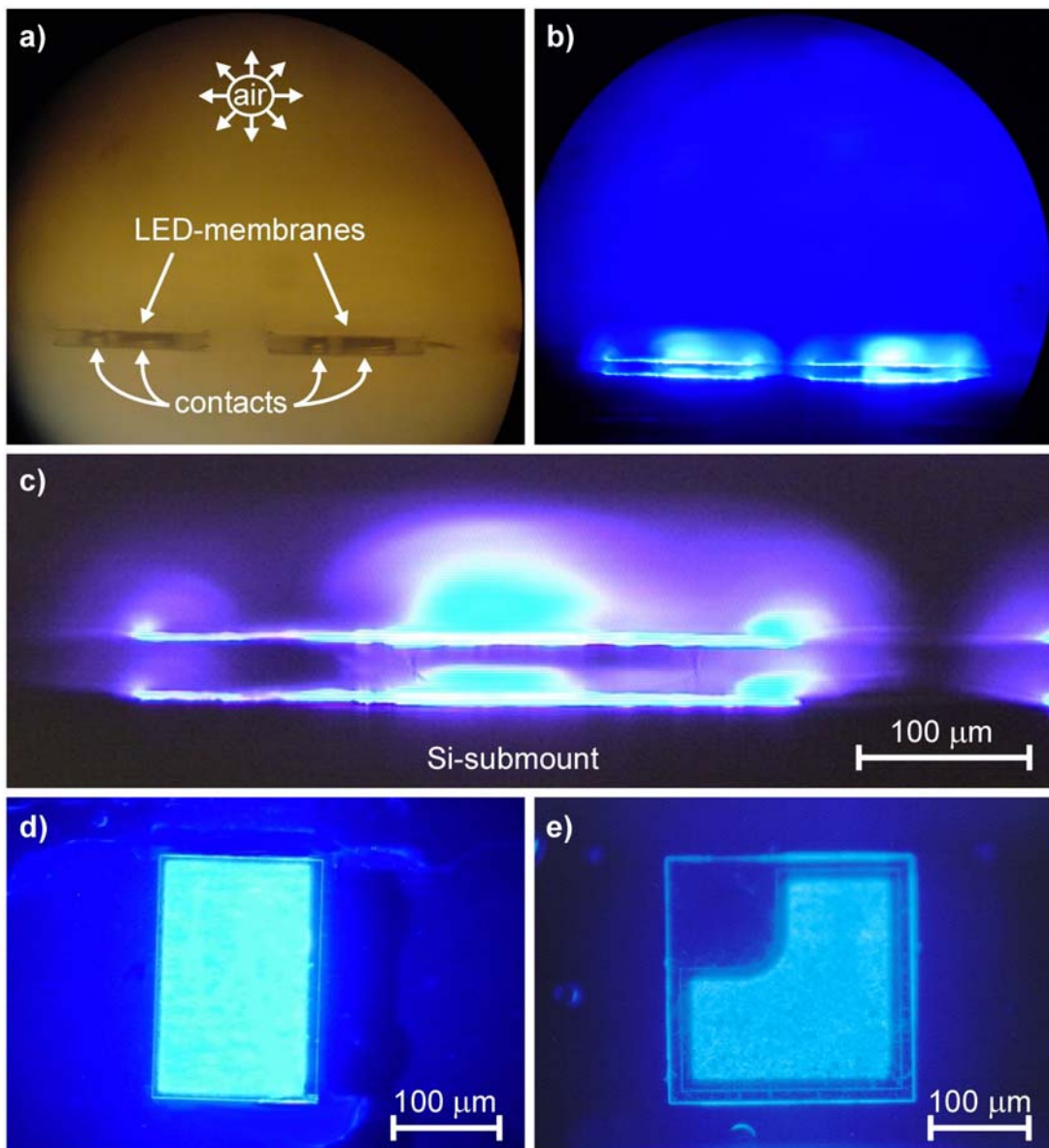


Fig. 2.39: Free flip-chip mounted InGaN-LEDs in operation. Side views a) and b) show two devices side by side without and with electrical bias; c) detailed side view of an operating LED, the light is back-reflected by the Si-submount; d) frontside view of a violet LED with $250 \times 150 \mu\text{m}$ of active area; e) frontside view of a violet LED with $250 \times 250 \mu\text{m}$ of active area.

2.9.5 Laser/Target Interaction

Using the liftoff technique we successfully and reproducibly could delaminate membranes of blue/violet InGaN MQW LEDs from their sapphire substrate. An important aspect to be considered here is the transient laser-target interaction. Principally, when working with thin heterostructures like our 3.8 μm thick LEDs, the laser irradiation and consequent temperature increase and diffusion throughout the material should not adversely affect the device properties. For irradiation intensities higher than 10^7 W/cm^2 a high density of hot carriers will be generated before the crystal lattice is considerably heated [276]. Thermal equilibration of the colliding carriers occurs very fast within a time scale of 10^{-14} sec and recombination processes will take place within some nanoseconds [277][278], practically on the same timescale as the short 6 ns Nd:YAG laser pulse. Indeed, the high energy flux density may cause plasma formation at the irradiated surface. The following numerical calculations will not consider phase changes or plasma generation during the laser shot. At the decomposition temperature of GaN, metallic Ga will be left, increasing the local thermal conductivity, but on the other side it will enhance the reflectivity and effectively diminish the light absorption at the interface. A consequent decrease in the temperature gradient due to these transient effects takes place. Nevertheless, this is not trivial to be modelled in detail and the simplified approach used here is sufficient to provide relevant information of temperature profiles in space and time for thin GaN film delamination.

A heat conduction analysis of the real case GaN/sapphire interface was numerically performed for the Nd:YAG and an KrF excimer laser single pulse. The comparison with a KrF excimer laser at 248 nm and 38 ns of pulse duration also used for GaN liftoff [279] is made to simulate the effect of pulse length on the temperature distribution in the irradiated region. The mathematical representation of heat conduction in Cartesian coordinates is given by the heat diffusion equation:

$$\frac{\partial}{\partial x} \left(\kappa \frac{\partial T}{\partial x} \right) + \frac{\partial}{\partial y} \left(\kappa \frac{\partial T}{\partial y} \right) + \frac{\partial}{\partial z} \left(\kappa \frac{\partial T}{\partial z} \right) + \dot{q} = \rho C_p \frac{\partial T}{\partial t} \quad \text{Eq. (2.3)}$$

where κ is the thermal conductivity, ρ the density and C_p the heat capacity of the medium. The term \dot{q} represents the rate at which energy is generated per unit volume of the medium. In our case it is the power density of the incident laser pulse that is absorbed by the GaN. The light absorption of the sapphire substrate is negligible in the ultraviolet spectral range ($\lambda \leq 400$ nm) [280]. The relevant coordinate for the time-dependant temperature solution of the heat equation is the direction perpendicular to the GaN/sapphire interface. So, \dot{q} can be written as:

$$\dot{q}(x,t) = I_L(t) (1-R) \alpha e^{-\alpha x} \quad \text{Eq. (2.4)}$$

where $I_L(t)$ is the incident laser energy density, $R = 0.3$ the reflectivity at the GaN surface and $\alpha = 10^5 \text{ cm}^{-1}$ the absorption coefficient of GaN at the laser wavelength of $\lambda = 355$ nm.

From Eq. (2.3) and (2.4) we get the one-dimensional heat equation for the case when heat is generated by laser irradiation:

$$\frac{\partial T}{\partial t} = \frac{\alpha}{\rho C_p} I_L (1-R) e^{-\alpha x} + \frac{1}{\rho C_p} \frac{\partial}{\partial x} \left(\kappa \frac{\partial T}{\partial x} \right) \quad \text{Eq. (2.5)}$$

To allow an accurate simulation of the laser interaction at the GaN/sapphire interface we have used temperature dependent values of κ and C_p from the literature. The curves for sapphire and wurtzite GaN are shown in the Fig. 2.40 to Fig. 2.43:

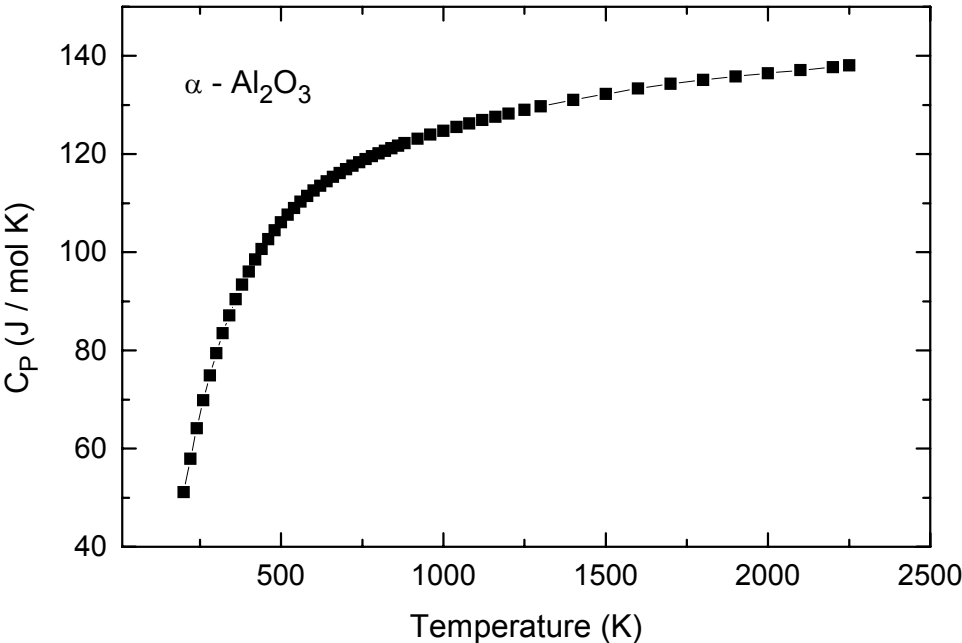


Fig. 2.40: Molar heat capacity of synthetic sapphire (α -Al₂O₃) from 10 to 2250 K [281].

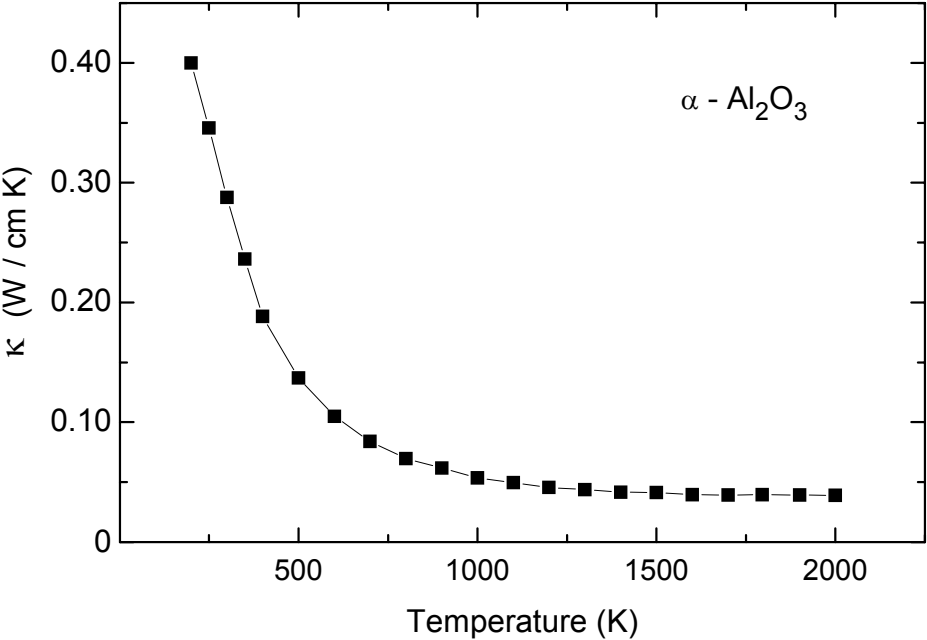


Fig. 2.41: Thermal conductivity of sapphire (α -Al₂O₃) along the *c*-axis [282].

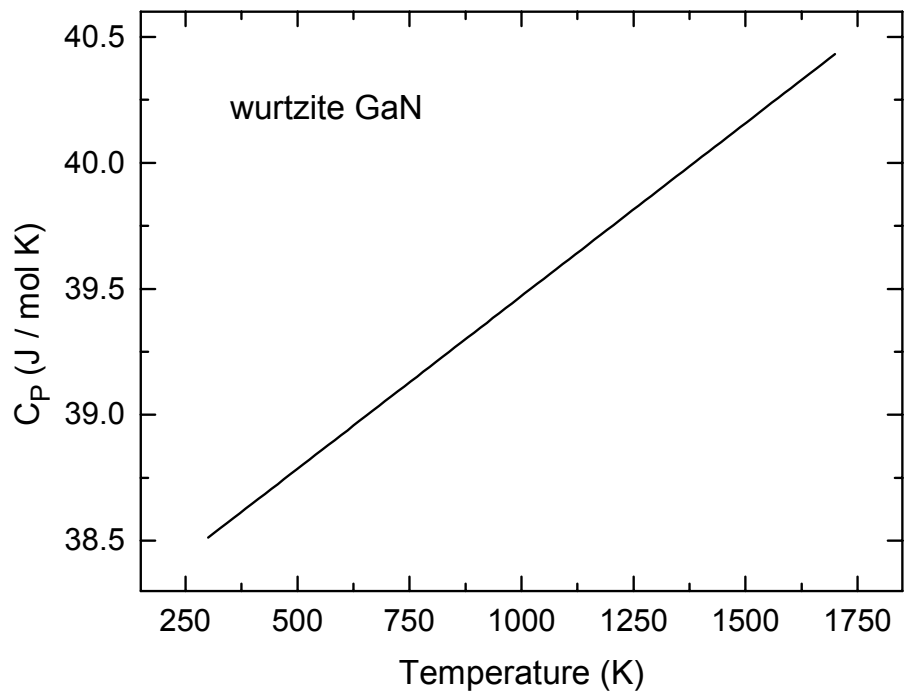


Fig. 2.42: Molar heat capacity of wurtzite GaN at constant pressure [283].

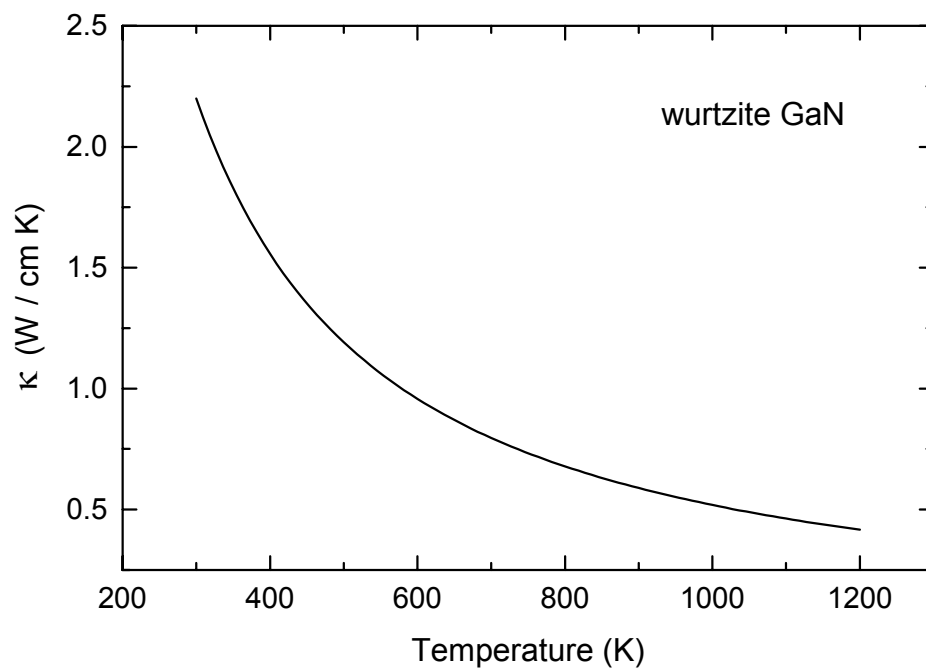


Fig. 2.43: Thermal conductivity of wurtzite GaN along the c -axis [284][285].

The volume change of sapphire and GaN from room temperature to 1500 K ($\Delta V_{T-300\text{ K}} / V_{300\text{ K}}$) is of the order of $\sim 10^{-5}$. Considering that the inherent experimental error in the other physical quantities in the heat equation is much higher, we therefore assumed the densities of GaN and Al_2O_3 to be temperature independent. The following values for ρ at room temperature were used:

$$\rho_{\text{sapphire}} = 3.904 \times 10^{-2} \text{ mol/cm}^3$$

$$\rho_{\text{GaN}} = 7.288 \times 10^{-2} \text{ mol/cm}^3$$

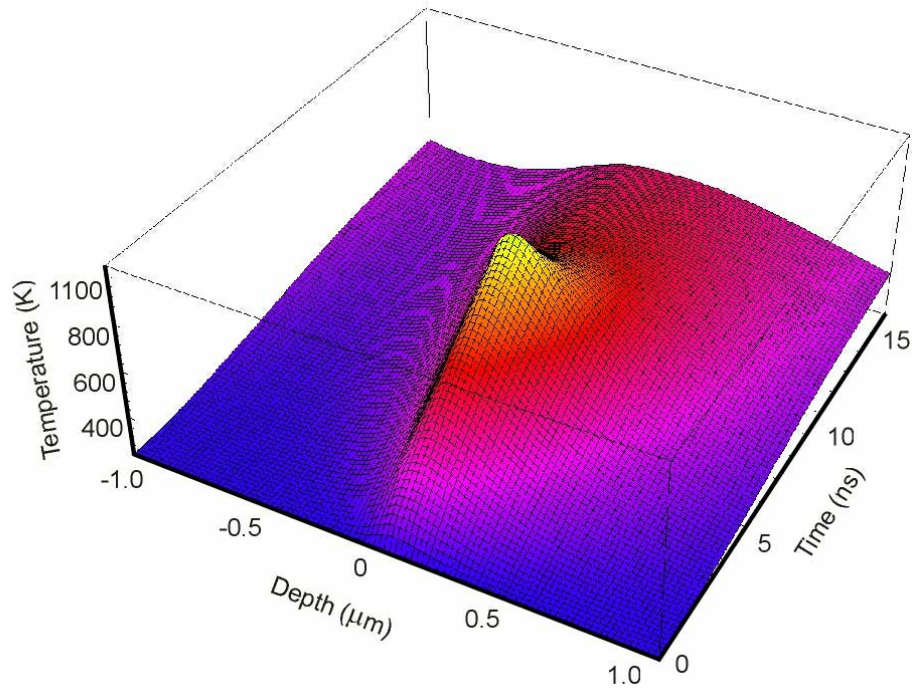
For the numerical solution of the heat equation we assumed $x = 0$ at the interface between sapphire and GaN and x positive in the GaN region. To avoid singularities at $x = 0$, an arctan function was chosen in the simulation to mathematically connect both materials, starting at -5 nm in the sapphire and ending at 5 nm in the GaN film. The finite boundary conditions are:

$$T[x, 0] = 300 \text{ (room temperature in K);}$$

$$T[-\infty, t] = T[\infty, t] = 300 \text{ K} = T[x, 0]$$

No phase changes occurs during the laser pulse, we are therefore looking for the threshold laser power necessary to heat the GaN to its decomposition temperature of about 830°C. The simulations were done with the *Mathematica* software version 4.1 for students. In Fig. 2.44 and Fig. 2.45 is shown the resulting temperature profile for a single pulse (6 ns, 300 mJ/cm²) of a Nd:YAG laser and a single pulse of a KrF (38 ns, 600 mJ/cm²), respectively.

a)



b)

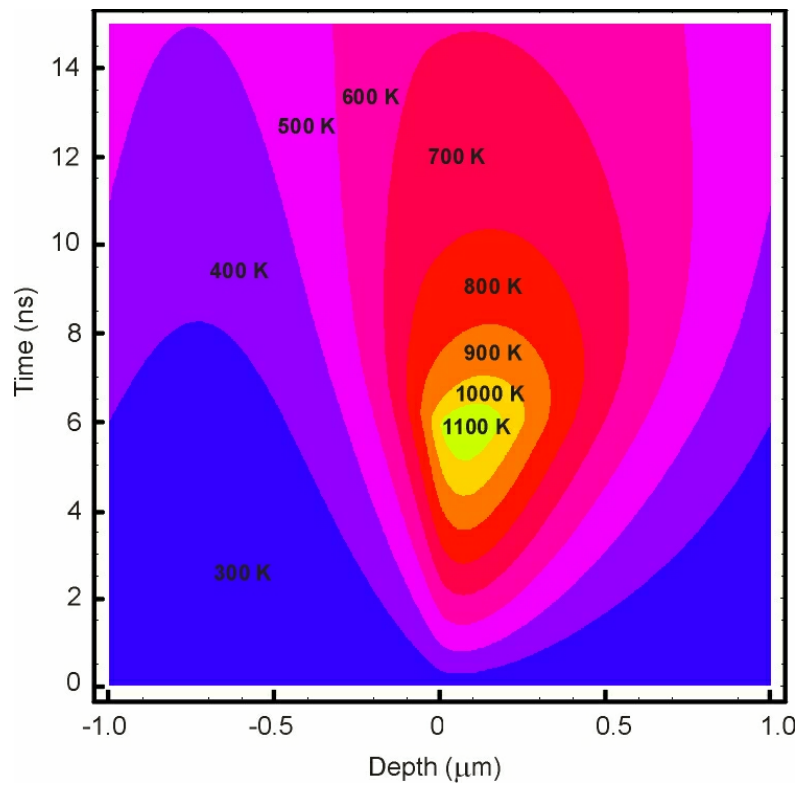
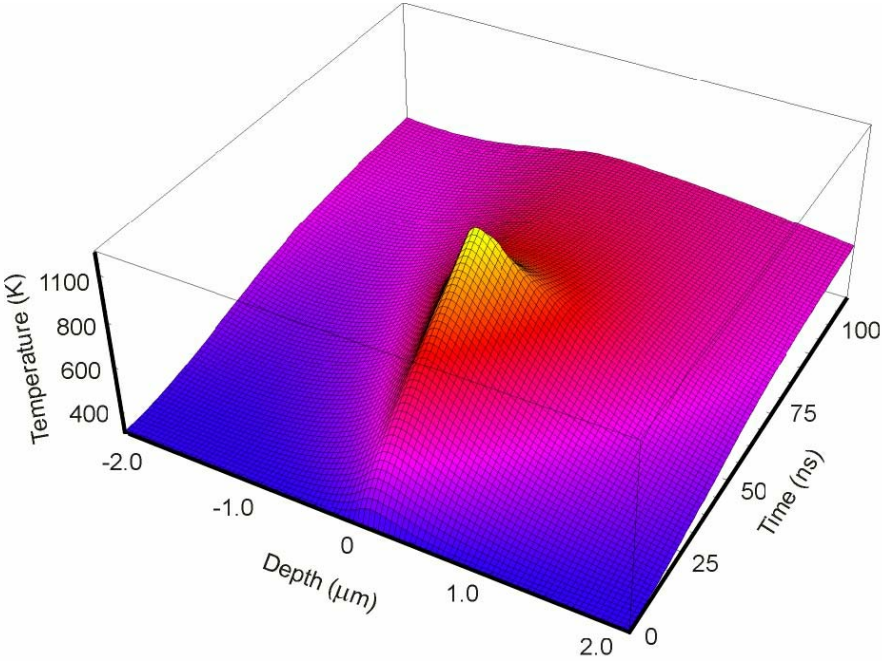


Fig. 2.44: Simulated temperature profiles for a single 6 ns, 300 mJ/cm^2 pulse from a Nd:YAG laser: a) three-dimensional view and b) bi-dimensional cut, in the depth axis the negative values corresponds to the sapphire substrate.

a)



b)

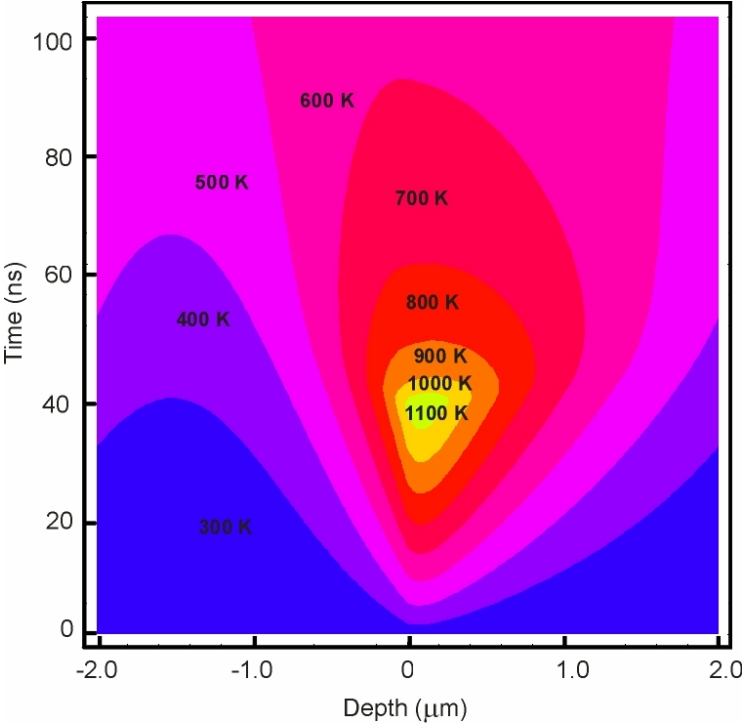


Fig. 2.45: Simulated temperature profiles for a single 38 ns, 600 mJ/cm² pulse from a KrF laser: a) three-dimensional view and b) bi-dimensional cut, in the depth axis the negative values corresponds to the sapphire substrate

The temperature rise, coupled with a large temperature gradient across the thickness of the GaN film, occurs in a highly localized heated area that is within 100 nm below the irradiated GaN/sapphire interface for the Nd:YAG laser and about 200 nm for the KrF laser. The simulations showed that in order to raise the interface temperature to 1100 K a 300 mJ/cm² pulse from a Nd:YAG laser is needed. The threshold power to reach the GaN decomposition temperature in case of the KrF laser is about 600 mJ/cm². This agrees with values from the literature [286][287]. The big power difference between the two lasers can be explained by the much larger pulse duration of the KrF laser, 38ns in comparison with the short 6 ns of the Nd:YAG. More power per unit of time is needed to reach the decomposition temperature of 1100 K. The result is a much higher overheating of the GaN film far away from the interface to sapphire.

As can be observed in Fig. 2.44 and Fig. 2.45, the short and less intense Nd:YAG pulse causes a narrower temperature propagation peak. A non-negligible temperature rise of the sapphire substrate during the laser irradiation is also found from the calculations. At 1 μm from the interface the temperature is around 400 K, for the KrF the value is higher than 600 K. Note that the depth scale limit is 1 μm for the Nd:YAG and 2 μm for the KrF laser. Consequently, the Nd:YAG laser is less aggressive to the film, *i.e.* a deterioration of doping and other characteristic properties is less probable. Furthermore, in case of wafer bonding the temperature at the GaN to the bonding layer interface should not exceed 200°C to maintain the maximum flexibility in choice of the bonding material and receptor substrate. This information is relevant and should also be considered in the design of GaN-based devices to be delaminated by laser induced liftoff. Nevertheless the characterization of the freestanding flip-chip bonded LEDs shows that no measurable device degradation occurred showing the large process latitude and flexibility of the simple laser-induced liftoff technique for GaN-based technology.

3 Homoepitaxy on Freestanding GaN Substrates

To fully explore the large application potential of group-III-nitrides, it is desirable to employ epitaxial growth on lattice-matched substrates. Although relatively small bulk GaN crystals can be reproducibly grown [288], large bulk single crystals of GaN for the fabrication of epi-ready substrates are not commercially available. Therefore, at present all GaN-based devices are deposited by heteroepitaxy, mostly on sapphire or silicon carbide substrates. Sapphire has a relatively low cost and is the most commonly used substrate material for optoelectronic devices because of its large band gap and good surface morphology for epitaxial growth [79][289][290]. However, the mismatch in lattice constants and thermal expansion coefficients between epitaxial layers of group-III-nitrides and the available substrates gives rise to a high density of dislocations and strain, limiting *e.g.* the electron mobility, doping efficiency and lifetime of devices [291][292].

The capability to produce superior material quality by homoepitaxial growth of GaN on GaN bulk crystals or bulk-like substrates has already been demonstrated [253]. A reduction of dislocation densities by six orders of magnitude, higher carrier mobilities and narrower photoluminescence line widths in comparison to the usual heteroepitaxial growth are obtained [217][218]. By homoepitaxy, two-dimensional step-flow growth of GaN can be achieved without the need for additional deposition steps such as surface nitridation, thin low temperature nucleation films, or thick buffer layers. Laser cavities can be fabricated with cleaved facets [222] instead by time-consuming reactive ion etching processes, which also produce defect states on the crystal surface. In addition, the GaN substrate can be doped n- or p-type, providing significant simplification in device processing and circuit integration.

An alternative to bulk crystals are bulk-like thick GaN films produced by hydride vapour phase epitaxy (HVPE) [162][293]. Recent developments in this technique have lead to a

significant improvement of the structural quality and to large-area crack-free films. Such thick GaN films (up to 2" in diameter and 300 μm thickness) can be separated from the sapphire substrate by the laser-induced liftoff process discussed in the previous chapter.

3.1 Preparation of Freestanding GaN Films for Homoepitaxy

The surface morphology of thick HVPE-GaN films grown by ATMI and used in this work was macroscopically characterized by optical microscopy and surface profiling. Complementary, the microscopic shape of the surface was measured with AFM. The typical surface morphology can be observed in the AFM image in Fig. 3.1, with a rms roughness of 0.4 nm. Dislocation densities between 8×10^6 and $5 \times 10^7 \text{ cm}^{-2}$ were estimated from the localized pin-hole concentration at the surface (black spots in the AFM image in Fig. 3.1) and are in range of the values published by Vaudo *et al.* [227]. However, on a larger scale, the Ga-face GaN growth surface exhibits hexagonal pyramids with diameters of several 10 μm and a height of 1 μm as shown in the left image in Fig. 3.1.

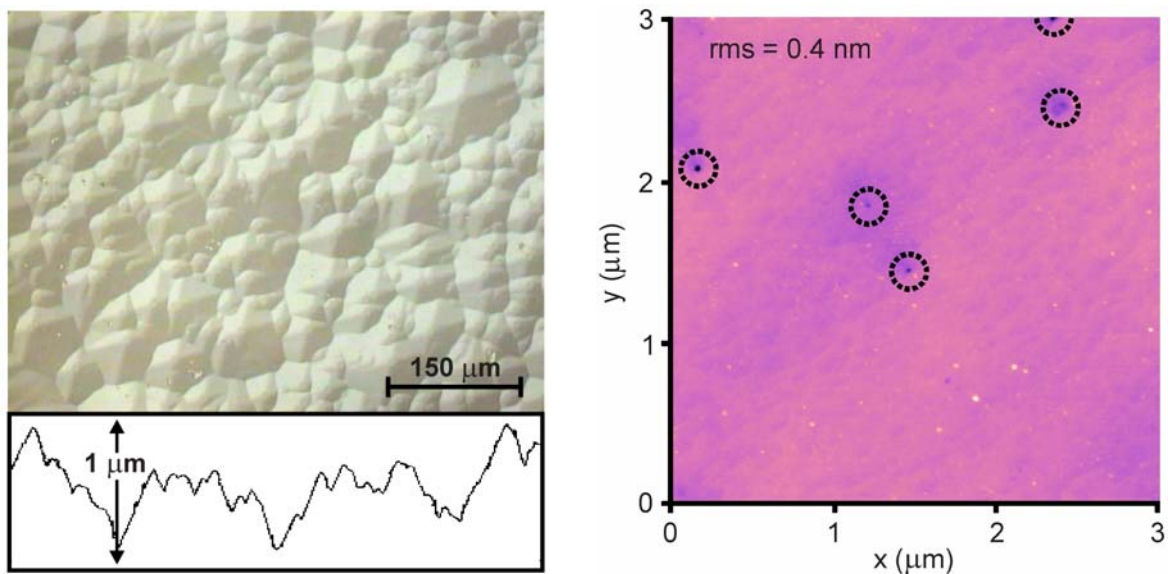


Fig. 3.1: As grown Ga-face surface of a thick HVPE-GaN film. On the left an optical micrograph with underlying surface profile is shown. The AFM image on the right presents the very smooth surface on a micrometric scale (rms = 0.4 nm). The maximum peak-to-valley amplitude is 1 nm. The circles mark isolated dislocations (pin-hole depth ≤ 5 nm).

Some samples also exhibited characteristic surface voids at the as-grown side, shown in Fig. 3.2. These large volume crystal defects are mostly localized at the borders of the 2” HVPE-GaN wafers, caused probably by a deviation from the optimal growth conditions combined with the fast growth rates of 100 $\mu\text{m}/\text{h}$ and higher. The voids are obviously detrimental for homoepitaxial overgrowth and have to be removed by lapping.

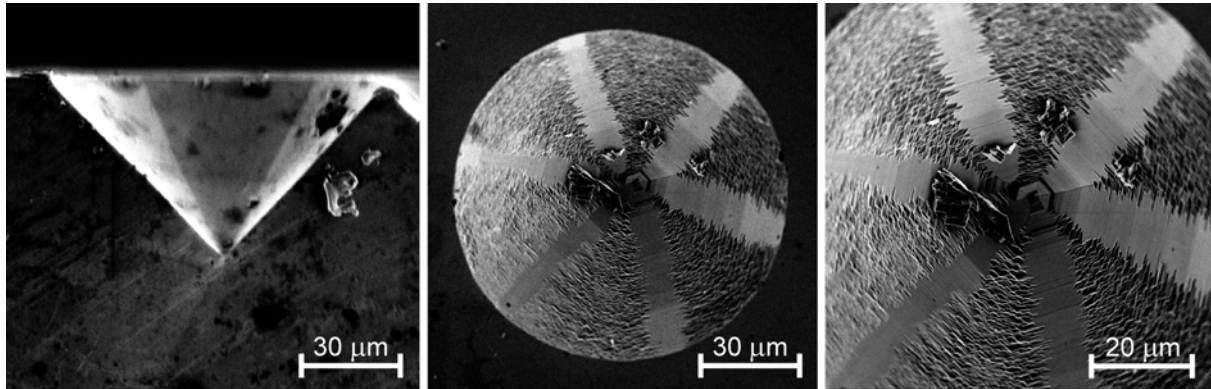


Fig. 3.2: Typical large scale defect found at the Ga-face surface of thick HVPE-GaN samples. The voids can reach a diameter of 100 μm and a depth of 50 μm as shown in the side view on the left image. From the top views it is possible to recognize the hexagonal geometry, despite of its almost perfect circular shape.

Also in a collaboration with the group of Prof B. Monemar of the Linköping University in Sweden, thick HVPE-GaN were delaminated by laser liftoff from the sapphire substrate for further characterization. The GaN structure was examined by low-temperature cathodoluminescence (CL) imaging applied to a cleaved sample cross-section [294]. Fig. 3.3 represents a cathode CL-panchromatic image of the freestanding HVPE-GaN. The brightness profile was inverted here to provide a better contrast between the regions. Three different structural areas in the GaN material structure can be identified, which are characteristic of the GaN growth without buffer layers and at high growth rates. The first one is a highly defective non-radiative nucleation layer with a thickness of about 1 μm , zone (A) in Fig. 3.3. The second one is a columnar bright emission region, zone (B) in Fig. 3.3. Some of these columns are protruding up to the Ga-face, but most of them stop very abruptly, as the CL-contrast shows.

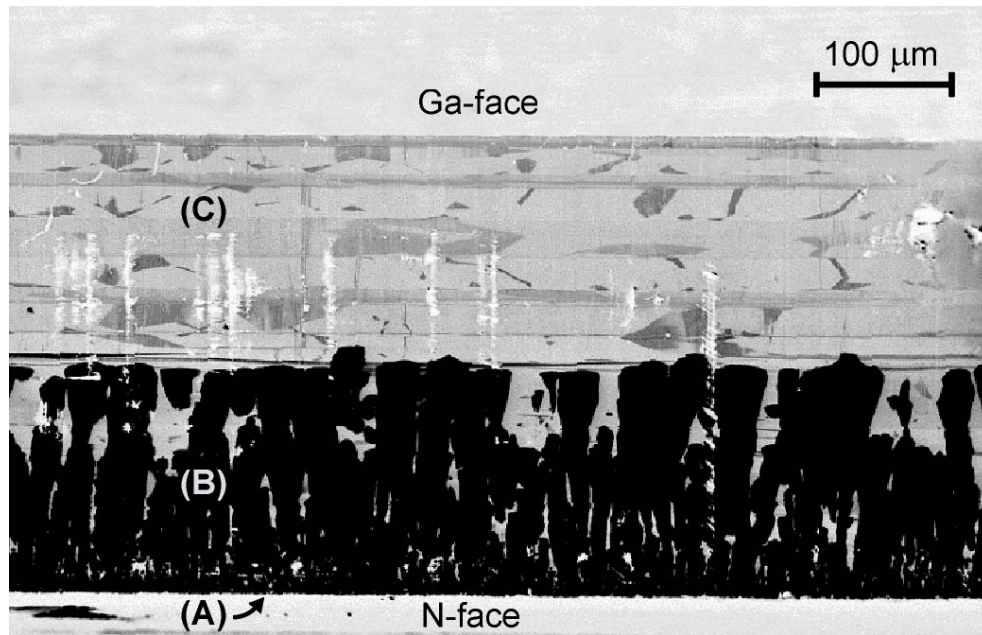


Fig. 3.3: Panchromatic cathodoluminescence image of a HVPE-GaN cross-section. The negative view of the original CL-image is shown to provide better contrast. Zone notation: (A) nucleation layer; (B) intermediate highly defective GaN; (C) high quality GaN.

This CL-feature is typical for high quality thick HVPE-GaN samples. When the width of the columnar area is thick enough to overcome the lattice and thermal expansion coefficients mismatch, a high quality crystalline zone (C) starts to grow. The material near the sapphire (B) has larger PL linewidths and brighter CL-emission presumably due to high oxygen content stemming from the sapphire substrate [294].

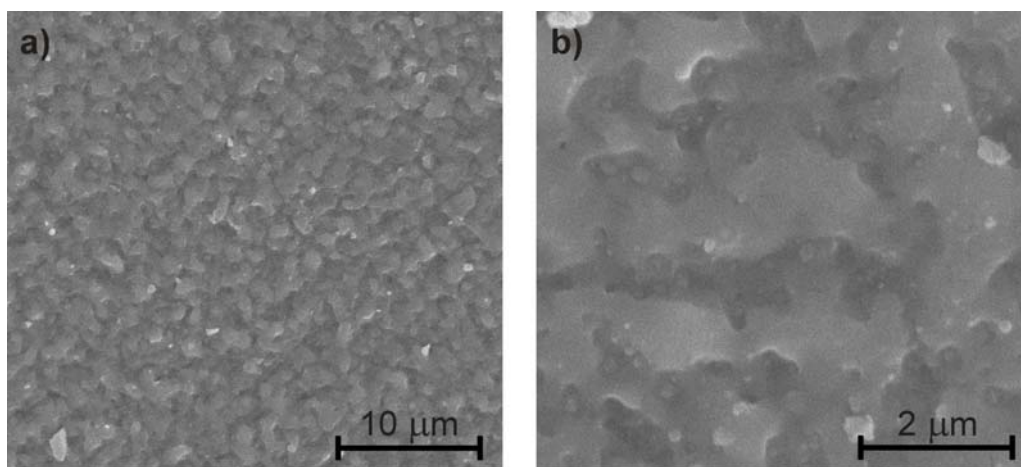


Fig. 3.4: SEM images of the N-face side of a HVPE-GaN sample after laser liftoff for sapphire removal: a) view with amplification of 3.5 K; b) amplification of 18 K.

The effect of laser-induced decomposition on the N-face surface morphology of GaN after delamination from the sapphire substrate can be observed in the SEM images in Fig. 3.4. The regular shape shows small grain formation with a size of $\sim 2 \mu\text{m}$, due to GaN decomposition, yielding rms roughness of about $3 \mu\text{m}$.

To produce freestanding GaN pseudo-substrates with adequate surface characteristics for further epitaxial overgrowth, a lapping and fine-polishing procedure was developed for the delaminated GaN films [295]. The freestanding substrates offer the possibility of growth on both side, which have opposite crystal polarity, Ga-face (0001) and N-face ($000\bar{1}$). Crystal polarity plays an important role in GaN epitaxy and processing, strongly influencing the growth morphology and chemical stability [296-298]. The N-face is chemically more reactive and can be easily etched or polished with KOH or NaOH, whereas the Ga-face is very stable, making a chemo-mechanical fine polishing more difficult.

After each polishing step, the surface morphology was inspected with surface profiling and optical and atomic force microscopy to check the progress of the procedure. A planarization step was introduced to get rid of residual sample bowing after laser liftoff by using a diamond lapping pad with grain size of $40 \mu\text{m}$. Afterwards, a polishing sequence under controlled pressure of about 2 kg/cm^2 was performed on hard cloth pads with diamond paste and grain sizes of 15, 7, 3 and $0.25 \mu\text{m}$ for approximately 10 minutes per step. The last step when preparing the Ga-face was a long mechanical polish with a special fine polishing solution (grain size of $0.04 \mu\text{m}$). For the N-face, a chemical polish with a 1:10 KOH : H₂O solution was applied to reach the final surface smoothness. The rms roughness, as measured by AFM, is of the order of 1 nm for N-face and 2.2 nm for Ga-face surfaces with peak to valley amplitudes smaller than 10 nm at surface scratches (Fig. 3.5). An additional chemo-mechanical polishing step to remove the subsurface region damaged by the aggressive mechanical polishing was found to be inefficient for Ga-face surfaces. For this purpose,

methods with chemical assisted ion beam etching (CAIBE) or reactive ion etching (RIE) have been investigated [256][299].

In this work, the mechanical treatment was followed by reactive ion etching with BCl_3 , upon which the average surface roughness did not change substantially. As confirmed by photoluminescence (PL) measurements, an electronic quality similar to the unpolished GaN could be recovered.

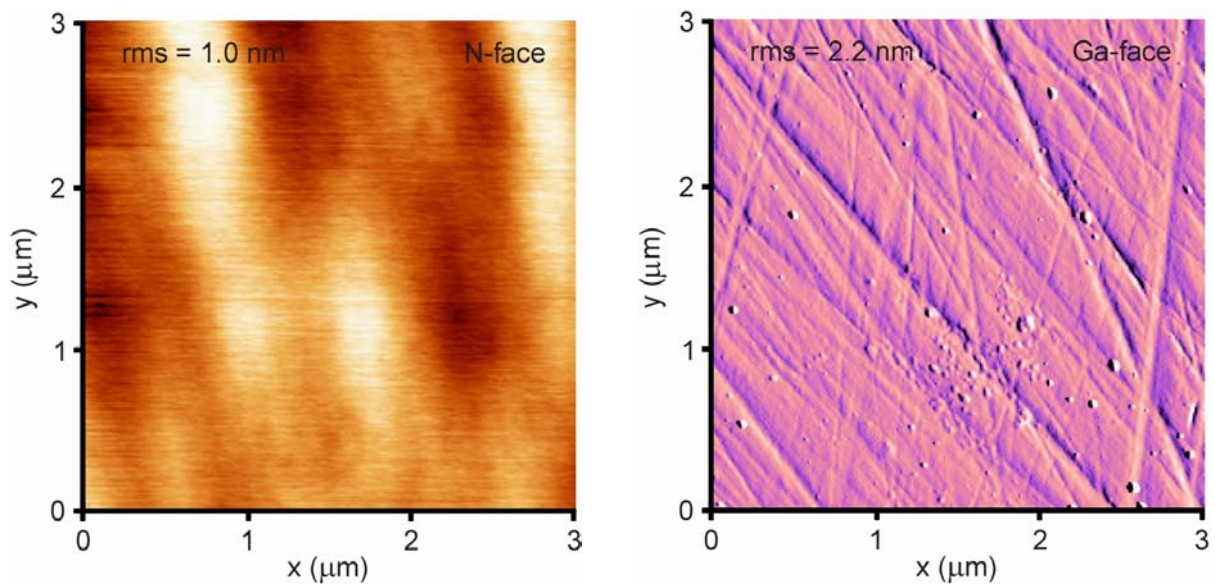


Fig. 3.5: The left AFM image shows the surface of N-face HVPE-GaN after chemo-mechanical fine polishing. No scratches are left. The maximum peak-to-valley amplitude is 6 nm. On the right AFM image the chemically stable Ga-face is shown after mechanical polishing. The scratches have a maximum peak-to-valley amplitude of 15 nm and result from the polishing procedure using diamond paste with different grain sizes.

In Fig. 3.6 the photoluminescence response is used as a quality parameter to evaluate the effect of different substrate preparation methods of the HVPE-GaN Ga-face surface after mechanical polishing. The peaks in Fig. 3.6 and Fig. 3.8 were identified as the free-exciton recombinations (X_A) and (X_B), the neutral donor or acceptor bound-exciton transition (D_2^0-X) and (A^0-X), respectively, and the donor or acceptor bounded exciton transitions (BE). A detailed description of the PL peak distribution will be presented later in

this chapter. Compared to the as grown sample, a strong decrease of the PL intensity is caused by mechanical polishing. The GaN surface is almost electronically dead, clearly showing the crystal degradation. To get rid of this damaged surface region, HVPE-GaN pieces were plasma etched with BCl_3 and laser ablation with a Nd:YAG laser until about $2\ \mu\text{m}$ of GaN was removed.

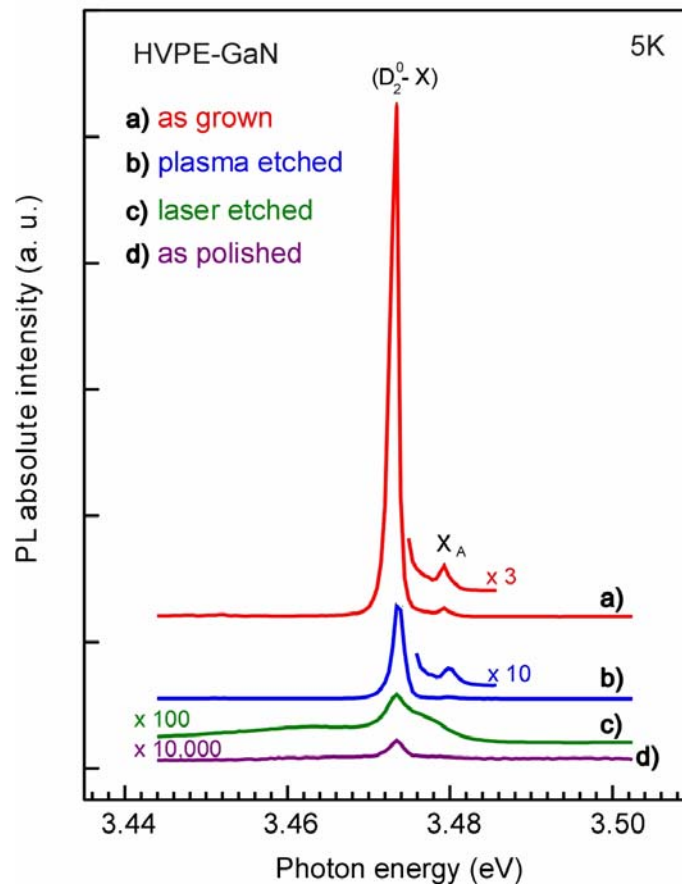


Fig. 3.6: Optical characterization of freestanding Ga-face HVPE-GaN samples with different surface preparation after mechanical polishing and compared to untreated GaN.

The photoluminescence spectra in Fig. 3.6 show a partial restoration of the luminescence activity for the etched films. Despite of the improvement of the PL intensity, the broader spectrum linewidth clearly shows that the laser ablation left a partially damaged crystalline region, probably due to N- and Ga-vacancies generated during the explosive GaN decomposition.

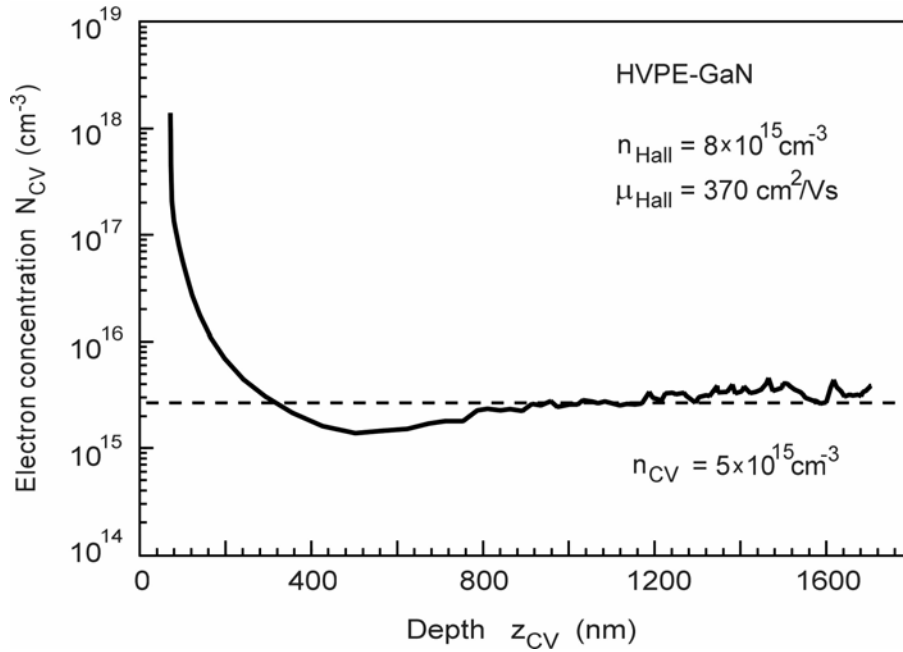


Fig. 3.7: C - V electron concentration profile (N_{CV}) vs depth (z_{CV}) of a 300 μm thick HVPE-GaN sample, measured at the Ga-face.

The electrical properties of the HVPE-GaN pseudo-substrates were determined by Hall effect and capacitance-voltage (C - V)-profiling measurements [297]. The free electron concentration and mobility of the freestanding GaN substrates at room temperature were measured as $8 \times 10^{15} \text{ cm}^{-3}$ and $350 \text{ cm}^2/\text{Vs}$, respectively. A typical C - V -profile is depicted in Fig. 3.7.

3.2 Homoepitaxy on Freestanding HVPE-GaN Substrates

To investigate the effect of the different surface preparation procedures on homoepitaxial films, the samples described above were overgrown with GaN. The MOCVD-system was used to simultaneously deposit 1 μm of GaN on top of three HVPE-GaN samples with laser ablated, plasma etched, and as polished Ga-face surfaces.

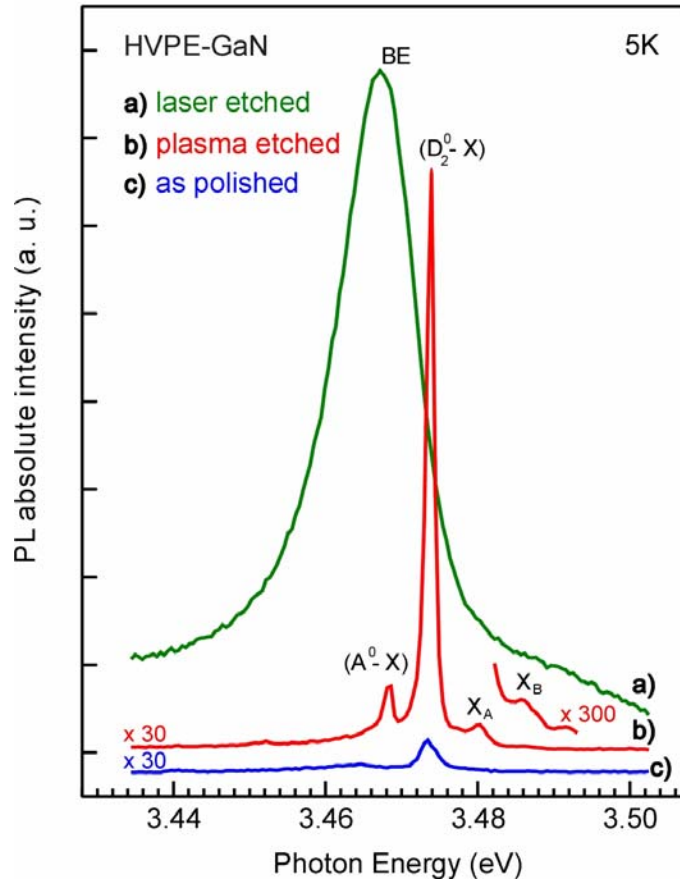


Fig. 3.8: Comparison of photoluminescence intensity of homoepitaxially overgrown GaN substrate s with different surface preparation stages after mechanical polishing of the Ga-face surface.

The optical response measured by photoluminescence shown in Fig. 3.8 again confirms the largely varying quality of the films. The weak peak of the film deposited on the as-polished GaN substrate indicates clearly the importance of a defect-free substrate surface for the overgrowth. The removal of the damaged region with laser ablation gives rise to a very strong *BE* peak in Fig. 3.8. The integrated peak intensity is of the same order of magnitude as of the as-grown HVPE-GaN film in Fig. 3.6. Nevertheless, the defects generated during GaN laser decomposition completely dominate the PL response, giving rise to the broad *BE* emission in the MOCD-GaN layer. More satisfactory is the effect of plasma etching with BCl_3 to remove the defective region caused by mechanical polishing. The PL peak intensity and shape shown in Fig. 3.8 proves that the original good crystalline surface quality was

recovered by plasma etching of the polished GaN substrate. Therefore, this procedure was adopted as the standard preparation technique for HVPE-GaN freestanding substrates and optimized to improve the quality of homoepitaxial films.

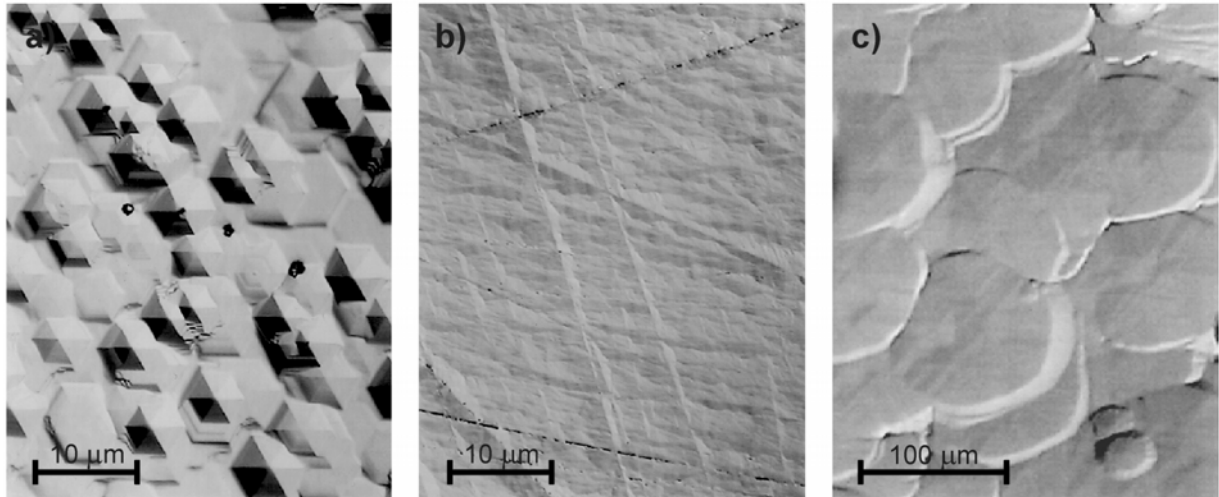


Fig. 3.9: Surface morphologies of MOCVD-GaN films grown on HVPE-GaN substrates: a) on chemo-mechanically polished N-face, b) on roughly mechanically polished Ga-face, and c) on unpolished Ga-face substrate.

The surface morphology of the overgrown Ga and N-face HVPE-GaN samples is shown in Fig. 3.9. The MOCVD growth was performed at 1030°C after cleaning the samples with organic solvents. In Fig. 3.9 a), the N-face surface developed a pyramidal three-dimensional morphology, which is typical for GaN heteroepitaxy on sapphire without a nucleation layer. For several MOCVD growth runs it was found that the N-face polarity of GaN did not produce a smooth surface, contrary to the Ga-face substrate, showing the strong influence of polarity in the GaN film characteristics [300]. In the Ga-face case (Fig. 3.9 b), a relatively smooth surface with still visible polishing lines was produced. These lines acted as preferential nucleation sites for the GaN overgrowth. In Fig. 3.9 c), a surface micrograph of GaN deposited on unpolished Ga-face HVPE-GaN is presented. The initial surface structure of the substrate (see Fig. 3.1) prevented the planarization of the final GaN film, giving rise to circular structural features, which indicate some kind of two-dimensional growth in MOCVD.

These results demonstrate the importance of a very smooth initial surface to achieve a smooth two-dimensional overgrowth.

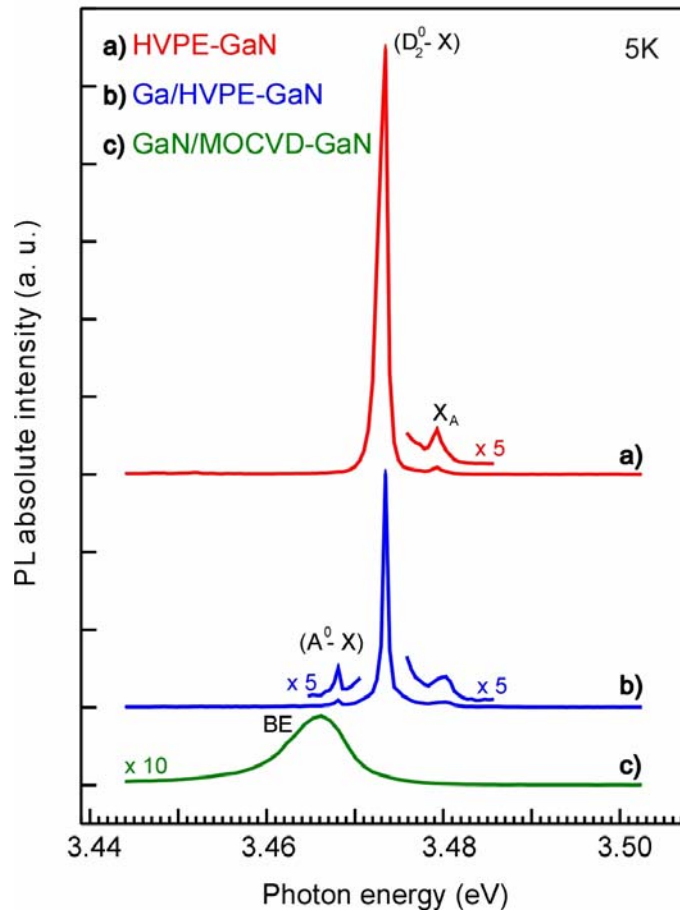


Fig. 3.10: Photoluminescence spectra of homoepitaxial GaN on HVPE-GaN substrates and on MOCVD-GaN template. The upper spectrum shows the PL response of the HVPE-substrate prior to overgrowth.

The improvement of the crystal quality due to homoepitaxy on high-quality GaN pseudo-substrates is clearly confirmed by PL measurements as shown in Fig. 3.10. A MOCVD-GaN template of 1 μm thickness, previously deposited on sapphire with a 50 nm AlN nucleation layer was overgrown together with the HVPE-GaN freestanding substrate to allow a direct comparison. The excitonic PL emission of the GaN/HVPE-GaN sample is similar to the original HVPE-GaN substrate, besides the (A^0-X) peak at 3.468 eV. Furthermore, the excitonic emission is about 10 times sharper than the BE emission of the GaN/MOCVD-GaN

sample, showing the significant quality enhancement obtained for the same growth conditions.

An optimization of the preparation of freestanding HVPE-GaN substrates and homoepitaxial growth by MOCVD resulted in the production of state of the art GaN films with excellent structural, optical, and electrical characteristics [231], fulfilling many of the requirements necessary for the development of devices with high performance.

Homoepitaxy was carried out at 100 mbar in a MOCVD quartz reactor with V/III ratio of 40,000. An annealing of the 300 μm thick HVPE-GaN substrate was performed at 800°C under a flow of 2 slm of nitrogen and hydrogen ($\text{N}_2 / \text{H}_2 = 1$) for 10 min. Then NH_3 was added to the transport gases and the temperature rose to 1050°C within a time period of 5 min. A 2 μm thick epitaxial GaN film was grown on the Ga-face side of the substrate with a growth rate of 600 nm/h.

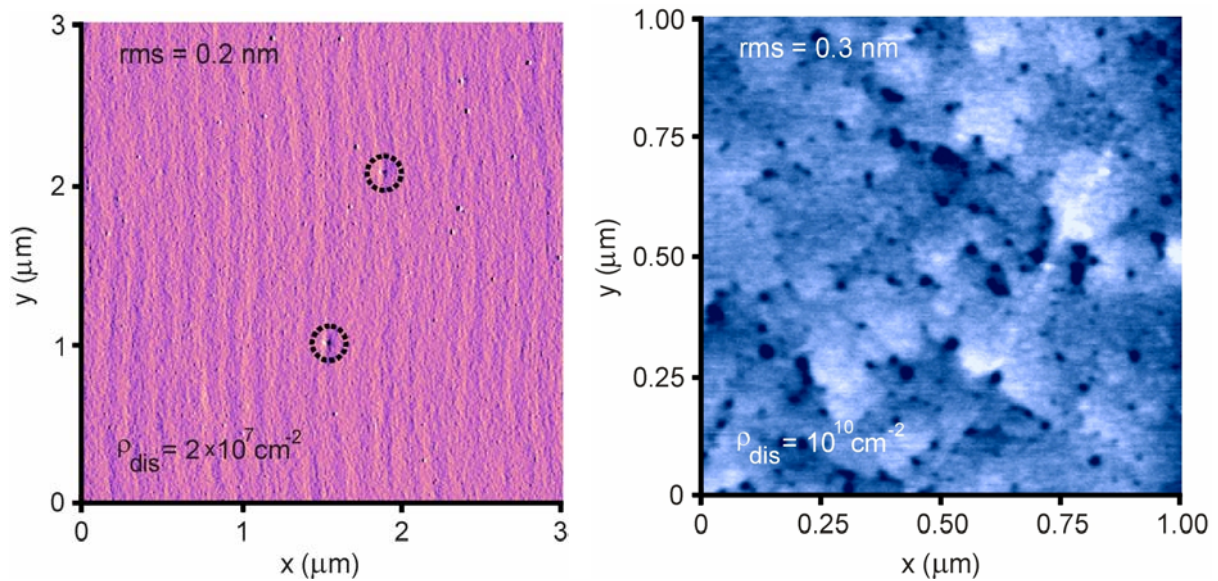


Fig. 3.11: AFM images of homoepitaxial GaN grown by MOCVD. On the left: growth on prepared HVPE-GaN substrate (rms = 0.2 nm). The maximum peak-to-valley amplitude is 0.8 nm. The circles mark isolated dislocations (pin-hole depth ≤ 3 nm). On the right: growth on MOCVD-GaN template (rms = 0.3 nm). The maximum peak-to-valley amplitude is 1.5 nm and the pin-hole depth ≤ 6 nm.

The outstanding surface morphology of the homoepitaxial film grown on a carefully prepared freestanding HVPE-GaN substrate can be seen from the left AFM image in

Fig. 3.11. In a transverse cross section it is possible to identify bilayer steps with terraces of about 200 nm width. Compared to an *in-situ* overgrown MOCVD-GaN sapphire based template, the estimated dislocation density is reduced by almost three orders of magnitude. The calculation of the dislocation density of $2 \times 10^{-7} \text{ cm}^{-2}$ was based on a series of AFM micrographs and is in agreement with the dislocation density determined for the original HVPE-GaN substrate.

3.3 Structural Characterization of Homoepitaxial GaN

High resolution X-ray diffraction (HRXRD) measurements were performed to check the structural quality, strain and mismatch between the GaN substrate and the epitaxial layer.

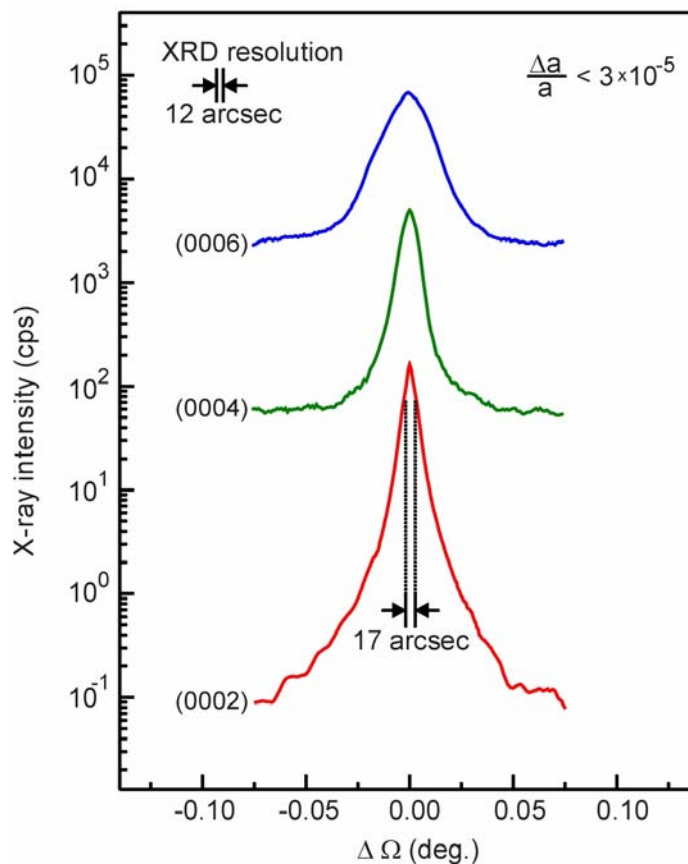


Fig. 3.12: HRXRD of GaN grown on the Ga-face of a 300 μm thick HVPE-GaN substrate. 2θ - ω FWHM is 17 arcsec at the (0002) reflection (XRD-system resolution: 12 arcsec). The corresponding FWHM of the rocking curve is 155 arcsec.

In Fig. 3.12, 2θ - ω scans of the (0002), (0004) and (0006) reflections are compared, showing a FWHM as small as 17 arcsec. From the high dispersion (0006) diffraction peak and reciprocal space maps of the (205) reflection, the maximum lattice mismatch between substrate and homoepitaxial GaN film can be estimated to $\Delta a/a = 3 \times 10^{-5}$. In rocking curve measurements, single symmetrical peaks of the (0002) and (205) reflections with FWHMs of 155 arcsec were observed. The FWHM of the rocking curves is limited by a residual small curvature of the freestanding GaN substrate due to the remaining biaxial compressive strain after laser delamination (section 3.7). From the reciprocal space map measured at the asymmetrical (205) diffraction peak, an in-plane compressive strain as low as 1.9×10^{-4} was calculated, indicating that the thick freestanding HVPE-GaN substrate is almost completely relaxed.

Complementary to optical analysis of the homoepitaxial GaN film performed by photoluminescence measurements, the good structural quality is confirmed by sharp optical phonon lines measured with micro-Raman spectroscopy at low temperature as shown in Fig. 3.13. The measurements were performed in backscattering configuration, with the laser beam along the c -axis of the wurtzite structure (z -direction). A microscope objective was employed to focus the 514.5 nm argon laser line on the sample surface to a spot size of about 2 μm , with a power density of the order of 10^5 W/cm^2 . Only the allowed E_2 (high energy) and $A_1(\text{LO})$ modes [301] were detected at 568 cm^{-1} and 735 cm^{-1} , respectively. The high energy E_2 phonon mode possesses a comparatively large strain coefficient, rendering both mode frequencies suitable to provide an estimate of the material strain [302].

The peak positioning obtained is consistent with data reported for pressure-dependent Raman scattering measurements for 50 μm thick freestanding GaN films, which are the most precise reference values for unstrained GaN material so far [303]. Thus, the micro-Raman scattering results confirm the conclusions from XRD that the freestanding GaN is practically strain-free.

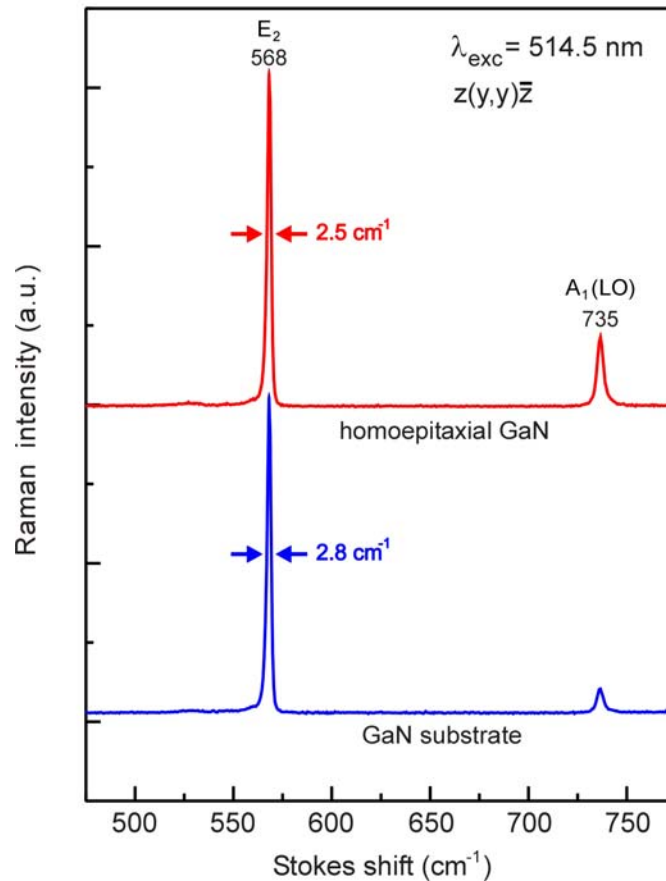


Fig. 3.13: Raman spectroscopy of homoepitaxial GaN grown on freestanding HVPE-GaN substrate.

3.4 Optical and Electrical Characterization of Homoepitaxial GaN

To evaluate the electronic quality of the homoepitaxial GaN layer, radiative excitonic recombination was measured by PL at 4.3 K (Fig. 3.14). The excitation source was the 333.6 nm emission line of an argon laser which was focused by a microscope objective to a spot of 25 μm diameter on top of the sample. The photoluminescence light was dispersed using a triple-grating spectrometer with a focal length of 800 mm and was detected by a LN₂ cooled CCD camera. With this setup, the energy resolution at 3.5 eV is better than 1 cm^{-1} or 120 μeV .

The detected transitions are typical for a nominally undoped GaN film with residual impurities. The high optical quality of the GaN film is confirmed by the presence of well resolved free-excitonic recombination peaks [304] X_A , X_B , and the excited $n=2$ state of X_A at 3.480, 3.486, and 3.500 eV, respectively. The spectra are dominated by the neutral donor bound-exciton transition (D_2^0-X) at 3.474 eV with a FWHM of 550 μeV . More visible lines are the neutral acceptor bound-exciton (A^0-X) at 3.469 eV, the neutral donor bound-exciton (D_1^0-X) at 3.478 eV, and the so-called “two-electron” transition ($(D_2^0-X)_{n=2}$) emerging at 3.453 eV, when the donor is left in an excited $2s$ -like state [305].

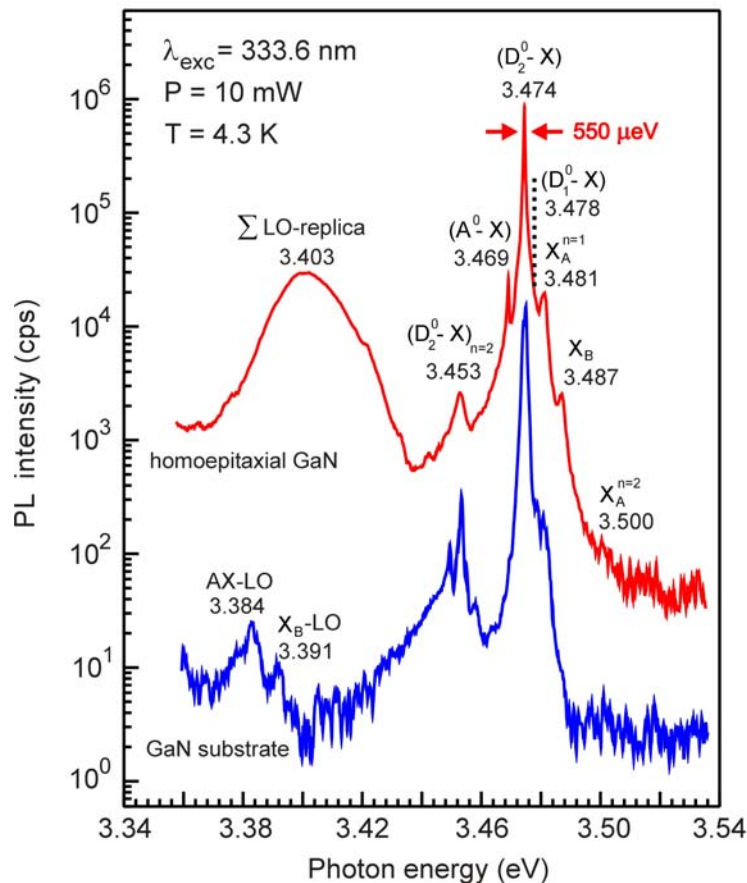


Fig. 3.14: Low temperature PL spectra of an optimized GaN epitaxial film on a freestanding HVPE-GaN substrate.

On the low energy side of the spectra in Fig. 3.14, in the GaN substrate small bands emerges at 3.384 eV and 3.391 eV, which are correlated with the LO phonon replica of the

free-exciton line and to acceptor bound-exciton transition, respectively. A strong broad band centered at 3.403 eV (FWHM = 19 meV) in the homoepitaxial GaN film appears as a result of the overlapping of several LO-phonon replica associated with the free and bound-exciton transitions. In these cases, the exciton decays with the generation of one longitudinal-optical phonon. A donor-acceptor ($D-A$) transition can be excluded in this energy range, as the typical donor and acceptor ionization energies are about 30 and 100 meV, respectively. Furthermore, no energy shift was observed in PL measurements with different excitation powers, confirming the LO-phonon replica assumption. Such an excitation power dependence towards higher energies is expected for a ($D-A$) recombination due to the Coulomb interaction between the charged donors and acceptors.

The above peak identification was based on the excitation and thermal power dependencies of the PL lines. The spectra were analyzed using a multi-Gaussian fit procedure in order to obtain an accurate determination of the PL energy and relative intensity of the individual peaks. Besides thermal energy, impurities, disorder, and defects in the crystal lattice cause broadening of the free-exciton recombination peaks compared to the narrower bound-exciton transitions, due to exciton localization at these centers [305]. For homoepitaxial GaN films grown by MOCVD and MBE on high pressure synthesized bulk GaN substrates, similar linewidths were reported [306][307]. However, the energy positions of the donor bound-exciton transition for those samples, 3.469 and 3.471 eV, are shifted indicating different residual strain. This difference compared to films grown on HVPE-GaN substrates could be caused by the ten times larger lattice constant mismatch of $\Delta a/a = 2 \times 10^{-4}$ between the homoepitaxial GaN film and the bulk substrate, due to the significantly higher residual carrier concentrations in bulk GaN, of the order of 10^{19} cm^{-3} , compared to $\sim 10^{17} \text{ cm}^{-3}$ for the epitaxial layer [306-308].

To obtain further information on the origin of the PL lines Fig. 3.15 shows the PL spectrum of the homoepitaxial GaN film on freestanding HVPE substrates for various

excitation intensities. The excitonic character of the transitions is confirmed by the absence of an energy shift with variation of the excitation intensity. The integrated intensities for each transition increase nonlinearly with the excitation power. According to Schmidt *et al.* [309], the dependence of luminescence intensity I on the excitation power P can be described by a power law, $I \propto P^k$. Since the rate of exciton formation depends on the product of the electron and hole densities, the exciton PL intensity is expected to be superlinear in excitation power. For excitation laser light with $h\nu$ exceeding the energy gap E_G of the semiconductor, the coefficient k is generally $1 < k < 2$ for the free and bound-exciton emission and $k < 1$ for free electron/hole to donor/acceptor center and donor-acceptor pair recombination. In Fig. 3.15, the excitation power was varied by three decades. All lines had an exponent $k \geq 1.4$, confirming the excitonic nature of the observed transitions.

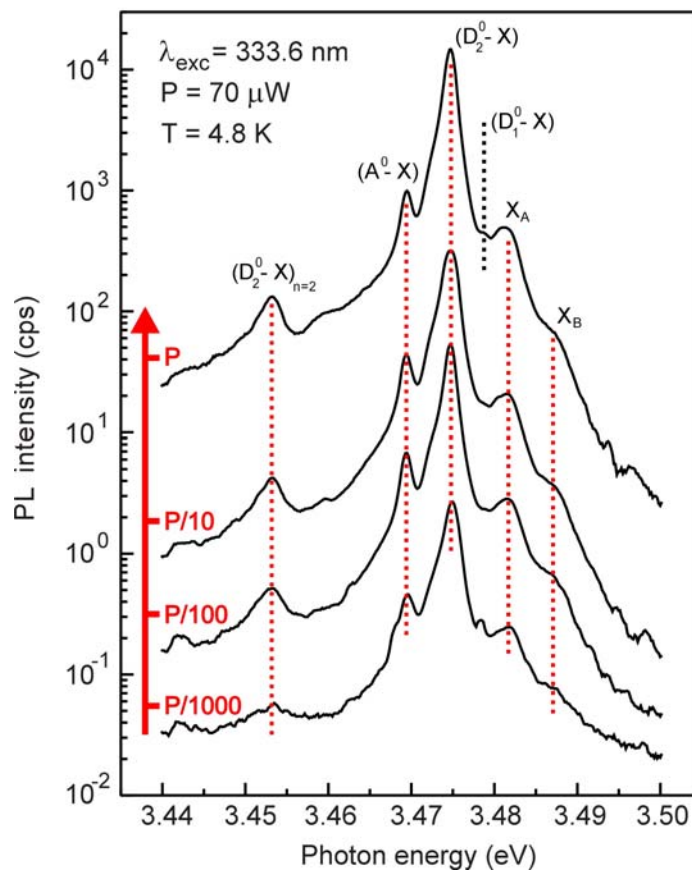


Fig. 3.15: Dependence of the PL emission on the excitation power for homoepitaxial GaN.

Complementary to the excitation power dependence of the PL spectra, the thermal behavior of the PL lines in Fig. 3.16 shows a significant change with increasing temperature in the range from 5 to 55 K [305]. The 3rd order Raman scattering of the optical phonon, $3A_1(LO)$ is resonant at the employed excitation energy and is overlapping the PL signal at 3.442 eV. This peak can be clearly observed at temperatures above 35 K, contrasting with the quenching behavior of the PL lines. Other Raman-modes were not identified in the performed PL measurements, but are probably hidden under the excitonic transition peaks.

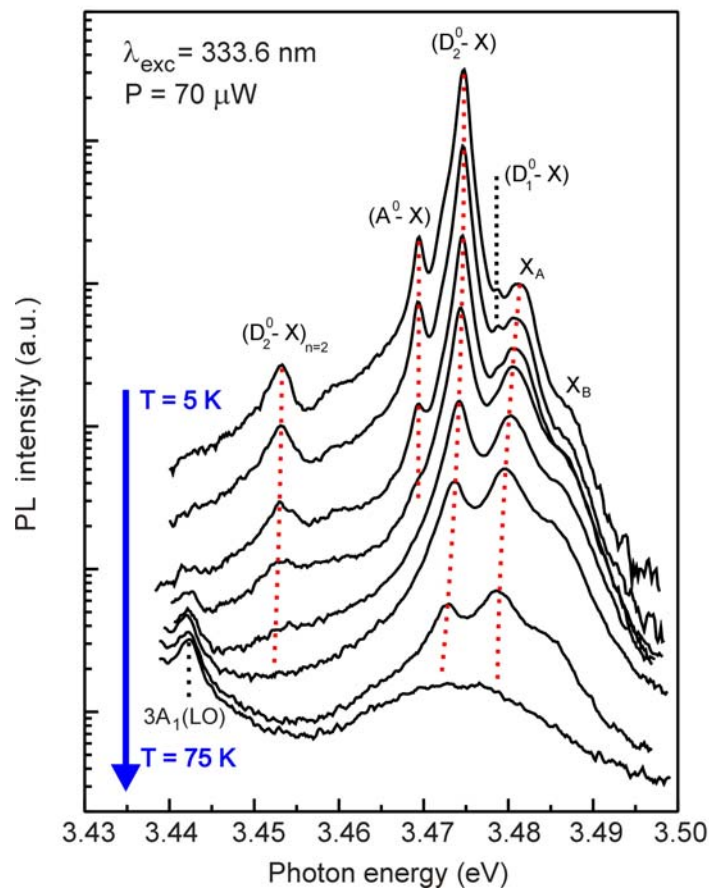


Fig. 3.16: Temperature dependence of the PL emission for homoepitaxial GaN. The 3rd order Raman scattering of the optical phonon, $3A_1(LO)$, emerges at 3.442 eV.

The higher energy levels X_A and X_B broaden and become relatively stronger, turning into the dominant recombination processes above $T = 50$ K. This is consistent with a free-exciton nature. Quenching due to thermal dissociation can be observed for the bound-exciton recombination peaks $(D_1^0 - X)$, $(D_2^0 - X)$, $(D_2^0 - X)_{n=2}$, and $(A^0 - X)$. The dominant shift in

the exciton peak positions is in agreement with the band gap shrinkage of wurtzite GaN [310], except for an energy offset due to different residual strain.

The Arrhenius plots in Fig. 3.17 show the Napierian logarithm of the integrated intensity and the corresponding activation energies for the free-exciton transition (X_A) and the neutral donor bound-exciton transition (D_2^0-X) of Fig. 3.16 in the temperature range from 5 to 75 K.

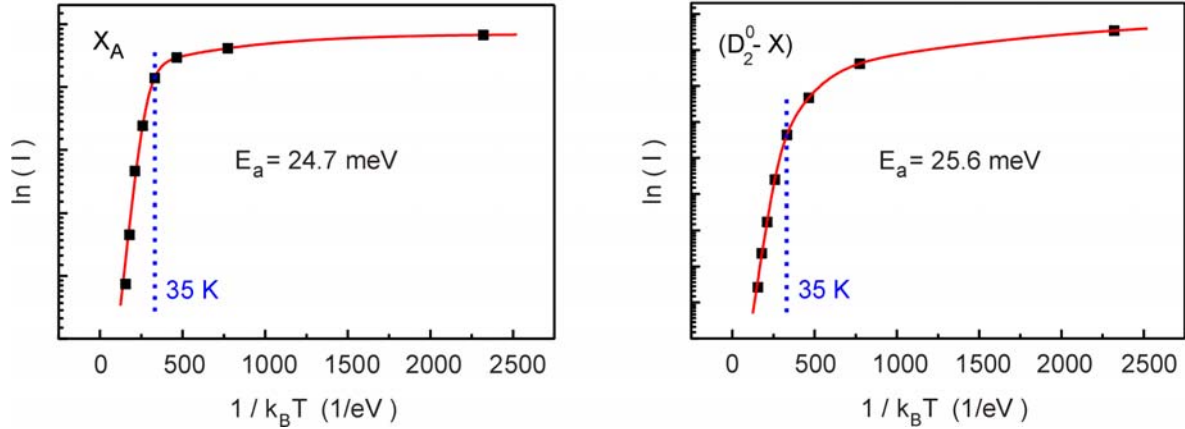


Fig. 3.17: Integrated peak intensity versus $1/k_B T$ for the free-exciton (X_A) and the neutral donor bound-exciton transition (D_2^0-X).

The data was analyzed using the well-known thermal activation relation proposed by Bimberg *et al.* [311]:

$$I = \frac{A}{1 + \sum_i B_i e^{-E_a^i / k_B T}} \quad \text{Eq. (3.1)}$$

The constants B_i are related to the high-temperature nonradiative lifetime characteristic of each recombination channel. The fitting parameters for X_A and (D_2^0-X) are summarized in Tab. 3.1 and the solid curves shown in Fig. 3.17 represent the corresponding fit.

Transition	E_a^1 (meV)	E_a^2 (meV)	E_a^3 (meV)	B_1	B_2	B_3	A
X_A	1.8	—	24.7	1.0	—	1600	2.3
(D_2^0-X)	1.4	7.2	25.6	5.1	244.5	1600	41.6

Tab. 3.1: Fitting parameters including the activation energies and prefactors according to Eq. (3.1).

At low temperatures up to 35 K, the intensity remains almost constant, with a very low activation energy E_a^1 . At higher temperatures, a rapid quenching is observed, indicating the thermal dissociation of the excitons. By adding the X_A exciton binding energy of $E_X = 24.7$ meV calculated from the Arrhenius plot in Fig. 3.17 to the PL peak position centered at 3.4810 eV, we obtain a band gap energy of 3.5057 eV for the strain-free homoepitaxial GaN at 4.3 K. The energy required to remove the bound exciton from the neutral donor, the exciton localization energy (E_{BX}), can be deduced from the difference of the free A exciton ($h\nu_{X_A}$) and donor bound-exciton ($h\nu_{(D_2^0-X)}$) energies, as follows:

$$h\nu_{(D_2^0-X)} = E_G - E_X - E_{BX} = h\nu_{X_A} - E_{BX} . \quad \text{Eq. (3.2)}$$

The obtained value of $E_{BX} = 6.5$ meV agrees within experimental accuracy with the activation energy of $E_a^2 = 7.2$ meV obtained in the second region of the donor bound exciton thermal quenching, as expected for thermal exciton dissociation from the donor. The corresponding free-exciton dissociation occurs with an activation energy $E_a^3 = 25.6$ meV. The excited state transition $(D_2^0-X)_{n=2}$ can be used to obtain information about the neutral donor binding energy, E_D . In this so-called “two-electron” transition, after the electron-hole excitonic recombination of the bound exciton, the neutral donor can either return to the ground state ($n = 1$) or absorb energy from the exciton to excite the donor electron in to an excited state ($n = 2$). The transition energy for the later case can be expressed as:

$$h\nu_{(D_2^0-X)_{n=2}} = E_G - E_X - E_{BX} - \Delta E = h\nu_{(D_2^0-X)} - \Delta E , \quad \text{Eq. (3.3)}$$

where ΔE is the energy necessary to bring the donor into its first excited state. Assuming the energy level sequence of a hydrogen atom:

$$\Delta E = E_D \left(\frac{1}{n_0^2} - \frac{1}{n_1^2} \right) = E_D \left(\frac{1}{1^2} - \frac{1}{2^2} \right) = \frac{3}{4} E_D , \quad \text{Eq. (3.4)}$$

a donor ionization energy of $E_0 = 28.6$ meV can be derived from Eq. (3.3). Such a donor ionization energy has been attributed to Si atoms on Ga sites [312]. Our value is slightly lower than the 31.7 meV obtained by Volm *et al.* [313], but is very close to the 29 meV in a moderately doped sample determined by Wang *et al.* [314]. Considering the respective uncertainties in the determination of these values in the published experiments, the obtained value of 28.6 meV for the ionization energy of the Si donor is a good compromise.

With the ionization energy of the residual donor it is possible to evaluate, as well, the electron and hole effective masses characteristic for high-quality GaN. The effective mass equation for hydrogenic states can be applied, despite of the anisotropy of the reduced effective masses and the dielectric constant in wurtzite GaN, a hexagonal crystal with axial symmetry. It has been demonstrated that, to a good approximation, the isotropic reduced masses and dielectric constant are still valid approaches [315]. In the effective mass approximation, the donor impurity induces a shallow hydrogenic state relative to the bottom of the conduction band with a binding energy given by:

$$E_D = \frac{m_e e^4}{2 \hbar^2 \varepsilon_0^2} = \frac{m_e R_H}{m_0 \varepsilon_0^2}, \quad \text{Eq. (3.5)}$$

where $R_H = 13.606$ eV is the Rydberg constant and the electron rest mass $m_0 = 9.108 \times 10^{-31}$ kg. With the dielectric constant of GaN $\varepsilon_0 = 9.5$ [316] the effective electron mass is estimated to $m_e = 0.19 m_0$, close to the value of $m_e = 0.20 m_0$ obtained by electron cyclotron resonance experiments in MOVPE-GaN [317]. The effective hole mass m_h can be derived from the free A exciton binding energy:

$$E_X = \frac{\mu e^4}{2 \hbar^2 \varepsilon_0^2} = \frac{R_H}{m_0 \varepsilon_0^2} \left(\frac{1}{m_e} + \frac{1}{m_h} \right)^{-1}. \quad \text{Eq. (3.6)}$$

The calculated effective hole mass of $m_h = 1.19 m_0$ again is in very good agreement with the value of $m_h = 1.20 m_0$ evaluated experimentally by PL and two-photon spectroscopy

[318], as well as by first-principles calculations [319]. Finally, the high quality of the homoepitaxial GaN and the good spectral resolution used in our PL experiments allowed the clear observation of two distinct donor bound-exciton transitions (D_1^0-X) and (D_2^0-X) separated by approximately 4 meV. These transitions could result from two independent donor bound-exciton lines due to the coexistence of two shallow donors. Alternative mechanisms are excited states of either the donor or the exciton. The observation of donor excited states is improbable, since the energy separation should be 3/4 of the donor ionization energy, $E_D = 28.6$ meV, which is too large to explain the observed shift of 4 meV. Similarly, an excited state of the neutral donor bound exciton would also be 3/4 of the binding energy in the effective mass approximation. With the binding energy of 25.8 meV, the first excited state should appear around 20 meV above the ground state. The possibility that the two lines originate from donor bound excitons relating to A and B valence bands can be excluded because their energy separation is also larger than 4 meV [306]. According to the presented arguments, we finally labeled the two transitions at 3.474 and 3.478 eV shown in Fig. 3.14 as resulting from two different residual donors. The donor centers responsible for the (D_2^0-X) transitions could be assigned to Si, as mentioned, but further investigation is necessary to identify the second donor accounted to the (D_1^0-X) recombination channel.

Hall effect measurements yielded a free carrier concentration of $5 \times 10^{16} \text{ cm}^{-3}$ and $\mu_{\text{Hall}} = 310 \text{ cm}^2/\text{Vs}$ at room temperature; at 77 K the mobility was of the order of $1200 \text{ cm}^2/\text{Vs}$. These results confirm that residual donor incorporation occurred during MOCVD growth.

In conclusion, freestanding high quality GaN substrates as large as 2" in diameter, obtained by applying the laser-induced liftoff process to GaN HVPE, are suitable as substrates for nitride homoepitaxy after careful preparation of the Ga-face surface. This was confirmed by the homoepitaxial growth of 2 μm thick GaN films by MOCVD. As observed by AFM and

HRXRD measurements, lattice-matched samples were grown with dislocation densities and surface roughnesses of about 10^7 cm^{-2} and 0.2 nm, respectively. The good electronic quality of the samples was confirmed by PL and Raman spectroscopy. In combination with the good electrical characteristics, these results establish freestanding HVPE-GaN films as attractive substrates for the fabrication of GaN-based devices.

Motivated by these results using the laser induced liftoff technique, some companies are incorporating this technology for the large scale production of freestanding GaN substrates. The Samsung Corporation is already planning the commercialization of GaN substrates developed by laser delamination and subsequent polishing to support the market of GaN-based devices.

4 AlN Heteroepitaxy on Diamond for Ultraviolet Light Emission

Among the different materials for light emission, strong progress has been made in III-N semiconductors. After the realization of high brightness InGaN-based quantum well LEDs with emission wavelength from the near ultraviolet (UV) to the green [320], there has been a growing interest in pursuing emitters with wavelengths in the deep UV spectral range (200 to 360 nm). The intense attention in deep UV emitters is due to a large number of potential applications. For instance, UV-LEDs can be coated with three-band phosphor (emitting red, green and blue light) to produce white light. Such LEDs may also be used to excite biological molecules that contain chemical bonds with strong optical transitions within the UV spectral region. Similarly, high-density optical storage devices, lithography instruments and chemical processes in both medical applications and waste processing take advantage of the short wavelength of UV radiation. In this chapter we discuss the feasibility of producing UV-light emitting diodes based on nitride heteroepitaxy on single crystalline diamond substrates.

4.1 Nitrides on Diamond: the Doping Issue

Nitride-based LEDs with emission below 360 nm require the use of the ternary AlGaN in the active region and the contact layers. The band structure of AlGaN is direct in the whole Al range and the band gap can be tailored from 3.4 eV (GaN) to 6.2 eV (AlN), *i.e.*, from 365 nm to 200 nm. Various groups have reported the continuous improvement of wavelength and performance for AlGaN-based quantum well UV emitters [321-326]. The incorporation of indium into AlGaN active layers gave rise to an improvement of the optical emission efficiency of LEDs compared to AlGaN-based devices [327][328]. Very promising AlInGaN-based UV emitters were reported recently [329][330]. All these encouraging results

suggest that the success of nitride LEDs in the visible spectra may also be repeated in the deep UV spectral range.

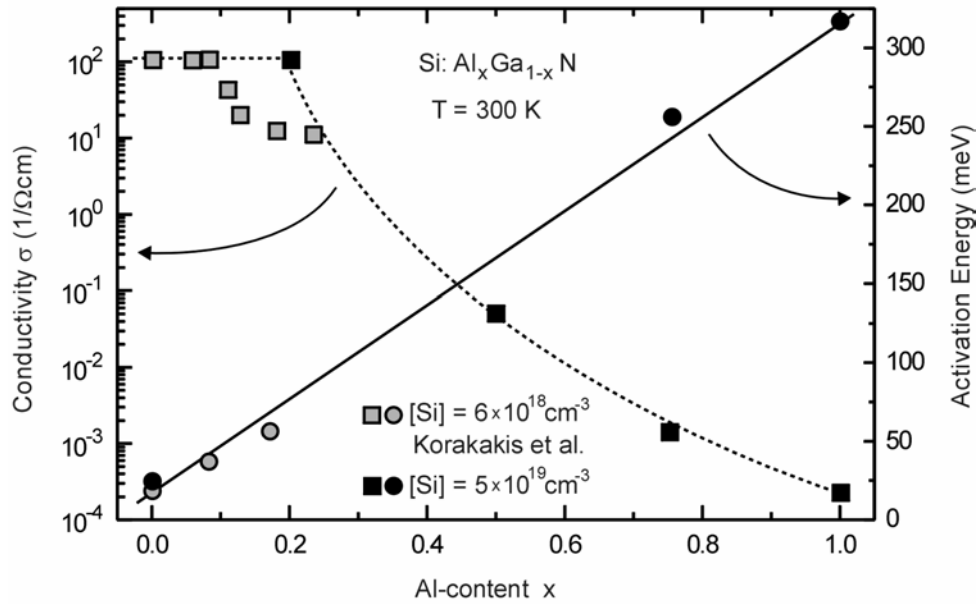


Fig. 4.1: Conductivity and activation energy of Si doped PIMBE-AlGaIn films at different Al-contents. The results from Korakakis *et al.* at of low Al-content are plotted for comparison [331].

The deeper the UV emission, the higher the Al-content required for the quantum well active region. In addition, the Al-content required for the n- and p-type contact layers is even larger than that of the active region. Thus, an important point for nitride-based UV LEDs is a sufficiently high conductivity of the AlGaIn contact layers. This is not a trivial problem for Al contents exceeding 30 % [332]. Indeed, using advanced deposition techniques, AlGaIn epitaxial layers on Al_2O_3 or SiC with good structural quality can now be obtained over the entire compositional range [333][334], and efficient n-type doping of AlGaIn with Si has been demonstrated as well [335]. Fig. 4.1 shows the Al-content dependence of the room temperature dark conductivity and conductivity activation energy of Si: $\text{Al}_x\text{Ga}_{1-x}\text{N}$ films grown by plasma induced molecular beam epitaxy (PIMBE). The donor ionization energy increases from 20 meV (GaN) to 320 meV (AlN) for a fixed Si concentration of $5 \times 10^{19} \text{ cm}^{-3}$. An electron concentration of 10^{16} cm^{-3} and a mobility of $5 \text{ cm}^2/\text{Vs}$ were determined by Hall

effect measurements at 500 K. However, a decrease by almost six orders of magnitude is observed for the AlGa_N conductivity at room temperature with increasing Al content. This is caused by the increase of the donor activation energy with the Al-content together with a strong decrease (two orders of magnitude) in the carrier mobility compared to GaN. Consequently, for AlGa_N-based heterodiodes, an optimization of the Si doping efficiency is required to reduce the serial resistance of AlGa_N films with high Al-content. Unfortunately, p-type doping of AlGa_N with high Al content so far has been not successful, therefore limiting the range of applications.

The electrical characteristics of the nitride-based UV-LEDs are also dependent on the two most common substrates used, namely sapphire and silicon carbide. In the case of the insulating sapphire substrates, a coplanar contact geometry is required. This results in higher series resistances and excessive heating of the device during operation. In addition, the heat generated can not be dissipated effectively due to the poor thermal conductivity of sapphire, thus further degrading device performance. In contrast, SiC can overcome these difficulties. Conducting SiC wafers allow vertical current flow design with lower series resistances, and the excellent thermal conductivity of SiC provides good heat sinking. Unfortunately, the emission efficiency of UV LEDs on SiC is significantly reduced because the substrate absorbs light with a wavelength below 360 nm. Therefore, the fact that sapphire remains transparent down to 200 nm might make it the preferred substrate material for nitride-based deep UV-LEDs. However, the use of sapphire requires additional technological steps, such as interdigitated finger geometry and flip-chip packaging, to enhance the performance of the devices [329]. An obvious alternative for the production of light emitting devices in the UV spectral range is given by GaN-based epitaxy on AlN due to its wide band gap of 6.2 eV, as far as AlN substrates with high epitaxial quality are commercially available (see section 1.7).

Although very rarely found in nature, IIb diamonds are natural p-type semiconductors due to the presence of substitutional boron. In 1971 Collins identified boron as the impurity

responsible for the hole conductivity [336]. For this reason, boron was also used in doping experiments of artificial p-type diamond. Substitutional boron is an acceptor with an ionization energy of 370 meV: p-type doping can be obtained by the high pressure-high temperature (HPHT) technique (see section 1.9), ion implantation followed by proper annealing [337], or by CVD with diborane (B_2H_6) as the dopant source. At present, homoepitaxial growth using microwave-plasma assisted CVD and B_2H_6 in the gas phase produce high quality doped diamond films with acceptor concentrations between 10^{15} cm^{-3} and 10^{21} cm^{-3} and hole mobilities up to $1840 \text{ cm}^2/\text{Vs}$ at room temperature for the lowest boron concentration [338-340].

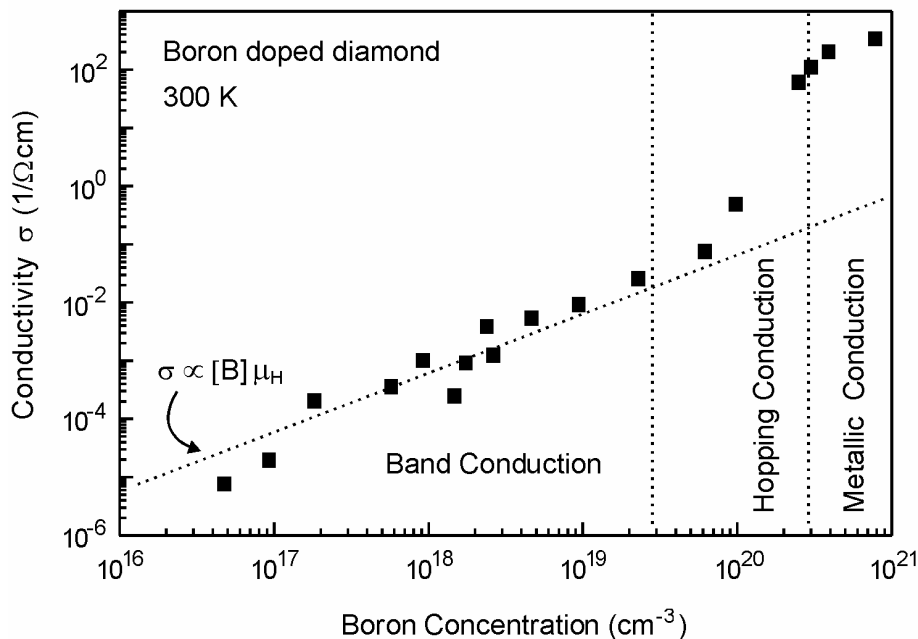


Fig. 4.2: Dependence of the dark conductivity on the boron concentration in diamond [340-342].

Due to the high ionization energy of the boron acceptors, for boron concentrations well below the Mott density only a small fraction ($\sim 0.2\%$) of them is ionized at room temperature. For all natural and synthetic material, partial compensation by deep donors, especially by nitrogen, seems to be unavoidable and plays an important role. Therefore, nearest neighbor hopping and impurity band conduction are more prominent than in other

semiconductors. For boron concentrations of up to the mid 10^{19} cm^{-3} in Fig. 4.2, the conductivity follows conventional valence-band conduction with $\sigma \propto [B] \mu_H$ with the boron concentration $[B]$. Also in this doping range, the apparent thermal activation energy equals the ionization energy 370 meV determined by optical experiments.

The metal-insulator transition (Mott transition) is expected for dopant concentrations $\sim 2 \times 10^{20} \text{ cm}^{-3}$ [341]. Therefore, for higher boron concentrations the conductivity activation energy is reduced and vanishes for $[B] \sim 2 \times 10^{20} \text{ cm}^{-3}$. The region between metallic and band conduction in Fig. 4.2 is characterized by hopping conduction between occupied and unoccupied acceptor sites. Such a conductivity mechanism has been observed at low temperatures in partially compensated silicon and germanium, but becomes important for diamond with its relatively deep boron acceptor already at room temperature for samples with an effective carrier concentration of $[N_A - N_D] > 10^{19} \text{ cm}^{-3}$ [342][343]. Typical concentrations of compensating deep nitrogen donors in CVD grown layers are in the range of 10^{16} cm^{-3} to 10^{18} cm^{-3} [342][343] and thus lead to sufficient compensated acceptor sites.

As discussed above, the substrate choice for UV-LEDs is far from clear. Among the different candidates, diamond is a very promising alternative. Firstly, the high thermal conductivity of diamond would provide an efficient dissipation of heat generated in the nitride LED structure enhancing device performance (the transfer of pre-fabricated GaN-based lasers from sapphire onto diamond or copper already takes advantage of this [344]). Secondly, the band gap of diamond is 5.47 eV, so that UV radiation will not be absorbed up to this photon energy. Thirdly, the viability to obtain synthetic high conductive p-type single crystal diamond substrates have already been reported [345], so the advantageous vertical contact geometry could be used. Finally, these substrates could serve as the p-type contact for UV emitters, at least up to 5.47 eV. As a result, the p-type high-Al-content AlGaIn contact would be eliminated, the electrical characteristics of the whole structure would improve, and the heating would be reduced. Moreover, the fact that diamond is an indirect semiconductor in

contrast to group-III nitrides can be beneficial for specific device applications. In a heterojunction bipolar transistor (HBT) for example, there would be fewer problems with optical recombination in a highly doped base region than for group-III nitrides. The longer minority carrier life time due to the indirect band structure of diamond would allow the transistor base to be thicker and highly doped, yielding a low base resistance. However, to take full advantage of these considerations, it has to be demonstrated that diamond substrates can support the heteroepitaxy of III-nitride materials with acceptable structural quality.

4.2 AlN Heteroepitaxy on Diamond

In this section we report about the first detailed study of the structural and morphological properties of AlN thin films heteroepitaxially grown on diamond (100) and (111) surfaces by molecular beam epitaxy. X-ray diffraction (XRD) analysis was used to prove epitaxial growth and particularly to determine the epitaxial orientation relationship of the AlN/diamond heterostructures. The crystal quality and structural details have been investigated in detail and are compared to morphological data as obtained by atomic force microscopy (AFM) [346][347].

The following types of diamond substrates and a sapphire reference substrate have been used in this study:

- $2 \times 2 \text{ mm}^2$ (100)-oriented synthetic IIb diamond with a boron content of about 10^{17} cm^{-3} , labeled $C_{\alpha}(100)$.
- $4 \times 4 \text{ mm}^2$ (111)-oriented CVD-grown diamond with about 10^{20} cm^{-3} B (achieved by implantation and anneal), labeled $C_{\alpha}(111)^A$.

- $2 \times 2 \text{ mm}^2$ (111)-oriented CVD-grown diamond with about 10^{18} - 10^{19} cm^{-3} B (achieved by *in-situ* doping during CVD), labeled $C_{\alpha}(111)^B$.
- $10 \times 10 \text{ mm}^2$ undoped (0001)-oriented sapphire as a reference substrate, labeled $Al_2O_3(0001)$.

The miscut of the diamond samples from their respective orientation ranged between 3 and 5°, the sapphire was cut on-axis. The substrate properties are summarized in Tab. 4.1. Prior to AlN-epitaxy, the substrates were cleaned for 30 min at a temperature of 160°C in a CrO_3/H_2SO_4 solution to remove contaminations or superficial graphite. Heteroepitaxial growth of the AlN films was performed by plasma induced molecular beam epitaxy using standard effusion cells for the evaporation of Al and Si as a donor impurity. An RF plasma source provided the reactive nitrogen radicals. This physical vapour deposition technique makes use of an ultra high vacuum environment to preserve the beam nature of mass transport, to minimize the incorporation of unintentional impurities and to analyze the wafer surface *in situ* with the help of reflection high energy electron diffraction. In addition, the precise shutter control of the source fluxes provides more abrupt interfaces than those which can be obtained by other growth techniques.

The samples were mounted in a 2" tantalum holder specially designed for the small substrates. AlN growth was performed without any nucleation layer at a substrate temperature of 815°C and a growth rate of 180 nm/h. The AlN films were doped *in-situ* with about 10^{19} cm^{-3} Si, which acts as a donor in AlN [335]. The resulting AlN:Si film thickness was about 500 nm for all samples as measured by an ultraviolet-visible range spectrometer (UV-VIS).

	$C_{\alpha}(111)^B$	$C_{\alpha}(111)^A$	$C_{\alpha}(100)$	$Al_2O_3(0001)$
Substrate				
Size (mm × mm)	2 × 2	4 × 4	2 × 2	10 × 10
Offcut (°)	4.8 to $[11\bar{2}]$	3.2 to $[11\bar{2}]$	4.3 to [011]	< 0.4
B doping (cm ⁻³)	10 ¹⁸ -10 ¹⁹	~ 10 ²⁰	~ 10 ¹⁷	-
AlN layer				
Thickness (nm)	~ 500	~ 500	~ 500	~ 500
RMS roughness (nm)	1.7	6.2	1.9	3.2
FWHM 002 ω (°)	0.55	1.27	1.36	0.51
FWHM 002 2θ (°)	0.11	0.12	0.17	0.049
FWHM 101 ϕ (°)	0.92	3.3	4.2 or 8.5	1.1
Lattice constant a (Å)	n/a	3.119(2)	3.113(5)	3.107(2)
Lattice constant c (Å)	4.9710(2)	4.9672(1)	4.9695(2)	4.9832(1)
Strain ($a-a_{rel}$)/ a_{rel} (%)	n/a	0.27	0.08	-0.12
Vertical Coherence Length XRD (nm)	79	71	53	178
Lateral Coherence Length XRD (nm)	49	21	20	53
Column diameter AFM (nm)	80	80	80	50
Relation of Epitaxy				
Epitaxial orientation relationship	(0001) $[10\bar{1}0]$ AlN (111) $[01\bar{1}]$ C_{α}		(0001) $[10\bar{1}0]$ AlN ^I (100) [011] C_{α} or (0001) $[\bar{1}2\bar{1}0]$ AlN ^{II} (100) [011] C_{α}	(0001) $[10\bar{1}0]$ AlN (0001) $[11\bar{2}0]$ Al ₂ O ₃
Deviation tilt (°)	< 0.2	< 0.2	-3 to [011]	< 0.002
Deviation twist (°)	< 1	6	1 or 3	< 0.1

Tab. 4.1: Properties of the substrates, X-ray diffraction, morphological data, and crystallographic details of different AlN/diamond and AlN/sapphire heterostructures.

High resolution X-ray diffraction (HRXRD) analysis was done using a commercial Philips X'Pert MRD triple-axis diffractometer. A high intensity monochromatic $CuK\alpha_1$ primary beam was obtained by a combination of a parabolic multilayer X-ray mirror and a $4 \times Ge(220)$ Bartels monochromator. Wide-range symmetric $2\theta/\omega$ -scans as well as pole figure measurements of asymmetric reflections were recorded in double-axis configuration using a 1° slit aperture. ω is the incident angle and 2θ is the diffraction angle, which determines the spacing d_{hkl} between the reflecting planes (hkl). The conversion rules between the cubic and hexagonal system for crystal planes and directions is given as follows:

- Crystal planes described by the set of indices h, k, i, l :

$$\text{cubic } (h\ k\ l) \Rightarrow \text{hexagonal } (h\ k\ i\ l), \text{ where } i = -(h+k)$$

- Crystal directions described by the set of indices u, v, t, w :

$$\text{cubic } [u\ v\ w] \Rightarrow \text{hexagonal } [u\ v\ .\ w] \rightarrow [(2u-v)\ (2v-u)\ -(u+v)\ 3w] \rightarrow [u^*\ v^*\ t^*\ w^*]$$

$$\text{hexagonal } [u^*\ v^*\ t^*\ w^*] \Rightarrow \text{cubic } [(u^*-t^*)\ (v^*-t^*)\ 0\ w^*] \rightarrow [u\ v\ .\ w]$$

Tab. 4.2 shows the crystal planes and directions in the cubic and hexagonal systems used in this chapter:

	Cubic	Hexagonal
Crystal plane	(001)	(0001)
	(100)	(10 $\bar{1}$ 0)
	(101)	(10 $\bar{1}$ 1)
	(110)	(11 $\bar{2}$ 0)
	(111)	(11 $\bar{2}$ 1)
Crystal direction	[001]	[0 0 0 1]
	[010]	[$\bar{1}$ 2 $\bar{1}$ 0]
	[011]	[$\bar{1}$ 2 $\bar{1}$ 3]
	[01 $\bar{1}$]	[$\bar{1}$ 2 $\bar{1}$ $\bar{3}$]
	[100]	[2 $\bar{1}$ $\bar{1}$ 0]
	[110]	[1 1 $\bar{2}$ 0]
	[11 $\bar{2}$]	[1 1 $\bar{2}$ $\bar{6}$]
	[$\bar{2}$ 10]	[1 0 $\bar{1}$ 0]

Tab. 4.2: Crystal planes and directions in the cubic and hexagonal systems.

For the pole figure scans, the sample normal has been tilted out of the measurement plane by the characteristic offset angle between the reflecting crystal planes and the substrate surface. Thus, it was possible to detect the AlN 101 reflection (offset 61.65°) as the most intense asymmetric reflection. For the precise determination of the AlN lattice constants and the linewidths of the symmetric AlN 002 reflections, diffractometry was also carried out in triple-axis configuration using a 3×Ge(220) channel-cut analyzing crystal with an angular

acceptance < 12 arcsec. Finally, for the investigation of the material morphology all samples have been imaged by atomic force microscopy.

4.2.1 Texture Analysis

Wide range $2\theta/\omega$ -scans of all samples were taken to check for a possible texture of the AlN films. Fig. 4.3 compiles the diffractograms recorded in double-axis configuration. For all substrates, including $C_\alpha(100)$, no reflections related to the cubic phase of AlN were observed, due to the considerably higher thermodynamic stability of wurtzite AlN compared to the cubic phase. A second general observation is that the symmetric AlN $00l$ reflections are the main features besides the characteristic substrate reflections, irrespective of the type and orientation of the substrate. Indeed, for cubic Si(111) and Si(100) substrates it is well known that wurtzite AlN structures preferably form with their c -axis oriented parallel to the substrate normal [335].

In detail, for the AlN/Al₂O₃(0001) reference sample, solely the symmetric AlN $00l$ reflections are observed in addition to the Al₂O₃ $00l$ substrate reflections, confirming the usual complete texture of the film with (0001) AlN || (0001) Al₂O₃. A similar behavior with texture (0001) AlN || (100) C_α is found for the C_α(100) substrate. However, a more precise investigation revealed that an angle of 3° separates both planes. Although the diamond substrate is cut off-axis with its [100] direction tilted from the surface normal by about 4° towards [011], the corresponding tilt is only about 1° for the [0001] direction of AlN. A similar effect with the AlN [0001] direction being oriented rather parallel to the substrate normal than to the [100] direction of the substrate was also observed for AlN films grown on off-axis Si(100) [348].

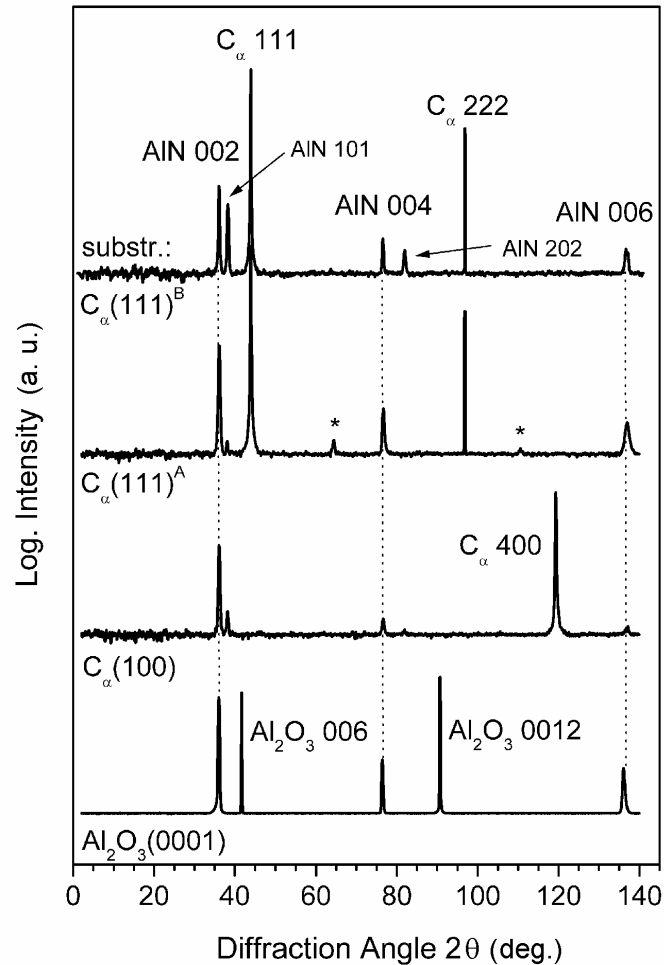


Fig. 4.3: Wide-range symmetric X-ray diffraction $2\theta/\omega$ -scans of different AlN/diamond as well as AlN/sapphire heterostructures, recorded in double-axis configuration using a 1° slit aperture.

Contrary to the Al_2O_3 substrate, for $\text{C}_\alpha(100)$ weak asymmetric AlN 101 and 202 reflections appear besides the AlN 00 l reflections and the C_α 400 substrate reflection. This could indicate a certain degree of polycrystallinity for the AlN layer. However, the corresponding AlN 100 reflection is not detected, although it should exhibit a similar intensity compared to the 101 reflection. Consequently, one has to conclude that the AlN 101 and 202 reflections rather represent a crystalline AlN phase with its $(10\bar{1}1)$ plane oriented parallel to the substrate surface. By comparing the peak intensities of the AlN 002 and 101 reflections, we can estimate a $(10\bar{1}1)$ -oriented crystal fraction of about 1% to be present in our AlN layers on $\text{C}_\alpha(100)$. Turning to the $\text{C}_\alpha(111)^A$ substrate, a preferential orientation with (0001)

AlN || (111) C_α is found also. The weak AlN 101 reflection again observed in addition to the symmetric AlN 00 l and the 111 substrate reflections indicates that about 0.2 % of the AlN layer material is (10 $\bar{1}$ 1)-oriented. Furthermore, the diffractogram exhibits an intense C_α 222 substrate reflection, which would normally be forbidden, but becomes visible, because the comparatively high boron doping level breaks the diamond crystal symmetry. Besides, there are some low intensity reflections (marked with an asterisk in Fig. 4.3) which we attribute to some boron carbide impurities or to some remaining Ti/Al metal used earlier for electrical contacts.

As expected, a similar behavior with (0001) AlN || (111) C_α is obtained for the $C_\alpha(111)^B$ substrate, too. However, in this case a pronounced fraction of about 20 % of the layer material is characterized by (10 $\bar{1}$ 1) AlN || (111) C_α indicating a two-phase structure in contrast to the $C_\alpha(111)^A$ sample. The reason for this noticeable deviation from c -axis oriented growth is not clear, but the local formation of (10 $\bar{1}$ 1)-oriented AlN might facilitate strain relaxation within the entire AlN film. AlN with orientations other than (0001) is known to form also on some special substrates. For example, the formation of (11 $\bar{2}$ 0)-oriented AlN has been reported for Si(100) substrates using a MnS buffer layer [349].

4.2.2 Epitaxial Relation: in-plane offset

For the determination of the epitaxial relationship between a crystalline film and a substrate, the in-plane orientation of both crystal lattices has to be known besides the crystal texture described above. Therefore, pole figures (ϕ -scans) of asymmetric AlN and substrate reflections were recorded by rotating the samples around their surface normal (Fig. 4.4).

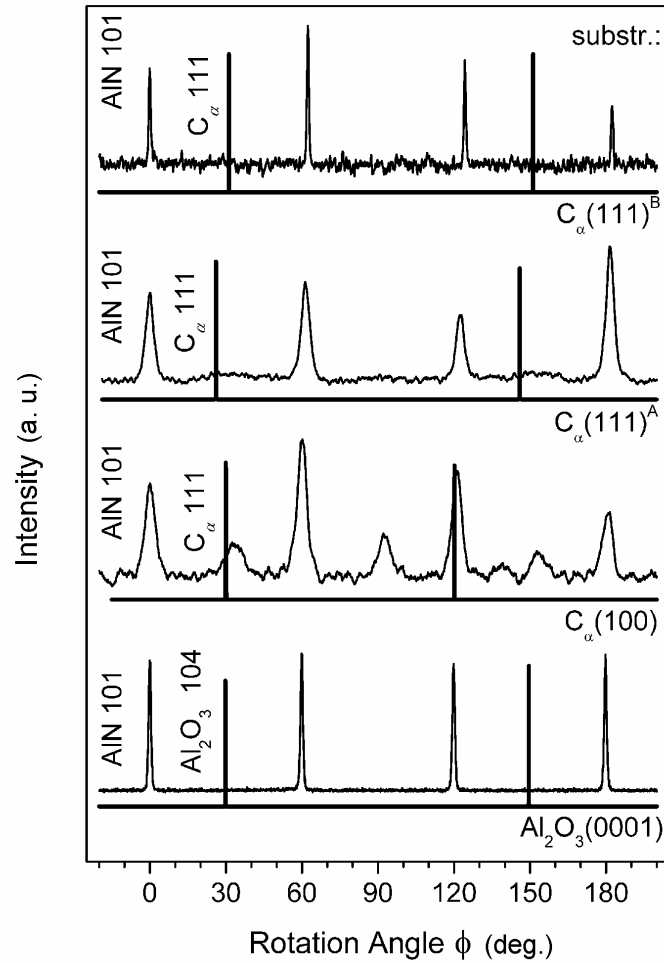


Fig. 4.4: X-ray diffraction pole figures (ϕ -scans) of the asymmetric AlN 101 reflections of different AlN/diamond and AlN/sapphire heterostructures compared to the corresponding asymmetric substrate reflections, *i.e.* C_α 111 and Al_2O_3 104 (slit aperture 1°).

Starting with the AlN/ Al_2O_3 reference sample, we find a 3-fold rotational symmetry of the substrate 104 reflection representing the trigonal crystal symmetry of sapphire. In contrast, for the 101 reflection of the AlN film, a 6-fold symmetry with an angular shift of 30° with respect to the substrate reflections is observed, which is the expected behavior of hexagonal wurtzite AlN. Thus, from the pole figures and the crystal texture, the well known epitaxial orientation relationship for AlN on *c*-plane sapphire [350] is confirmed as $(0001)[10\bar{1}0]$ AlN \parallel $(0001)[11\bar{2}0]$ Al_2O_3 . A closer inspection revealed a deviation of less than 0.1° for the in-plane orientation (twist) and 0.002° for the out-of-plane orientation (tilt), as listed in Table I. The quality of the in-plane orientation is also represented by the line width of the

AlN 101 ϕ -scan. For the AlN/Al₂O₃ heterostructure, a FWHM of 1.1° is obtained, which, however, has to be taken as an upper limit due to the 1° slit aperture used.

Turning to the C_α(100) substrate in Fig. 4.4, one finds the expected 4-fold symmetry of the asymmetric C_α 111 reflections. However, for the AlN film, we now obtain a 12- instead of a 6-fold symmetry with alternating high and low intensity reflections indicating the presence of a double-domain structure. Such a structure with the domains rotated by an angle of 30° or 90° with respect to each other has already been described for heteroepitaxial AlN layers on Si(100) and was found to depend on the degree of substrate miscut [348]. Indeed, due to the 4-fold symmetry of the (100) planes of the cubic C_α(100) and Si(100) substrates, both AlN domains would be equivalent in a first approximation if grown on an on-axis cut substrate, thus leading to a double-domain growth. Lebedev *et al.* explain the nucleation of these two AlN in-plane orientations on on-axis Si(100) by the different in-plane alignment of surface dangling bonds located on neighboring crystal terraces, which are separated by single atomic step boundaries. On the other hand, the same authors observe single-domain AlN forming on the double-stepped surface of substrates with an offcut > 5°, which they attribute to the uniform alignment of the surface dangling bonds in this case [348]. Accordingly, the formation of two differently marked AlN domains on C_α(100) can be explained by the lower substrate offcut of 4.3°, which is apparently not sufficient for the formation of a single-domain structure.

Comparing the angular positions of the AlN 101 and C_α 111 reflections, the epitaxial orientation relationship (0001)[10 $\bar{1}$ 0] AlN^I || (100)[011] C_α for the predominant AlN domains (type I) and (0001)[$\bar{1}$ 2 $\bar{1}$ 0] AlN^{II} || (100)[011] C_α for the other domains (type II) is obtained. Thus, the epitaxial relationship is identical to that of AlN on Si(100) [351], also shown by the schematic illustration of Fig. 4.5 a,b). However, with a tilt of about 3° and a twist of 1 and 3° for the two domains a small deviation from this relation is found for the C_α(100) substrate

(Tab. 4.1). In addition, with ϕ -scan line widths of about 4 and 9°, respectively, the degree of in-plane orientation is distinctly lower than for the reference film on sapphire.

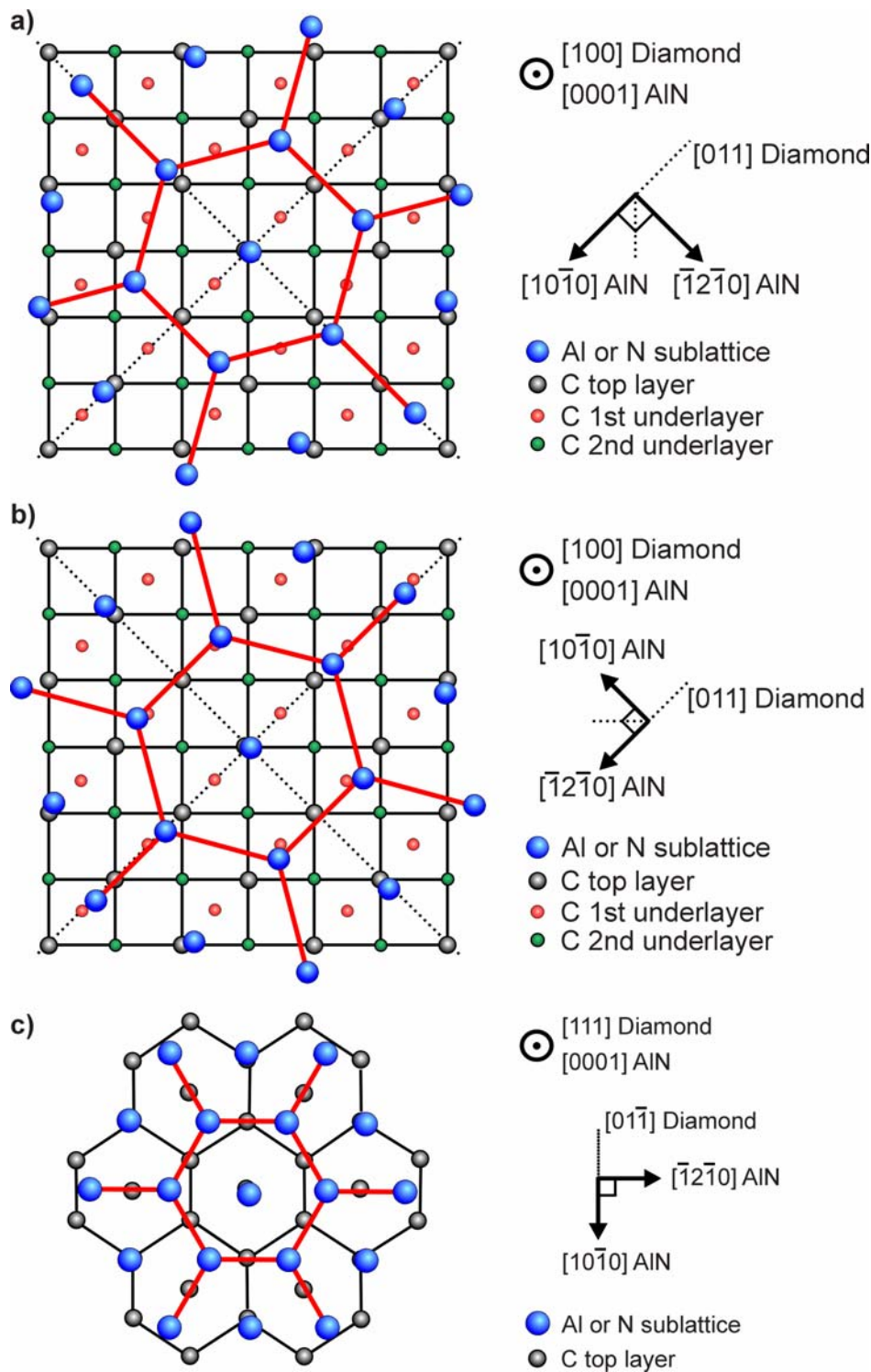


Fig. 4.5: Schematic illustration of the epitaxial in-plane orientation relationship of a,b) wurtzite-AlN/ $C_{\alpha}(100)$ and c) wurtzite-AlN/ $C_{\alpha}(111)$ heterostructures. For the diamond substrates the three carbon top layers are shown, whereas the AlN crystal is represented by a single plane of the constituent Al or N sublattice.

For the $C_\alpha(111)$ substrates, the symmetry of the asymmetric 111 reflections is 3-fold, with a 120° angular shift between two reflections. The AlN 101 reflections of both samples represent the expected 6-fold rotational symmetry as already observed for the sapphire substrate, which in particular means a single-domain structure for the AlN/ $C_\alpha(111)$ heterostructures. The 30° angular shift between the AlN 101 and the C_α 111 reflections leads to the epitaxial orientation relationship $(0001)[10\bar{1}0]$ AlN \parallel $(111)[01\bar{1}]$ C_α as illustrated in Fig. 4.5c). This result means a different behavior, *i.e.* a 30° rotation of the AlN basal plane, compared to the relation $(0001)[2\bar{1}\bar{1}0]$ AlN \parallel $(111)[01\bar{1}]$ Si found for AlN grown on Si(111) [352]. To our knowledge, the only publication about epitaxial growth of AlN on $C_\alpha(111)$ reported the epitaxial relationship $(0001)[11\bar{2}0]$ AlN \parallel $(111)[110]$ C_α [249]. Assuming that $[110]$ C_α in this relation shall represent the $[1\bar{1}0]$ or $[\bar{1}10]$ directions of diamond, a similar discrepancy with a 30° rotation of the AlN basal plane compared to our data is found also.

Despite the marked substrate miscut, both AlN/ $C_\alpha(111)$ heterostructures solely exhibit a deviation of $< 0.2^\circ$ (tilt) from this relation contrary to the AlN/ $C_\alpha(100)$ heterostructure. However, with less than 1 and about 6° , respectively, the in-plane deviation (twist) differs significantly between samples $C_\alpha(111)^B$ and $C_\alpha(111)^A$. The same holds for the ϕ -scan line widths as well. Here, with 3.3° sample $C_\alpha(111)^A$ shows a FWHM three times larger than sample $C_\alpha(111)^B$ (0.9°). Again, the latter value has to be taken as an upper limit due to the 1° slit aperture used. Possible reasons for the different behavior of both samples will be discussed below.

4.2.3 Relaxation and Film Quality

For the determination of the lattice constants of the different AlN films, the 002 and 105 reflections have been measured by HRXRD in triple-axis configuration. The results are also compiled in Tab. 4.1. With respect to the relaxed bulk AlN lattice parameters of $a = 3.1106 \text{ \AA}$ and $c = 4.9795 \text{ \AA}$ [6], the absolute residual strain of all AlN films studied is found to be less than 0.3 %. Therefore, compared to the nominal lattice mismatch of about – 13 % for the AlN/C $_{\alpha}$ (100) and 23 % for the AlN/C $_{\alpha}$ (111) heterostructure, the films are almost completely relaxed.

In general, the line width of an XRD reflection provides information about the quality and structure of the crystal investigated. For a symmetric reflection of a crystalline film, the line width of a $2\theta/\omega$ -scan is mainly characterized by a limited coherence length perpendicular to the substrate surface and by a heterogeneous strain contribution caused by the strain fields around crystal dislocations. Neglecting the latter, a minimum coherence length L_{\perp} can be derived from the line width $\Delta 2\theta$ by Scherrer's equation $L_{\perp} = 0.94 \lambda / (\Delta 2\theta \times \cos\theta)$, with λ the wavelength of X-rays and $\Delta 2\theta$ the line width in radians [353]. On the other hand, an ω -scan of a symmetric reflection may be broadened by a limited coherence length parallel to the substrate surface and by the tilt of the constituent single crystallites forming the film. Neglecting the tilt contribution, a minimum coherence length parallel to the substrate surface L_{\parallel} can be calculated from the line width $\Delta\omega$ by a modified Scherrer equation $L_{\parallel} = 0.94 \lambda / (\Delta\omega \times \sin\theta)$, with $\Delta\omega$ the line width in radians.

Fig. 4.6 compiles the ω - and $2\theta/\omega$ -scans of the symmetric AlN 002 reflection for all samples investigated. The resulting line widths and coherence lengths are also listed in Tab. 4.1. For the AlN/Al $_2$ O $_3$ heterostructure, the line widths are $\Delta\omega = 0.5^\circ$ and $\Delta 2\theta = 0.05^\circ$, representing a columnar crystal structure with a higher vertical coherence length of about

180 nm, corresponding to one third of the entire film thickness of 500 nm (see Tab. 4.1). The line width values are larger than generally obtained for AlN on sapphire ($0.03 < \Delta\omega < 0.07^\circ$) [263]. However, this result is not surprising, since the growth conditions used here have not been optimized for sapphire substrates. In particular no nucleation layer has been applied.

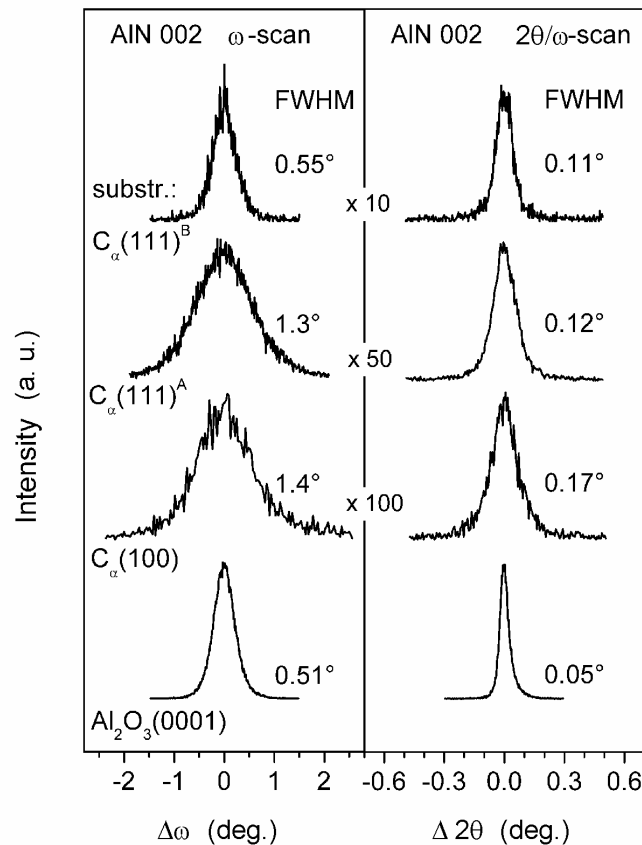


Fig. 4.6: Normalized X-ray diffraction ω - and $2\theta/\omega$ -scans of the symmetric AlN 002 reflection of different AlN/diamond and AlN/sapphire heterostructures, recorded in triple-axis configuration.

For the AlN/ $C_\alpha(100)$ heterostructure we have observed line widths about three times larger than for the sapphire reference sample, for both the $2\theta/\omega$ - (0.17°) and the ω -scan (1.36°). This corresponds to a reduced coherence length or increased crystallite tilt. However, the crystalline quality is still surprisingly high compared to *e.g.* AlN/Si(100) heterostructures with a FWHM of the $2\theta/\omega$ -scan of 0.54° reported for a 500 nm thick AlN layer [351]. This is rather remarkable considering the significantly different lattice constants ($\Delta a = 15\%$) and

thermal expansion coefficients ($\Delta\alpha = 70\%$) of AlN and diamond, as well as the fact that no intentional buffer or nucleation layer has been grown prior to AlN epitaxy.

A similar result with a comparable $\Delta\omega$ value of 1.3° and a reduced $\Delta 2\theta$ value of 0.12° is obtained for the AlN/ $C_\alpha(111)^A$ sample, confirming that high quality epitaxial growth is feasible for both substrate orientations. Moreover, with 0.55° an even lower line width $\Delta\omega$ is found for sample AlN/ $C_\alpha(111)^B$, which compares well with XRD data of MBE-AlN grown directly on Si(111) [354], and with the AlN/sapphire reference sample (0.51°). Since the $\Delta 2\theta$ line width (0.1°) is merely about two times larger than on sapphire, a comparable crystal quality for both the sapphire and the $C_\alpha(111)^B$ substrate can be expected.

Complementary to the structural analysis presented, the HRXRD data in Fig. 4.7 show a reciprocal space maps (RSM) of symmetric 002 and asymmetric 105 reflections for the epitaxial AlN:Si layer grown on (100) boron doped diamond substrate.

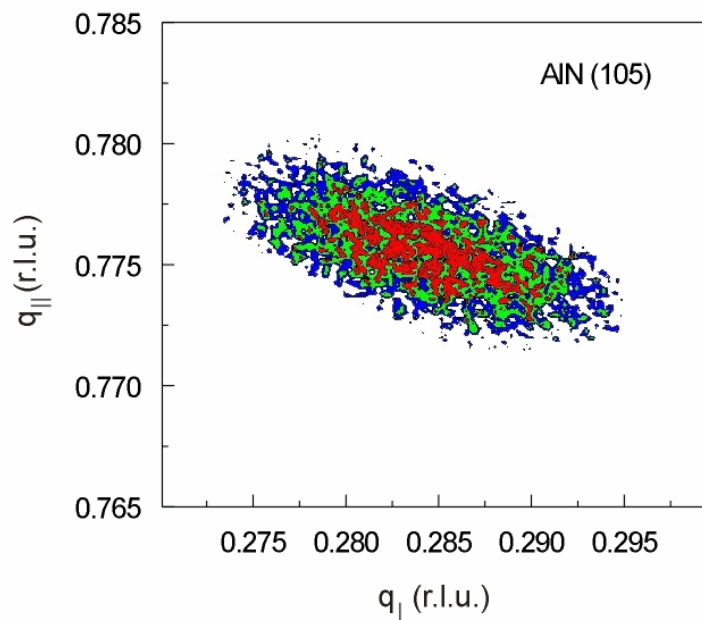


Fig. 4.7: HRXRD reciprocal space map showing the AlN 105 reflection of the AlN heteroepitaxial film on diamond (100) substrate. The reciprocal scattering vector (q) is inversely proportional to the lattice constant parameter of the crystal and is given in relative lattice units.

From triple-axis measurements of the AlN 002 and 105 reflections (Fig. 4.7) the lattice constants $a_{\text{AlN}} = 3.113 \text{ \AA}$ and $c_{\text{AlN}} = 4.970 \text{ \AA}$ are determined representing almost complete layer relaxation compared to bulk material ($a_{\text{AlN}} = 3.112 \text{ \AA}$, $c_{\text{AlN}} = 4.982 \text{ \AA}$ [355]). This corresponds to a biaxial tensile strain of 6.9×10^{-3} or tensile stress of 3.18 GPa perpendicular to the growth direction. Indeed, cracking was observed on the AlN epilayer of 500 nm thickness. In contrast, the film was intact in the regions with thickness of less than ~ 200 nm, close to the borders of the diamond substrate. The more pronounced peak-broadening parallel to the a -axis (q_{\parallel}) in Fig. 4.7 reflects a columnar growth character of the AlN:Si film, with a coherence length perpendicular to the crystal surface larger than parallel to it. The tilting of the ellipse towards the q_{\parallel} axis may be due to a small degree of mosaicity of the AlN crystallites.

4.2.4 Surface Morphology

For morphological characterization, all samples have been investigated by AFM as shown in Fig. 4.8 to Fig. 4.10. Before growth, the surface roughness of the different diamond samples was between 0.5 and 0.7 nm (rms), as exemplarily shown for $C_{\alpha}(100)$ in the micrograph of Fig. 4.8. For the AlN/Al₂O₃ heterostructure, a grainy film surface with an rms roughness value of 3.2 nm is observed, indicating a columnar growth character. In fact, MBE growth of group III nitrides on sapphire without an AlN nucleation layer generally leads to the formation of N-face polarity material with its typical columnar layer structure and rougher surface morphology [69].

From the corresponding AFM micrograph of Fig. 4.9 a), a column diameter of about 50 nm can be derived, which is in good agreement with the lateral coherence length of 53 nm

calculated from the XRD ω -scan of the AlN 002 reflection as discussed above (Tab. 4.1). This result, on the other hand, means that no relevant tilt between the single columns contributes to the XRD line width in this case, and that these columns are single crystalline in the lateral direction.

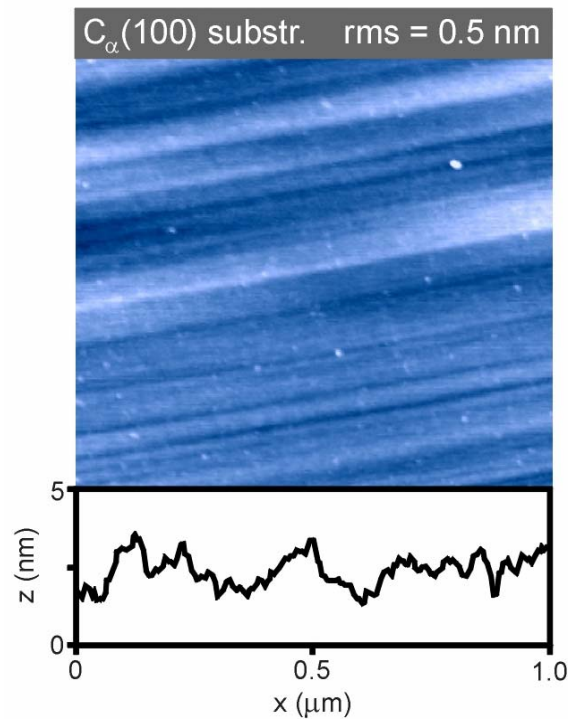


Fig. 4.8: Surface of the diamond (100) substrate prior to overgrowth.

A different behavior is found for the AlN/C_α(100) sample. Here, a smaller rms value of 1.9 nm and a larger column diameter of about 80 nm are observed by AFM (Fig. 4.9 b). However, with only 20 nm, the lateral coherence length deduced from XRD is significantly smaller. Therefore, assuming that the columns are single crystalline as well, the major contribution to the XRD 002 ω -scan width has to be caused by the tilt between the single columns and not by a limited coherence length as for the AlN/Al₂O₃ heterostructure.

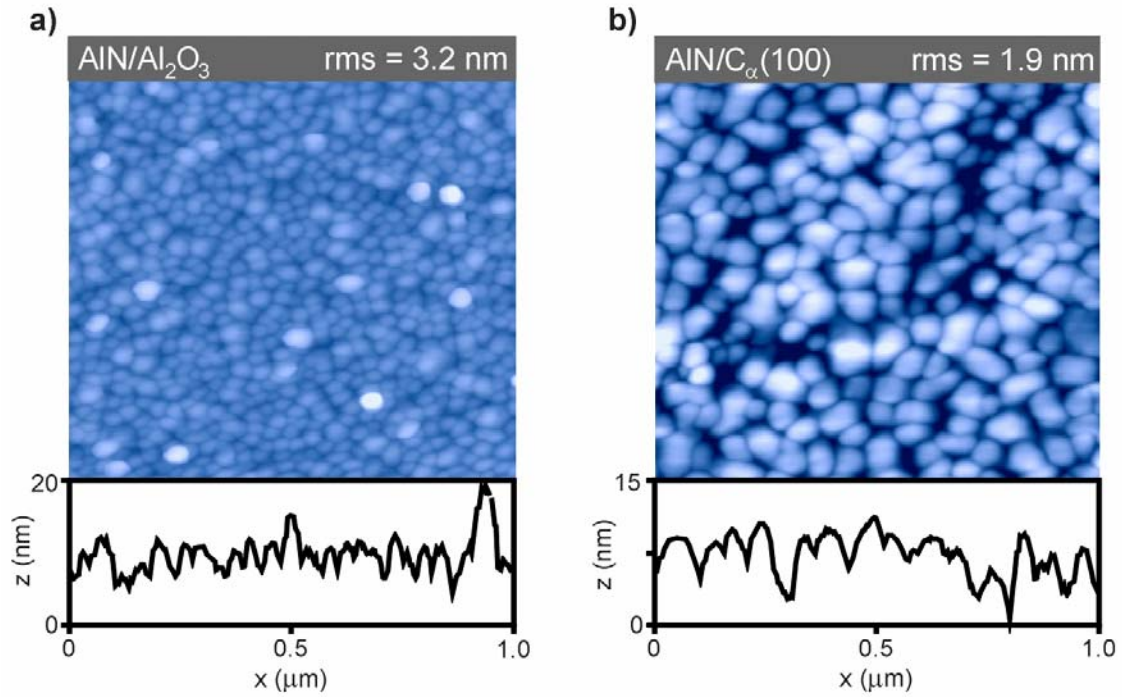


Fig. 4.9: AFM micrographs of 500 nm thick epitaxial AlN films grown on a) sapphire (0001) and on b) diamond (100).

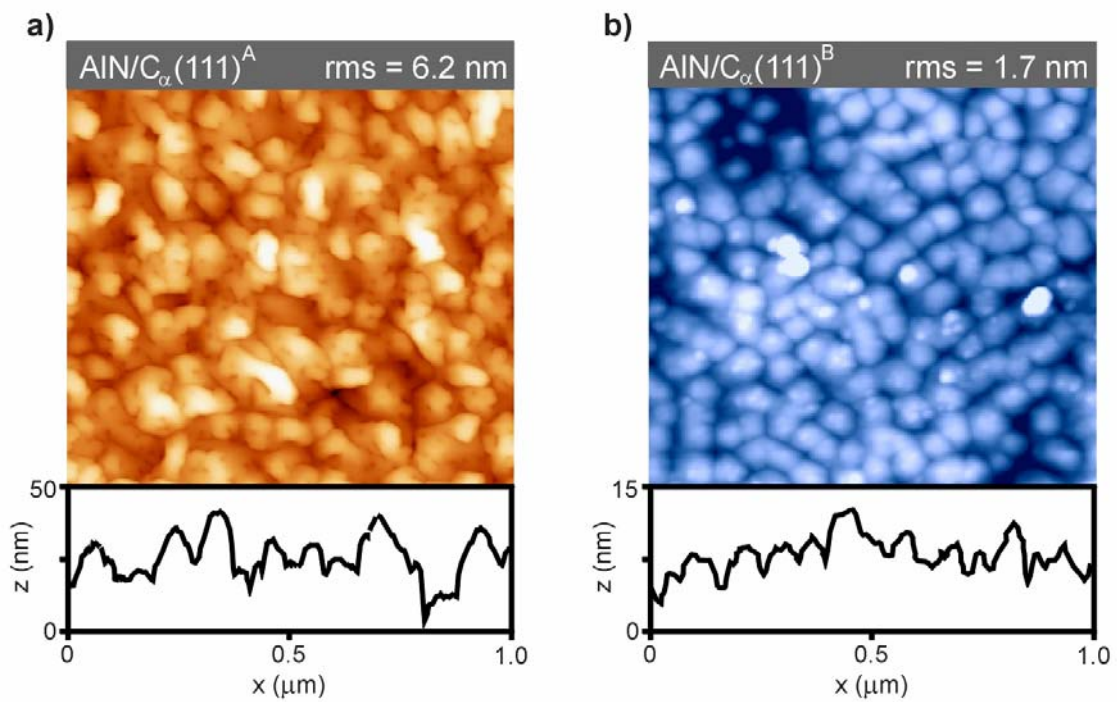


Fig. 4.10: AFM micrographs of 500 nm thick epitaxial AlN films grown on two different diamond substrates with (111) crystallographic orientation.

The same argument also holds for the AlN/C $_{\alpha}$ (111)^A heterostructure (Fig. 4.10 a). Again, the coherence length of 21 nm calculated from XRD does not correlate with the AFM column diameter of about 80 nm, so that crystallite tilt mainly has to cause the XRD line width. Compared to the morphology of the AlN/C $_{\alpha}$ (100) sample, the crystal columns are not as well separated and shaped in this case, suggesting a generally lower crystal quality for this sample, which is confirmed by the distinctly higher rms roughness value of 6.2 nm.

In contrast, for the AlN/C $_{\alpha}$ (111)^B sample, with an rms value of 1.7 nm and a column diameter of about 80 nm, we observe a surface morphology very similar to the AlN/C $_{\alpha}$ (100) heterostructure (Fig. 4.10 b). However, with 49 nm the XRD coherence length does fit much better to the AFM column diameter, indicating a markedly lower tilt between the crystallite columns and, therefore, a better crystal quality in this case.

From the upper results, high quality epitaxial growth of AlN is obtained for both diamond (111) and (100) substrates. As expected, the crystal quality of AlN/C $_{\alpha}$ (111) is generally higher than that of AlN/C $_{\alpha}$ (100), since the trigonal/hexagonal symmetry of the (111) diamond surface matches the symmetry of wurtzite AlN. However, a different behavior is found for the two types of (111)-oriented diamond substrates. Compared to the AlN/C $_{\alpha}$ (111)^A heterostructure, the AlN films on C $_{\alpha}$ (111)^B show a more distinct in-plane orientation as well as a better crystalline quality and surface roughness. On the other hand, with about 20 %, a significantly higher fraction of (10 $\bar{1}$ 1)-oriented AlN is observed for the C $_{\alpha}$ (111)^B substrate. Since the growth conditions were similar for both types of samples, the differences are obviously caused by the substrate quality. Indeed, with a boron concentration of 10²⁰ cm⁻³, the C $_{\alpha}$ (111)^A substrate is very highly doped compared to the C $_{\alpha}$ (111)^B substrate only containing 10¹⁸ to 10¹⁹ cm⁻³ of boron. Moreover, the high doping level of C $_{\alpha}$ (111)^A was achieved by ion implantation followed by an anneal step, whereas C $_{\alpha}$ (111)^B was *in-situ* doped during diamond CVD-overgrowth. Thus, it is not surprising that the crystalline quality of the C $_{\alpha}$ (111)^A

substrate is lower than that of $C_{\alpha}(111)^B$. In fact, with 0.01° the rocking curve line width $\Delta\omega$ of the 111 reflection of $C_{\alpha}(111)^A$ is by a factor of four higher than that of $C_{\alpha}(111)^B$.

The observation of such high quality heteroepitaxial growth of AlN on diamond (111) and (100) is surprising at first sight, since the absolute lattice mismatch of about 23 and 13 %, respectively, is much too high for conventional epitaxy. However, as has been pointed out for a variety of highly mismatched heterostructures, high quality films can be grown as well by the formation of crystal domains matching integral multiples of major crystal planes between substrate and film (domain matching epitaxy) [356]. According to this theory, systematic variations of the domain sizes additionally can accommodate residual strain falling between the integral multiples. Since the critical thickness is less than a few monolayers for the large misfits discussed here, the dislocations needed for lattice relaxation are created directly at the interface, whereas a relaxed film with a comparatively low dislocation density can form upon.

4.3 AlN/Diamond Heterojunction Diode

In this section, we describe the successful attempt to combine n-type AlN with p-type diamond (100) to obtain a heterojunction bipolar p-n diode. Already this first attempt has led to surprisingly good structural quality of the AlN, a good diode characteristics, and efficient light emission in the blue and ultraviolet. The AlN deposition was performed at a growth rate of $0.18 \mu\text{m/h}$ and a substrate temperature of 815°C , which is an adequate temperature for growing good quality MBE-AlN on sapphire.

The particular electronic properties of p-diamond and n-AlN are summarized in Fig. 4.11. We have used the published optical and electronic properties of AlN (electron affinity $\chi_{\text{AlN}} = 0.3 \text{ eV}$ [357], band gap $E_{\text{g AlN}} = 6.2 \text{ eV}$, silicon donor level $E_{\text{D}}(\text{Si}) = 320 \text{ meV}$ below

the conduction band [335]) and of diamond ($\chi_D = 0.5$ eV [358], $E_{g \text{ diam.}} = 5.47$ eV, boron acceptor level $E_A(B) = 360$ meV above the valence band edge). A hetero-epitaxial growth of n-AlN on p-diamond can reasonably be expected to lead to a wide band gap p-n heterojunction. However, to our knowledge no high quality AlN/diamond heterojunction has been reported so far.

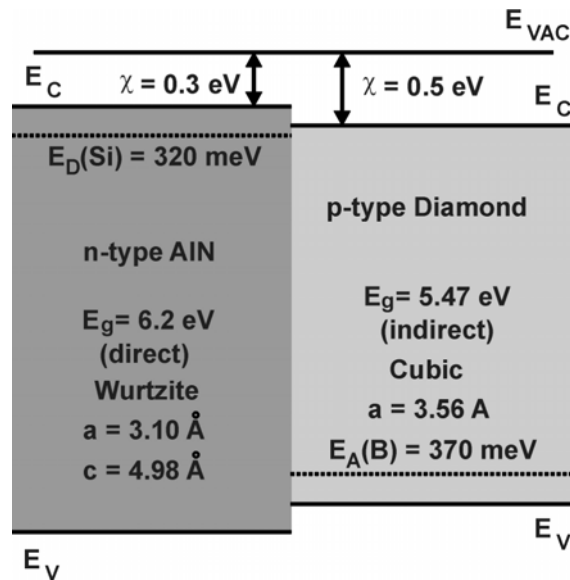


Fig. 4.11: Schematic sketches of the band diagrams of n-AlN and p-diamond.

MBE-grown AlN can be doped n-type by silicon, which creates a DX-like donor level 320 meV below the conduction band [335]. From AlN:Si calibration runs on sapphire we estimate the silicon concentration in the deposited film to about 10^{19} cm^{-3} . The diamond substrate was characterized by Hall effect measurements at room temperature. The boron concentration of about 10^{17} cm^{-3} leads to a free hole concentration of $8.5 \times 10^{13} \text{ cm}^{-3}$, with a mobility of $850 \text{ cm}^2/\text{Vs}$.

In order to study the optoelectronic properties of the p-n heterojunction, ohmic Ti/Al contacts (20 nm/100 nm) were evaporated on both sides of the sample. Circular contacts with a diameter of 150 μm on the AlN:Si side and 300 μm on the backside of the boron doped diamond were used. The metal deposition was followed by a thermal anneal for 5 minutes in N_2+H_2 atmosphere at 500°C . Fig. 4.12 shows the room-temperature current-voltage (I - V)

characteristics of the p-n heterojunction with a clear rectifying behavior. A diode ideality factor of 3 is calculated.

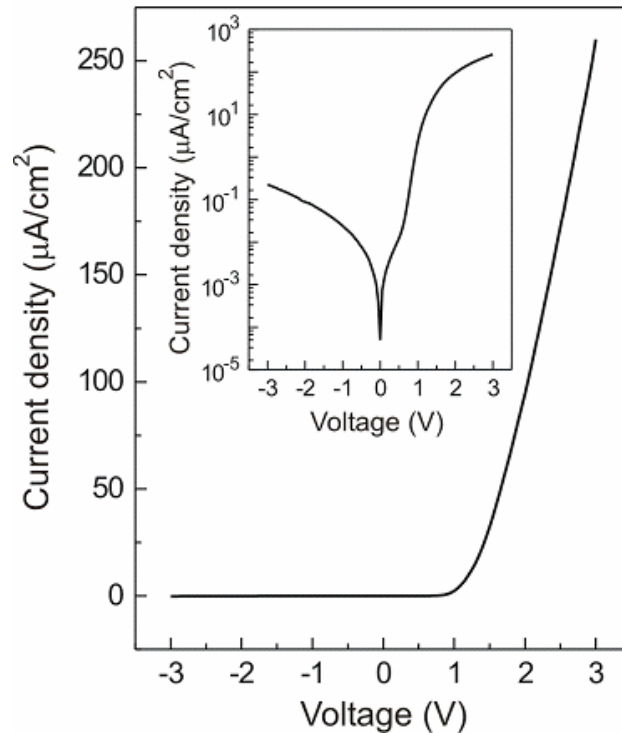


Fig. 4.12: Current voltage characteristics of an AlN/diamond p-n heterojunction at room temperature. The IV -curve can be simulated with a diode ideality factor $n = 3$, a series resistance R_s of $\approx 1 \text{ M}\Omega$, and a bias-dependent parallel resistance R_p of (20-70) $\text{G}\Omega$.

The high leakage current in reverse direction indicates a significant amount of structural defects at the AlN/diamond interface. Device isolation by mesa etching should result in a significant reduction of the leakage current. A large series resistance is limiting the forward current density to $250 \text{ }\mu\text{A}/\text{cm}^2$ at 3V . This can be improved by higher doping levels and/or different contact geometries. No breakdown could be measured by applying a maximum reverse bias of 90 V . The toughness of the device was also evident under forward polarization. With an applied voltage of about 70 V and a current of 100 mA flowing through the microscopic contact area, the heat generation in the device brought the ceramic socket to temperatures much higher than 300°C . Nevertheless, beside a small increase in the reverse leakage current, no degradation of the characteristic of the diode was observed.

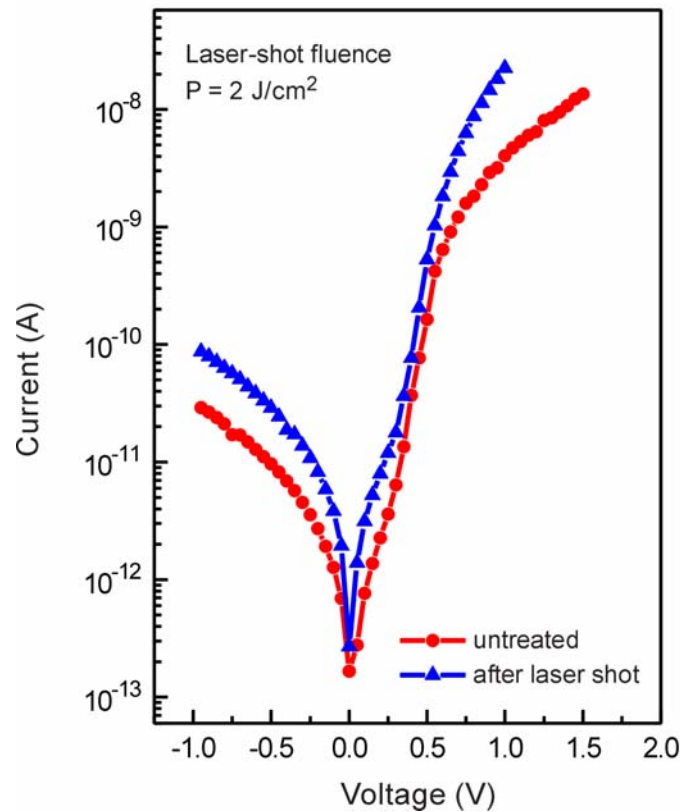


Fig. 4.13: Effect of laser processing on the *I**V*-characteristic of the heterodiode.

The contacts on the AlN:Si surface were in addition thermally treated with Excimer laser shots to improve the ohmic behavior and to ameliorate the electrical conductivity on the very resistive n-type AlN layer. The short laser pulse of about 30 ns and the wavelength of 193 nm allow very high power fluencies resulting in an ultra-fast increase of temperature in the shot area. The effect of this ultra-fast annealing procedure on the electrical characteristics of the diode is shown in Fig. 4.13. Despite the increased reverse leakage current, there is a significant drop of the series resistance in forward bias from 43 to 14 M Ω , confirming the improvement of the electrical contact on top of the AlN film. There was no considerable change in the ideality factor of the processed diode.

The built-in voltage (V_{bi}) is a relevant parameter of a p-n junction. It indicates the height of the potential barrier for electrons and holes formed at the physical junction, and is directly

related to the structural interface characteristics. Fig. 4.14 a) shows a schematic representation of the band alignment for the n-AlN on p-diamond.

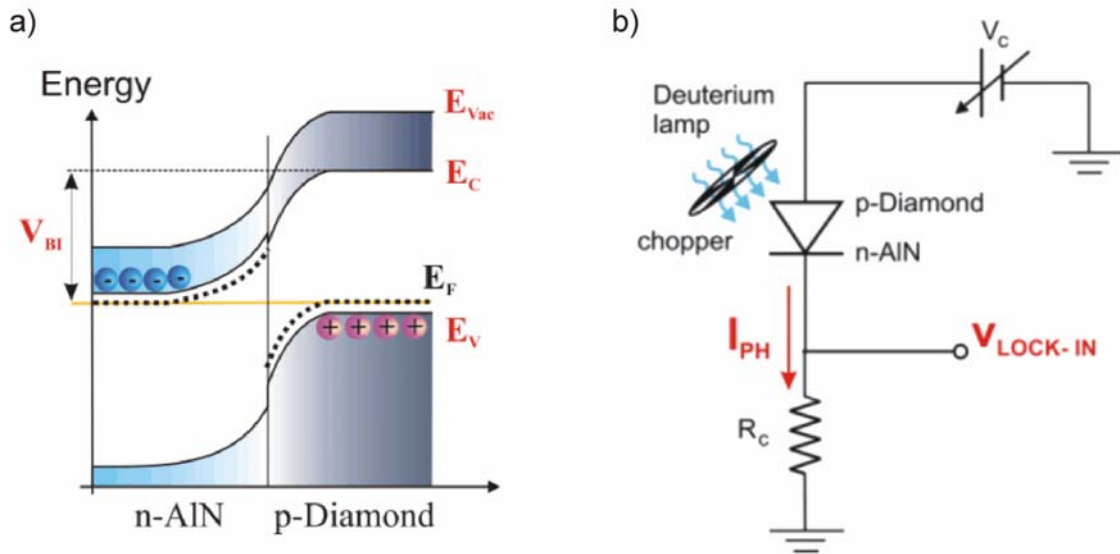


Fig. 4.14: a) Schematic representation of the AlN/diamond heterojunction in the ideal case. b) circuit used for the determination of the built-in voltage in the n-AlN/p-diamond diode.

Different from the case of lower band gap semiconductors, the very high resistivity of the AlN film with its deep Si donor doping level does not allow capacitance methods to be applied for the determination of the built-in potential in the n-AlN/p-diamond heterostructure. Instead, the built-in voltage was determined under UV-light illumination. The light-induced carrier generation and resulting band-bending cause a shift of the I - V curve to positive voltage as observed in Fig. 4.14 a). By measuring the junction in the circuit configuration shown in Fig. 4.14 b), the compensating potential V_c necessary to cancel the generated photocurrent can be interpreted as the effective V_{bi} of the heterodiode. The diode equation under illumination can be written as:

$$I_D = I_S [\exp(e \cdot V / n k \cdot T) - 1] - I_{ph} \quad \text{Eq. (4.1)}$$

where I_S is the saturation current of the diode, n is the non-ideality factor ($n = 1$ for an ideal diode), and I_{ph} is the photocurrent. With the diode under illumination ($I_{ph} \neq 0$), the positive voltage, V_c , compensates the built-in potential, V_{bi} , forcing $I_D \rightarrow 0$.

To perform these measurements, Ti/Pt/Au (20 nm/10 nm/200 nm) was deposited on two different regions of the sample with 500 nm and 250 nm thick AlN, respectively. The contacts on the AlN:Si surface were also laser annealed to improve the electrical contact to the very resistive n-type AlN layer. Two different measurement configurations were used. In the first approach (Fig. 4.14 b), the AlN:Si film (250 nm thick) was illuminated with chopped light of a Deuterium-lamp (UV range from 190 nm to 385 nm). The corresponding photocurrent was measured with a lock-in amplifier and cancelled by a compensating potential, V_c in Fig. 4.14 b). As shown in Fig. 4.15, a V_{bi} value of about 0.85 V was determined for a maximum power fluence of $0.5 \mu\text{J}/\text{cm}^2$ of the Deuterium lamp.

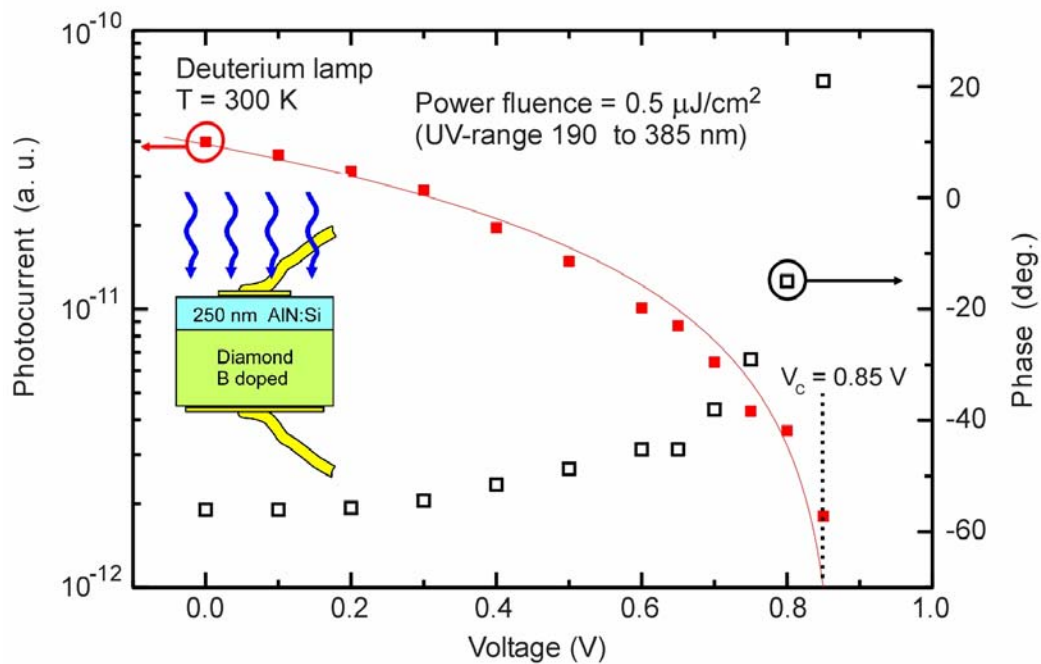


Fig. 4.15: Generated photocurrent vs. applied voltage in the n-AlN/p-diamond heterostructure under Deuterium-lamp illumination.

In a second approach, the Deuterium lamp was replaced by a pulsed Excimer laser and the open circuit photo-voltage was measured directly by an oscilloscope. Much higher power fluences can be produced with a pulsed Excimer-laser. A laser wavelength of 193 nm (6.42 eV), above the band gap of AlN (6.2 eV) was chosen to illuminate the diode from the n-type side. The energy density reaching the heterointerface can be calculated from the

absorption coefficient of $2 \times 10^5 \text{ cm}^{-1}$ for AlN at 193 nm [359]. For an incident laser intensity of 2.0 J/cm^2 , only 13.3 mJ/cm^2 will reach the interface after traversing the 250 nm thick AlN film region.

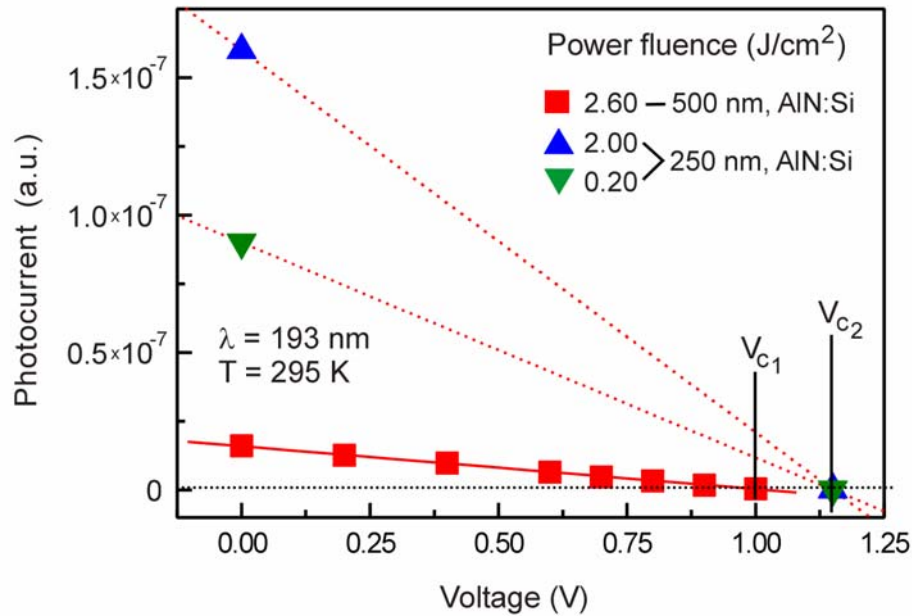


Fig. 4.16: Photocurrent vs. applied voltage under pulsed Excimer-laser illumination at 193 nm. Compensation voltages: $V_{c1} = 1.0 \text{ V}$, $V_{c2} = 1.15 \text{ V}$.

In Fig. 4.16 is shown that a maximum V_{bi} value of 1.15 V is obtained for the 250 nm thick AlN:Si film region by irradiating the diode with 0.2 J/cm^2 , with effectively 1.3 mJ/cm^2 reaching the heterointerface. By irradiating the diode with an energy fluence as high as 2 J/cm^2 , the same maximum voltage value of 1.15 V was needed to compensate the current flow. The power fluence dependence to V_{bi} can be clearly observed by comparing the two illuminated regions with 250 and 500 nm thick AlN film. For an initial power fluence of 2.6 J/cm^2 and an AlN film thickness of 500 nm, the effective energy of $120 \mu\text{J/cm}^2$ at the heterointerface is not sufficient to cause the maximum shift in the I - V characteristic, and already $V_c = 1 \text{ V}$ is sufficient to cancel the generated photocurrent (Fig. 4.16).

The measurements could be reproducibly repeated at several prepared contacts and corroborated also the results obtained with Deuterium lamp illumination. For the wide band gap materials, AlN and diamond, one would expect a higher value for the built-in voltage.

Nevertheless, the performance is limited by the large concentration of defects present in the vicinity of the heterointerface and affecting the diode depletion layer.

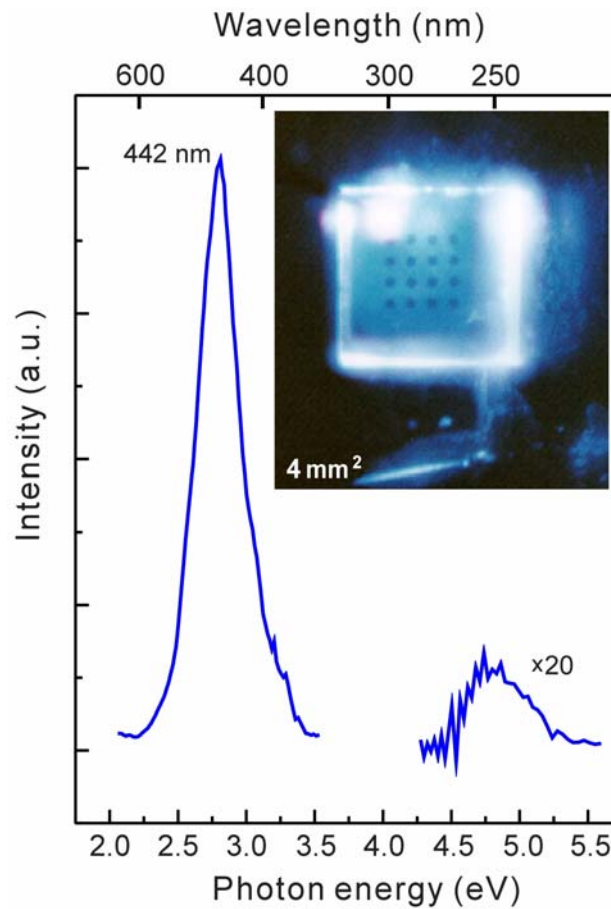


Fig. 4.17: Electroluminescence emission spectra of a AlN/diamond p-n heterojunction biased in forward direction with a current density of 12.7 A/cm^2 . The inset shows the blue light emission of the LED. Current is injected only through the small ohmic contact at the top right of the AlN layer and at the backside of the diamond substrate.

Electroluminescence (EL) measurements were done at room temperature using a double-grating monochromator with a focal length of 800 mm and a photomultiplier. The typical EL emission spectrum of the AlN/diamond (100) diode is presented in Fig. 4.17. The inset shows the bright blue emission emerging from the entire $2 \times 2 \text{ mm}^2$ sample. Because of the large refractive index of diamond ($n = 2.41$) the light is mainly coupled out at the edges of the sample. We obtain a strong EL peak centered on 442 nm (2.7 eV), with a FWHM of about 250 meV. This emission was also observed in cathodoluminescence measurements of AlN

and is caused by a defect-related transition. A second emission peak is observed in the ultraviolet at 4.8 eV, with a FWHM of 600 meV. Its intensity is about 1% of the emission at 2.7 eV. At the present stage we have no reliable information concerning the origin of the UV-emission. However, both the UV and the blue light emission were only detected under forward bias of the diode, pointing to an electron-hole recombination process close to the interface. The presence of defects at the heterojunction interface will also allow tunneling assisted recombination processes, which is also suggested by the diode ideality factor of 3 [122].

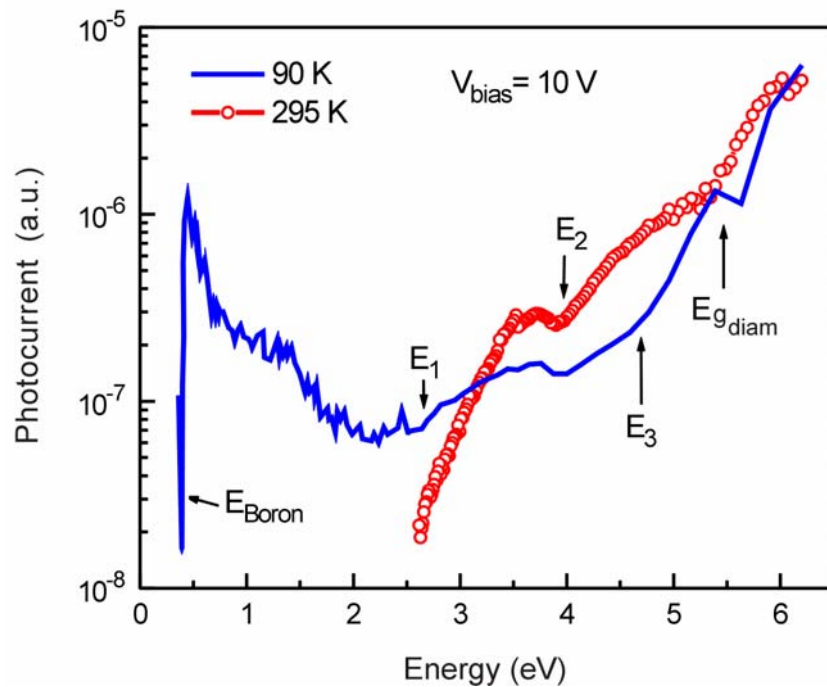


Fig. 4.18: Spectrally resolved photoconductivity of the p-n AlN/diamond heterojunction.

So far, no information is available about the AlN/diamond interface. Spectrally resolved photoconductivity measurements can give further hints to understand the electroluminescence emission of the diode. In Fig. 4.18 the photocurrent spectra of the heterodiode with forward biasing at 295 K and 90 K are shown. The absorption edges at 2.5 eV and 4 eV, labeled E_1 and E_2 , were associated with defects in the AlN layer. For comparison, Fig. 4.19 shows the photocurrent spectra of the Si doped PIMBE-AlN film grown on sapphire (see Tab. 4.1) and

the bare boron doped diamond (100) substrate. The photoconductivity curve of the n-AlN film on insulating sapphire also shows the absorption levels E_1 and E_2 . E_1 is probably related to oxygen impurities in the crystal lattice, whereas aluminum vacancies have been suggested to absorb at E_2 [263].

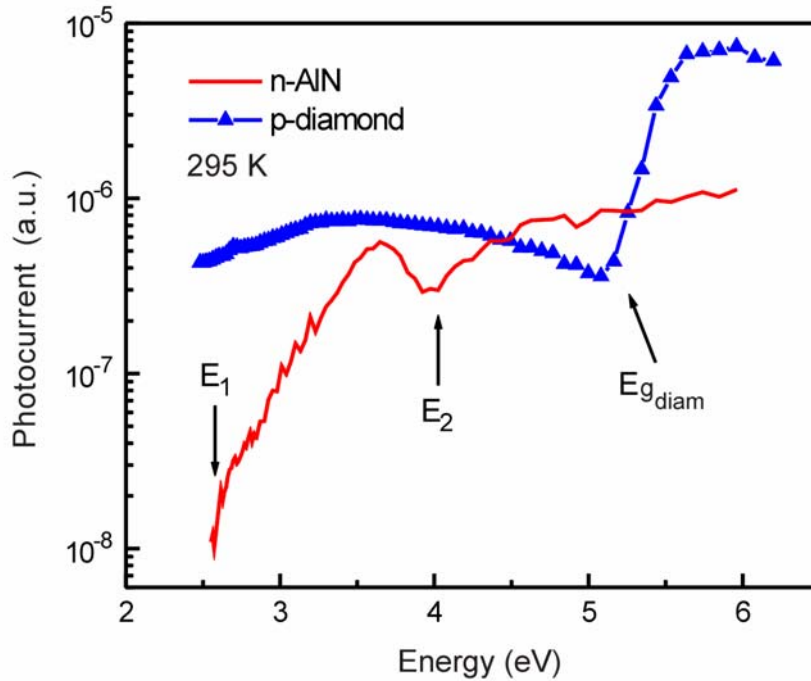


Fig. 4.19: Spectrally resolved photoconductivity: a) boron doped diamond (100) substrate prior to AlN epitaxy; b) Si doped MBE-AlN reference film grown on sapphire.

The oxygen related level E_1 could be responsible for the blue light emission observed at 2.75 eV (Fig. 4.17). A third level E_3 at about 4.7 eV was identified, which is present neither in the n-AlN film on sapphire nor in the p-diamond substrate photocurrent spectra (Fig. 4.19). This could indicate its origin at the heterojunction interface, probably related to a defect transition. The UV-electroluminescence emission observed at 4.8 eV (Fig. 4.17) is likely related to this defect center, but the transition mechanism is not clear yet.

4.4 Concluding Remarks and Outlook

In summary, epitaxial wurtzite (0001) AlN:Si (n-type) has been successfully grown on (100) naturally boron doped diamond (p-type) substrates by PIMBE. The structural quality of the AlN film has been assessed by high resolution X-ray diffraction. It is surprisingly good, in spite of the absence of an intentional buffer layer and the mismatch of both the lattice constants ($\Delta a = 15\%$) and the thermal expansion coefficients ($\Delta\alpha = 70\%$). The fabricated p-n heterojunction diodes show clear diode characteristics with rectifying ratios between 10^3 and 10^4 at low voltages. Under forward bias, an intense light emission in the blue (2.7eV) and UV (4.8 eV) is obtained. The morphological characterization discussed in section 4.2.4 showed a relatively smooth surface profile with rms roughness of 1.9 nm and columnar structure shape. Spectrally resolved photoconductivity measurements suggested that the blue light emission of the heterodiode in the AlN layer is due to oxygen impurities and that the UV-emission is related to recombination at the interface and not in the AlN film or diamond substrate. The built-in voltage of lower than 1.15 V measured under Excimer laser illumination is in agreement with the presence of a recombination center at the heterointerface. Further work is necessary for the identification of the defect centers and recombination mechanism for an improvement of the light emission efficiency in the UV. Additionally, at this stage it was not possible to identify the polarity of the AlN film on top of the diamond substrates. A mixture of both Al- and N-face (many inversion domain boundaries) is quite probable, considering the surface morphology of the AlN films. However, the results clearly confirm the viability of heteroepitaxial growth of III-nitrides on diamond, thereby opening interesting perspectives for future optoelectronic devices operating in the far UV. There are still many opportunities for the optimization of all fabrication steps, such as growth parameters, AlN and diamond doping levels, contacts and device technology.

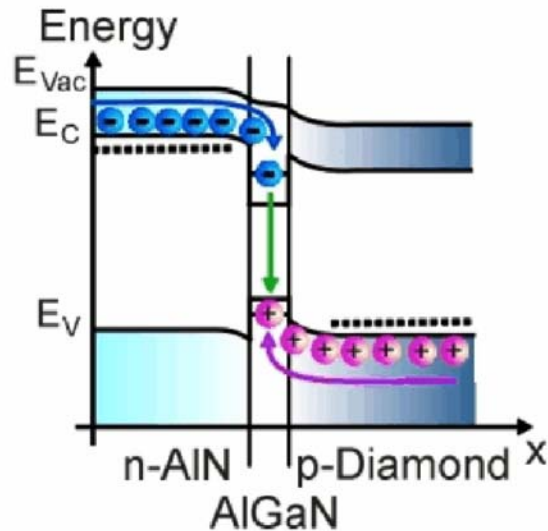


Fig. 4.20: Schematic view of an AlGaN/diamond based laser structure with an active AlGaN quantum well (QW). The wavelength of the stimulated emission can be controlled by the Al-concentration of the well.

Group-III-nitrides allow the preparation of heterostructures with variable band gaps and offsets within the same material system. A challenge for future activities is to combine this convenient band gap engineering capability with the advantages of heteroepitaxy on diamond for the fabrication of stable and efficient ultraviolet light emitting diodes and lasers. Heterostructures with AlGaN quantum wells (Fig. 4.20) should enable spontaneous and maybe even stimulated emission of photons with energies between 3.4 and 5.5 eV, giving rise to efficient and tunable UV-light sources suitable for UV-lithography or for sensor applications.

Most importantly, further work has to be done to investigate the role of the crystal polarity of the nitride film on the interfacial structure and on the electrical properties of the heterojunction. Similarly to epitaxy of GaN on sapphire, the MBE parameters at the initial growth state could be adapted to modify the atomic interface dipole at the diamond surface, enabling crystal polarity control of the subsequent AlGaN film. This may be achieved with the deposition of a very thin Al-layer on top of H-terminated diamond or through nitridation

of the diamond surface in a N-plasma. In group-III nitrides the intrinsic pyroelectricity will strongly influence the electronic configuration of the heterojunction besides the surface dipole effect. The atomic sequence at the AlN/diamond interface with the corresponding dipoles is illustrated in Fig. 4.21 considering the two different polarities of AlN.

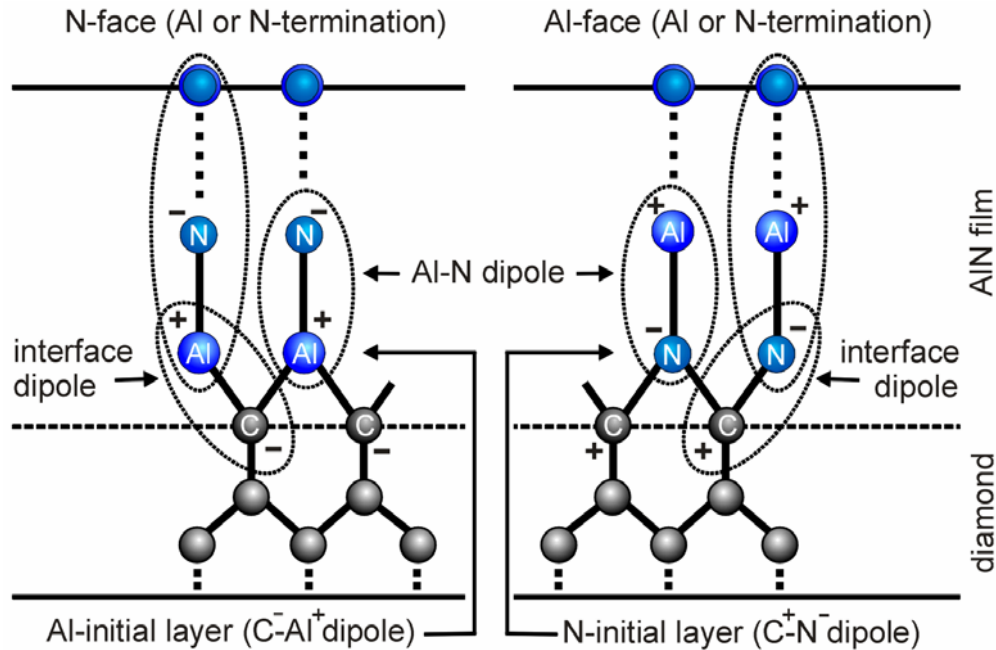


Fig. 4.21: Schematic illustration of the atomic sequence at the AlN/diamond heterointerface from different initial layers.

Regarding technical issues, in order to facilitate and improve the quality of epitaxial growth, p-type diamond substrates with outstanding structural quality and atomically smooth surfaces are desirable. For future investigations, the structure to be deposited directly onto the p-type diamond substrate would consist of an active intrinsic region plus an n-type contact. The active region would be either a single quantum well (SQW) or a multiple quantum well structure (MQW). The SQW structure would consist of an AlGa_xN (AlInGa_xN) well embedded within higher Al-content AlGa_xN (AlInGa_xN) barriers. The MQW structure would be formed from a repetition of the SQW structure.

The optimization of the active region on diamond is one of the challenges. The quality of this region is critical for both the performance of the light emitting device and the growth of

the rest of the structure. Thus, a systematic study of the effect of different growth conditions (growth rate, growth temperature and III/V flux ratio) on the active region characteristics should be performed. Atomic force microscopy, transmission electron microscopy (TEM) and X-ray diffraction are necessary to determine the structural properties of the heterostructure. The optical quality of the active region can be assessed by temperature-dependent photoluminescence (PL). The efficiency and peak wavelength of the emission would provide information about the behavior of the structure as an emitter and could be used for reference in the optimization procedure. The objective is to optimize layers with emission up to 5.47 eV, the band gap of diamond.

Another issue is to optimize the structural and electrical quality of silicon-doped AlGaN contact with high-Al-content. Different Al-contents and thicknesses have to be investigated. Different growth conditions should be used to optimize both, the crystal quality and doping efficiency.

In conclusion, for the near future one can reasonably expect a demonstration of the reliability of nitride-based deep UV emitters on p-type diamond substrates and a further enhancement of the performance of these emitters.

5 Summary

The amazing challenge of group-III nitrides in basic physics but also in technological applications seems to be unlimited. No other material has the potential to change the world which we know, see and hear, in the near future, as much as GaN and related alloys. The paradigm change has already started, with electric light giving place to electronic light slowly, similar to the replacement of candles, oil- and gas lamps by light bulbs. But this is not all, there is much more. To explore a small fraction of these possibilities and the ensuing problems is the aim of this thesis.

In the GaN-based thin-film technology, the commonly used substrate materials have very different material properties than to the device layer itself. The commercial success of GaN-based devices has brought a change in the conventional thinking about the material requirements for device fabrication. In contrast to the majority of commercially available semiconductors, commercialization of GaN-based devices was achieved exclusively by using heteroepitaxial substrates. As a result, GaN and its related materials are currently being produced with a surprisingly high density of dislocations, approximately four orders or magnitude higher than the minimum which was thought to be required for efficient luminescence. However, none of these drawbacks have limited the success of GaN-based light emitters from the visible to the ultraviolet spectral range. For device production on an industrial scale, the substrate of choice has to fulfill a number of criteria, such as a minimum size (2"), atomically flat surfaces and availability in large quantities at an acceptable price. Due to its wide availability and relatively low cost, sapphire was and still is the most common choice for GaN-based light-emitting diodes (LEDs). However, several of the properties of sapphire, such as its large lattice constant and the mismatch of the thermal expansion coefficient with GaN, are seemingly unsuitable according to the usual assumptions made in

choosing a substrate for epitaxy. As a consequence, the choice of sapphire introduces important limits on the final quality of the epitaxial film despite its versatility in the GaN-based processing technology. Thus, commercial exploitation of other potential applications of GaN, such as laser diodes operating at high power densities and high mobility transistors, with more critical material requirements than LEDs have been hindered due to, for instance, the high density of dislocations.

However, heteroepitaxy has been the only alternative for GaN growth up to date, since bulk wafers are still not commercially available. The properties and quality of the GaN film are primarily dependent on the substrate on which it is deposited, which determines the crystal orientation, polarity, surface morphology, strain, and the defect concentration of the GaN. Many different materials have been investigated for GaN epitaxy including metal oxides, metal nitrides, and other semiconductors, although the results have been discouraging so far.

To fully exploit the large application potential of group-III-nitrides, it is desirable to employ epitaxial growth on lattice-matched substrates. The capability to produce superior material quality by homoepitaxial growth of GaN on GaN bulk crystals or bulk-like substrates has already been demonstrated. A reduction of dislocation densities by six orders of magnitude, higher carrier mobilities and narrower photoluminescence line widths in comparison to the usual heteroepitaxial growth were obtained. Two-dimensional step-flow growth of GaN can be achieved by homoepitaxial growth without the need for additional deposition steps such as surface nitridation, low temperature nucleation films, or thick buffer layers. Laser cavities can be fabricated with cleaved facets instead by time-consuming reactive ion etching processes, which also produce defects on the crystal surface. In addition, a significant simplification in device processing and circuit integration can be easily introduced by choosing the proper n- or p-type doping of the GaN substrate. Thus, the promise of a better material quality achievable using homoepitaxial growth has concentrated

research on methods of producing GaN and AlN bulk crystals. But also much work was focused on the production of large and thick GaN and AlN freestanding films to be used as pseudosubstrates in the group III nitride-based epitaxy.

In this thesis we have discussed the material properties of GaN and its epitaxy on sapphire, SiC, Si, GaAs, or LiGaO₂. Special attention was given to the production of freestanding GaN pseudo-substrates. The remarkable optical and structural properties resulting from GaN homoepitaxy on such substrates have been demonstrated. A laser liftoff technique has been optimized for the delamination of GaN films with thickness ranging from a few micrometers up to 120 μm , and the effect of laser ablation on the surface of irradiated GaN and sapphire has been investigated. Furthermore, the flexibility of laser-induced liftoff was demonstrated in the processing of thin InGaN/GaN heterostructures for the production of freestanding flip-chip bonded blue/violet LEDs. A thermal transport model has been developed to simulate the effect of the sudden temperature rise during a laser pulse during the high power laser processing.

An alternative to bulk crystals are bulk-like thick GaN films produced by hydride vapour phase epitaxy (HVPE). Freestanding high quality GaN substrates as large as 2" in diameter and 300 μm thickness, obtained by applying the laser-induced liftoff process to HVPE GaN are suitable as substrates for nitride homoepitaxy after careful pretreatment of the Ga-face surface. This was confirmed by homoepitaxial growth of 2 μm thick GaN films by MOCVD. The good electrical and optical characteristics of the homoepitaxial layers establish freestanding HVPE-GaN as an attractive substrate for the fabrication of GaN-based devices. Motivated by these successes of the laser induced liftoff technique, several companies are presently incorporating this technology for the large scale production of freestanding GaN substrates and flip-chip bonded GaN-based devices.

Besides the GaN issue, diamond has been evaluated as a possible substrate material for group III nitrides epitaxy because it represents a novel approach for the development of a new

generation of devices for deep UV-light emission and high power applications. The intense attention in deep UV emitters is due to a vast array of potential applications, such as white light generation (U-LEDs coated with three-band phosphor), high-density optical storage devices, lithography instruments, and chemical processes in both medical applications and waste processing.

In this thesis we have investigated the growth of epitaxial wurtzite (0001) AlN:Si (n-type) on (100) naturally boron doped diamond (p-type) substrates by PIMBE. The surprisingly good structural quality of the AlN film has been assessed by high resolution X-ray diffraction. p-diamond/n-AlN heterojunction diodes have been successfully fabricated, showing clear diode characteristics with rectifying ratios between 10^3 and 10^4 at low voltages. Under forward bias light emission in the blue and UV is obtained. The presence of interface defects have been assessed by studying optical (photocurrent experiments) and electronic (built-in voltage analysis) properties of the p-n heterojunction.

The obtained results clearly confirm the viability of heteroepitaxial growth of III-nitrides on diamond, thereby opening interesting perspectives for future optoelectronic devices operating in the deep UV.

References

- [1] S. Nakamura, *Semicond. Sci. Technol.* 14 (1999) R27.
- [2] F.A. Ponce, in: B. Gil (Ed.), *Group III Nitride Semiconductor Compounds*, Oxford University Press, Oxford, 1998, p. 123.
- [3] R.R. Reeber, K. Wang, *Mater. Res. Soc. Symp.* 622 (2000) T6.35.1.
- [4] D.P. Xu, Y.T. Wang, H. Yang, S.F. Li, D.G. Zhao, Y. Fu, S.M. Zhang, R.H. Wu, Q.J. Jia, W.L. Zheng, X.M. Jiang, *J. Appl. Phys.* 88 (2000) 3762.
- [5] P. E. Van Camp, V. E. Van Doren, J. T. Devreese, *Solid State Commun.* 82 (1992) 23.
- [6] M. Tanaka, S. Nakahata, K. Sogabe, H. Nakata, M. Tobioka, *Jpn. J. Appl. Phys.* 36 (1997) L1062.
- [7] S. Okubo, N. Shibata, T. Saito, Y. Ikuhara, *J. Cryst. Growth* 189/190 (1998) 452.
- [8] H. Okumura, H. Hamaguchi, T. Koizumi, K. Balakrishnan, Y. Ishida, M. Arita, S. Chichibu, H. Nakanishi, T. Nagatomo, S. Yoshida, *J. Cryst. Growth* 189/190 (1998) 390.
- [9] V. Pankov, M. Evstigneev, R. H. Prince, *Appl. Phys. Lett.* 80 (2002) 4142.
- [10] E.S. Hellman, D.N.E. Buchanan, D. Wiesmann, I. Brener, *MRS Internet J. Nitride Semicond. Res.* 1 (1996) 16.
- [11] F. Hamdani, M. Yeadon, D.J. Smith, H. Tang, W. Kim, A. Salvador, A.E. Botchkarev, J.M. Gibson, A.Y. Polyakov, M. Skowronski, H. Morkoç, *J. Appl. Phys.* 83 (1998) 983.
- [12] G.L. Harris, in: G.L. Harris (Ed.), *Properties of Silicon Carbide*, Inspec/IEE, 1995, p. 4.
- [13] Kh.S. Bagdasarov, E.R. Dobrovinskaya, V.V. Pishchik, M.M. Chernik, Yu. Yu, A.S. Gershun, I.F. Zvyagintseva, *Sov. Phys. Crystallogr.* 18 (1973) 242.
- [14] G. Davies, *Properties and Growth of Diamond*, INSPEC, IEE, 1994, London.
- [15] P.M. Dryburgh, *J. Mater. Sci. Mater. Electron.* 9 (1998) 237.
- [16] J. C. Brice, in: M.R. Brozel, G.E. Stillman (Eds.), *Properties of Gallium Arsenide*, 3rd Edition, Inspec/IEE, 1996, p. 8.
- [17] Y. Xin, P.D. Brown, R.E. Dunin-Borkowski, C.J. Humphreys, T.S. Cheng, C.T. Foxon, *J. Cryst. Growth* 171 (1997) 321.
- [18] V.Yu. Davydov, I.N. Goncharuk, A.N. Smirnov, R.V. Zolotareva, A.V. Subashiev, T.S. Cheng, C.T. Foxon, *J. Cryst. Growth* 189/190 (1998) 430.
- [19] Y. Okada, in: Robert Hull (Ed.), *Properties of Crystalline Silicon*, IEE, London, 1999.
- [20] H. Morkoç, S. Strite, G. B. Gao, M. E. Lin, B. Sverdlov, M. Burns, *J. Apply. Phys.* 76 (1994) 1363
- [21] L.M. Belyaev, *Ruby and Sapphire*, Amerind Publishing Co., New Delhi (translated from Russian, RUBIN I SAPFIR, Nauka Publishers, Moscow, 1974), 1980.
- [22] M.T. Duffy, C.C. Wang, G.D. O'Clock, S.H. McFarlane, P.J. Zanzhchi, *J. Electron. Mater.* 2 (1973) 359.

- [23] S. Nakamura, M. Senoh, S. Nagahama, N. Iwasa, T. Yamada, T. Matsushita, H. Kiyoku, Y. Sugimoto, *Appl. Phys. Lett.* 68 (1996) 2105.
- [24] H. Ohsato, T. Kato, S. Koketsu, R.D. Saxena, T. Okuda, *J. Cryst. Growth* 189/190 (1998) 202.
- [25] J.R. Heffelfinger, D.L. Medlin, K.F. McCarty, *J. Mater. Res.* 13 (1998) 1414.
- [26] C.J. Rawn, J. Chaudhuri, *J. Cryst. Growth* 225 (2001) 214.
- [27] E.S. Hellman, Z. Liliental-Weber, D.N.E. Buchanan, *MRS Internet J. Nitride Semicond. Res.* 2 (1997) 30.
- [28] C. Klemenz, H.J. Scheel, *J. Cryst. Growth* 211 (2000) 62.
- [29] P. Waltereit, O. Brandt, M. Ramsteiner, R. Uecker, P. Reiche, K.H. Ploog, *J. Cryst. Growth* 218 (2000) 143.
- [30] H. Okazaki, A. Arakawa, T. Asahi, O. Oda, K. Aiki, *Solid-State Electron.* 41 (1997) 263.
- [31] C. Fechtmann, V. Kirchner, S. Einfeldt, H. Heinke, D. Hommel, T. Lukasiewicz, Z. Luczynski, J. Baranowski, *Mater. Res. Soc. Symp. Proc.* 482 (1997) 295.
- [32] V.V. Mamutin, S.V. Sorokin, V.N. Jmerik, T.V. Shubina, V.V. Ratnikov, S.V. Ivanov, P.S. Kop'ev, M. Karlsteen, U. Södervall, M. Willander, *J. Cryst. Growth* 201/202 (1999) 346.
- [33] E.S. Hellman, C.D. Brandle, L.F. Schneemeyer, D. Wiesmann, I. Brener, T. Siegrist, G.W. Berkstresser, D.N.E. Buchanan, E.H. Hartford Jr., *Mater. Res. Soc. Symp. Proc.* 395 (1996) 51.
- [34] E.S. Hellman, C.D. Brandle, L.F. Schneemeyer, D. Wiesmann, I. Brener, T. Siegrist, G.W. Berkstresser, D.N.E. Buchanan, E.H. Hartford, *MRS Internet J. Nitride Semicond. Res.* 1 (1996) 1.
- [35] A. Yoshikawa, V.V. Kochurikhin, N. Futagawa, K. Shimamura, T. Fukuda, *J. Cryst. Growth* 204 (1999) 302.
- [36] A. Yamada, K.P. Ho, T. Akaogi, T. Maruyama, K. Akimoto, *J. Cryst. Growth* 201/202 (1999) 332.
- [37] A. Yamada, K.P. Ho, T. Maruyama, K. Akimoto, *Appl. Phys. A* 69 (1999) 89.
- [38] J.J. Lee, Y.S. Park, C.S. Yang, H.S. Kim, K.H. Kim, K.Y. Yang, T.W. Kang, S.H. Park, J.Y. Lee, *J. Cryst. Growth* 213 (2000) 33.
- [39] J. Ohta, H. Fujioka, H. Takahashi, M. Oshima, *phys. stat. sol. (a)* 188 (2001) 487.
- [40] R. Beresford, K.S. Stevens, C. Briant, R. Rai, D.C. Paine, *Mater. Res. Soc. Symp. Proc.* 395 (1996) 55.
- [41] R. Beresford, D.C. Paine, C.L. Briant, *J. Cryst. Growth* 178 (1997) 189.
- [42] S.D. Wolter, B.P. Luther, S.E. Mohney, R.F. Karliceck Jr., R.S. Kern, *Electrochem. Solid-State Lett.* 2 (1999) 151.
- [43] R. Kaplan, S.M. Prokes, S.C. Binari, G. Kelner, *Appl. Phys. Lett.* 68 (1996) 3248.
- [44] F. Perjeru, X. Bai, M.I. Ortiz-Libreros, R. Higgins, M.E. Kordesch, *Appl. Surf. Sci.* 175/176 (2001) 490.

- [45] M.I. Kotelyanski, I.M. Kotelyanski, V.B. Kravchenko, *Technol. Phys. Lett.* 26 (2000) 163.
- [46] S. Ruvimov, Z. Liliental-Weber, J. Washburn, K.J. Duxstad, E.E. Haller, Z.-F. Fan, S.N. Mohammad, W. Kim, A.E. Botchkarev, H. Morkoç, *Mater. Res. Soc. Symp. Proc.* 423 (1996) 201.
- [47] P. Ruterana, G. Nouet, Th. Kehagias, Ph. Komninou, Th. Karakostas, M.A. di Forte Poisson, F. Huet, *Mater. Res. Soc. Symp. Proc.* 595 (2000) W11.75.
- [48] L.T. Romano, in: J.H. Edgar, S.S. Strite, I. Akasaki, H. Amano (Eds.), *Properties, Processing and Applications of Gallium Nitride and Related Semiconductors*, INSPEC, The Institution of Electrical Engineers, Stevenage, UK, 1999, p. 209.
- [49] J.E. Northrup, L.T. Romano, in: J.H. Edgar, S.S. Strite, I. Akasaki, H. Amano (Eds.), *Properties, Processing and Applications of Gallium Nitride and Related Semiconductors*, INSPEC, The Institution of Electrical Engineers, Stevenage, UK, 1999, p. 213.
- [50] T. Suski, J. Jun, M. Leszczyski, H. Teisseyre, S. Strite, A. Rockett, A. Pelzmann, M. Kamp, K.J. Ebeling, *J. Appl. Phys.* 84 (1998) 1155.
- [51] H. Amano, M. Iwaya, T. Kashima, M. Katsuragawa, I. Akasaki, J. Han, S. Hearne, J.A. Floro, E. Chason, J. Figiel, *Jpn. J. Appl. Phys.* 37 (1998) L1540.
- [52] B. Beaumont, Ph. Venneures, P. Gibart, *phys. stat. sol. (b)* 227 (2001) 1.
- [53] T.S. Zheleva, S.A. Smith, D.B. Thomson, K.J. Linthicum, P. Rajagopal, R.F. Davis, *J. Electron. Mater.* 28 (1999) L5.
- [54] H. Lahreche, P. Venneures, B. Beaumont, P. Gibart, *J. Cryst. Growth* 205 (1999) 245.
- [55] C.I.H. Ashby, C.C. Mitchell, J. Han, N.A. Missert, P.P. Provencio, D.M. Follstaedt, G.M. Peake, L. Griego, *Appl. Phys. Lett.* 77 (2000) 3233.
- [56] T. Detchprohm, M. Yano, S. Sano, R. Nakamura, S. Mociiduki, T. Nakamura, H. Amano, I. Akasaki, *Jpn. J. Appl. Phys.* 40 (2001) L16.
- [57] S. Porowski, Grzegory, in: J.H. Edgar (Ed.), *Properties of Group III Nitrides*, INSPEC, The Institution of Electrical Engineers, Stevenage, UK, 1994, p. 76.
- [58] D.I. Florescu, V.M. Asnin, F.H. Pollak, A.M. Jones, J.C. Ramer, M.J. Schurman, I. Ferguson, *Appl. Phys. Lett.* 77 (2000) 1464.
- [59] S. Krukowski, M. Leszcynski, S. Porowski, in: J.H. Edgar, S.S. Strite, I. Akasaki, H. Amano (Eds.), *Properties, Processing and Applications of Gallium Nitride and Related Semiconductors*, INSPEC, The Institution of Electrical Engineers, Stevenage, UK, 1999, p. 21.
- [60] S.O. Kucheyev, J.E. Bradby, J.S. Williams, C. Jagasish, M. Toth, M.R. Phillips, M.V. Swain, *Appl. Phys. Lett.* 77 (2000) 3373.
- [61] I. Yonenaga, K. Motoki, *J. Appl. Phys.* 90 (2001) 6539.
- [62] I. Yonenaga, T. Hoshi, A. Usui, *Jpn. J. Appl. Phys.* 39 (2000) L200.
- [63] M. Leroux, B. Gil, in: J.H. Edgar, S.S. Strite, I. Akasaki, H. Amano (Eds.), *Properties, Processing and Applications of Gallium Nitride and Related Semiconductors*, INSPEC, The Institution of Electrical Engineers, Stevenage, UK, 1999, p. 45.
- [64] D.C. Look, J.R. Sizelove, *Appl. Phys. Lett.* 79 (2001) 1133.

- [65] U. Kaufmann, P. Schlotter, H. Obloh, K. Kohler, M. Maier, *Phys. Rev. B* 62 (2000) 10867.
- [66] D. Doppalapudi, T.D. Moustakas, in: H.S. Nalwa (Ed.), *Handbook of Thin Film Materials*, Vol. 4, 2002, p. 57.
- [67] O. Ambacher, R. Dimitrov, M. Stutzmann, B.E. Foutz, M.J. Murphy, J.A. Smart, J.R. Shealy, N.G. Weimann, K. Chu, M. Chumbes, B. Green, A.J. Sierakowski, W.J. Schaff, L.F. Eastman, *phys. stat. sol. (b)* 216 (1999) 381.
- [68] E.T. Yu, X.Z. Dang, P.M. Asbeck, S.S. Lau, G.J. Sullivan, *J. Vac. Sci. Technol. B* 17 (1999) 1742.
- [69] R. Dimitrov, M. Murphy, J. Smart, W. Schaff, J.R. Sealy, L.F. Eastman, O. Ambacher, M. Stutzmann, *J. Appl. Phys.* 87 (2000) 3375.
- [70] M.A. Khan, J.W. Yang, G. Simin, R. Gaska, M.S. Shur, A.D. Bykhovski, *Appl. Phys. Lett.* 75 (1999) 2806.
- [71] G. Tamulaitis, K. Kazlauskas, S. Jursenas, A. Zukauskas, M.A. Khan, J.W. Yang, J. Zhang, G. Simin, M.S. Shur, R. Gaska, *Appl. Phys. Lett.* 77 (2000) 2136.
- [72] E.S. Hellman, *MRS Internet J. Nitride Semicond. Res.* 3 (1998) 11.
- [73] H.P. Maruskas, J.J. Tietjen, *Appl. Phys. Lett.* 15 (1969) 327.
- [74] S. Kaiser, H. Preis, W. Gebhardt, O. Ambacher, H. Angerer, M. Stutzmann, A. Rosenauer, D. Gerthsen, *Japan. J. Appl. Phys.* 37 (1998) 84
- [75] K. Hiramatsu, T. Detchprohm, I. Akasaki, *Jpn. J. Appl. Phys., Part 2* 32 (1993) L1528.
- [76] E.V. Etzkorn, D.R. Clarke, *J. Appl. L. Liu, J.H. Edgar, Mater. Sci. Eng. R37* (2002) 119
- [77] W.E. Lee, K.P.D. Lagerlof, *J. Electron. Microsc. Technol.* 2 (1985) 247.
- [78] J.H. Edgar, C.H. Wei, D.T. Smith, T.J. Kistenmacher, W.A. Bryden, *J. Mater. Sci. Mater. Electron.* 8 (1997) 307
- [79] O. Ambacher, *J. Phys. D: Appl. Phys.* 31 (1998) 2653.
- [80] C.R. Eddy, Jr., T.D. Moustakas, J. Scanlon, *J. Appl. Phys.* 73 (1993) 448.
- [81] T. Lei, K. F. Ludwig, Jr., T. Moustakas, *J. Appl. Phys.* 74 (1993) 4430.
- [82] S. Nakamura, M. Senoh, S. Nagahama, N. Iwasa, T. Yamada, T. Matsushita, H. Kiyoku, Y. Sugimoto, *Jpn. J. Appl. Phys.* 35 (1996) L217.
- [83] T. Shibata, Y. Hori, K. Asai, Y. Nakamura, M. Tanaka, K. Kaigawa, J. Shibata, H. Sakai, in: *Proceedings of the IEEE Ultrasonics Symposium, 2000*.
- [84] P. Sharma, K. Sreenivas, *Appl. Phys. Lett.* 83 (2003) 3617.
- [85] S. Tripathy, R.K. Soni, H. Asahi, K. Iwata, R. Kuroiwa, K. Asami, S. Gonda, *J. Appl. Phys.* 85 (1999) 8386.
- [86] T. Matsuoka, E. Higiwara, *phys. stat. sol. (a)* 188 (2001) 485.
- [87] A.D. Hanser, R.F. Davis, in: J.H. Edgar, S.S. Strite, I. Akasaki, H. Amano (Eds.), *Properties, Processing and Applications of Gallium Nitride and Related Semiconductors*, INSPEC, The Institution of Electrical Engineers, Stevenage, UK, 1999, p. 386.

- [88] H. Lahreche, M. Leroux, M. Laugt, M. Valle, B. Beaumont, P. Gibart, *J. Appl. Phys.* 87 (2000) 577.
- [89] Q. Wahab, A. Ellison, A. Henry, E. Janze 'n, C. Hallin, J. Di Persio, R. Martinez, *Appl. Phys. Lett.* 76 (2000) 2725.
- [90] A. R. Powell, L. B. Rowland, *Proceedings of the IEEE*, Volume: 90 Issue: 6, June 2002, p. 942.
- [91] U. Zehnder, A. Weimar, U. Strauss, M. Fehrer, B. Hahn, H. -J. Lugauer, V. Härle, *J. Cryst. Growth* 230 (2001) 497
- [92] R. F. Davis, *Proceedings of the International Conference in SiC and Related Materials-93*, Washington DC, USA, November 1993, *Inst. Phys. Conf. Ser. No 137* (1994) p. 1.
- [93] J. Gith, W.T. Petusky, *J. Phys. Chem. Solids* 48 (1987) 541.
- [94] Y.M. Tairov, V.F. Tsvetkov, *J. Cryst. Growth* 43 (1978) 209.
- [95] M. Dudley, X. Huang, *Mater. Sci. Forum* 338–342 (2000) 431.
- [96] C.H. Carter, V.F. Tsvetkov, R.C. Glass, D. Henshall, M. Brady, St.G. Muller, O. Kordina, K. Irvine, J.A. Edmond, H.-S. Kong, R. Singh, S.T. Allen, J.W. Palmour, *Mater. Sci. Eng. B61/62* (1999) 1.
- [97] P.G. Neudeck, *Mater. Sci. Forum* 338–342 (2000) 1161.
- [98] R.C. Weast, M.J. Astle, W.H. Beyer (Eds.), *CRC Handbook of Chemistry and Physics*, 66th Edition, CRC Press, Boca Raton, FL, 1986, p. E-99.
- [99] G.L. Harris, in: G.L. Harris (Ed.), *Properties of Silicon Carbide*, Inspec/IEE, 1995, p. 3.
- [100] *Ibid.*, p. 5.
- [101] *Ibid.*, p. 9.
- [102] *Ibid.*, p. 8.
- [103] J.B. Casady, R.W. Johnson, *Solid-State Electron.* 39 (1996) 1409.
- [104] R.R. Siergiej, R.C. Clarke, S. Siram, A.K. Agarwal, R.J. Bojko, A.W. Morse, V. Balakrishna, M.F. MacMillan, A.A. Burk Jr., C.D. Brandt, *Mater. Sci. Eng. B61/62* (1999) 9.
- [105] K. Byungwhan, C. Hyun Jun, L. Byung-Teak, *J. Vac. Sci. Technol. A*, 20 (2002) 424.
- [106] E. K. Sanchez, S. Ha, J. Grim, M. Skowronski, W. M. Vetter, M. Dudley, R. Bertke, W. C. Mitchel, *J. Electrochem. Soc.* 149 (2002) G131.
- [107] C.J. Anthony, A.J. Pidduck, M.J. Uren, *Mater. Sci. Forum* 264–268 (1998) 367.
- [108] Z.Y. Xie, C.H. Wei, L.Y. Li, Q.M. Yu, J.H. Edgar, *J. Cryst. Growth* 217 (2000) 115.
- [109] J.A. Powell, D.J. Larkin, A.J. Trunek, *Mater. Sci. Forum* 264–268 (1998) 421.
- [110] V.M. Torres, J.L. Edwards, B.J. Wilkens, D.J. Smith, R.B. Doak, *Appl. Phys. Lett.* 74 (7) (1999) 985.
- [111] A. Kawasuso, K. Kojima, M. Yoshikawa, H. Itoh, *Appl. Phys. Lett.* 76 (9) (2000) 1119.
- [112] P.H. Yin, V. Saxena, A.J. Steckl, *phys. stat. sol. (b)* 202 (1997) 605.

- [113] K. Xie, J.R. Flemish, J.H. Zhao, W.R. Buchwald, L. Casas, *Appl. Phys. Lett.* 67 (1995) 368.
- [114] K.H. Ploog, O. Brandt, R. Muralidharan, A. Thamm, P. Waltereit, *J. Vac. Sci. Technol. B* 18 (2000) 2290.
- [115] P. Waltereit, O. Brandt, *Appl. Phys. Lett.* 74 (1999) 3660.
- [116] T. Ito, K. Ohtsuka, K. Kuwahara, M. Sumiya, Y. Takano, S. Fuke, *J. Cryst. Growth* 205 (1999) 22.
- [117] D.D. Koleske, R.L. Henry, M.E. Twigg, J.C. Culbertson, S.C. Binari, A.E. Wickenden, M. Fatemi, *Appl. Phys. Lett.* 80 (2002) 4372.
- [118] J.R. Shealy, V. Kaper, V. Tilak, T. Prunty, J.A. Smart, B. Green, L.F. Eastman, *J. Phys.: Condens. Matter* 14 (2002) 3499.
- [119] H. Lahreche, M. Vaille, P. Vennéguès, M. Laügt, B. Beaumont, P. Gibart, *Diam. Relat. Mater.* 9 (2000) 452.
- [120] A. Thamm, O. Brandt, Y. Takemura, A. Trampert, K.H. Ploog, *Appl. Phys. Lett.* 75 (1999) 944.
- [121] Q.K. Yang, A.Z. Li, Y.G. Zhang, B. Yang, O. Brandt, K. Ploog, *J. Cryst. Growth* 192 (1998) 28.
- [122] J.T. Torvik, C. Qiu, M. Leksono, J. Pankove, *Appl. Phys. Lett.* 72 (1998) 945.
- [123] K.H. Ploog, O. Brandt, H. Yang, B. Yang, A. Trampert, *J. Vac. Sci. Technol. B* 16 (1998) 2229.
- [124] J.T. Torvik, M.W. Leksono, J.I. Pankove, C. Heinlein, J.K. Grepstad, C. Magee, *J. Electron. Mater.* 28 (3) (1999) 234.
- [125] W. Shan, *Appl. Phys. Lett.* 69 (1996) 740.
- [126] S. Tanaka, R.S. Kern, J. Bentley, R.F. Davis, *Appl. Phys. Lett.* 66 (1) (1995) 37.
- [127] D.J. Smith, D. Chandrasekhar, B. Sverdlov, A. Botchkarev, A. Salvador, H. Morkoç, *Appl. Phys. Lett.* 67 (1995) 1830.
- [128] B.N. Sverdlov, G.A. Martin, H. Morkoç, *Appl. Phys. Lett.* 67 (14) (1995) 2063.
- [129] R.F. Davis, S. Tanaka, L.B. Rowland, R.S. Kern, Z. Sitar, S.K. Ailey, C. Wang, *J. Cryst. Growth* 164 (1996) 132.
- [133] J.N. Stirman, F.A. Ponce, A. Pavlovska, I.S.T. Tsong, D.J. Smith, *Appl. Phys. Lett.* 76 (7) (2000) 822.
- [130] R.B. Capaz, H. Lim, J.D. Joannopoulos, *Phys. Rev. B* 51 (17) (1995) 755.
- [131] S. Ren, J.D. Dow, *J. Electron. Mater.* 26 (4) (1997) 341.
- [132] A. Kazimirov, N. Faleev, H. Temkin, M. J. Bedzyk, V. Dmitriev, Yu. Melnik, *J. Appl. Phys.* 89 (2001) 6092.
- [134] Q.K. Xue, Q.Z. Xue, S. Kuwano, K. Nakayama, T. Sakurai, I.S.T. Tsong, X.G. Qiu, Y. Segawa, *J. Cryst. Growth* 229 (2001) 41.
- [135] M.A. Sanchez-Garcia, F.B. Naranjo, J.L. Pau, A. Jimenez, E. Calleja, E. Munoz, *J. Appl. Phys.* 87 (3) (2000) 1569.
- [136] A. Krost, A. Dadgar, *Mater. Sci. Eng. B* B93 (2002) 77.

- [137] Y. Cordier, F. Semond, J. Massies, B. Dessertene, S. Cassette, M. Surrugue, D. Adam, S.L. Delage, *Electron. Lett.* 38 (2002) 91.
- [138] R.F. Davis, T. Gehrke, K.J. Linthicum, P. Rajagopal, A.M. Roskowski, T. Zheleva, E.A. Preble, C.A. Zorman, M. Mehregany, U. Schwarz, J. Schuck, R. Grober, *MRS Internet J. Nitride Semicond. Res.* 7S1 (2002).
- [139] Wang Feng, Zhang Rong, Chen Zhizhong, Zhu Jianmin, Gu Shulin, Shen Bo, Chen Peng, Zhou Yugang, Li Weiping, Shi Yi, Zheng Youdou, *High Technol. Lett.* 12 (2002) 47.
- [140] J.C. Brice, in: Robert Hull (Ed.), *Properties of Crystalline Silicon*, IEE, London, 1999, p. 155.
- [141] Y. Okada, in: Robert Hull (Ed.), *Properties of Crystalline Silicon*, IEE, London, 1999, p. 91.
- [142] Y. Okada, Y. Tokumaru, *J. Appl. Phys.* 56 (2) (1984) 314.
- [143] M.N. Wybourne, in: Robert Hull (Ed.), *Properties of Crystalline Silicon*, IEE, London, 1999, p. 165.
- [144] W.E. Beadle, J.C.C. Tsai, R.D. Plummer, *Quick Reference Manual for Silicon Integrated Circuit Technology*, Wiley, New York, 1985, p. 1.
- [145] A. George, in: Robert Hull (Ed.), *Properties of Crystalline Silicon*, IEE, London, 1999, p. 98.
- [146] H. Craig Casey, *Devices for Integrated Circuits*, Wiley, New York, 1999, p. 45.
- [147] P.J. Mole, J.M. Rorison, J.A. del Alamo, D. Lancefield, in: Robert Hull (Ed.), *Properties of Crystalline Silicon*, IEE, London, 1999, p. 430.
- [148] P.J. Mole, J.A. del Alamo, in: Robert Hull (Ed.), *Properties of Crystalline Silicon*, IEE, London, 1999, p. 443.
- [149] B. Yang, A. Trampert, O. Brandt, B. Jenichen, K.H. Ploog, *J. Appl. Phys.* 83 (7) (1998) 3800.
- [150] J.H. Boo, S.B. Lee, Y.S. Kim, J.T. Park, S. Yu, Y. Kim, *phys. stat. sol. (a)* 176 (1999) 711.
- [151] V. Lebedev, J. Jinschek, U. Kaiser, B. Schoroter, W. Richter, J. Kraußlich, *Appl. Phys. Lett.* 76 (15) (2000) 2029.
- [152] T. Egawa, T. Moku, H. Ishikawa, K. Ohtsuka, T. Jimbo, *Jpn. J. Appl. Phys.* 41 (2002) L663
- [153] H. Marchand, L. Zhao, N. Zhang, B. Moran, R. Coffie, U. K. Mishra, J. S. Speck, S. P. DenBaars, J. A. Freitas, *J. Appl. Phys.* 12 (2001) 7846.
- [154] J.L. Pau, E. Munoz, M.A. Sanchez, E. Calleja, *Proc. SPIE - Int. Soc. Opt. Eng.* 4650 (2002) 104.
- [155] E. Calleja, M.A. Sanchez-Garcia, F.J. Sanchez, F. Calle, F.B. Naranjo, E. Munoz, S.I. Molina, A.M. Sanchez, F.J. Pacheco, R. Garcia, *J. Cryst. Growth* 201/202 (1999) 296.
- [156] S. Zamir, B. Meyler, E. Zolotoyabko, J. Salzman, *J. Cryst. Growth* 218 (2000) 181.
- [157] L. Zhao, H. Marchand, P. Fini, S.P. Denbaars, U.K. Mishra, J.S. Speck, *MRS Internet J. Nitride Semicond. Res.* 5S1 (2000) W3.3.

- [158] S.A. Nikishin, N.N. Faleev, V.G. Antipov, S. Francoeur, L. Grave de Peralta, G.A. Seryogin, H. Temkin, T.I. Prokofyeva, M. Holtz, S.N.G. Chu, *Appl. Phys. Lett.* 75 (14) (1999) 2073.
- [159] D.M. Follstaedt, J. Han, P. Provencio, J.G. Fleming, *MRS Internet J. Nitride Semicond. Res.* 4S1 (1999) G3.72.
- [160] H. Ishikawa, G.Y. Zhao, N. Nakada, T. Egawa, T. Soga, T. Jimbo, M. Umeno, *phys. stat. sol. (a)* 176 (1999) 599.
- [161] E. Feltrin, B. Beaumont, M. Lau'gt, P. De Mierry, P. Venne'gue's, H. Lahre'che, M. Leroux, P. Gilbert, *Appl. Phys. Lett.* 79 (2001) 3230.
- [162] M. Kim, Y. Bang, N. Park, C. Choi, T. Seong, S. Park, *Appl. Phys. Lett.* 78 (2001) 2858.
- [162] S.T. Kim, Y.J. Lee, D.C. Moon, C.H. Hong, T.K. Yoo, *J. Crystal Growth* 194 (1998) 37.
- [163] D. Wang, S. Yoshida, M. Ichikawa, *J. Cryst. Growth* 236 (2002) 311.
- [164] J. Ristic, M.A. Sanchez-Garcia, E. Calleja, A. Perez-Rodriguez, C. Serre, A. Romano-Rodriguez, J.R. Morante, V.R. Koegler, W. Skorupa, *Mater. Sci. Eng. B93* (2002) 172.
- [165] *Compound Semiconductor* November 2001, p. 63.
- [166] *Compound Semiconductor* March 2001, p. 17.
- [167] S. Adachi, in: M.R. Brozel, G.E. Stillman (Eds.), *Properties of Gallium Arsenide*, 3rd Edition, Inspec/IEE, 1996, p. 36.
- [168] *Ibid.*, p. 3.
- [169] *Ibid.*, p. 32.
- [170] *Ibid.*, p. 27.
- [171] S. Adachi, *GaAs and Related Materials: Bulk Semiconducting and Superlattice*, World Scientific, Singapore, 1994.
- [172] H. Okumura, K. Ohta, G. Feuillet, K. Balakrishnan, S. Chichibu, H. Hamaguchi, P. Hacke, S. Yoshida, *J. Cryst. Growth* 178 (1997) 113.
- [173] B.J. Min, C.T. Chan, K.M. Ho, *Phys. Rev. B* 45 (1992) 1159.
- [174] S. Shokhovets, R. Goldhahn, T.S. Cheng, C.T. Foxon, *Semicond. Sci. Technol.* 14 (1999) 181.
- [175] M. Namerikawa, T. Sato, O. Takahashi, T. Suemasu, F. Hasegawa, *J. Cryst. Growth* 237 (2002) 1089.
- [176] K. Motoki, T. Okahisa, S. Nakahata, N. Matsumoto, H. Kimura, H. Kasai, K. Takemoto, K. Uematsu, M. Ueno, Y. Kumagai, A. Koukitu, H. Seki, *J. Cryst. Growth* 237 (2002) 912.
- [177] C.J. Rawn, J. Chaudhuri, *J. Cryst. Growth* 225 (2001) 214.
- [178] T. Ishii, M. Mukaida, T. Nishihara, S. Hayashi, M. Shinohara, *Jpn. J. Appl. Phys.* 37 (1998) L672.

- [179] W.A. Doolittle, T. Kropewnicki, C. Carter-Coman, S. Stoke, P. Kohl, N.M. Jokerst, R.A. Metzger, S. Kang, K.K. Lee, G. May, A.S. Brown, *J. Vac. Sci. Technol. B* 16 (3) (1998) 1300.
- [180] G. A. Slack, *J. Phys. Chem. Solids* 34 (1973) 321.
- [181] S. Kuck, S. Hartung, *Chem. Phys.* 240 (1999) 387.
- [182] J.T. Wolan, G.B. Hoflund, *J. Vac. Sci. Technol. A* 16 (6) (1998) 3414.
- [183] W.A. Doolittle, A.S. Brown, *Mater. Res. Soc. Symp. Proc.* 570 (1999) V4.2.
- [184] W.A. Doolittle, S. Kang, A. Brown, *Solid-State Electron.* 44 (2000) 229.
- [185] P. Kung, A. Saxler, X. Zhang, D. Walker, R. Lavado, M. Razeghi, *Appl. Phys. Lett.* 69 (1996) 2116.
- [186] O. Kryliouk, M. Reed, T. Dann, T. Anderson, B. Chai, *Mater. Sci. Eng. B* 59 (1999) 6.
- [187] W.A. Doolittle, S. Kang, T.P. Kropewnicki, S. Stock, P.A. Kohl, A.S. Brown, *J. Electron. Mater.* 27 (1998) L58.
- [188] O. Kryliouk, M. Reed, T. Dann, T. Anderson, B. Chai, *Mater. Sci. Eng. B* 66 (1999) 26.
- [190] R.R. Tummala, E.J. Rymaszewski, *Microelectronics Packaging Handbook*, Van Nostrand-Reinhold, 1989.
- [191] D. Zhuang, J.H. Edgar, Lianghong Liu, B. Liu, L. Walker, *MRS Internet J. Nitride Semicond. Res.* 7, 4 (2002).
- [192] D.J. Smith, S.-C.Y. Tsen, B.N. Sverdlov, G. Martin, H. Morkoç, *Solid-State Electron.* 41 (1997) 349.
- [193] R.R. Lee, *J. Am. Ceram. Soc.* 74 (9) (1991) 2242.
- [194] I. Yonenaga, A. Nikolaev, Y. Melnik, V. Dmitriev, *Jpn. J. Appl. Phys.* 40 (2001) L 426.
- [195] J.-S. Chun, P. Desjardins, C. Lavoie, C.-S. Shin, C. Cabral, Jr., I. Petrov, J. E. Greene, *J. Appl. Phys.* 89 (2001) 7841.
- [196] R.J. Bruls, H.T. Hintzen, G. de With, R. Metselaar, J.C. van Miltenburg, *J. Phys. Chem. Solids* 62 (2001) 783.
- [197] D.K. Gaskill, L. B. Rowland, K. Doverspike, in: J.H. Edgar (Ed.), *Properties of Group III Nitrides*, INSPEC, Stevenage, 1994, p. 101.
- [198] G.A. Slack, *Mater. Res. Soc. Symp. Proc.* 512 (1998) 35.
- [199] G.A. Slack, T.F. McNelly, *J. Cryst. Growth* 34 (1976) 263.
- [200] J.C. Rojo, G.A. Slack, K. Morgan, B. Raghathamachar, M. Dudley, L.J. Schowalter, *J. Cryst. Growth* 231 (2001) 317.
- [201] L. J. Schowalter, Y. Shusterman, R. Wang, I. Bhat, G. Arunmozhi, G. A. Slack, *Appl. Phys. Lett.* 76 (2000) 985.
- [202] J.C. Rojo, G.A. Slack, K. Morgan, L.J. Schowalter, M. Dudley, *Mater. Res. Soc. Symp.* 639 (2001) G1.10.1.
- [203] C. M. Balkas, Z. Sitar, T. Zheleva, L. Bergman, R. Nemanich, R. F. Davis, *J. Cryst. Growth* 179 (1997) 363.

- [204] W.L. Sarney, L. Salamanca-Riba, T. Hossain, P. Zhou, H.N. Jayathirtha, H.H. Kang, R.D. Vispute, M. Spencer, K.A. Jones, *MRS Internet J. Nitride Semicond. Res.* 5S1 (2000) W5.5.
- [205] R. Schlessler, Z. Sitar, *J. Cryst. Growth* 234 (2002) 349.
- [206] A. Nikolaev, I. Nikitina, A. Zubrilov, M. Mynbaeva, Y. Melnik, V. Dmitriev, *MRS Internet J. Nitride Semicond. Res.* 5S1 (2000) W6.5.
- [207] J.C. Rojo, L.J. Schowalter, R. Gaska, M. Shur, M.A. Khan, J. Yang, D.D. Koleske, *J. Cryst. Growth* 240 (2002) 508.
- [208] G. Kamler, J. Zachara, S. Podsiadlo, L. Adamowicz, W. Gebicki, *J. Cryst. Growth* 212 (2000) 39.
- [209] Yu.A. Vodakov, E.N. Mokhov, A.D. Roenkov, M.E. Boiko, P.G. Baranov, *J. Cryst. Growth* 183 (1998) 10.
- [210] K. Nishino, D. Kikuta, S. Sakai, *J. Cryst. Growth* 237–239 (2002) 922.
- [211] J.W. Kolis, S. Wilcenski, R.A. Laudise, *Mater. Res. Soc. Symp. Proc.* 495 (1998) 367.
- [212] M. Yano, M. Okamoto, Y.K. Yap, M. Yoshimura, Y. Mori, T. Sasaki, *Diamond Relat. Mater.* 9 (2000) 512.
- [213] I. Grzegory, S. Porowski, *Thin Solid Films* 367 (2000) 281.
- [214] S. Porowski, *J. Cryst. Growth* 189/190 (1998) 153.
- [215] S. Porowski, M. Bockwoski, B. Lucznik, I. Grzegory, M. Wroblewski, H. Teissetre, M. Leszczynski, E. Litwin-Staszewska, T. Suski, P. Trautman, K. Pakula, J. Baranowski, *Acta Phys. Polonica A* 92 (1997) 958.
- [216] K. Saarinen, J. Nissilä, P. Hautojärvi, J. Likonen, T. Suski, I. Grzegory, B. Lucznik, S. Porowski, *Appl. Phys. Lett.* 75 (1999) 2441.
- [217] M. Leszczynski, B. Beaumont, E. Frayssinet, W. Knap, P. Prystawko, T. Suski, I. Gregory, S. Porowski, *Appl. Phys. Lett.* 75 (1999) 1276.
- [218] C. Kirchner, V. Schwegler, F. Eberhard, M. Kamp, K.J. Ebeling, K. Kornitzer, T. Ebner, K. Thonke, R. Sauer, P. Prystawko, M. Leszczynski, I. Grzegory, S. Porowski, *Appl. Phys. Lett.* 75 (1999) 1098.
- [219] V. Kirilyuk, A.R.A. Zauner, P.C.M. Christiansen, J.L. Weyher, P.R. Hageman, P.L. Larsen, *Appl. Phys. Lett.* 76 (2000) 2355.
- [220] A. Pelzmann, C. Kirchner, M. Mayer, V. Schwegler, M. Schauler, M. Kamp, K.J. Ebeling, I. Grzegory, M. Leszczynski, G. Nowak, S. Porowski, *J. Cryst. Growth* 189/190 (1998) 167.
- [221] M. Mayer, A. Pelzmann, H.Y. Chung, M. Kamp, K.J. Ebling, *J. Cryst. Growth* 201/202 (1999) 318.
- [222] S. Nakamura, M. Senoh, S. Nagahama, N. Iwasa, T. Yamada, T. Matsushita, H. Kiyoku, Y. Sugimoto, T. Kozaki, H. Umemoto, M. Sano, K. Chocho, *Appl. Phys. Lett.* 72 (1998) 2014.
- [223] Y. Melnik, A. Nikolaev, I. Nikitina, K. Vassilevski, V. Dimitriev, *Mater. Res. Soc. Symp. Proc.* 482 (1998) 269.
- [224] K. Tomita, T. Kachi, S. Nagai, A. Kojima, S. Yamasaki, M. Koike, *phys. stat. sol. (a)* 194 (2002) 563.

- [225] M.K. Kelly, R.P. Vaudo, V.M. Phanse, L. Görgens, O. Ambacher, M. Stutzmann, *Jpn. J. Appl. Phys.* 38 (1999) 217.
- [226] S.S. Park, I.-W. Park, S.H. Choh, *Jpn. J. Appl. Phys.* 39 (2000) L1141.
- [227] R.P. Vaudo, V.M. Phanse, X. Wu, Y. Golan, J.S. Speck, 2nd Int. Conf. Nitride Semiconductors, Tokushima, 1997.
- [228] P. Visconti, K.M. Jones, M.A. Reschchikov, F. Yun, R. Cingolani, H. Morkoç, S.S. Park, K.Y. Lee, *Appl. Phys. Lett.* 77 (2000) 3743.
- [229] W. Götz, L.T. Romano, J. Walker, N.M. Johnson, R.J. Molnar, *Appl. Phys. Lett.* 72 (1998) 1214.
- [230] N.I. Kuznetsov, A.E. Nikolaev, A.S. Zubrilov, Yu.V. Melnek, V.A. Dmitriev, *Appl. Phys. Lett.* 75 (1999) 3138.
- [231] C.R. Miskys, M.K. Kelly, O. Ambacher, G. Martínez-Criado, M. Stutzmann, *Appl. Phys. Lett.* 77 (2000) 1858.
- [232] J.Y. Dickinson, *The Book of Diamonds*, Avenel Books, 1965, New York.
- [233] J.E. Field, *The Properties of Natural and Synthetic Diamond*, Academic Press, 1992, London.
- [234] H. Malzahn, *Diamant: Der extreme Edelstein, das geniale Werkzeug*, extraLapis No. 18, 2000, Germany.
- [235] A.P. Jones, L. d'Hendecourt, *Astron. Astrophys.* 355 (2000) 1191.
- [236] S.T. Lee, Z. Lin, X. Jiang, *Mater. Sci. Eng. Reports* 25 (1999) 123.
- [237] M. Seal, *Diamond Anvils*, High Temperatures-High Pressures, 1984, vol. 16, pp. 573-579.
- [238] K.E. Spear, J.P. Dismukes, *Synthetic Diamond: Emerging CVD Science and Technology*, Wiley, 1994.
- [239] P.W. May, *Endeavour Magazine* 19 (1995) 101.
- [240] P.W. May, *Phil Trans. R. Soc. Lond. A*, 358 (2000) 473.
- [241] S. Koizumi, M. Kamo, Y. Sato, H. Ozaki, Y. Inuzuka, *Appl. Phys. Lett.* 71 (1997) 1065.
- [242] I. Sagakuchi, M. Nishitani-Gamo, Y. Kikuchi, E. Yasu, H. Haneda, T. Suzuki, T. Ando, *Phys. Rev. B* 60/4 (1999) R2139.
- [243] Z. Teukam, J. Chevallier, C. Saguy, R. Kalish, D. Ballutaud, M. Barbe, F. Jomard, A. Tromson-Carli, C. Cytermann, J.E. Butler, M. Bernard, C. Baron, A. Deneuveille, *Nature Mater.* 21 (2003) 482
- [244] O. Elmazria, V. Mortet, M. El Hakiki, M. Nesladek, P. Alnot, *IEEE Trans. Ultrason., Ferroelect., Freq. Contr.* 50 (2003) 710.
- [245] V. Mortet, O. Elmazria, M. Nesladek, J. D'Haen, G. Vanhoyland, M. El Hakiki, A. Tajani, E. Bustarret, E. Gheeraert, M. D'Olieslaeger, P. Alnot, *Diamond Relat. Mater.* 12 (2003) 723.
- [246] M.B. Assouar, O. Elmazria, L. Le Brizoual, P. Alnot, *Diamond Relat. Mater.* 11 (2002) 413.

- [247] P.R. Chalker, T.B. Joyce, C. Johnston, J.A.A. Crossley, J. Huddleston, M.D. Whitfield, R.B. Jackman, *Diamond Relat. Mater.* 8 (1999) 309.
- [248] B.V. Spitsyn, W.L. Hsu, A.E. Gorodetsky, R.Kh. Zalavutdinov, A.P. Zakharov, L.L. Bouilov, V.P. Stoyan, V.F. Dvoryankin, G.V. Chaplygin, *Diamond Relat. Mater.* 7 (1998) 356.
- [249] A.E. Gorodetsky, R.Kh. Zalavutdinov, A.P. Zakharov, W.L. Hsu, B.V. Spitsyn, L.L. Bouilov, V.P. Stoyan, *Diamond Relat. Mater.* 8 (1999) 1267.
- [250] C.R. Miskys, J.A. Garrido, C.E. Nebel, M. Hermann, O. Ambacher, M. Eickhoff, M. Stutzmann, *Appl. Phys. Lett.* 82 (2003) 290.
- [251] S. Koizumi, K. Watanabe, M. Hasegawa, H. Kanda, *Science* 292 (2001) 1899
- [252] M. Mayer, A. Pelzmann, M. Kamp, K. J. Ebeling, H. Teisseyre, G. Nowak, M. Leszczynski, I. Grzegory, S. Porowsky, G. Karczewski, *Jpn. J. Appl. Phys.* 36 (1997) L1634.
- [253] F. A. Ponce, D. P. Bour, W. Götz, N. M. Johnson, H. I. Helava, I. Grzegory, J. Jun, S. Porowsky, *Appl. Phys. Lett.* 68 (1996) 917.
- [254] S. Nakamura, M. Senoh, S. Nagahama, N. Iwasa, T. Yamada, T. Matsushita, H. Kiyoku, Y. Sugimoto, T. Kozaki, H. Umemoto, M. Sano, K. Chocho, *Appl. Phys. Lett.* 73 (1998) 832.
- [255] M. Kuramoto, C. Sasaoka, Y. Hisanaga, A. Kimura, A. A. Yamaguchi, H. Sunakawa, N. Kuroda, M. Nido, A. Usui, M. Mizuta, *Jpn. J. Appl. Phys.* 38 (1999) L184.
- [256] S.J. Pearton, J.C. Zolper, R.J. Shul, F. Ren, *J. Appl. Phys.* 86 (1999) 1.
- [257] O. Ambacher, M.S. Brandt, R. Dimitrov, T. Metzger, M. Stutzmann, R.A. Fischer, A. Miehr, A. Bergmaier, G. Dollinger, *J. Vac. Sci. Technol. B*14 (1996) 3532.
- [258] M.K. Kelly, O. Ambacher, B. Dahlheimer, G. Groos, R. Dimitrov, H. Angerer, M. Stutzmann, *Appl. Phys. Lett.* 69 (1996) 1749.
- [259] M.K. Kelly, O. Ambacher, R. Dimitrov, R. Handschuh, M. Stutzmann, *phys. stat. sol. (a)* 159 (1997) R3.
- [260] *User's Manual for Quanta-Ray pulsed Nd:YAG lasers*, Spectra-Physics, p. 1-18.
- [261] W.S. Wong, T. Sands, N.W. Cheung, M. Kneissl, D.P. Bour, P. Mei, L.T. Romano, N.M. Johnson, *Appl. Phys. Lett.* 75 (1999) 1360.
- [262] O. Ambacher, M.K. Kelly, C.R. Miskys, L. Höppel, C. Nebel, M. Stutzmann, *Mat. Res. Soc. Symp.* 617 (2000) J1.7.1.
- [263] O. Ambacher, R. Dimitrov, D. Lentz, T. Metzger, W. Rieger, M. Stutzmann, *J. Cryst. Growth* 170 (1997) 335.
- [264] M. Leszczynski, T. Suski, H. Teisseyre, P. Perlin, I. Grzegory, J. Jun, S. Porowski, T.D. Moustakas, *J. Appl. Phys.* 76 (1994) 4909.
- [265] W.S. Wong, T. Sands, N.W. Cheung, M. Kneissl, D.P. Bour, P. Mei, L.T. Romano, N.M. Johnson, *Appl. Phys. Lett.* 77 (2000) 2822.
- [267] J. Jasinski, Z. Liliental-Weber, S. Estrada, E. Hu, *Appl. Phys. Lett.* 81 (2002) 3152.
- [268] E.V. Etzkorn, D.R. Clarke, *J. Appl. Phys.* 89 (2001) 1025.
- [269] N. Itoh, J. Rhee, T. Kawabata, S. Koike, *J. Appl. Phys.* 58 (1985) 1828.

- [270] T. Detchprohm, K. Hiramatsu, K. Itoh, I. Akasaki, *Jpn. J. Appl. Phys.* 31 (1992) L1454.
- [271] P.R. Tavernier, D.R. Clarke, *J. Appl. Phys.* 89 (2001) 1533.
- [272] V. Darakchieva, P.P. Paskov, T. Paskova, E. Valcheva, B. Monemar, M. Heuken, *Appl. Phys. Lett.* 82 (2003) 703.
- [273] D.C. Reynolds, D.C. Look, B. Jogai, J.E. Hoelscher, R.E. Sherriff, R.J. Molnar, *J. Appl. Phys.* 88 (2000) 1460.
- [274] CompoundSemiconductor.NET, January 2002.
- [275] Private communication with Dr. Peter Schlotter from Fraunhofer Institute in Freiburg (IAF), Germany.
- [276] J.M. Poate, J.W. Mayer, *Laser Annealing of Semiconductors*, Academic Press, New York, (1982) 54.
- [277] J. Dziewior, W. Schmid, *Appl. Phys. Lett.* 31 (1977) 346.
- [278] K. Okamoto, Y. Kawakami, S. Fujita, M. Terazima, S. Nakamura, *Proc. Int. Workshop on Nitride Semiconductors, IPAP Conf. Series 1* p. 540.
- [279] F.P. Incropera, D.P. Dewitt, *Fundamentals of Heat and Mass Transfer*, 4th Edition, New York: John Wiley and Sons.
- [280] D.A. Gryvnak, D.E. Burch, *J. Opt. Soc. Am.* 55 (1965) 625.
- [281] D.A. Ditmars, S. Ishihara, S.S. Chang, G. Berstein, E.D. West, *J. Res. Natl. Bur. Stand. (USA)* 87 (1982) 159.
- [282] Union Carbide Corporation-Crystal Products, *Properties of Sapphire Manual*.
- [283] X.L. Chen, Y.C. Lan, J.K. Liang, X.R. Chen, Y.P. Xu, T. Xu, P.Z. Jiang, K.Q. Lu, *Chin. Phys. Lett.* 16 (1999) 107.
- [284] R.P. Vaudo, G.R. Brandes, J.S. Flynn, X. Xu, M.F. Chriss, C.S. Christos, D.M. Keogh, F.D. Tamweber, *Int. Workshop on Nitride Semiconductors, Nagoya, Japan 2000*.
- [285] I. Barin, O. Knacke, O. Kubaschewski, *Thermochemical Properties of Inorganic Substances*, Springer (1977) Berlin.
- [286] T. Bret, V. Wagner, D. Martin, P. Hoffmann, M. Ilegems, *phys. stat. sol. (a)* 194 (2002) 559.
- [287] W.S. Wong, A.B. Wengrow, Y. Cho, A. Salleo, N.J. Quitoriano, N.W. Cheung, T. Sands, *J. Electron. Mater.* 28 (1999) 1409.
- [288] H. Teisseyre, P. Perlin, T. Suski, I. Grzegory, S. Porowski, J. Jun, A. Pietraszko, T.D. Moustakas, *J. Appl. Phys.* 76 (1994) 2429.
- [289] S. Nakamura, G. Fasol, *The Blue Laser Diodes*, Springer, Heidelberg (1997).
- [290] J.I. Pankove, T.D. Moustakas, *GaN*, Academic Press, New York (1998).
- [291] N.G. Weimann, L.F. Eastman, D. Doppalapudi, H.M. Ng, T.D. Moustakas, *J. Appl. Phys.* 83 (1998) 3656.
- [292] S. Nakamura, M. Senoh, S. Nagahama, N. Iwasa, T. Yamada, T. Matsushita, H. Kiyoku, Y. Sugimoto, T. Kozaki, H. Umemoto, M. Sano, K. Chocho, *Jpn. J. Appl. Phys.* 36 (1997) L1568.

- [293] Y. Golan, X.H. Wu, J.S. Speck, R.P. Vaudo, V.M. Phanse, *Appl. Phys. Lett.* 73 (1998) 3090.
- [294] D. Gogova, A. Kasic, H. Larsson, B. Pécz, R. Yakimova, B. Magnusson, B. Monemar, F. Tuomisto, K. Saarinen, C. Miskys, M. Stutzmann, C. Bundesmann, M. Schubert, *Jpn. J. Appl. Phys.* 143 (2004) 1264.
- [295] C.R. Miskys, M.K. Kelly, O. Ambacher, M. Stutzmann, *phys. stat. sol. (a)* 176 (1999) 443.
- [296] J.L. Rouviere, J.L. Weyher, M. Seelmann-Eggebert, S. Porowski, *Appl. Phys. Lett.* 73 (1998) 668.
- [297] O. Ambacher, J. Smart, J.R. Shealy, N.G. Weimann, K. Chu, M. Murphy, W.J. Schaff, L.F. Eastman, R. Dimitrov, L. Wittmer, M. Stutzmann, W. Rieger, J. Hilsenbeck, *J. Appl. Phys.* 85 (1999) 3222.
- [298] J.L. Weyher, S. Müller, I. Grzegory, S. Porowsky, *J. Crystal Growth* 182 (1997) 17.
- [299] M. Schauler, F. Eberhard, C. Kirchner, V. Schwegler, A. Pelzmann, M. Kamp, K.J. Ebeling, F. Bertram, T. Riemann, J. Christen, P. Prystawko, M. Leszczynski, I. Grzegory, S. Porowsky, *Appl. Phys. Lett.* 74 (1999) 1123.
- [300] A. Setoguchi, K. Yoshimura, M. Sumiya, A. Uedono, S.F. Chichibu, *GaN Related Alloys - 2000 Symposium*, G11.6.1. (2001).
- [301] A. Cros, R. Dimitrov, H. Angerer, O. Ambacher, M. Stutzmann, S. Christiansen, M. Albrecht, H.P. Strunk, *J. Cryst. Growth* 181 (1997) 197.
- [302] J.-M. Wagner, F. Bechstedt, *Phys. Rev. B* 66 (2002) 115202.
- [303] A.R. Goñi, H. Siegle, K. Syassen, C. Thomsen, J.-M. Wagner, *Phys. Rev. B* 64 (2001) 35205.
- [304] B.J. Skromme, J. Jayapalan, R.P. Vaudo, V.M. Phanse, *Appl. Phys. Lett.* 74 (1999) 2354.
- [305] G. Martínez-Criado, C.R. Miskys, A. Cros, O. Ambacher, A. Cantarero, M. Stutzmann, *J. Appl. Phys.* 90 (2001) 5627.
- [306] Z.X. Liu, K.P. Korona, K. Syassen, J. Kuhl, K. Pakula, J.M. Baranowski, I. Grzegory, S. Porowski, *Solid State Commun.* 108, (1998) 433.
- [307] T. Taliercio, M. Gallart, P. Lefebvre, A. Morel, B. Gil, J. Allègre, N. Grandjean, J. Massies, I. Grzegory, S. Porowski, *Solid State Commun.* 117 (2001) 445.
- [308] I. Grzegory, S. Porowski, *Thin Solid Films* 367 (2000) 281.
- [309] T. Schmidt, K. Lischka, W. Zulehner, *Phys. Rev. B* 45 (1992) 8989.
- [310] F. Calle, F.J. Sánchez, J.M.G. Tijero, M. A. Sánchez-García, E. Calleja, R. Beresford, *Semicond. Sci. Technol.* 12 (1997) 1396.
- [311] D. Bimberg, M. Sondergeld, E. Grobe, *Phys. Rev. B* 4 (1971) 3451.
- [312] N.E. Christensen, P. Perlin, in: J. I. Pankove, T. D. Moustakas (Eds.), *Gallium Nitride I*, Semiconductors and Semimetals Series, Academic, New York, 1998, Vol. 50.
- [313] D. Volm, K. Oettinger, T. Streibl, D. Kovalev, M. Ben-Chorin, J. Diener, B. K. Meyer, J. Majewski, L. Eckey, A. Hoffmann, *Phys. Rev. B* 53, (1996) 16543.

- [314] Y.J. Wang, R. Kaplan, H.K. Ng, K. Doverspike, D.K. Gaskill, T. Ikedo, I. Akasaki, H. Amano, *J. Appl. Phys.* 79, (1996) 8007.
- [315] W. Shan, B.D. Little, A.J. Fischer, J.J. Song, B. Goldenberg, W.G. Perry, M.D. Bremser, R.F. Davis, *Phys. Rev. B* 54 (1996) 16369.
- [316] A.S. Barker, M. Ilegems; *Phys. Rev. B* 7 (1973) 743.
- [317] M. Drechsler, D.M. Hofmann, B.K. Meyer, T. Detchprohm, H. Amano, I. Akasaki, *Jpn. J. Appl. Phys., Part 2-34* (1995) L1178.
- [318] K. Reimann, M. Steube, D. Fröhlich, S.J. Clarke, *J. Cryst. Growth* 189/190 (1998) 652.
- [319] R. Hull, R.M. Osgood, Jr., H. Sakaki, A. Zunger, in: H. Morkoç (Ed.), *Nitride Semiconductors and Devices*, Springer Series in Materials Science, Vol. 32, 1999, p. 54.
- [320] S. Nakamura, *Semicond. Sci. Technol.* 14 (1999) R27.
- [321] A. Kinoshita, H. Hiramaya, M. Ainoya, Y. Aoyagi, A. Hirata, *Appl. Phys. Lett.* 77 (2000) 175.
- [322] T. Nishida, H. Saito, N. Kobayashi, *Appl. Phys. Lett.* 78 (2001) 3927.
- [323] T. Nishida, H. Saito, N. Kobayashi, *Appl. Phys. Lett.* 79 (2001) 711.
- [324] M.M. Wong, J.C. Denyszyn, C.J. Collins, U. Chowdhury, T.G. Zhu, K.S. Kim, R.D. Dupuis, *Electron. Lett.* 37 (2001) 1188.
- [325] V. Adivarahan, J. Zhang, A. Chitnis, W. Shuai, J. Sun, R. Pachipulusu, M. Shatalov, M.A. Khan, *Jpn. J. Appl. Phys.* 41 (2002) L435.
- [326] A. Chitnis, R. Pachipulusu, V. Mandavilli, M. Shatalov, E. Kuokstis, J.P. Zhang, V. Adivarahan, S. Wu, G. Simin, M.A. Khan, *Appl. Phys. Lett.* 81 (2002) 2938.
- [327] J. Han, M.H. Crawford, A.V. Nurmikko, *Proc. LEOS 2000 IEEE Annual Meeting Conf.*, Nov. 2000, p.557.
- [328] H. Hirayama, A. Kinoshita, A. Hirata, Y. Aoyagi, *phys. stat. sol. (a)* 188 (2001) 83.
- [329] M. Shatalov, J. Zhang, A.S. Chitnis, V. Adivarahan, J. Yang, G. Simin, M.A. Khan, *IEEE Journal of Selected Topics in QE*, 8 (2002) 302.
- [330] A. Yasan, R. McClintock, K. Mayes, S.R. Darvish, P. Kung, M. Razeghi, *Appl. Phys. Lett.* 81 (2002) 801.
- [331] D. Korakakis, H.M. Ng, K.F. Ludwig, T.D. Moustakas, *Mat. Res. Soc. Symp. Proc.* 449 (1996) 233.
- [332] J. Li, T.N. Oder, M.L. Nakarmi, J.Y. Lin, H.X. Jiang, *Appl. Phys. Lett.* 80 (2002) 1210.
- [333] H.M. Ng, T.D. Moustakas, S.N.G. Chu, *Appl. Phys. Lett.* 76 (2000) 2818.
- [334] R.W. Martin, P.R. Edwards, H.S. Kim, K.S. Kim, T. Kim, I.M. Watson, M.D. Dawson, Y. Cho, T. Sands, N.W. Cheung, *Appl. Phys. Lett.* 79 (2001)3029.
- [335] R. Zeisel, M.W. Bayerl, S.T.B. Goennenwein, R. Dimitrov, O. Ambacher, M.S. Brandt, M. Stutzmann, *Phys. Rev. B* 61 (2000) R16283.
- [336] A.T. Collins, A.W.S. Williams, *J. Phys. C: Sol. St. Phys.* 4 (1971) 1789.
- [337] G. Braunstein, R. Kalish, *J. Appl. Phys.* 54 (1983) 2106.

- [338] J.P. Lagrange, A. Deneuve, E. Gheeraert, *Diam. Relat. Mater.* 7 (1998) 1390.
- [339] H. Okushi, *Diam. Relat. Mater.* 10 (2001) 281.
- [340] D. Takeuchi, H. Watanabe, S. Yamanaka, H. Okushi, K. Kajimura, *Diam. Relat. Mater.* 9 (2000) 231.
- [341] D. Belitz, T.R. Kirkpatrick, *Rev. Mod. Phys.* 66 (1994) 261.
- [342] T.H. Borst, O. Weis, *phys. stat. sol. (a)* 154 (1996) 423.
- [343] M. Werner, R. Locher, W. Kohly, D.S. Holmes, S. Klose, H.J. Fecht, *Diam. Relat. Mater.* 6 (1997) 308.
- [344] W.S. Wong, M. Kneissl, D.W. Treat, M. Teepe, N. Miyashita, N.M. Johnson, *Compound Semiconductor* 7 (2001) 47.
- [345] J. Isberg, J. Hammersberg, E. Johansson, T. Wilkström, D.J. Twitchen, A.J. Whitehead, S.E. Coe, G.A. Scarsbrook, *Science* 297 (2002) 1670.
- [346] G. Vogg, C.R. Miskys, J.A. Garrido, M. Hermann, M. Eickhoff, M. Stutzmann, *J. Appl. Phys.* 96 (2004) 895.
- [347] C.R. Miskys, G. Vogg, J.A. Garrido, M. Hermann, M. Eickhoff, C.E. Nebel, M. Stutzmann, *Appl. Phys. Lett.* 85 (2004) 3699.
- [348] V. Lebedev, J. Jinschek, J. Kräußlich, U. Kaiser, B. Schröter, W. Richter, *J. Crystal Growth* 230 (2001) 426.
- [349] J.-H. Song, T. Chikyow, Y.-Z. Yoo, P. Ahmet, H. Koinuma, *Jpn. J. Appl. Phys.* 41 (2002) L1291.
- [350] K. Dovidenko, S. Oktyabrsky, J. Narayan, M. Razeghi, *J. Appl. Phys.* 79 (1996) 2439.
- [351] V. Lebedev, J. Jinschek, U. Kaiser, B. Schröter, W. Richter, J. Kräußlich, *Appl. Phys. Lett.* 76 (2000) 2029.
- [352] R.D. Vispute, J. Narayan, H. Wu, K. Jagannadham, *J. Appl. Phys.* 77 (1995) 4724.
- [353] B.E. Warren, *X-Ray Diffraction*, Addison-Wesley, Reading, MA, 1969.
- [354] S. Karmann, H.P.D. Schenk, U. Kaiser, A. Fissel, W. Richter, *Mater. Sci. Eng. B50* (1997) 228.
- [355] W.M. Xim, E.J. Stofko, P.J. Zanzucchi, J.I. Pankove, M. Ettenberg, S.L. Gilbert, *J. Appl. Phys.* 44 (1973) 292.
- [356] J. Narayan, B.C. Larson, *J. Appl. Phys.* 93 (2003) 278.
- [357] S.P. Grabowski, M. Schneider, H. Nienhaus, W. Mönch, R. Dimitrov, O. Ambacher, M. Stutzmann, *Appl. Phys. Lett.* 78 (2001) 2503.
- [358] F. Maier, J. Ristein, L. Ley, *Phys. Rev. B* 64 (2001) 1654.
- [359] D. Brunner, H. Angerer, E. Bustarret, F. Freudenberg, R. Höppler, R. Dimitrov, O. Ambacher, M. Stutzmann, *J. Appl. Phys.* 82 (1997) 5090.
- [360] T. Paskova, P.P. Paskov, J. Birch, E. Valcheva, M. Abrashev, S. Tungasmita, B. Monemar, *Proc. Int. Workshop on Nitride Semiconductors, IPAP Conf. Series 1* (2001) pp. 19.

List of Publications

1. “*Structural and Interface Properties of an AlN/Diamond Ultraviolet Light Emitting Diode*”
C.R. Miskys, G. Vogg, J.A. Garrido, M. Hermann, M. Eickhoff, C.E. Nebel, M. Stutzmann, Appl. Phys. Lett. 85 (2004) 3699.
2. “*High quality heteroepitaxial AlN films on diamond*”
G. Vogg, **C.R. Miskys**, J.A. Garrido, M. Hermann, M. Eickhoff, M. Stutzmann, J. Appl. Phys. 96 (2004) 895.
3. “*Two-Dimensional Electron Gas Recombination in Undoped AlGa_N/Ga_N Heterostructures*”
G. Martínez-Criado, **C. Miskys**, U. Karrer, O. Ambacher, M. Stutzmann, Jpn. J. Appl. Phys. 43 (2004) 3360.
4. “*Optical and structural characteristics of virtually unstrained bulk-like Ga_N*”
D. Gogova, A. Kasic, H. Larsson, B. Pécz, R. Yakimova, B. Magnusson, B. Monemar, F. Tuomisto, K. Saarinen, **C. Miskys**, M. Stutzmann, C. Bundesmann, M. Schubert, Jpn. J. Appl. Phys. 143 (2004) 1264.
5. “*Free-standing Ga_N grown on epitaxial lateral overgrown Ga_N substrates*”
G. Martinez-Criado, M. Kuball, M. Benyoucef, A. Sarua, E. Frayssinet, B. Beaumont, P. Gibart, **C.R. Miskys**, M. Stutzmann, J. Cryst. Growth 255 (2003) 277.
6. “*AlN/diamond heterojunction diodes*”
C.R. Miskys, J.A. Garrido, C.E. Nebel, M. Hermann, O. Ambacher, M. Eickhoff, M. Stutzmann, Appl. Phys. Lett. 82 (2003) 290.
7. “*Pyroelectric properties of Al(In)Ga_N/Ga_N hetero- and quantum well structures*”
O. Ambacher, J. Majewski, **C. Miskys**, A. Link, M. Hermann, M. Eickhoff, M. Stutzmann, F. Bernardini, V. Fiorentini, V. Tilak, B. Schaff, L.F. Eastman, J. Phys.-Condens. Mat. 14 (2002) 3399.

8. *“Excitonic transitions in homoepitaxial GaN”*
G. Martinez-Criado, **C.R. Miskys**, A. Cros, A. Cantarero, O. Ambacher, M. Stutzmann,
phys. stat. sol. (b) 228 (2001) 497.
9. *“Photoluminescence study of excitons in homoepitaxial GaN”*
G. Martinez-Criado, **C.R. Miskys**, A. Cros, O. Ambacher, A. Cantarero, M. Stutzmann,
J. Appl. Phys. 90 (2001) 5627.
10. *“Residual strain effects on the two-dimensional electron gas concentration of AlGaN/GaN heterostructures”*
G. Martinez-Criado, A. Cros, A. Cantarero, O. Ambacher, **C.R. Miskys**, R. Dimitrov,
M. Stutzmann, J. Smart, J.R. Shealy, J. Appl. Phys. 90 (2001) 4735.
11. *“Spatially resolved photoluminescence of inversion domain boundaries in GaN-based lateral polarity heterostructures”*
P.J. Schuck, M.D. Mason, R.D. Grober, O. Ambacher, A.P. Lima, **C. Miskys**,
R. Dimitrov, M. Stutzmann, Appl. Phys. Lett. 79 (2001) 952.
12. *“Photoluminescence of Ga-face AlGaN/GaN single heterostructures”*
G. Martinez-Criado, A. Cros, A. Cantarero, **C.R. Miskys**, O. Ambacher, R. Dimitrov,
M. Stutzmann, Mater. Sci. Eng. B 82 (2001) 200.
13. *“Growth of quaternary AlInGaN/GaN heterostructures by plasma-induced molecular beam epitaxy”*
A.P. Lima, **C.R. Miskys**, U. Karrer, O. Ambacher, A. Wenzel, B. Rauschenbach,
M. Stutzmann, J. Cryst. Growth 220 (2000) 341.
14. *“GaN homoepitaxy by metalorganic chemical-vapor deposition on free-standing GaN substrates”*
C.R. Miskys, M.K. Kelly, O. Ambacher, G. Martinez-Criado, M. Stutzmann,
Appl. Phys. Lett. 77 (2000) 1858.
15. *“Influence of oxygen and methane plasma on the electrical properties of undoped AlGaN/GaN heterostructures for high power transistors”*
R. Dimitrov, V. Tilak, W. Yeo, B. Green, H. Kim, J. Smart, E. Chumbes, J.R. Shealy,
W. Schaff, L.F. Eastman, **C. Miskys**, O. Ambacher, M. Stutzmann,
Solid State Electron. 44 (2000) 1361.

16. *“Characterization of InGaN thin films using high-resolution x-ray diffraction”*
L. Gorgens, O. Ambacher, M. Stutzmann, **C. Miskys**, F. Scholz, J. Off,
Appl. Phys. Lett. 76 (2000) 577.
17. *“MOCVD-epitaxy on free-standing HVPE-GaN substrates”*
C.R. Miskys, M.K. Kelly, O. Ambacher, M. Stutzmann,
phys. stat. sol. (a) 176 (1999) 443.
18. *“Detonations of gallium azides: A simple route to hexagonal GaN nanocrystals”*
A.C. Frank, F. Stowasser, H. Sussek, H. Pritzkow, **C.R. Miskys**, O. Ambacher,
M. Giersig, R.A. Fischer, J. Am. Chem. Soc. 120 (1998) 3512.
19. *“Characterization of InP grown by LEC using glassy carbon, silica and PBN crucibles”*
C.E.M. de Oliveira, M.M.G. de Carvalho, C.A.C. Mendonca, **C.R. Miskys**,
G.M. Guadalupi, M. Battagliarin, M.I.M.S. Bueno,
J. Cryst. Growth 186 (1998) 487.
20. *“Nanoscale hexagonal gallium nitride from single molecule precursors: Microstructure and crystallite size dependent photoluminescence”*
A.C. Frank, F. Stowasser, **C.R. Miskys**, O. Ambacher, M. Giersig, R.A. Fischer,
phys. stat. sol. (a) 165 (1998) 239.
21. *“Growth of InP by LEC using glassy carbon crucibles”*
C.E.M. de Oliveira, M.M.G. de Carvalho, **C.R. Miskys**,
J. Cryst. Growth 173 (1997) 214.


List of Abbreviations

2DEG	Two-Dimensional Electron Gas
a.u.	arbitrary units
AFM	Atomic Force Microscopy
ARC	Anti-Reflective Coating
CAIBE	Chemical Assisted Ion Beam Etching
CBE	Chemical Beam Epitaxy
CCD	Charge-Coupled Device
CL	Cathodoluminescence
CMP	Chemical–Mechanical Polishing
DC	Direct Current
ECR	Electron Cyclotron Resonance
EL	Electroluminescence
ELOG	Epitaxial Lateral Overgrowth
EPD	Etch Pit Density
FWHM	Full-Width at Half-Maximum
HBT	Heterojunction Bipolar Transistor
HEMT	High Electron Mobility Transistor
HFCVD	Hot Filament Chemical Vapour Deposition
HNPS	High Nitrogen Pressure Solution
HPHT	High Pressure-High Temperature
HRXRD	High Resolution X-Ray Diffraction
HVPE	Hydride Vapour Phase Epitaxy
ICP	Inductively Coupled Plasma
I-O	Input-Output
IR	Infrared
LC	Liquid Crystal
LD	Laser Diode
LED	Light Emitting Diode
LN ₂	Liquid Nitrogen
LO	Longitudinal Optical
LT	Low Temperature

MBE	Molecular Beam Epitaxy
MEMS	Micro-Electro-Mechanical Systems
MOCVD	Metalorganic Chemical Vapour Deposition
MQW	Multiple Quantum Well
MTP	Multiply Twinned Particles
PIMBE	Plasma Induced Molecular Beam Epitaxy
PL	Photoluminescence
r.l.u.	relative lattice units
r.u.	relative units
RF	Radio Frequency
RHEED	Reflection High-Energy Electron Diffraction
RIE	Reactive Ion Etching
RIE-MIE	Magnetron Reactive Ion Etching
RMS	Root Mean Square
SAW	Surface Acoustic Wave
SEM	Scanning Electron Microscopy
SMB	Stacking Mismatch Boundaries
SQW	Single Quantum Well
TEM	Transmission Electron Microscopy
UV-VIS	Ultraviolet-Visible
VPE	Vapour Phase Epitaxy
XRD	X-Ray Diffraction

Acknowledgements

“I am Alpha and Omega, the beginning and the ending, saith the LORD, which is, and which was, and which is to come, the Almighty. ...The LORD our God is one Lord: and thou shalt love the LORD thy God with all thy heart, and with all thy soul, and with all thy mind, and with all thy strength: this is the first commandment. And the second is like, namely this, Thou shalt love thy neighbour as thyself. There is none other commandment greater than these” Revelation 1:8, St. Mark 12:29-31. According to my faith I want to thank my Lord and Saviour Jesus Christ for his love and shelter during all these years.



It is surely difficult to express in words my gratitude to all the people who have supported me in accomplishing this PhD work during the last years. I sincerely hope to have fairly thanked everyone who helped me to close this quite long chapter of my life.

I would like to express my most grateful thanks to Prof. Dr. Martin Stutzmann for giving me the great opportunity to be part of his group in the Walter Schottky Institute at the Technical University Munich. It was a honor and a big pleasure to be his PhD student for so many years, profiting from his outstanding scientific skills and remarkable argumentation capability. Not only that, but it was finally his very friendly and fine way of interacting with people that filled me with a deep respect to his person. For his patience with me, principally in the last phase of my PhD, I should write another thesis only to express my gratitude. As this can take some time, I just want to say here: *Muito obrigado Martin!*

I am also deeply indebted to Prof. Dr. Oliver Ambacher for being my direct guide and advisor during the first years of my time at the WSI. His efficiency and organization at work impressed me since the beginning and I am glad to have learned a lot from him. Besides the scientific interaction, there were also many pleasant moments with him and other colleagues of our group. To mention are the casual visits to the beer garden in Garching, the amazing boat trips along the beautiful Isar river, and the Bayern-München soccer games we have seen at his place, enjoying also the presence of his beloved wife and kids. After all, I want also to express here my respect and gratitude, and wish him much success in Ilmenau.

Mister Assistant-Professor Dr. José Antonio Garrido deserves many, a lot of thanks from me. Much beyond the very fruitful scientific interaction, discussions, and collaborations, in which he showed me some of his multiple capabilities and skills, much beyond diamonds and nitrides, and Chapter 4, it is his sincere friendship that I am deeply thankful. But I am also indebted to him for his help in correcting this thesis, for his suggestions and almost 24 hours availability. It is not in the scope of this work to mention my gratitude for his attendance in a critical personal situation from the last years, so I want simply to say here: *“Muchas gracias por todo José!”*

I have been very fortunate to have known Dr. Gema Martínez Criado in the WSI some years ago. Since the beginning there was a productive scientific interaction growing together with our friendship. Both did not stop until now and seems to continue without an end. I have to thank her for her impressive analysis capability and skills in optical characterization with the PL and Raman techniques, specifically in our work with GaN. *“Muchas gracias Gemita!”*

I have also the pleasure to thank my friend Dr. Günther Anton Johann Vogt for the inspiring and pleasant interaction since the good old times in the MBE laboratory. His outstanding expertise in X-ray diffraction and structure analysis of crystals, much bigger than all the

unexpected difficulties we encountered, gave rise to the new interesting insights about the heteroepitaxy of diamond/AlN in Chapter 4. “*Vielen Dank Günther!*” and what about “*Toc-toc?!*”

My thanks also to Priv.-Doz. Dr. Christoph Nebel to introduce me in the precious, but not trivial world of diamonds, and for being part of the initial task force in the challenging project to meet ceramics with gems to produce an UV-emitting heterodiode. Thanks for the friendly and productive interaction during my PhD time in the WSI. I sincerely wish him much success in Japan.

A very special thank has to be directed to Dr. Mike K. Kelly: the laser liftoff man. Due to his spectacular cleverness with lasers and optics, he discovered and implemented the laser induced liftoff method for the delamination of GaN/sapphire. I had first to step on his footprints to then be able to explore the amazing application potential of this elegant technique for the GaN-based technology.

For his help showing me how to use the *Mathematica* software for the laser/target simulation in Chapter 2, and for all the productive discussions I am indebted to thank Dr. Tobias Graph. His big enthusiasm with physics and his extraordinary mathematical skills always impressed and motivated me to work even harder.

I am indebted to thank Mr. Paul Schmidt for the translation of a scientific paper from Russian to German, which allowed me to get important data about the thermal expansion coefficient of GaN as a function of temperature for the computer simulations of the laser/target interaction in Chapter 2.

I particularly wish to express my gratitude to Dr. Stephan Kaiser and Claudia Kriegler from OSRAM Optoelectronics in Regensburg for the exceptionally friendly interaction and productive collaboration concerning the laser liftoff of wafer bonded GaN layers. It was very interesting to be part of the project for the implementation of the laser liftoff technique for industrial scale production of GaN-based LEDs.

My thanks also to Dr. Joachim Wagner and Peter Schlotter from the Fraunhofer Institut (IAF) in Freiburg for the successful collaboration involving the laser delamination of flip-chip bonded blue/violet InGaN/GaN-LEDs.

I am indebted to thank Dr. Alexandre Pimenta Lima, Mr. MBE, for the first attempts to optimize the growth of PIMBE-AlN/diamond, but also for the “Brazilian” friendship and many suggestive scientific discussions. Not to forget the wonderful time when Brazil won the world soccer championship for the 5th time: *“Pentacampeão!!!”*

My thanks to Martin Herrmann for the growth of the last MBE-AlN film on diamond. I wish that he can go on with the results about the heteroepitaxy of nitrides on diamond presented in this thesis, and successfully finish his PhD work.

In this place I want to thank Dr. Martin Eickhoff for correcting a part of this thesis and for the nice interaction and scientific collaboration at the WSI.

Here I want to express my thanks to Priv.-Doz. Dr. Martin S. Brandt for his very nice way of being, but also for his good advice and motivating words at the WSI’s corridors from time to time.

I would like to thank Dr. Roman Dimitrov from the old staff, even if I do not know anymore where he is, for innumerable nice hours spent together in the WSI's laboratories, and on the soccer fields with sunny, rainy, snowy or apocalyptic weather.

There is a lot of people from the "old" staff that I would also like to thank for the nice time together in the WSI building, for all the interesting discussions, for the good and bad jokes, ladies first: Andrea Mitchell, Angela Link, Andreas Janotta, Helmut Angerer, Lutz Görgens, Martin Bayerl, Robert Handschuh, Uwe Karrer, Roland Zeisel, Sebastian Gönnerwein, and Thomas Wimbauer.

Now, my thanks to the "new" generation staff for the pleasant time together, the nice hours in the yellow technology room, for some shared pizza late at night, soccer tournaments, WSI's summer parties, etc, etc: to the lovely Barbara Baur, the smiley Andrea Baumer (geb. Lehner), Mr. Andreas Härtl, the guy with a broken laptop Edgar Zaus, the Bavarian Georg Steinhoff, the spinner Hans Hübl, the Spanish Jorge Hernando, the polite Olaf Weidemann, the funny Mario Gjukic, the young Robert Lechner, the experienced Svetoslav Koynov, the baby-PhD student Thomas Wassner, and the "dangerous" Tobias Heimbeck.

My big gratitude is also devoted to our technical staff: Sonja Matich, Michael Fischer, Ralph Wasserrab, Bernhard Kratzer, Fritz Sedlmaier, and Wolfgang Bendak for innumerable important technical helps during my time in the WSI. Many sincere thanks for the friendly atmosphere and cooperativeness.

I want to expose here my special thank to Veronika Enter, who was ever an efficient and essential helping hand in all variations of the secretarial works, always followed by her friendly smiling and unbreakable good mood.

In this place I want sincerely to thank the Coordination for the Advancement of Higher Education Personnel - Brazil (CAPES) for the financial support, which primarily enabled the realization of my PhD work in Germany at the Technical University Munich.

To my angel Eli Elisia Deifeld I want to thank from the bottom of my heart for her sweet presence and more than motivating words during the time she spent on my side while I was writing this thesis. I wish her all success to conclude her graduation study and a never-ending happiness.

My special thanks to Dr. Vitor Zaia. His friendship and open ears helped me to stand a very critical situation I had to experience in the last years of my PhD.

For the nice hours together, the delicious dinners, trips, the house move-outs, for so many nice remembrances, I want to thank my dear friends Núria and José, Nina-Honey (Hurny) and Alexandre, Steffi, Renate and Vitor, Jorge, Silvia Celini, Gema and Alejandro. Our ways may separate us, but I will never forget you. Real friendships do not fade away: *“Valeu a força!”*

Also my friends in my beloved Brazil I want to thank for their sincere friendship: Edvaldo, Laércio, Ari and family, Luciana from Campinas, Prof. Mauro, Francisca and family, Clóvis and family - Shalom to Israel!

In Germany, Austria, Switzerland, France, Poland, Slovenia, etc., I simply thank from the bottom of my heart all my beloved brothers and sisters in Jesus Christ for the wonderful time together, the submarine day or *“Schiffe versenken”* at the Niers, the blessed meetings in Lossburg, the trip to Israel, the tours around Germany. You all are already part of me. Finally, the *“Nur noch drei Monate”* is finished !!!

To my family:

Last but not least, I would like to express my deepest gratitude to my whole family: to my beloved parents Walter and Anita Miskys for all the love and support since I was born; to my dear brother Helmut, his wife Erika, and their beloved children, Mathias+??, Andreas+Sabine+?, Tanja+Stephan+Natanael+Noemi, Christina+Andreas+?, Markus, Stefan, Rahel, and Daniela; to my dear sister Helga, her husband and my friend Heinz Sippach, and their beloved kids Marcel and Jessica; to my dear brother Thomas and his lovely wife Eunice in Brazil; to my dear Tante Käte, and my lovely cousin Rosinha. I want also to deeply thank my uncle Manfred Sauer and his beloved wife Wiltrud for their love and support. My uncle passed away some years ago, but he is still present in all our hearts.

Even if I would write down dozens of pages thanking for the prayers and listing everything they did to help me since I arrived in Germany, these written lines would not be sufficient to express my real gratitude. So, my sincere thanks and God bless you all is my heartfelt wish.


Jim